

**Gregor Kiedorf**

**Mechanistic and kinetic  
analysis of homogeneously  
and heterogeneously catalyzed  
reactions**



MAX PLANCK INSTITUTE  
FOR DYNAMICS OF COMPLEX  
TECHNICAL SYSTEMS  
MAGDEBURG



OTTO VON GUERICKE  
UNIVERSITÄT  
MAGDEBURG

# **Mechanistic and kinetic analysis of homogeneously and heterogeneously catalyzed reactions**

## **Dissertation**

zur Erlangung des akademischen Grades

## **Doktoringenieur (Dr.-Ing.)**

von Dipl.-Ing. Gregor Kiedorf  
geboren am 11. Februar 1985 in Wolfen

genehmigt durch die Fakultät für Verfahrens- und Systemtechnik  
der Otto-von-Guericke Universität

Promotionskommission: Prof. Dr. rer. nat. Helmut Weiß  
Prof. Dr.-Ing. Andreas Seidel-Morgenstern  
Prof. Dr.-Ing. Ulrich Niekem  
Prof. Dr. rer. nat. Reinhard Schomäcker  
Prof. Dr.-Ing. Christof Hamel

eingereicht am: 06.06.2017  
Promotionskolloquium am: 27.10.2017



Forschungsberichte aus dem Max-Planck-Institut  
für Dynamik komplexer technischer Systeme

Band 49

**Gregor Kiedorf**

**Mechanistic and kinetic analysis of homogeneously  
and heterogeneously catalyzed reactions**

Shaker Verlag  
Aachen 2018

**Bibliographic information published by the Deutsche Nationalbibliothek**

The Deutsche Nationalbibliothek lists this publication in the Deutsche Nationalbibliografie; detailed bibliographic data are available in the Internet at <http://dnb.d-nb.de>.

Zugl.: Magdeburg, Univ., Diss., 2017

Copyright Shaker Verlag 2018

All rights reserved. No part of this publication may be reproduced, stored in a retrieval system, or transmitted, in any form or by any means, electronic, mechanical, photocopying, recording or otherwise, without the prior permission of the publishers.

Printed in Germany.

ISBN 978-3-8440-5768-3

ISSN 1439-4804

Shaker Verlag GmbH • P.O. BOX 101818 • D-52018 Aachen

Phone: 0049/2407/9596-0 • Telefax: 0049/2407/9596-9

Internet: [www.shaker.de](http://www.shaker.de) • e-mail: [info@shaker.de](mailto:info@shaker.de)

## Vorwort

Diese Arbeit entstand während meiner Tätigkeit als wissenschaftlicher Mitarbeiter am Max-Planck-Institut für Dynamik komplexer Technischer Systeme in Magdeburg und in Kooperation mit dem Sonderforschungsberich Transregio 63 (SFB-TR 63) der Deutschen Forschungsgemeinschaft. An dieser Stelle möchte ich die Chance nutzen, um mich für die tatkräftige Unterstützung zu bedanken, welche mir hier zu Teil wurde.

Mein besonderer Dank gilt Herrn Prof. Seidel-Morgenstern für die Möglichkeit, mich diesem interessanten und vielfältigen Thema zu widmen, die ideal geschaffenen Rahmenbedingungen und die wissenschaftlichen Freiheiten, welche mir hier gewährt wurden. Für dieses Vertrauen bedanke ich mich ausdrücklich. Im gleichen Atemzug bedanke ich mich bei Herrn Prof. Hamel für die exzellente Betreuung, den zahlreichen Ratschlägen, Anmerkungen und das freundschaftliche Umfeld in „seiner“ Reaktionstechnik.

Herrn Prof. Ulrich Nicken und Herrn Prof. Reinhard Schomäcker danke ich für die eingebrachten Ideen zum Reaktoraufbau bzw. für die tatkräftige Unterstützung bei der Ableitung der Katalysezyklen zur Hydroformylierung. Darüber hinaus danke ich Ihnen für die Begutachtung dieser Arbeit.

Bei den Mitarbeitern der Gebäude übergreifenden Reaktionstechnik möchte ich mich für die hervorragende Zusammenarbeit und das einmalige Arbeitsklima bedanken. Hierbei möchte insbesondere Matthias Felischak, Martin Gerlach, Andreas Jörke, Thomas Munkelt, Henning Haida, Jens Markert, Tino Lehmann, Luise Blach, Jutta Wilke und Dr. Tanya Wolff für die gemeinsame Zeit danken. Darüber hinaus möchte ich meinen direkten Bürokollegen Dr.-Ing. Kamila Gałan, Stephan Münzberg und Susann Triemer für den „interdisziplinären“ Austausch und die nie enden wollenden Diskussionen meinen Dank aussprechen. Für die schnelle und unkomplizierte Hilfe in organisatorischen Angelegenheiten danke ich Sophia Pistorius, Nancy Ziebell, Stephanie Geyer und Marion Hesse.

Für den technischen Support bei Planung und Aufbau diverser Versuchsanlagen sowie für die tatkräftige Unterstützung bei zahlreichen Störfällen möchte ich mich bei Detlef Franz, Stefan Hildebrandt, Steve Haltenhof, Reiner Könning, Klaus-Dieter Stoll, Martin Stengel und Jan Protzmann bedanken.

Zum Schluss gilt mein Dank meiner Familie und insbesondere meiner Frau Marielle für ihre Geduld, Motivation und mentale Unterstützung vor allem in den Phasen der wissenschaftlichen Stagnation.



## Abstract

The experimental study of novel reactor concepts is financially expensive and time consuming. In order to optimize the reactor and process development, model based optimization strategies are becoming more popular. Basic requirement of these strategies are general reaction kinetics in a broad temperature and concentration range. Quite often simple empirical rate expressions, e.g. power laws, are in good agreement with available experimental data. However, there are several limits of such rate equations with respect to extrapolation. For this reason, the present work focuses on mechanistic reaction kinetic analysis and the corresponding parameter estimation in homogeneous and heterogeneous catalysis and their model application in innovative dynamic reactor concepts. The efficient and phase independent "General Catalytic Cycle Kinetics (GCCK)" approach (or *Christiansen* methodology) is used to derive mechanistic kinetic rate approaches based on catalytic cycles. Due to high number of unknown kinetic parameters included in the mechanistically based GCCK approach, suitable model reduction techniques, such as the subset selection method or additional independent specific dynamic experimental data, support parameter estimation. Sensitive parameters can be identified and determined for the reduced kinetic models. In the presented case studies, the GCCK approach is successfully applied for the homogeneously catalyzed hydroformylation and the heterogeneously catalyzed total oxidation.

In a first part, the homogeneously catalyzed hydroformylation of 1-dodecene was studied using a rhodium-biphenos catalyst complex exploiting a thermomorphic multicomponent solvent system. In order to describe the kinetics of the main and the most relevant side reactions the experiments were performed in a batch reactor. The formation of the active catalyst was studied in individual experiments. Based on a postulated catalytic cycle mechanistic kinetic models were developed considering isomerization, hydrogenation and hydroformylation reactions as well as the formation of not catalytically active Rh-species. The complex overall network was decomposed to support parameter estimation. The main and side reactions were investigated as a function of temperature, total pressure and partial pressures of carbon monoxide and hydrogen, respectively. Four sub-networks of increasing size and the total network were analyzed sequentially in order to identify kinetic models and to estimate the corresponding parameters applying the subset selection technique. Based on this quantified reaction model advanced reactor concepts were experimentally validated applying various operation modes, such as batch, semi-batch, perturbed batch and continuous operation. On the extended experimental data basis, the kinetic models were adjusted by an additional carbon monoxide order and the parameters of the reaction kinetics were refined to give reliable model predictions. Finally, a recycling strategy is theoretically studied to maximize the selectivity towards the desired linear aldehyde.

In a second part, the reaction kinetics of the heterogeneously catalyzed partial and total oxidation of  $C_2H_4$ ,  $C_3H_6$  separately and in mixtures and CO on a  $CrO_x/\gamma-Al_2O_3$  catalyst

were studied. Based on well-established reaction simplified mechanisms, mechanistic kinetic models of all reactions were derived. In order to support the parameter estimation and to describe the adsorption behavior of the components involved, *Langmuir* adsorption isotherm models were applied. Using these models, the single component adsorption behavior could be characterized quite well. By means of the *Multi-Langmuir* model, based exclusively on the parameters of the single component isotherms, the competitive adsorption behavior of ethylene and propylene mixtures could be predicted. Using these separately determined adsorption parameters within the kinetic analysis, a more profound description of the reaction rates was feasible by separating kinetic and thermodynamic effects. The subsequent kinetic analysis of the total oxidation reaction network occurred considering three different sub-networks and the total network. The kinetic parameters of each sub-network were transferred to the progressively larger sub-network and finally to the total network. All sub-networks and the total reaction network could be well described by using one set of kinetic parameters.

The determined total oxidation reaction kinetics were validated using the periodic operation of the challenging multi fixed-bed Loop Reactor (LR) concept. As general characterization of the LR concept, a simulation study for single component and multi-component feeds was performed using simplified reaction kinetic models adopted from literature. To understand the reaction and temperature front velocities as well as the maximum temperature within the reactor cascade, the most relevant operating and reactor parameters were varied in a wide range. Based on these theoretical results, an experimental study was performed. Systematic experiments of the LR operation using closed loop control revealed the domain of ignited reactor states as function of the reactant inlet concentrations and the total volumetric fluxes. Additionally, step experiments altering reactant inlet concentrations demonstrated the applicability of the LR concept for the purification of industrial volatile organic compound exhaust streams. Simulation results using an extended reactor model and the mechanistic kinetic models of the total oxidation reactions determined via the GCCK approach gave a relative good qualitative agreement with respect to the temperature profiles.

The methods and tools developed and used in this work for the derivation of mechanistic kinetic rate models are suitable for homogeneous as well as for heterogeneous catalysis and provide the basis for the development of new reactor concepts.

## Kurzfassung

Experimentelle Studien neuartiger innovativer Reaktorkonzepte, welche ein effizientes und ressourcenschonendes Arbeiten ermöglichen, sind finanziell und zeitlich sehr aufwendig. Um diese Reaktor- aber auch Prozessentwicklung zu beschleunigen, existiert eine Reihe von modellbasierten Optimierungsstrategien um oft eingeschränkte Betriebsfenster zu bestimmen. Diese erfordern jedoch eine allgemeingültige Reaktionskinetik für einen großen Anwendungsbereich. Häufig genutzte empirische und semi-empirische Modelle beschreiben aber nur kleine Betriebsfenster. Eine Extrapolation dieser Reaktionskinetiken in Konzentrations- oder Temperaturbereiche außerhalb des Messregimes ist somit nicht möglich. Aus diesem Grund liegt der Fokus dieser Arbeit auf der Ableitung mechanistischer Reaktionsmodelle für die homogene und heterogene Katalyse, der Abschätzung der jeweiligen kinetischen Parameter und der Anwendung der quantifizierten Reaktionsmodelle für die Untersuchung von innovativen Reaktorkonzepten. Eine effiziente und phasenunabhängige Methode zur Ableitung mechanistischer Modelle anhand katalytischer Zyklen ist der „General Catalytic Cycle Kinetics“ Ansatz (auch *Christiansen* Methode genannt). Diese wurde für alle präsentierten Fallbeispiele angewendet. Um die physikalische Bedeutung der kinetischen Parameter zu gewährleisten, müssen diese überparametrierten Reaktionsmodelle für gewöhnlich reduziert werden. Hierfür existierten mathematische Parametersensitivitätsanalysen, mit der Parameterkorrelationen während der Abschätzung identifiziert werden können. Aber auch zusätzliche individuelle Messungen, wie z.B. von thermodynamischen Phasengleichgewichten der Reaktanten oder Produkte konnten in die reaktionskinetischen Analysen integriert werden und somit die Parameterschätzung vereinfachen. Diese beiden Vorgehensweisen sind innerhalb dieser Arbeit erfolgreich zum Einsatz gekommen.

Das erste betrachtete Reaktionssystem ist die homogene Rhodium-biphephos katalysierte Hydroformylierung von 1-Dodecen in einem temperaturgesteuerten Multikomponenten Lösungsmittelsystem. Die reaktionskinetische Netzwerkanalyse zur Beschreibung der wichtigsten Haupt- und Nebenreaktionen erfolgte experimentell in einem Batch-Reaktorsystem. Mechanistische Reaktionsmodelle wurden für die Isomerisierung, Hydrierung und Hydroformylierung von 1-Dodecen anhand des allgemeingültigen *Wilkinson* Katalysezyklus aufgestellt. Die hierfür notwendige aktive Katalysatorspezies wurde durch einen Gleichgewichtsansatz beschrieben, welches auch inaktive Rhodiumdimere berücksichtigt. Die Parameterschätzung erfolgte an vier Subnetzwerken mit steigender Größe und Komplexität sowie am Gesamtreaktionsnetzwerk in einem breiten Temperatur-, Druck- und Konzentrationsbereich. Existierende Parameterkorrelationen wurden mittels Sensitivitätsanalyse identifiziert und durch geschickte Modellreduktion beseitigt. Mit Hilfe des mechanistischen Reaktionsmodells wurden verschiedene Operationsweisen wie Batch, Semi-Batch, Perturbationsexperimente und kontinuierlicher Betrieb eines Rührkessels experimentell validiert. Auf Basis einer sensitiven Versuchsmatrix wurde das kinetische Modell nochmals

verbessert und erweitert, wodurch es nun möglich war, die verschiedenen Operationsweisen in einem großen Temperatur-, Druck-, und Konzentrationsbereich über die experimentell untersuchten Bereiche hinaus zu beschreiben. Zum Abschluss ist eine Modellstudie für eine Recyclingstrategie von 1-Dodecen und dessen Isomere aufgezeigt, womit die Selektivität des gewünschten linearen Aldehyds Tridecanal maximiert werden konnte.

Als zweites Beispiel ist die heterogen katalysierte Totaloxidation von kurzkettigen Kohlenwasserstoffen einzeln und in Mischung sowie von Kohlenstoffmonoxid an einem  $\text{CrO}_x/\gamma\text{-Al}_2\text{O}_3$  Katalysator untersucht wurden. Basierend auf einfachen etablierten Reaktionsmechanismen konnten mechanistische reaktionskinetische Modelle für alle betrachteten Reaktionen abgeleitet werden. Zur Vereinfachung der Parameterschätzung kamen zusätzliche individuelle Messungen von Einzelstoff- und Gemischadsorptionsisothermen der verschiedenen Reaktanten und Produkte zur Parametrierung von Adsorptionskonstanten innerhalb der kinetischen Modelle zum Einsatz. Mit der individuellen Beschreibung der Adsorptionskonstanten wurde eine fundierte Beschreibung der Reaktionskinetik durch Trennung kinetischer und thermodynamischer Effekte erst ermöglicht und die Konfidenzintervalle reduziert. Zusätzlich zu dieser Vorgehensweise der Modellreduktion wurde das Reaktionsnetzwerk in drei verschiedene Subnetzwerke zerlegt. Somit konnten die kinetischen Parameter quantifiziert und validiert werden.

Basierend auf der erarbeiteten Reaktionskinetik wurde die Funktionalität des Loop Reaktor Konzepts demonstriert. Hierfür wurde zuerst mit einer Modellkinetik eine Simulationsstudie durchgeführt um die verschiedenen Aspekte des zyklisch stationären Betriebs zu analysieren. Auf Grund der vereinfachten Rechnung konnten sehr schnell die verschiedenen Einflussmöglichkeiten auf die Frontengeschwindigkeiten, die maximal erreichte Temperatur und die Schaltzeit der einzelnen Takte für Gemische mit unterschiedlichen Zündtemperaturen untersucht werden. Die einzelnen Experimente zum Loop Reaktor wurden in einer Versuchsanlage im Pilotmaßstab durchgeführt. Ein stabiler gezündeter Betrieb konnte für ein breites Spektrum an Eintrittskonzentrationen und Volumenströmen gezeigt werden. Zusätzliche Perturbationsexperimente für schrittweise Konzentrations- und Volumenstromänderungen für Ethen und Propen im Reaktionsgemisch konnten die Funktionalität unter Beweis stellen. Modellierungsergebnisse unter Verwendung eines detaillierten Reaktormodells und der abgeleiteten vollständigen Reaktionskinetik für das Totaloxidationsnetzwerk ergaben gute Qualitative Übereinstimmungen von zu erwartenden Temperaturprofilen.

Die in dieser Arbeit entwickelten und genutzten Methoden und Werkzeuge zur Herleitung mechanistischer, extrapolierbarer Kinetikmodelle sind sowohl für die homogene, als auch für die heterogene Katalyse geeignet und bilden somit die Grundlage für die Entwicklung neuer Reaktorkonzepte.

# Table of Contents

<b>I</b>	<b>Challenges in Homogeneous and Heterogeneous Catalysis</b>	<b>1</b>
<b>1</b>	<b>Introduction</b>	<b>3</b>
<b>2</b>	<b>Theoretical Basics</b>	<b>7</b>
2.1	Mechanistic kinetic rate models	8
2.1.1	Application of the GCCK approach in homogeneous catalysis	9
2.1.2	Application of the GCCK approach in heterogeneous catalysis	10
2.2	Parameter estimation, statistical evaluation and model reduction techniques	13
2.2.1	Objective functions	14
2.2.2	Optimization methods and procedure	15
2.2.3	Model reduction techniques	16
2.2.4	Statistical evaluation of estimated parameters	19
2.3	Reactor models	19
2.3.1	Stirred tank reactor models	20
2.3.2	Model of single tubular reactor	21
2.3.3	Models of reactor cascade (Loop Reactor)	22
2.4	Conclusions	24
<b>II</b>	<b>Analysis of a Homogeneously Catalyzed Reaction</b>	<b>25</b>
<b>3</b>	<b>Reaction Network and Kinetics of the Hydroformylation of 1-Dodecene</b>	<b>27</b>
3.1	Solvent system, ligand and reaction network	29
3.2	Catalytic cycle and mechanistic models	30
3.2.1	Catalytic cycle and the resting state of the catalyst species	30
3.2.2	Mechanistic approach to describe the rates in a network of reactions	34
3.2.3	Reduced models with a single rate determining step	34
3.2.4	Reduced empirical models based on formal kinetics	34
3.2.5	Summary of considered kinetic models	35
3.3	Experimental equipment and procedures	36
3.3.1	Reactor type	36
3.3.2	Kinetic experiments	36
3.3.3	Concentration analysis	37
3.4	Results of preliminary experiments	38
3.4.1	Initial investigation of gas solubilities	38
3.4.2	Formation of active catalyst species	39
3.5	Network analysis	40
3.5.1	Free parameters and estimation strategy	41

3.5.2 Isomerization of 1-dodecene: sub-network I .....	42
3.5.3 Hydrogenation of iso-dodecene: sub-network II.....	46
3.5.4 Hydrogenation of 1-dodecene: sub-network III .....	47
3.5.5 Hydroformylation of iso-dodecene: sub-network IV .....	49
3.5.6 Hydroformylation of 1-dodecene: total network .....	50
3.5.7 Evaluation of the overall approach followed and the kinetic parameters estimated .....	54
3.6 Conclusions.....	55
<b>4 Application of Kinetic Models: Different Reactor Operations .....</b>	<b>57</b>
4.1 Experimental equipment and procedures .....	57
4.2 Preliminary experiments.....	58
4.3 Evaluation of different operation modes.....	60
4.3.1 Batch operation mode.....	62
4.3.2 Semi-batch operation mode.....	62
4.3.3 Dynamic operation mode (perturbation experiments).....	63
4.3.4 Continuous operation mode.....	64
4.4 Parametric study of feed variation.....	66
4.5 Conclusions.....	68
<b>III Analysis of Heterogeneously Catalyzed Reactions .....</b>	<b>71</b>
<b>5 Kinetics of the Total Oxidation of Short-Chain Hydrocarbons .....</b>	<b>73</b>
5.1 Catalyst characterization and reaction network .....	75
5.1.1 Catalyst preparation and characterization .....	75
5.1.2 Reaction network .....	76
5.2 Catalytic cycle and mechanistic models.....	77
5.3 Experimental equipment and procedures .....	78
5.4 Preliminary determination of gas/solid adsorption equilibria .....	80
5.4.1 Determination of single component adsorption isotherms .....	81
5.4.2 Determination of mixture adsorption isotherms .....	83
5.4.3 Experimental equipment and methods for adsorption isotherms.....	84
5.4.4 Single component adsorption measurements.....	85
5.4.5 Prediction and validation of mixture adsorption isotherms.....	90
5.4.6 Conclusions regarding additional adsorption investigation .....	92
5.5 Kinetic investigation and network analysis.....	93
5.5.1 Carbon monoxide oxidation: sub-network I.....	93
5.5.2 Ethylene oxidation: sub-network II .....	96
5.5.3 Propylene oxidation: sub-network III .....	99
5.5.4 Evaluation of the total oxidation reaction network.....	102
5.6 Conclusions.....	104

---

<b>6</b>	<b>Application of Kinetic Models: Multi Fixed-Bed Loop Reactor .....</b>	<b>107</b>
6.1	Principle and history of the Loop Reactor .....	107
6.2	Characterization of the Loop Reactor .....	109
6.2.1	Definition of switching times .....	110
6.2.2	Definition of control concepts .....	111
6.3	Simulation studies using simplified kinetics .....	111
6.3.1	Simplified kinetics and reactor model .....	112
6.3.2	Single reactant simulation study .....	112
6.3.3	Multi reactant simulation study .....	122
6.4	Experimental results of hydrocarbon total oxidation using LR concept .....	125
6.4.1	Experimental Loop Reactor equipment .....	125
6.4.2	Experimental observed periodic operation .....	128
6.4.3	Single component feed gas: ethylene or propylene .....	131
6.4.4	Mixture feed gas: ethylene and propylene.....	133
6.5	Validation of detailed kinetic model using single feed propylene.....	135
6.6	Conclusions .....	137
<b>IV</b>	<b>Summary .....</b>	<b>139</b>
<b>7</b>	<b>Overall Conclusions and Outlook .....</b>	<b>141</b>
7.1	Overall conclusions.....	141
7.2	Suggestions for further activities.....	145
	<b>References .....</b>	<b>147</b>
	<b>Nomenclature.....</b>	<b>163</b>
<b>A</b>	<b>Derivation of Mechanistic Models .....</b>	<b>167</b>
A.1	Homogeneous catalysis.....	167
A.2	Heterogeneous catalysis: <i>Langmuir/Hinshelwood</i> approach .....	169
A.3	Biological catalysis.....	171
A.4	Equilibrium constant.....	173
<b>B</b>	<b>Reactor Models .....</b>	<b>175</b>
B.1	Mass balance.....	175
B.2	Energy balance.....	176
B.3	Two phase mass transfer model.....	177
B.4	Loop reactor model for experimental data prediction.....	178
B.5	Simulation study for improved Loop Reactor operation .....	182
B.6	Estimation of ignition temperature .....	184
B.7	Determination of traveling front velocities .....	184
<b>C</b>	<b>Single Component Adsorption Isotherms .....</b>	<b>187</b>
<b>D</b>	<b>Schematic Illustrations of the Loop Reactor Plant.....</b>	<b>189</b>



**Part I**

**Challenges in Homogeneous and  
Heterogeneous Catalysis**



# 1 Introduction

Based on exhaustible raw materials and an enhanced demand for clean technologies, advances in chemical industries are aimed to intensify processes to increase product selectivity and for optimal resource utilization. The general chemical process design is based on reactant pretreatment followed by the reaction unit and product separation. Accordingly, for overall process optimization, several options are available. For an efficient process performance, specific reactor types were developed and optimized in regard to process conditions. Further strategies are based on process design, single unit operation improvements or process unit coupling in an integrative manner. The latter allows enhancements in productivity, selectivity and energy efficiency (Sundmacher et al., 2005). However, integrative reactor concepts require superposition of reaction, separation and material performance, which increases complexity regarding reactor design, process control and decreasing degrees of freedom.

In chemical reaction engineering, reactors will be classified in regard to the phases involved (Levenspiel, 1999; Baerns, 2006; Beller et al., 2012). If the reactants, products and if required the chemical catalyst are in a single phase, the system is called as homogeneous reaction system. In contrast, a heterogeneously catalyzed system is defined by different phases of the reactants and the catalyst, respectively. As an example, can be mentioned two gaseous components react on a solid catalyst surface. In this regard, interphase mass transport of the reactants and products affects the reaction performance significantly and have to be taken into account (Helfferich, 2004).

A further classification of chemical reactors can be done by the operation mode. Batch and continuous operation provide the boundary conditions. Between these cases semi or perturbed batch operation can be mentioned. Accordingly if a highly exothermal chemical reaction occurs or a high productivity is required, the optimal reactor operation concept must be selected (Agar and Ruppel, 1988; Levenspiel, 1999).

For selection, design and optimization of chemical reactors for specialty as well as bulk chemicals, basic information about the reaction network and reaction rates are required. The main branches of the reaction network including the main, side and consecutive reactions have to be identified and quantified. The main chemical pathway within a complex reaction network is mostly affected by chemical catalyst design. Hence, product selectivity improvements are based on the optimal catalyst design studies to obtain the defined requirements (Ertl et al., 2008). The definition of a catalyst is given by Ostwald in 1923 (Ostwald, 1924; Freund et al., 2014):

*“A catalyst is a substance that accelerates the rate of a chemical reaction without being part of its final products.”*

However, according to Hamel (Hamel, 2016) and Salmi (Zheng et al., 2016) optimization potential for desired product selectivity is given by process structure developments such as advanced reactor concepts or simple recycle streams as well. In general, innovative novel reactor and process optimization strategies are model based (Freund and Sundmacher, 2008; Steimel and Engell, 2016). These strategies requires quantitative knowledge about the kinetics of the reactions involved (Levenspiel, 1999) and reactor

models describing the laboratory reactors used to generate the experimental data basis (Froment and Bischoff, 1990; Baerns, 2006). Suitable kinetic expressions can be determined by several concepts in order to achieve the degree of detail and the precision required. Due to the complexity of the kinetics of simultaneously occurring reactions frequently simple empirical rate expressions are applied, as e.g. power laws. They can capture main features of the reaction kinetics and are in some cases in good agreement with available experimental data. However, due to their simplicity there are clear limitations of such non-mechanistic rate equations. Consequently, extrapolations beyond the range of measurements are highly uncertain.

For this purpose, this thesis applied a widely applicable strategy to determine and quantify mechanistic reaction kinetics for both homogeneously and heterogeneously catalyzed reactions. Subsequently, these quantified kinetics will be used to investigate challenging innovative dynamic reactor concepts. The aim of this thesis is to study the reactor concepts and to validate the determined mechanistic reaction kinetics.

### **Catalytic cycles**

To obtain universal reaction kinetics, mechanistic rate approaches are required. The basis of an adequate mechanistic rate approach is an established catalytic cycle, which is often unknown or only partly. In homogeneous catalysis the identification of catalytic cycles occurs using spectroscopic methods such as UV/VIS, high-pressure infrared spectroscopy, nuclear magnetic resonance spectroscopy, mass spectroscopy, extended X-ray absorption fine structure analysis or inductively coupled plasma emission spectroscopy (Behr, 2008; Beller et al., 2012). In contrast, in heterogeneous catalysis detailed molecular studies often have to limit themselves to the investigation of single elementary steps of the overall catalytic cycle (Beller et al., 2012). For example Sattler et al. (Sattler et al., 2014) reveals several active sites on a  $\text{CrO}_x/\gamma\text{-Al}_2\text{O}_3$  catalyst. Using Raman and UV-VIS technique four different active oxidation states and chromium centers were observed. Thus, several catalytic cycles for one reaction are present. The experimental and model based catalytic cycle investigation is a challenging task. Nevertheless, transient and isotope-labeled kinetic studies as well as sophisticated ex situ and in situ spectroscopy measurements such as far-infrared spectroscopy in combination with density functional theory calculations (Koch and Holthausen, 2001) are global trends to reveal catalytic cycles (Baerns, 2004; Freund et al., 2011; Beller et al., 2012). In-situ spectroscopic analytic systems and quantum chemistry methods are improved all the time. Accordingly, detailed catalytic cycles are the basis of mechanistic kinetic rate approaches.

In this work, the determination of catalytic cycles is beyond the scope. Rather well-established chemical reaction mechanisms will be used in this thesis to derive kinetic rate approaches.

### **Mechanistic models**

By means of a postulated catalytic cycle, global kinetic rate approaches for homogeneous and heterogeneous catalysis can be determined. Therefore, the formalized "General Catalytic Cycle Kinetics (GCCK)" approach first suggested by *Christiansen* is used (Christiansen, 1931, 1935, 1953; Helferich, 2004; Murzin and Salmi, 2005; Marin and Yablonsky, 2011). Based on the general catalytic cycle (Insertion  $\leftrightarrow$  Reaction  $\leftrightarrow$  Elimination) the structure of several rate approaches is similar (Behr, 2008).

---

The generally admitted model basics for mechanistic rate law determination will be presented in section 2.1. The differences occurred only from variable cycle steps. Basic requirement of this method is the pseudo-first order rate assumption of all elementary reaction steps in the catalytic cycle considered. In addition, no step involves more than one intermediate active catalyst species. Using this methodology without any assumptions an equilibrium limited rate approach without rate determining step (rds) is obtained. However, justified chemical reaction mechanism assumptions reduce these usually overparameterized rate approaches to a minimum (Körkel, 2002; Marin and Yablonsky, 2011). In addition, based on the rate law determination identified kinetic parameters and inhibition constants can be directly related to certain cyclic steps. Thus, the corresponding parameter estimation and kinetic analysis reveal additional information about the reaction mechanism. Furthermore, the development of advanced experimental measurements in order to identify the reactant concentration or temperature effect on specific cycle steps increases the mechanism knowledge. If these additional measurements are nonexistent, mathematical model reduction techniques are suitable. These methods allow the identification of ill-conditioned parameter subsets in order to exclude the parameters from the estimation task. As a result, a reduced model with estimable parameters and small confidence intervals can be suggested (Kiedorf et al., 2014; Kiedorf et al., 2016b).

**Structure of the thesis** As aforementioned, the present thesis deals with the determination and quantification of mechanistic rate approaches for complex reaction networks in homogeneous and heterogeneous catalysis. Further, based on these reaction kinetics novel dynamic reactor concepts will be studied both model based and experimentally. The required model basics such as the GCCK approach (or *Christiansen* methodology), reaction parameter estimation algorithm and reactor models independent from phases involved will be introduced in section 2.

As reaction model cases are selected for the mechanistic reaction kinetic analysis in homogeneous and heterogeneous catalysis the hydroformylation of 1-dodecene (section 3) and the total oxidation of ethylene and propylene (section 5), respectively.

The hydroformylation reaction is one step in the production of synthetic material, dyes or dyestuffs. Until now the reaction is limited on short-chain olefins due to the limited solubility of long chain olefins in the aqueous catalyst phase (Behr, 2008). To establish renewable raw material as feedstock in hydroformylation process novel catalyst-ligand complexes and solvent systems were investigated by several researchers (Börner and Franke, 2016). In this work a thermomorphic solvent system in combination with a Rh/biphospho catalyst is applied (Brunsch and Behr, 2013). Parameter estimation is supported by reaction network decomposition and selectivity analysis. Using the determined and quantified reaction kinetic of the hydroformylation network, several dynamic continuous operated process applications can be predicted and consequently optimal reaction properties identified (section 4).

The total oxidation of volatile organic compounds in exhaust streams requires special attention in order to meet emission standards. The idea to purify these gases more energy-efficient was studied several times (Silveston and Hudgins, 2012). Inspired by well-known countercurrent movement separation processes a promising innovative concept is the

Loop Reactor. The investigation of this novel reactor concept requires reliable reaction kinetic data in a broader concentration and temperature range. Based on this, the partial and total oxidation of ethylene, propylene separately and in mixtures, and carbon monoxide on a  $\text{CrO}_x/\gamma\text{-Al}_2\text{O}_3$  catalyst will be studied to describe the reaction kinetics in section 5. Using catalytic cycles, mechanistic kinetic models of all reactions will be derived. For reduction of adjustable parameters individually measured adsorption isotherms will be used to parameterize adsorption constants in the kinetic models. The complex reaction network will be decomposed in three sub-networks to support parameter estimation, to quantify and validate kinetic rate approaches.

Based on the estimated reaction kinetics, the Loop Reactor concept suggested in 1994 by Haynes and Caram (Haynes and Caram, 1994) will be introduced and studied model based in section 6. To reduce the computational effort the general model-study will be performed using a power law kinetic taken from (Haynes and Caram, 1994) for single and multi-component inlet conditions. Subsequently, an experimental evaluation of the Loop Reactor concept using an ethylene/propylene/air mixture will be shown on a special designed pilot plant. Selected experimental data will be validated using the complex reaction kinetics for the total oxidation determined in section 5.

General aspects and results of the concept applied to quantify reaction kinetics and their application in innovative reactor concepts will be summarized in the concluding section 7.

## 2 Theoretical Basics

The design and optimization of chemical reactors requires quantitative knowledge about the kinetics of the reactions involved (Levenspiel, 1999). The challenge in reaction kinetic investigation is the derivation of suitable mathematical expressions quantifying the impact of concentrations and temperature. There are several concepts to derive suitable rate equations. Hereby, the degree of detail depends on the precision required in order to achieve certain objective. Quite often simple empirical rate expressions, e.g. power laws, were found to be in good agreement with available experimental data. However, there are severe limits of such rate equations with respect to extrapolation (Helfferich, 2004). More realistic formulations of rate expressions evaluate in more detail subsets of the catalytic cycles formulated and exploited in homogeneous catalysis (Behr, 2008). Well-known comparable kinetic concepts in heterogeneous catalysis are the *Langmuir/Hinshelwood/Hougen/Watson* or the *Mars/van Krevelen* mechanism (Helfferich, 2004; Baerns, 2006).

The analysis performed in this thesis is based on a very general approach originally suggested by *Christiansen* already in the 1930's (Christiansen, 1931, 1935, 1953). The approach quantifies in a very general way catalytic cycles and provides explicit expressions in a generic way. The concept will be designated in this thesis as the "General Catalytic Cycle Kinetics (GCCK)" approach. This GCCK approach was a long time ignored in the literature. The fact that it contains many widely used kinetic approaches as subsets was only recently elucidated and summarized (Helfferich, 2004; Murzin and Salmi, 2005; Marin and Yablonsky, 2011). These authors have demonstrated the potential of the GCCK approach investigating various reaction systems. The GCCK approach will be the unifying basis of this thesis. It will be applied to quantify the kinetics of selected reaction systems originating both from homogeneous and from heterogeneous catalysis. Due to a large number of unknown kinetic parameters arising from the mechanistically based GCCK approach, suitable model reduction techniques and statistical parameter evaluation methods are needed, which will be also evaluated and applied in this thesis.

Parts of the theoretical work presented in section 2 are already published in the following two papers:

- 1) G. Kiedorf, D.M. Hoang, A. Müller, A. Jörke, J. Markert, H. Arellano-Garcia, A. Seidel-Morgenstern and C. Hamel, Kinetics of 1-dodecene hydroformylation in a thermomorphic solvent system using a rhodium-biphephos catalyst. *Chemical Engineering Science* 115, 31–48, 2014
- 2) G. Kiedorf, T. Wolff, A. Seidel-Morgenstern and C. Hamel, Kinetic analysis of the hydrocarbon total oxidation using individual measured adsorption isotherms, *Chemie Ingenieur Technik* 88 (11), 1746–1760, 2016

In both papers the author of this thesis contributed as the first author essentially to the results presented. In paper 1 the contributions include the deviation of the mechanistic rate model for the isomerization of 1-dodecene and the derivation of the subset selection method. In paper 2 the contributions include the deviation of the *Eley/Rideal* and the *Mars/van Krevelen* rate laws originating from the GCCK approach.

## 2.1 Mechanistic kinetic rate models

The mathematical fundamentals of an uniform derivation of mechanistic reaction rate approaches were introduced by *Christiansen* in the 1930's (Christiansen, 1931, 1935, 1953) and recently "rediscovered", reviewed and evaluated by several authors (Helfferich, 2004; Murzin and Salmi, 2005; Marin and Yablonsky, 2011). The "General Catalytic Cycle Kinetics (GCCK)" approach assumes pseudo-first order rate laws for all elementary steps and includes explicitly one catalyst species. More than one catalyst species involved in the reaction mechanism cannot be handled by this GCCK approach. The general reaction rate formula of a  $N_{\text{step}}$  catalytic cycle is given by eq. 2.1 (Helfferich, 2004; Murzin and Salmi, 2005).

$$r = \frac{\left( \prod_{j_w=1}^{N_{\text{step}}} \omega_{j_w}^+ - \prod_{j_w=1}^{N_{\text{step}}} \omega_{j_w}^- \right) c_{\text{cat}}}{\Omega} \quad (2.1)$$

By means of using the individual forward (+) and backward (-) cycle step frequencies  $\omega_{j_w}$  the pseudo-first order rate for an elementary reaction step assumption is achieved. The total catalyst concentration  $c_{\text{cat}}$  yields from the sum of the concentration of the catalyst in resting state and all intermediate steps as well as sub and parallel reactions. The denominator  $\Omega$  corresponds to the *Christiansen* matrix and consider each intermediate catalyst concentration. The composition of the matrix for a general three step catalytic cycle follows eq. 2.2. The rigorous derivation of the *Christiansen* matrix will be omitted.

$$\Omega = \begin{bmatrix} \omega_2^+ \omega_3^+ & \omega_1^+ \omega_3^+ & \omega_1^- \omega_2^- \\ \omega_2^+ \omega_3^- & \omega_1^+ \omega_2^- & \omega_2^- \omega_3^- \\ \omega_1^+ \omega_2^+ & \omega_2^- \omega_3^- & \omega_1^- \omega_3^- \end{bmatrix} \begin{array}{l} \rightarrow \text{resting state} \\ \rightarrow \text{intermediate 1} \\ \rightarrow \text{intermediate 2} \end{array} \quad (2.2)$$

Each row of the *Christiansen* matrix corresponds to the concentration of one catalyst species in the cycle involved (fig. 2.1). Accordingly, one row balances one catalyst species.

In reaction networks, several reactions are catalyzed by the same catalyst. Thus, the reaction rate can be inhibiting by one another if significant catalyst amounts are contained in other catalytic cycles. To avoid such behavior the catalyst amount has to be in excess (Helfferich, 2004; Murzin and Salmi, 2005).

However, the method is not able to handle catalytic cycles with more than one catalyst species involved. Thus, the derivation of the *Langmuir/Hinshelwood/Hougen/Watson* (LHHW) rate model failed by the GCCK approach. Such rate approach has to be determined via the classical way (Helfferich, 2004; Murzin and Salmi, 2005; Baerns, 2006).

To illustrate the application of the GCCK approach several mechanistic rate equations will be derived for selected examples in homogeneous and heterogeneous catalysis. As a model example in homogeneous catalysis the rhodium complex catalyzed isomerization of 1-dodecene will be presented in section 2.1.1. With respect to heterogeneous catalysis the total oxidation of short-chain hydrocarbons diluted in air on a  $\text{CrO}_x/\gamma\text{-Al}_2\text{O}_3$  catalyst will be considered and discussed in section 2.1.2.

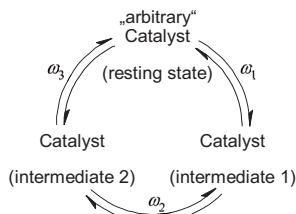


**Figure 2.1:** General three step catalytic cycle

### 2.1.1 Application of the GCCK approach in homogeneous catalysis

The hydroformylation of terminal olefins with carbon monoxide and hydrogen to the associated aldehyde are a well-known example of successfully applying homogeneous catalysis. Detailed information about this single reaction and the corresponding reaction network can be gleaned from section 3. As a selective and instructive example of the GCCK approach application in homogeneous catalysis the isomerization (iso) from the terminal (nOL) to branched olefins (iOL) will be presented in the following.

In fig. 2.2 the respective catalytic cycle of the isomerization of long-chain olefins, according to the *Wilkinson* catalytic cycle, is presented (Markert et al., 2013; Kiedorf et al., 2014). Based on the catalyst in resting state the first step ( $\omega_{\text{iso},1}$ ) describes the olefin coordination at the catalyst-ligand-complex. Afterwards this  $\pi$ -complex formed the alkyl-complex in the second step ( $\omega_{\text{iso},2}$ ). Subsequently, a  $\beta$ -H-elimination ( $\omega_{\text{iso},3}$ ) is followed by the reductive elimination ( $\omega_{\text{iso},4}$ ) of the branched olefin, which completes the isomerization catalytic cycle. By means of this reaction mechanism the overall reaction rate is expressed by the individual step frequencies  $\omega_{j,\omega}$  and the sum of all involved catalyst species  $C_{\text{cat}}$ . The resultant rate equation is shown in eq. 2.3.

$$r_{\text{iso}} = \frac{(\omega_{\text{iso},1}^+ \omega_{\text{iso},2}^+ \omega_{\text{iso},3}^+ \omega_{\text{iso},4}^+ - \omega_{\text{iso},1}^- \omega_{\text{iso},2}^- \omega_{\text{iso},3}^- \omega_{\text{iso},4}^-) C_{\text{cat}}}{\left( \begin{aligned} &\omega_{\text{iso},2}^+ \omega_{\text{iso},3}^+ \omega_{\text{iso},4}^+ + \omega_{\text{iso},1}^+ \omega_{\text{iso},3}^+ \omega_{\text{iso},4}^+ + \omega_{\text{iso},1}^+ \omega_{\text{iso},2}^+ \omega_{\text{iso},4}^+ + \omega_{\text{iso},1}^+ \omega_{\text{iso},2}^+ \omega_{\text{iso},3}^+ \\ &+ \omega_{\text{iso},1}^+ \omega_{\text{iso},3}^+ \omega_{\text{iso},4}^+ + \omega_{\text{iso},1}^+ \omega_{\text{iso},2}^+ \omega_{\text{iso},4}^+ + \omega_{\text{iso},1}^+ \omega_{\text{iso},2}^+ \omega_{\text{iso},3}^+ + \omega_{\text{iso},2}^+ \omega_{\text{iso},3}^+ \omega_{\text{iso},4}^+ \\ &+ \omega_{\text{iso},1}^+ \omega_{\text{iso},2}^+ \omega_{\text{iso},4}^+ + \omega_{\text{iso},1}^+ \omega_{\text{iso},2}^+ \omega_{\text{iso},3}^+ + \omega_{\text{iso},2}^+ \omega_{\text{iso},3}^+ \omega_{\text{iso},4}^+ + \omega_{\text{iso},1}^+ \omega_{\text{iso},3}^+ \omega_{\text{iso},4}^+ \\ &+ \omega_{\text{iso},1}^+ \omega_{\text{iso},2}^+ \omega_{\text{iso},3}^+ + \omega_{\text{iso},2}^+ \omega_{\text{iso},3}^+ \omega_{\text{iso},4}^+ + \omega_{\text{iso},1}^+ \omega_{\text{iso},3}^+ \omega_{\text{iso},4}^+ + \omega_{\text{iso},1}^+ \omega_{\text{iso},2}^+ \omega_{\text{iso},4}^+ \end{aligned} \right)} \quad (2.3)$$

By substitution of all individual forward and backward step frequencies by the associated reaction step constants and the terminal and branched olefin concentration (e.g.  $\omega_{\text{iso},1}^+ = k_{\text{iso},1}^+ \cdot c_{\text{nOL}}$ ), respectively, the eq. 2.3 can be replaced.

$$r_{\text{iso}} = \frac{(k_{\text{iso},1}^+ k_{\text{iso},2}^+ k_{\text{iso},3}^+ k_{\text{iso},4}^+ c_{\text{nOL}} - k_{\text{iso},1}^- k_{\text{iso},2}^- k_{\text{iso},3}^- k_{\text{iso},4}^- c_{\text{iOL}}) C_{\text{cat}}}{\left( \begin{aligned} &k_{\text{iso},2}^+ k_{\text{iso},3}^+ k_{\text{iso},4}^+ + k_{\text{iso},1}^+ k_{\text{iso},3}^+ k_{\text{iso},4}^+ + k_{\text{iso},1}^+ k_{\text{iso},2}^+ k_{\text{iso},4}^+ + k_{\text{iso},1}^+ k_{\text{iso},2}^+ k_{\text{iso},3}^+ \\ &+ k_{\text{iso},1}^+ k_{\text{iso},3}^+ k_{\text{iso},4}^+ c_{\text{nOL}} + k_{\text{iso},1}^+ k_{\text{iso},2}^+ k_{\text{iso},4}^+ c_{\text{nOL}} + k_{\text{iso},1}^+ k_{\text{iso},2}^+ k_{\text{iso},3}^+ c_{\text{nOL}} + k_{\text{iso},2}^+ k_{\text{iso},3}^+ k_{\text{iso},4}^+ c_{\text{iOL}} \\ &+ k_{\text{iso},1}^+ k_{\text{iso},2}^+ k_{\text{iso},4}^+ c_{\text{nOL}} + k_{\text{iso},1}^+ k_{\text{iso},2}^+ k_{\text{iso},3}^+ c_{\text{nOL}} + k_{\text{iso},2}^+ k_{\text{iso},3}^+ k_{\text{iso},4}^+ c_{\text{iOL}} + k_{\text{iso},1}^+ k_{\text{iso},3}^+ k_{\text{iso},4}^+ c_{\text{iOL}} \\ &+ k_{\text{iso},1}^+ k_{\text{iso},2}^+ k_{\text{iso},3}^+ c_{\text{nOL}} + k_{\text{iso},2}^+ k_{\text{iso},3}^+ k_{\text{iso},4}^+ c_{\text{iOL}} + k_{\text{iso},1}^+ k_{\text{iso},3}^+ k_{\text{iso},4}^+ c_{\text{iOL}} + k_{\text{iso},1}^+ k_{\text{iso},2}^+ k_{\text{iso},4}^+ c_{\text{iOL}} \end{aligned} \right)} \quad (2.4)$$

If the step reaction constants from step 2, 3 and 4 are excluded and rearranged, the eq. 2.4 results in eq. 2.5.

$$r_{\text{iso}} = \frac{k_{\text{iso},1}^+ (c_{\text{nOL}} - k_{\text{iso},1}^- k_{\text{iso},2}^- k_{\text{iso},3}^- k_{\text{iso},4}^- \cdot (k_{\text{iso},1}^+ k_{\text{iso},2}^+ k_{\text{iso},3}^+ k_{\text{iso},4}^+)^{-1} c_{\text{iOL}}) C_{\text{cat}}}{\left( \begin{aligned} &1 + \frac{k_{\text{iso},1}^-}{k_{\text{iso},2}^+} + \frac{k_{\text{iso},1}^- k_{\text{iso},2}^-}{k_{\text{iso},2}^+ k_{\text{iso},3}^+} + \frac{k_{\text{iso},1}^- k_{\text{iso},2}^- k_{\text{iso},3}^-}{k_{\text{iso},2}^+ k_{\text{iso},3}^+ k_{\text{iso},4}^+} \\ &+ \frac{k_{\text{iso},1}^+}{k_{\text{iso},2}^+} c_{\text{nOL}} + \frac{k_{\text{iso},1}^+ k_{\text{iso},2}^-}{k_{\text{iso},2}^+ k_{\text{iso},3}^+} c_{\text{nOL}} + \frac{k_{\text{iso},1}^+ k_{\text{iso},2}^- k_{\text{iso},3}^-}{k_{\text{iso},2}^+ k_{\text{iso},3}^+ k_{\text{iso},4}^+} c_{\text{nOL}} + \frac{k_{\text{iso},2}^- k_{\text{iso},3}^- k_{\text{iso},4}^-}{k_{\text{iso},2}^+ k_{\text{iso},3}^+ k_{\text{iso},4}^+} c_{\text{iOL}} \\ &+ \frac{k_{\text{iso},1}^+}{k_{\text{iso},3}^+} c_{\text{nOL}} + \frac{k_{\text{iso},1}^+ k_{\text{iso},2}^-}{k_{\text{iso},3}^+ k_{\text{iso},4}^+} c_{\text{nOL}} + \frac{k_{\text{iso},3}^- k_{\text{iso},4}^-}{k_{\text{iso},3}^+ k_{\text{iso},4}^+} c_{\text{iOL}} + \frac{k_{\text{iso},1}^- k_{\text{iso},2}^- k_{\text{iso},3}^-}{k_{\text{iso},2}^+ k_{\text{iso},3}^+ k_{\text{iso},4}^+} c_{\text{iOL}} \\ &+ \frac{k_{\text{iso},1}^+}{k_{\text{iso},4}^+} c_{\text{nOL}} + \frac{k_{\text{iso},4}^-}{k_{\text{iso},4}^+} c_{\text{iOL}} + \frac{k_{\text{iso},1}^- k_{\text{iso},2}^-}{k_{\text{iso},2}^+ k_{\text{iso},4}^+} c_{\text{iOL}} + \frac{k_{\text{iso},1}^- k_{\text{iso},2}^- k_{\text{iso},3}^-}{k_{\text{iso},2}^+ k_{\text{iso},3}^+ k_{\text{iso},4}^+} c_{\text{iOL}} \end{aligned} \right)} \quad (2.5)$$

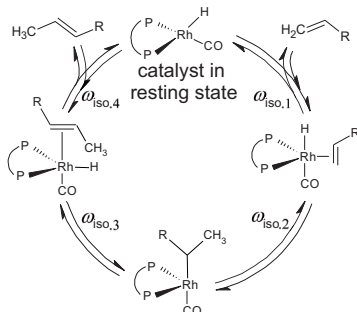


**Figure 2.2:** Postulated catalytic cycle for the isomerization of long-chain olefins at a rhodium catalyst supported by a biphospho ligand based on a *Wilkinson* reaction mechanism (Markert et al., 2013; Kiedorf et al., 2014)

If no further assumptions are considered (i.e. a rate determining step) and a lumped rate constant  $k_{\text{iso}}$ , a lumped equilibrium constant  $K_{\text{eq,iso}}$  and three lumped inhibition parameters  $K_{\alpha,\dots,\gamma,\text{iso}}$  are used, eq. 2.5 can be finally written simpler:

$$r_{\text{iso}} = \frac{k_{\text{iso}}(T) \cdot (c_{\text{nOL}} - c_{\text{IOL}} \cdot K_{\text{eq,iso}}^{-1}) c_{\text{cat}}}{(1 + K_{\alpha,\text{iso}} \cdot c_{\text{nOL}} + K_{\beta,\text{iso}} \cdot c_{\text{IOL}} + K_{\gamma,\text{iso}})} \quad (2.6)$$

The application of the overall isomerization kinetic equation determined by the GCKK approach within the hydroformylation reaction network analysis will be presented in section 3. The derivation of corresponding overall kinetic rate equation for the other sub-cycles in the hydroformylation network, shown in fig. 3.2, describing the hydrogenation and hydroformylation can be performed in an analogous manner. The final set of kinetic equations will be shown in section 3.2.5. Details regarding the derivation of these expressions will be provided in the appendix A.1.

In the following, the GCKK approach will be applied to quantify the rates of heterogeneously catalyzed reactions.

### 2.1.2 Application of the GCKK approach in heterogeneous catalysis

Studying heterogeneously catalyzed systems additional phase equilibria data of the components involved have to be considered in kinetic modeling. Moreover, the identification of catalytic cycles is hindered by missing in-situ spectroscopic techniques. Therefore, the GCKK approach was applied so far rarely for heterogeneously catalyzed reactions. In order to demonstrate its corresponding potential, the total oxidations of gaseous short-chain hydrocarbons (ethylene and propylene) and carbon monoxide diluted in air on a solid catalyst ( $\text{CrO}_x/\gamma\text{-Al}_2\text{O}_3$ ) will be studied.

In this thesis, detailed information regarding the total oxidation reaction mechanisms are not available. Therefore, the formulation of mechanistic kinetic rate approaches via the GCKK approach is based on well-established simplified reaction mechanisms such as e.g. the *Mars/van Krevelen* and *Eley/Rideal* mechanisms. Irrespective of the chemical equation two established major reaction mechanisms exist. The selection depends on the oxygen

storage capacity of the active catalyst species. If no or only slightly lattice oxygen capacities available, adsorption–desorption mechanisms are often validated (Helferich, 2004; Baerns, 2006). If the catalyst species provide lattice oxygen as well, an oxidation–reduction mechanism can be observed (Mars and van Krevelen, 1954; Murzin, 2013). However, oxidation reactions consume lattice, adsorbed and gas phase oxygen, respectively (Yao, 1973; Heynderickx et al., 2010a; Gómez et al., 2014), which complicates the catalytic cycle identification even more.

For demonstration of the derivation of mechanistic rate laws in heterogeneous catalysis the adsorption based *Eley/Rideal* and the oxidation–reduction mechanism (*Mars/van Krevelen*) will be shown in this section. A schematic illustration of the ER mechanism for the hydrocarbon total oxidation is presented in fig. 2.3. In this figure, oxygen  $O_2$  adsorbs at the active catalyst species first. Afterwards the short-chain hydrocarbon  $C_nH_{2n}$  (HC) reacts with the adsorbed oxygen from gas phase. The reaction products (carbon dioxide  $CO_2$  and water  $H_2O$ ) can adsorb at the catalyst surface and limit the free adsorption sites as well. This mechanism results in a three steps catalytic cycle. Moreover, two competitive inhibition steps for the carbon dioxide and water adsorption at the active catalyst species in resting state occur, respectively. The resultant mechanistic kinetic reaction rate described by the forward and backward single step frequencies without the dissociation step of the adsorbed oxygen can be written in general as follows (eq. 2.7):

$$r_{ER} = \frac{(\omega_1^+ \omega_2^+ - \omega_1^- \omega_2^-) c_{cat}}{(\omega_2^+ + \omega_1^- + \omega_1^+ + \omega_2^-) + (\omega_2^+ + \omega_1^-) (K_{CO_2} p_{CO_2} + K_{H_2O} p_{H_2O})} \quad (2.7)$$

Working from the assumption of a rate determining step ( $\omega_2^+ \ll \omega_1^+$  and  $\omega_2^- \ll \omega_1^-$ ) and irreversible reaction step ( $\omega_2^- = 0$ ) the kinetic rate law can be reduced to:

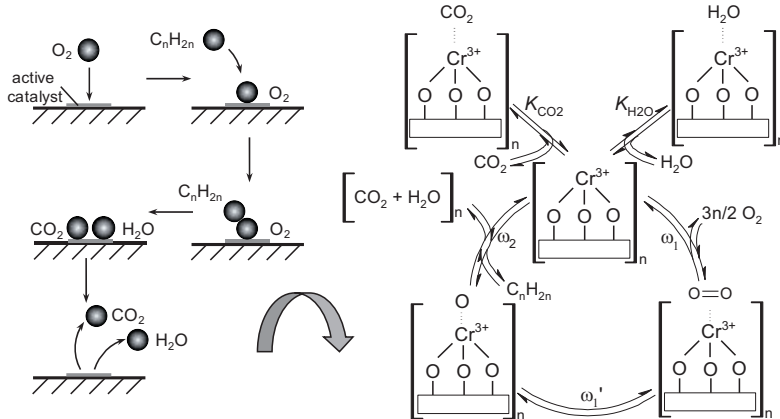


**Figure 2.3:** Schematic illustration of an adsorption reaction mechanism where adsorbed oxygen react with a hydrocarbon molecule from the gas phase (*Eley/Rideal* mechanism) and the corresponding catalytic cycle of the total oxidation of an olefin in gas phase and dissociated oxygen to carbon dioxide and water (Kiedorf et al., 2016b)

$$r_{\text{ER}} = \frac{\omega_1^+ \omega_2^+ C_{\text{cat}}}{\omega_1^+ + \omega_1^- (1 + K_{\text{CO}_2} \rho_{\text{CO}_2} + K_{\text{H}_2\text{O}} \rho_{\text{H}_2\text{O}})} \quad (2.8)$$

By inserting the individual step constants and the corresponding partial pressures (i.e.  $\omega^{+2} = k^{+2} \cdot \rho_{\text{HC}}$ ) and exclude the desorption constant of oxygen in the denominator, the reaction rate becomes to:

$$r_{\text{ER}} = \frac{k_1^+ \rho_{\text{O}_2} k_2^+ \rho_{\text{HC}} C_{\text{cat}}}{k_1^- \left( \frac{k_1^+}{k_1^-} \rho_{\text{O}_2} + 1 + K_{\text{CO}_2} \rho_{\text{CO}_2} + K_{\text{H}_2\text{O}} \rho_{\text{H}_2\text{O}} \right)} \quad (2.9)$$

Using the adsorption equilibrium constant of oxygen ( $K_{\text{O}_2} = k_1^+/k_1^-$ ) the reaction rate approach of the ER mechanism follows eq. 2.10:

$$r_{\text{ER}} = \frac{k_{\text{ER}}(T) K_{\text{O}_2} \rho_{\text{O}_2} \rho_{\text{HC}} C_{\text{cat}}}{(1 + K_{\text{O}_2} \rho_{\text{O}_2} + K_{\text{CO}_2} \rho_{\text{CO}_2} + K_{\text{H}_2\text{O}} \rho_{\text{H}_2\text{O}})} \quad (2.10)$$

This approach corresponds to the general ER equation. If oxygen dissociation is considered, eq. 2.10 can be reformed to the universal eq. 2.11.

$$r_{\text{ER}} = \frac{k_{\text{ER}}(T) (K_{\text{O}_2} \rho_{\text{O}_2})^{0.5} \rho_{\text{HC}} C_{\text{cat}}}{(1 + (K_{\text{O}_2} \rho_{\text{O}_2})^{0.5} + K_{\text{CO}_2} \rho_{\text{CO}_2} + K_{\text{H}_2\text{O}} \rho_{\text{H}_2\text{O}})} \quad (2.11)$$

The description of the phase equilibria as well as the quantification of the single component and mixture adsorption constants  $K_{\text{jc}}$  can be realized by adsorption isotherm measurements. Typical adsorption isotherm models will be presented in section 5.4.1.

As a second case study for the GCCK approach in heterogeneous catalysis, the oxidation of carbon monoxide to carbon dioxide ( $\text{CO} + 0.5 \text{O}_2 \leftrightarrow \text{CO}_2$ ) is investigated. Using a chromium catalyst ( $\text{CrO}_x/\gamma\text{-Al}_2\text{O}_3$ ), a MvK mechanism can be often validated (Murzin and Salmi, 2005). A schematic illustration of the carbon monoxide oxidation via the MvK mechanism is shown in fig. 2.4. The oxygen is provided directly from the active species via a catalyst reduction. Consequently, the catalyst species have to re-oxidize by gas phase oxygen. The resulting catalytic cycle is illustrated in fig. 2.4 as well. For a two-step catalytic cycle, the mechanistic rate approach follows eq. 2.12.

$$r_{\text{MvK}} = \frac{\omega_{\text{red}}^+ \omega_{\text{ox}}^+ - \omega_{\text{red}}^- \omega_{\text{ox}}^-}{(\omega_{\text{red}}^+ + \omega_{\text{ox}}^+ + \omega_{\text{red}}^- + \omega_{\text{ox}}^-)} \quad (2.12)$$

Insertion of several step kinetics (e.g.  $\omega^{+1} = k^{+1} \cdot \rho_{\text{CO}}$ ) yields in eq. 2.13.

$$r_{\text{MvK}} = \frac{k_{\text{red}}^+ \rho_{\text{CO}} k_{\text{ox}}^+ \rho_{\text{O}_2} - k_{\text{red}}^- \rho_{\text{CO}_2} k_{\text{ox}}^-}{(k_{\text{red}}^+ \rho_{\text{CO}} + k_{\text{ox}}^+ \rho_{\text{O}_2} + k_{\text{red}}^- \rho_{\text{CO}_2} + k_{\text{ox}}^-)} \quad (2.13)$$

Assuming an irreversible catalytic cycle, eq. 2.13 can be reduced to the general MvK reaction kinetic equation (eq. 2.14).

$$r_{\text{MvK}} = \frac{k_{\text{red}}^+(T) \rho_{\text{CO}} k_{\text{ox}}^+(T) \rho_{\text{O}_2}}{(k_{\text{red}}^+(T) \rho_{\text{CO}} + k_{\text{ox}}^+(T) \rho_{\text{O}_2})} \quad (2.14)$$

Considering the assumptions used in deriving the ER and MvK reaction mechanisms, it can be shown that the resulting rate expressions form subsets of the general rate equations obtained from the GCCK approach. However, this applied reaction mechanism reduction approach by assuming rate determining steps or irreversible catalytic cycle steps

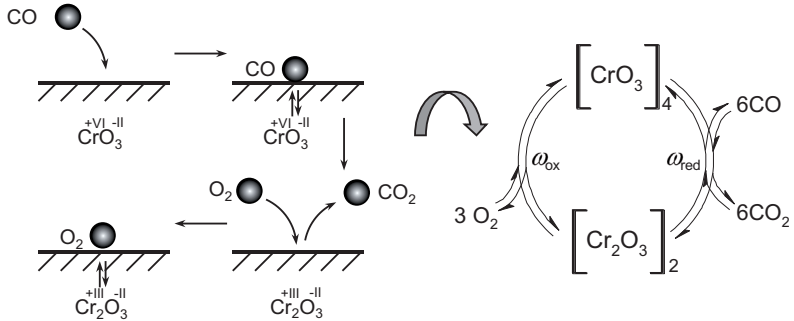


**Figure 2.4:** Schematic illustration of a reduction–oxidation reaction mechanism using the example of the carbon monoxide oxidation on a  $\text{CrO}_3/\gamma\text{-Al}_2\text{O}_3$  catalyst and the resulting catalytic cycle (*Mars/van Krevelen mechanism*) (Kiedorf et al., 2016b)

illustrates the flexibility of the GCKK approach. Accordingly, using these two instructive examples the GCKK approach could be successfully demonstrated.

However, especially in heterogeneous catalysis reaction mechanisms where an adsorbed species react with one another are in common practice. But this general approach is not able to handle more than one active catalytic site in a cycle, which limits this methodology (Helfferich, 2004).

The rate laws derived in section 2.1 postulate ideal gas or liquid phase behavior of the reactants and products. If no ideal behavior is assumed the concentration of liquid phase components can be described by the activity coefficient and gas phase components by the fugacity coefficient (Atkins and Paula, 2006).

## 2.2 Parameter estimation, statistical evaluation and model reduction techniques

The section 2.1 presented the mechanistic rate models derivation. Dependent on the number of single reaction steps, a multiplicity of kinetic parameters is available. To quantify such models, an appropriate parameter estimation is required. In chemical engineering the model structure of material and energy balances with respect to the kinetic parameters is mostly nonlinear. The basic algebraic nonlinear equation is defined by eq. 2.15. The observed model response vector  $\mathbf{y}_{\text{obs}}^{\text{mod}}$  depends on the model input  $\mathbf{y}^{\text{in}}$  and the free optimization parameter vector  $\boldsymbol{\theta}_{\text{opt}}$ .

$$\mathbf{y}_{\text{obs}}^{\text{mod}} = f(\mathbf{y}^{\text{in}}, \boldsymbol{\theta}_{\text{opt}}) \quad (2.15)$$

The nonlinear model equation system is presented by the material and thermal energy reactor balances, which will be explained in detail in section 2.3. In order to obtain the reactor or process optimum the model response varied between final concentrations and the integral performance parameters. The most established performance parameters are the reactant conversion  $X_{\text{reactant}}$  (eq. 2.16) as well as the product selectivity  $S_{\text{product}}$  (eq. 2.17) and the yield  $Y_{\text{product}}$  (eq. 2.18), respectively.

The integral reactant conversion is defined as the ratio of converted reactant to the feed substance. Generally, the conversion is stated to the limiting or valuable reactant. In case of continuous operated reactors, the conversion is calculated using the molar flux.

$$X_{\text{reactant}} = \frac{\dot{n}_{\text{reactant}}^0 - \dot{n}_{\text{reactant}}}{\dot{n}_{\text{reactant}}^0} \quad (2.16)$$

The integral selectivity describes the ratio of the formed product to the consumed reactant in consideration of the stoichiometric factors of the components  $v_{jc}$ . Thus, the selectivity is a characteristic for the reaction pathway in a complex reaction network.

$$S_{\text{product}} = \frac{\dot{n}_{\text{product}}(-v_{\text{reactant}})}{(\dot{n}_{\text{reactant}} - \dot{n}_{\text{reactant}}^0)(v_{\text{product}})} \quad (2.17)$$

The product yield is the ratio of the formed product to the reactant feed in consideration of the stoichiometric factors as well. A further possibility to describe the product yield is given by the product of the conversion and selectivity.

$$Y_{\text{product}} = \frac{\dot{n}_{\text{product}}(-v_{\text{reactant}})}{\dot{n}_{\text{reactant}}^0(v_{\text{product}})} = X_{\text{reactant}} \cdot S_{\text{product}} \quad (2.18)$$

### 2.2.1 Objective functions

To quantify the model agreement with observed experimental data, the sum of squares of residuals  $SSR$  is used. In general, the iterative minimization procedure of the objective function requires an initial optimization parameter set. By means of these values, an optimization technique and a suitable objective function, the  $SSR$  minimum can be found. Unfortunately, the improved parameter outcome is significantly affected by these influencing factors (Joshi, 2007).

If no information of measurement errors is available the ordinary least square (OLS) method (eq. 2.19) is commonly used (Bates and Watts, 2007). Therefore, an independently and identically measurement error distribution is assumed. This type of objective function will be applied in kinetic parameter estimation in sections 3.5 and 5.5.

$$SSR(\boldsymbol{\theta}_{\text{opt}})^{\text{OLS}} = \sum_{j_{\text{obs}}=1}^{N_{\text{obs}}} (\mathbf{y}_{j_{\text{obs}}}^{\text{exp}}(\mathbf{y}^{\text{in}}) - \mathbf{y}_{j_{\text{obs}}}^{\text{mod}}(\mathbf{y}^{\text{in}}, \boldsymbol{\theta}_{\text{opt}}))^2 \quad (2.19)$$

The advanced weighted least square (WLS) method (eq. 2.20) is used to weight all terms to the corresponding experimental value. Thus, differences in size can be compensated, which supports parameter estimation. Here, too, no experimental measurement error information is included. This type of objective function will be applied in section 5.4.

$$SSR(\boldsymbol{\theta}_{\text{opt}})^{\text{WLS}} = \sum_{j_{\text{obs}}=1}^{N_{\text{obs}}} \left( \frac{\mathbf{y}_{j_{\text{obs}}}^{\text{exp}}(\mathbf{y}^{\text{in}}) - \mathbf{y}_{j_{\text{obs}}}^{\text{mod}}(\mathbf{y}^{\text{in}}, \boldsymbol{\theta}_{\text{opt}})}{\mathbf{y}_{j_{\text{obs}}}^{\text{exp}}(\mathbf{y}^{\text{in}})} \right)^2 \quad (2.20)$$

More sophisticated  $SSR$  approaches including experimental data error distribution are presented in (Joshi, 2007).

### 2.2.2 Optimization methods and procedure

As aforementioned in section 2.2.1, the numerical kinetic parameter estimation can be explained as an optimization problem (Joshi, 2007). In this iterative process, the *SSR* will be minimized to obtain the estimated parameter vector. The selection of the optimizer affects the estimation results significantly. The used optimizer methods are the *Levenberg-Marquardt* and the *trust-region-reflective* algorithms, which are already implemented in the modeling software *MatLab*®. Therefore, the introduction of the algorithms will be given shortly below.

The *Levenberg-Marquardt* algorithm is a combination of the *Gauss-Newton* method and the *Steepest-Gradient* algorithm. Because of using the sequential quadratic programming divergent oscillations can be avoided. Thus, the algorithm converges to a solution with a high probability. Simply the calculating time increase for initial values close to solution (Levenberg, 1944; Marquardt, 1963; Joshi, 2007).

The *trust-region-reflective* algorithm based on the *Levenberg-Marquardt* method. This optimizer uses an approximation of the real objective function by a simpler function, which reasonable reflects the *SSR* close to the initial point. Standardly a quadratic approximation by the first two terms of the *Taylor* series is given (Moré and Sorensen, 1983). The actual computing occurs at the trust region sub-problem. However, the maximum step size depends on the quality of the approximate function and is limited deterministically (Papageorgiou, 2006).

However, if there are no suitable initial optimization values available, the identification of kinetic parameters is difficult. For that reason, the estimation procedure was carried out in two steps (Toch et al., 2015). At first, initial values were generated using an isothermal regression at each of the experimental investigated temperatures. The second step includes a non-isothermal regression based on the initial values of the first regression. The modeling of the thermal effect in reaction engineering is considered in the rate constant (see eqs. 2.6, 2.11 and 2.14) by the classical *Arrhenius* approach (eq. 2.21).

$$k_{jR}(T) = k_{s,jR} \exp\left(\frac{-E_{A,jR}}{R \cdot T}\right) \quad (2.21)$$

However, to minimize parameter correlations special formulations of the *Arrhenius* approach were developed. In this work, a transformation introduced by (Schwaab and Pinto, 2007) is used that allows to estimate the activation energy  $E_A$  and the frequency factor  $k_\infty$  independently (eq. 2.22).

$$k_{jR}(T) = \exp\left(\underbrace{\ln(k_{s,jR})}_{\Theta_{\text{opt},1}} - \frac{E_{A,jR}}{R \cdot T^{\text{ref}}} + \underbrace{\frac{E_{A,jR}}{R \cdot T^{\text{ref}}}}_{\Theta_{\text{opt},2}} \left(\frac{T - T^{\text{ref}}}{T}\right)\right) \quad (2.22)$$

In this approach, a reference temperature  $T^{\text{ref}}$  is used to estimate on the one hand the ratio of the activation energy, universal gas constant and the reference temperature ( $\Theta_{\text{opt},2}$ ) and on the other hand the sum of the first parameter and the logarithm of the frequency factor ( $\Theta_{\text{opt},1}$ ). Subsequent, the reference temperature can be canceled out within the final formulation. Thus, finally the general *Arrhenius* approach (eq. 2.21) can be applied. An alternative *Arrhenius* equation formulation is defined in eq. 2.23.

$$k_{j_r}(T) = k_{\infty, j_r}^{\text{ref}} \exp\left(\frac{-E_{A, j_r}}{R} \left(\frac{1}{T} - \frac{1}{T^{\text{ref}}}\right)\right) \quad (2.23)$$

This transformation of the *Arrhenius* approach is used to reduce the parameter correlation between the frequency factor  $k_{\infty, j_r}$  and the activation energy  $E_A$ , which improves the kinetic parameter estimation. An example will be given for the hydroformylation of 1-dodecene in sections 3 and 4.

### 2.2.3 Model reduction techniques

After introducing the general framework, below concepts will be introduced and discussed devoted to reduce the sizes of the models originating from the GCK approach. The difficult inverse parameter estimation problems will be treated in this thesis by means of reaction network decomposition and mathematical model reduction techniques.

The general problem in quantifying kinetics within complex reaction networks is the large number of difficult to estimate and often correlated parameters (Körkel, 2002; Marin and Yablonsky, 2011). As a consequence, the analysis of experimental data causes ill-posed inverse parameter estimation problems and tends to give parameter values with huge confidence intervals. Research in this field was focused on answering questions of identifiability, correlation and predictability of model parameters, initially mainly in the field of linear systems and control theory. (Bellman and Åström, 1970) defined the concept of structural identifiability and (Reid, 1977) developed a method for linear systems based on sensitivity identifiability, which takes the sensitivity of states with respect to the parameters into account. More recently, (Brun et al., 2001) considered nonlinear systems and the eigenvalues of sub-matrices of the *Fisher-Information matrix FIM*, to determine identifiability of parameters. These efforts inspired the development of the concept of parameter subset selection exploiting singular value decomposition and rank revealing QR factorization techniques (Saad, 2003; Fink et al., 2007; Cintrón-Arias et al., 2009), which will be described below.

Further model reduction techniques are referred to additional experimental or reaction mechanistic information. Using additional experimental data, thermodynamic and kinetic effects can be separated strictly in parameter estimation. Using additional chemical reaction mechanistic assumptions, complex reaction kinetic rate laws can be simplified and the number of estimation parameters can be reduced considerably. Examples leading to model reduction are the assumption of rate determining steps or irreversible reactions.

**Mathematical model reduction technique** Assuming, that the objective function *SSR* of the parameter estimation task is of some least square type of the model errors (eq. 2.19), the *Newton* algorithm can be used as the standard optimizer method to solve the problem with a quadratic approximation (eq. 2.24) in order to obtain the minimum (eq. 2.25).

$$\begin{aligned} SSR(\Theta_{\text{opt}}) &\approx SSR^* \left( \Theta_{\text{opt}, j_i} + \Delta \Theta_{\text{opt}} \right) = SSR \left( \Theta_{\text{opt}, j_i} \right) + \nabla SSR \left( \Theta_{\text{opt}, j_i} \right) \Delta \Theta_{\text{opt}} \\ &\quad + \frac{1}{2} \Delta \Theta_{\text{opt}} \nabla^2 SSR \left( \Theta_{\text{opt}, j_i} \right) \Delta \Theta_{\text{opt}} \end{aligned} \quad (2.24)$$

$$\frac{dSSR(\boldsymbol{\theta}_{opt})}{d\boldsymbol{\theta}_{opt}} = 0 = \nabla SSR(\boldsymbol{\theta}_{opt,j_k}) + \nabla^2 SSR(\boldsymbol{\theta}_{opt,j_k}) \Delta \boldsymbol{\theta}_{opt} \quad (2.25)$$

Thus, the optimization parameter vector for the next iterative step is possible (eq. 2.25) if the inverse of the *Hessian* matrix exists.

$$\boldsymbol{\theta}_{opt,j_k+1} = \boldsymbol{\theta}_{opt,j_k} - \left( \nabla^2 SSR(\boldsymbol{\theta}_{opt,j_k}) \right)^{-1} \nabla SSR(\boldsymbol{\theta}_{opt,j_k}) \quad (2.26)$$

Moreover, the *Hessian* matrix can be approximated with the *Jacobian* matrix for small curvature as follows:

$$\nabla^2 SSR(\boldsymbol{\theta}_{opt,j_k}) = 2 \frac{\partial \mathbf{y}}{\partial \boldsymbol{\theta}_{opt}} \frac{\partial \mathbf{y}}{\partial \boldsymbol{\theta}_{opt}} + \mathbf{y} \frac{\partial^2 \mathbf{y}}{\partial \boldsymbol{\theta}_{opt}^2} \approx 2 \frac{\partial \mathbf{y}}{\partial \boldsymbol{\theta}_{opt}} \frac{\partial \mathbf{y}}{\partial \boldsymbol{\theta}_{opt}} = 2\mathbf{S}^T \mathbf{S} = \mathbf{FIM} \quad (2.27)$$

Therefore, a relaxed conclusion is that optimal parameter values can be found if the *Jacobian* matrix of the objective function is invertible. Since  $\mathbf{S}$  is the inner derivation of the *Jacobian* matrix with respect to the optimization parameter vector  $\boldsymbol{\theta}_{opt}$ , it is sufficient to test only the invertibility of  $\mathbf{S}$ . The sensitivity parameter  $\mathbf{S}$  is dependent on the related initial settings and the control profiles of each observed data. Therefore, by knowing all performed and planned experiments and first guesses of the whole parameter set, it can be concluded that all parameters are estimable if  $\mathbf{S}$  is invertible. The parameter sensitivities can be defined by the derivatives of the observed model with respect to the optimization parameters (eq. 2.28 or in matrix form in eq. 2.29).

$$S_{j_o/j_{exp}} = \left. \frac{\partial y_{j_o/j_{exp}}^{mod}}{\partial \theta_{opt,j_o}} \right|_{\theta_{opt}} \quad (2.28) \quad \mathbf{S} = \begin{bmatrix} S_{11} & \cdots & S_{1j_o} & \cdots & S_{1N_o} \\ \vdots & \ddots & \vdots & & \vdots \\ S_{j_{obs}1} & \cdots & S_{j_{obs}j_o} & \cdots & S_{j_{obs}N_o} \\ \vdots & & \vdots & \ddots & \vdots \\ S_{N_{obs}1} & \cdots & S_{N_{obs}j_o} & \cdots & S_{N_{obs}N_o} \end{bmatrix} \quad (2.29)$$

The inner derivatives of the *Jacobian* matrix can be solved using the analytical solutions or approximated numerically for instances by applying one-sided (eq. 2.30) or symmetric difference equations (eq. 2.31).

$$S_{j_o/j_{exp}} = \frac{y_{j_o/j_{exp}}^{mod}(\theta_{opt,j_o} + \Delta \theta_{opt,j_o}) - y_{j_o/j_{exp}}^{mod}(\theta_{opt,j_o})}{\Delta \theta_{opt,j_o}} \quad (2.30)$$

$$S_{j_o/j_{exp}} = \frac{y_{j_o/j_{exp}}^{mod}(\theta_{opt,j_o} + \Delta \theta_{opt,j_o}) - y_{j_o/j_{exp}}^{mod}(\theta_{opt,j_o} - \Delta \theta_{opt,j_o})}{2\Delta \theta_{opt,j_o}} \quad (2.31)$$

For the determination of the difference  $\Delta \theta_{opt,j_o}$  several approximations are commonly. Mostly conventional the product of the machine accuracy and the estimation parameter is used.

If experimental observations are not available for steady state conditions, parameter sensitivities could be time dependent. Dynamic operations offer the possibility to increase parameter sensitivities and estimability. The first derivative of the parameter sensitivity (eq. 2.28 or eq. 2.29) with respect to time can be defined as follows:

$$\frac{\partial \mathbf{S}}{\partial t} = \frac{\partial y^{mod}}{\partial x} \mathbf{S} + \frac{\partial y^{mod}}{\partial \theta_{opt}} \quad (2.32)$$



duction was already illustrated in section 2.1.

Additionally, adsorption and desorption steps of reactants and products in heterogeneous catalytic cycles can be included, too. Such additional “up- and downstream” reaction steps can be eventually measured separately. Thus, kinetic parameter estimation can be simplified and the physical meaning of model parameters is conserved by strictly separation of kinetic and thermodynamic effects (see also section 5.4) (Pöpken et al., 2000; Kiedorf et al., 2016a, 2016b).

Another bottom-up approach as model reduction technique is to evaluate sequentially data sets of increasing complexity, starting with the smallest sub-network and ending with the complete network, as presented e.g. by (Hu et al., 2011) and applied below in the sections 3.5 and 5.5 (Kiedorf et al., 2014; Kiedorf et al., 2016b).

### 2.2.4 Statistical evaluation of estimated parameters

The application of the parameter sensitivity is widely used to analyze the statistical significance of estimated parameters. The *Fisher-Information matrix (FIM)* with dimension  $N_{\Theta} \times N_{\Theta}$  was already introduced in connection with the subset selection method (eq. 2.27). The confidence interval according to the *Cramer-Rao* inequality is defined by eq. 2.37 (Ljung, 1999; Joshi, 2007).

$$\sigma_{\hat{\theta}_{j_0}}^2 \geq (\text{FIM}_{j_0 j_0})^{-1} \quad (2.37)$$

The variance  $\sigma^2$  of all observations (eq. 2.38) is based on the ordinary *SSR* (eq. 2.33) divided by the degree of freedom ( $d_f = N_{\text{obs}} - N_{\Theta}$ ). A weighted *SSR* (eq.2.20) can be applied as well.

$$\sigma^2 = \frac{1}{d_f} \sum_{j_{\text{obs}}=1}^{N_{\text{obs}}} (y_{j_{\text{obs}}}^{\text{exp}} - y_{j_{\text{obs}}}^{\text{mod}})^2 \quad (2.38)$$

Using the quantile of the *Student-t* distribution, the lower and upper confidence interval of an optimization parameter  $\Theta_{\text{opt},j_0}$  is defined in eq. 2.39.

$$\underbrace{\hat{\Theta}_{\text{opt},j_0} - \sigma_{\hat{\theta}_{j_0}} t_{\alpha/2}^{d_f}}_{\text{lowerbound}} \leq \Theta_{\text{opt},j_0} \leq \underbrace{\hat{\Theta}_{\text{opt},j_0} + \sigma_{\hat{\theta}_{j_0}} t_{\alpha/2}^{d_f}}_{\text{upperbound}} \quad (2.39)$$

Using the *Student-t* distribution, the confidence interval of the estimated parameter is a function of the level of significance  $\alpha$  (e.g. 99.9 %, 97.5 % or 95 %). Often the relative notation of the parameter uncertainties is preferred.

$$\% \Delta \hat{\Theta}_{\text{opt}} = \frac{\sigma_{\hat{\theta}_{j_0}} t_{\alpha/2}^{d_f}}{\hat{\Theta}_{\text{opt},j_0}} \cdot 100 \quad (2.40)$$

Using the eqs. 2.27-2.31 and 2.37-2.40, the confidence interval of an estimated parameter can be identified. However, the *Cramer-Rao* inequality (eq. 2.37) calculates correctly only the lower confidence interval. Nevertheless, mostly the upper bound as described by this method is considered as well (Joshi, 2007).

## 2.3 Reactor models

To accomplish an identification and quantification of mechanistic kinetic rate equations, also suitable models are needed describing the laboratory reactors used to generate the

experimental data basis. Therefore, in this section various reactor models valid for different types of reactors and operation modes will be shortly presented. In chemical reaction engineering, reactors are first classified in regard to the phases involved (Levenspiel, 1999; Baerns, 2006; Beller et al., 2012). Homogeneously catalyzed liquid reaction systems are often realized using stirred tank reactors (fig. 2.5a). Using such ideal mixed system, large specific interphases (i.e. gaseous/liquid) can be achieved. Thus, no mass transport limitations exist (Behr, 2008). Heterogeneously catalyzed systems (i.e. gaseous reactants/solid catalyst) are often performed using tubular reactors (fig. 2.5b). Modeling heterogeneously catalyzed systems, phase characteristics and transport phenomena are relevant and have to be considered in reactor modeling (see void fraction  $\varepsilon$  in fig. 2.5b) (Helfferich, 2004; Baerns, 2006). In gaseous/solid systems the coupling between the solid and fluid phases is typically established by adsorption equilibria. These equilibria relate the partial pressures  $p_{j_c}$  in the fluid phase to the loading in the solid phase  $q_{j_c}$ , typically in a nonlinear manner (i.e. *Langmuir* adsorption model). Detailed information on adsorption isotherm models will be given in section 5.4.

In this thesis three different types of reactor models will be used. The homogeneously catalyzed reactions will be investigated using a stirred tank reactor applying batch, semi-batch and continuous operation mode (section 2.3.1). The heterogeneously catalyzed system will be studied using a continuously operated tubular reactor (section 2.3.2). Finally, a challenging innovative multi fixed-bed Loop Reactor concept will be studied, for which two different reactor models will be introduced in section 2.3.3.

### 2.3.1 Stirred tank reactor models

Stirred tank reactors (fig. 2.5a) are mainly applied to carry out liquid phase reactions. Various operation modes are conceivable. In industry, the continuous mode is mainly used. In lab scale or to increase flexibility and control batch and semi-batch experiments are useful (Helfferich, 2004). For kinetic parameter investigation, dynamic (perturbed batch) experiments are suitable as well. In such experiments one or more reactants are dosed additionally after a certain reaction time. The resulting transient reactor dynamics can be used to estimate the kinetic parameters more precisely. The evaluation of the concentration profiles versus time can be performed considering the applied tank reactors as perfectly mixed and the gas phases as ideal. Frequently, it can be assumed that the reactions take place exclusively in the liquid phase. Coupled component material balances in the gas (partial pressure  $p_{j_c}$ ) and liquid phase (concentration  $c_{j_c}$ ) are presented in eq. 2.41 and eq. 2.42, respectively (Baerns, 2006; Kiedorf et al., 2014).

$$\frac{dp_{j_c}}{dt} = -k_{\text{eff},j_c} (p_{j_c} - p_{j_c}^*) + \frac{dp_{j_c}^{\text{dos}}}{dt} \quad (2.41)$$

$$\frac{dc_{j_c}}{dt} = \tau^{-1} (c_{j_c} - c_{j_c}^{\text{in}}) - k_{\text{eff},j_c} \cdot (c_{j_c,\text{li}} - c_{j_c,\text{li}}^*) + c_{\text{cat,rs}} (c_{j_c,\text{li}}) \cdot \tilde{M}_{\text{cat}} \cdot \sum_{j_R=1}^{N_R} \nu_{j_R,j_c} \cdot r_{j_R} (T, c_{j_c,\text{li}}) \quad (2.42)$$

In eq. 2.42 there are  $N_R$  reactions assumed taking place in the liquid phase. The rates are proportional to the concentration of the active catalyst in resting state  $c_{\text{cat,rs}}$ . Besides the reaction rate models  $r_{j_R}$ , the solution of eqs. 2.41 and 2.42 requires knowledge regarding the phase equilibrium ( $p_{j_c}^*$ ,  $c_{j_c}^*$ ) and the mass transfer coefficients  $k_{\text{eff},j_c}$ . Further param-

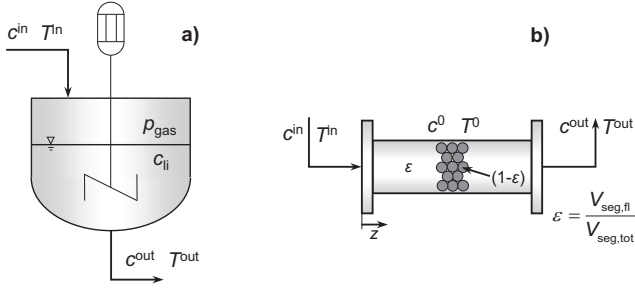


**Figure 2.5:** Schematic principle of (a) continuous stirred tank reactor (CSTR) and (b) a single tubular tank reactor including catalyst particles (packed bed reactor)

ters are the residence time  $\tau$ , molar catalyst mass  $\tilde{M}_{cat}$  and the stoichiometric coefficient  $\nu_{j/R_j}$ . Further for solving the system of ordinary differential equations (eqs. 2.41 and 2.42) the closure condition of the fluxes between the gas and the liquid phase ( $J_{gas} = J_{li}$ ) and the appropriate initial conditions are required (appendix B.3).

$$p_{j_c}(t=0) = p_{j_c}^0 \quad c_{j_c,li}(t=0) = c_{j_c,li}^0 \quad (2.43)$$

To avoid parameter correlations in kinetic investigations, isothermal experiments are preferable (Helfferich, 2004). In case of non-isothermal experimental conditions, the energy balance is needed (eq. 2.44). The energy balance of the applied continuous stirred tank reactor (CSTR) model includes the accumulation, convection, reaction term and the heat transfer through the reactor-shell. For calculations the following parameters are required: total concentration  $c_{tot}$ , heat capacity  $c_p$ , total volumetric flux  $\dot{V}_{tot}$ , reaction enthalpy  $\Delta h_{R_j/R}$ , heat transfer coefficient  $k_W$ , reactor circumference  $U_{seg}$  and surface  $A_B$ .

$$c_{tot} c_p \frac{dT}{dt} = c_{tot} c_p \dot{V}_{tot} (T^{in} - T) + c_{cat,rs} \tilde{M}_{cat} \sum_{j_r=1}^{N_{R_j}} (-\Delta h_{R_j/R}) r_{j_r} + k_W \frac{U_{seg}}{A_B} (T_W - T) \quad (2.44)$$

The determined reactor model for stirred tank reactors (eqs. 2.41–2.44) is valid for batch, semi-batch and perturbation operation modes. To distinguish these operation modes different boundary conditions, have to be applied as listed in tab. 2.1.

**Table 2.1:** Boundary conditions for different operation modes of the applied stirred tank reactor model (eqs. 2.41-2.44)

	Batch	Semi-Batch	Dynamic (Perturbation)		
Inlet	$p_{j_c}^{in} = 0$ $c_{j_c}^{in} = 0$	$p_{j_c}^{in} \neq 0$ $c_{j_c}^{in} \neq 0$	$p_{j_c}^{in}(t < t_{per}) = 0$ $c_{j_c}^{in}(t < t_{per}) = 0$	$p_{j_c}^{in}(t = t_{per}) \neq 0$ $c_{j_c}^{in}(t = t_{per}) \neq 0$	$p_{j_c}^{in}(t > t_{per}) = 0$ $c_{j_c}^{in}(t > t_{per}) = 0$
Outlet	$p_{j_c}^{out} = 0$ $c_{j_c}^{out} = 0$	$p_{j_c}^{out} = 0$ $c_{j_c}^{out} = 0$	$p_{j_c}^{out} = 0$ $c_{j_c}^{out} = 0$		

### 2.3.2 Model of single tubular reactor

Tubular reactor models are more complex than perfectly mixed tank models. Froment and Bischoff (1990) classified continuum models of tubular reactors according to the phases

involved. In heterogeneous catalysis models will be distinguished between pseudo-homogeneous and heterogeneous phases consideration (Baerns, 2006).

Below, the material balances were formulated considering a pseudo-homogeneous ideal plug flow tubular reactor (PFTR) model, neglecting interphase transport limitations and radial gradients corresponding to the experimental equipment used. The corresponding balance of each component in the fluid phase (eq. 2.45) contains an accumulation, axial convection and the reaction term. If no transient behavior needs to be considered in kinetic modeling the accumulation can be neglected.

$$\varepsilon \frac{\partial \dot{n}_{j_c}}{\partial t} = -u_{\text{gas}} \frac{\partial \dot{n}_{j_c}}{\partial z} + \frac{m_{\text{cat}} \dot{V}_{\text{tot}}}{V_{\text{seg}}} \sum_{j_R=1}^{N_R} v_{j_R/j_c} \cdot r_{j_R} \quad (2.45)$$

The initial and boundary conditions are defined by:

$$\dot{n}_{j_c}(t=0, z) = \dot{n}_{j_c}^0 \quad \dot{n}_{j_c}(t, z=0) = \dot{n}_{j_c}^{\text{in}} \quad (2.46)$$

The pressure drop and the gas phase velocity across the catalyst bed can be correlated using the semi-empirical *Ergun*-equation (eq. 2.47) which includes the dynamic viscosity  $\eta_{\text{tot}}$ , the catalyst particle diameter  $d_p$ , the total gas density  $\rho_{\text{tot}}$  and the gas velocity  $u_{\text{gas}}$ .

$$\frac{d\rho_{\text{tot}}}{dz} = -150 \frac{(1-\varepsilon)^2}{\varepsilon^3} \frac{\eta_{\text{tot}}}{d_p^2} u_{\text{gas}} - 1.75 \frac{(1-\varepsilon)}{\varepsilon^3} \frac{\rho_{\text{tot}}}{d_p} u_{\text{gas}}^2 \quad (2.47)$$

More detailed information for the *Ergun*-equation can be found in (Ergun and Orning, 1949; Ergun, 1952; Giese et al., 1998).

Based on the individual adjustable volume-surface-ratio of a reactor tube the heat transfer through the reactor shell can be improved. Thus, various thermal operation modes are useable. As aforementioned kinetic experiments should be organized isothermal to avoid superposed heat transport phenomena (Helfferich, 2004). If an isothermal operation mode in kinetic experiments is not realistic because of e.g. high exothermicity, a temperature profile calculation along the length of the catalytic fixed-bed is required based on an energy balance (see next section).

### 2.3.3 Models of reactor cascade (Loop Reactor)

The Loop Reactor (LR) concept exploits a tubular reactor cascade with time variable in- and outlet ports (fig. 2.6a). The design and working principle will be explained in detail in section 6. Based on the (single) tubular reactor model (eq. 2.45), the mass balance can be defined for each reactor segment in an analogues manner. In addition to the simplified tubular tank reactor model, axial dispersion is included leading to the following mass balance:

$$\varepsilon \frac{\partial \dot{n}_{j_c}}{\partial t} = -u_{\text{gas}} \frac{\partial \dot{n}_{j_c}}{\partial z} + D_{j_c} \frac{\partial^2 \dot{n}_{j_c}}{\partial z^2} + \frac{m_{\text{cat}} \dot{V}_{\text{tot}}}{V_{\text{seg}}} \sum_{j_R=1}^{N_R} v_{j_R/j_c} \cdot r_{j_R} \quad (2.48)$$

The initial and boundary conditions according to eq. 2.46 will be extended to (Danckwerts, 1953):

$$\dot{n}_{j_c}(t=0, z) = \dot{n}_{j_c}^0 \quad u_{\text{gas}} \dot{n}_{j_c} = u_{\text{gas}} \dot{n}_{j_c} \Big|_{z=0} - D_{j_c} \frac{d\dot{n}_{j_c}}{dz} \Big|_{z=0} \quad \frac{d\dot{n}_{j_c}}{dz} \Big|_{z=L_{\text{seg}}} = 0 \quad (2.49)$$

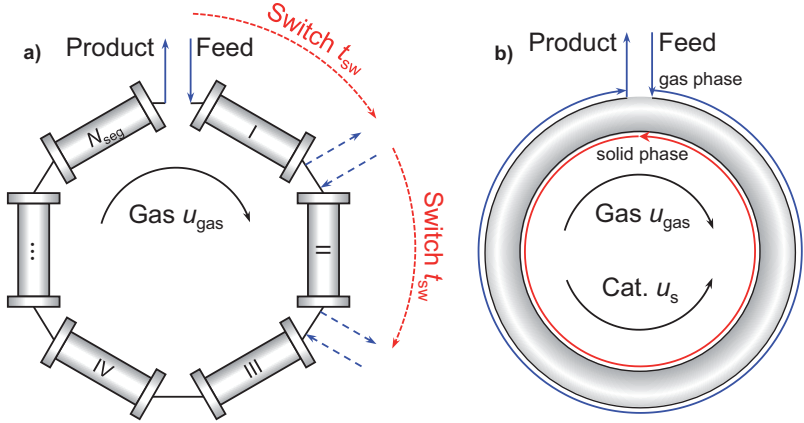


**Figure 2.6:** (a) Principle of the Loop Reactor exploiting a periodic operated reactor cascade of  $N_{\text{seg}}$  catalytic fixed beds based on periodically switching in- and outlet positions in the gas flow direction and (b) the corresponding true moving bed reactor model for an infinite number of segments (Zahn et al., 2011)

The individual specific diffusion component coefficients  $D_{j,c}$  are substituted by effective diffusion coefficients  $D_{\text{eff}}$  available for all components (appendix B.4) (Froment and Bischoff, 1990).

The Loop Reactor concept is based on the recycling the heat of the exothermal reaction to heat up the gas phase at the reactor entrance (see also section 6). To guarantee a stable ignited state the energy loss across and between the catalytic fixed beds have to be marginal. Adiabatic reactor behavior is most desirable.

The corresponding adiabatic pseudo-homogeneous energy balance for the fluid phase is shown in eq. 2.50.

$$\left( \varepsilon (\rho c_p)_{\text{gas}} + (1 - \varepsilon) (\rho c_p)_s \right) \frac{\partial T}{\partial t} = - (\rho c_p)_{\text{gas}} u_{\text{gas}} \frac{\partial T}{\partial z} + \lambda_{\text{eff}} \frac{\partial^2 T}{\partial z^2} + \frac{m_{\text{cat}}}{V_{\text{seg}}} \sum_{j_R=1}^{N_R} (-\Delta h_R)_{j_R} r_{j_R} \quad (2.50)$$

With the initial and boundary conditions:

$$T(t=0, z) = T^0 \quad (\rho c_p)_{\text{gas}} u_{\text{gas}} T^{\text{in}} = (\rho c_p)_{\text{gas}} u_{\text{gas}} T \Big|_{z=0} - \lambda_{\text{eff}} \frac{dT}{dz} \Big|_{z=0} \quad \frac{dT}{dz} \Big|_{z=L_{\text{seg}}} = 0 \quad (2.51)$$

The effective axial heat dispersion will be described by the heat conductivity coefficient  $\lambda_{\text{eff}}$ , which depends on the system properties and gas phase velocity (Verein Deutscher Ingenieure, 2006).

The numerical solution of the catalytic steady state of the transient pseudo-homogeneous LR model (eqs. 2.48 and 2.50) is quite time-consuming (Nieken et al., 1995; Sheintuch and Nekhamkina, 2005; Zahn, 2012). To decrease the simulation efforts for parametric studies the use of reduced models is desirable. For that reason, several concepts for model reduction of periodic operation of multi-bed processes were introduced. First the use of just mean internal profiles are suitable (Zahn, 2012). A second approach is based

on assuming an infinitely fast switching asymptote which results in a true countercurrent process (Nieken et al., 1995; Sheintuch and Nekhamkina, 2005; Zahn, 2012).

As a useful simulation model to describe the LR concept the true moving bed countercurrent reactor (TMBR) process model is used in this work. In the chromatography community, this model approach is well-established and widely applied (Ruthven and Ching, 1989; Haus et al., 2007; Rajendran et al., 2009; Schmidt-Traub et al., 2012). Also in reaction engineering to model the LR concept the TMBR model has been successfully used (Zahn, 2012). The schematic principle of the TMBR model is shown in fig. 2.6b. Additional to the switched LR model a continuous movement of the solid catalyst phase  $u_s$  is considered. The material balance of the periodically operated LR concept (eq. 2.48) is also valid for the TMBR model.

The corresponding continuous model thermal energy balance equation is eq. 2.52.

$$(\rho c_p)_m \frac{\partial T}{\partial t} = -(\rho c_p)_{\text{gas}} u_{\text{gas}} \frac{\partial T}{\partial z} + (\rho c_p)_s u_s \frac{\partial T}{\partial z} + \lambda_{\text{eff}} \frac{\partial^2 T}{\partial z^2} + \frac{m_{\text{cat}}}{V_{\text{seg}}} \sum_{j_R=1}^{N_R} (-\Delta h_R)_{j_R} r_{j_R} \quad (2.52)$$

It needs to respect the corresponding initial and boundary conditions (Danckwerts, 1953):

$$T(t=0, z) = T^0 \quad (\rho c_p)_{\text{gas}} u_{\text{gas}} T^{\text{in}} = (\rho c_p)_{\text{gas}} u_{\text{gas}} T \Big|_{z=0} - \lambda_{\text{eff}} \frac{dT}{dz} \Big|_{z=0} \quad \frac{dT}{dz} \Big|_{z=L_{\text{seg}}} = 0 \quad (2.53)$$

More details of the LR model used later will be given in section 6 and appendix B.4.

## 2.4 Conclusions

The mechanistic kinetic rate analysis described above was based on postulated catalytic cycles. Both for homogeneous and heterogeneous catalysis, a powerful tool for providing mechanism based rate models is provided by the ‘‘General Catalytic Cycle Kinetics (GCCK)’’ approach originally suggested by *Christiansen*. Using this approach, complex reaction rate models can be derived for different phase situation (Helfferich, 2004; Murzin and Salmi, 2005). However, the derived mechanistic rate approaches generate a multitude of unknown kinetic and thermodynamic parameters. To estimate these parameters from experimental data, an adequate experimental design is required. Regarding homogeneous catalysis several spectroscopic methods are suitable to identify and quantify single elementary cycle steps. In heterogeneous catalysis detailed molecular studies are more difficult and face often limits. After parameter estimation, frequently correlations are observed. Then, mathematical model reduction techniques, as e.g. the subset selection method, or dedicated additional measurements are necessary.

By means of the described GCCK approach and the introduced reactor models, the kinetic parameter estimation as well as parametric studies will be possible for stirred tank reactors and single tubular and multi fixed-bed tubular reactors. Two different reaction system examples will be studied in detail in Part II and Part III, respectively.

**Part II**

**Analysis of a Homogeneously  
Catalyzed Reaction**



### 3 Reaction Network and Kinetics of the Hydroformylation of 1-Dodecene

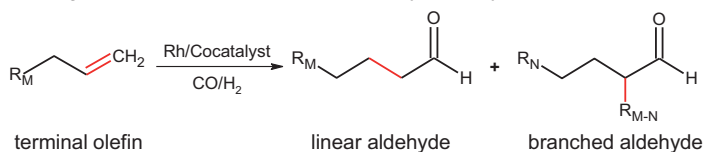
This section describes results of studying a challenging example of a homogeneously catalyzed reaction, namely the hydroformylation of the long-chain olefin 1-dodecene. Several sub-networks and the total reaction network were studied separately performing numerous batch runs (section 3). Analyzing the acquired experimental data kinetic parameters for the main and most important side reactions were estimated sequentially. Subsequently, the determined reaction kinetics were applied for analyzing other operation modes beyond batch operation (section 4). Finally, additional perturbation experiments were carried out to validate and improve the reaction kinetics, respectively.

The results presented in this section regarding the reaction kinetic analysis were acquired within in a DFG-funded larger project (SFB-TR 63). Parts of them were already published in:

G. Kiedorf, D.M. Hoang, A. Müller, A. Jörke, J. Markert, H. Arellano-Garcia, A. Seidel-Morgenstern and C. Hamel, Kinetics of 1-dodecene hydroformylation in a thermomorphic solvent system using a rhodium-biphephos catalyst. *Chemical Engineering Science* 115, 31–48, 2014

The author of this thesis contributed essentially to the results presented in this paper. His contribution was the reaction network analysis of the sub- and overall network and the determination of the mechanistic rate models for the isomerization, hydrogenation and hydroformylation of 1-dodecene.

The hydroformylation of olefins, also designated as oxo synthesis, is a reaction where alkenes react with hydrogen and carbon monoxide in the presence of transition metal catalysts (e.g. cobalt or rhodium and suitable ligands) to form terminal and branched aldehydes. The general scheme is illustrated for the hydroformylation of a terminal olefin.



Hydroformylation is an important building block synthesis and a well-known example of successfully applying homogeneous catalysis. A large amount of complexes between transition metals and various ligands were investigated in the last decades (Behr, 2008).

The major industrial application of hydroformylation converts short-chain olefins using the *Ruhrchemie/Rhône-Poulenc* process. This process exploits an aqueous biphasic catalytic system, wherein the catalyst is soluble in the aqueous phase and the reactants and products are present essentially in the organic phase, respectively (Beller et al., 1995; Wachsen et al., 1998; Desset and Cole-Hamilton, 2009). The separation of the formed aldehydes and the precious rhodium is a critical issue in industrial scale (Fang et al., 2007; Janssen et al., 2010; Fang et al., 2011). The formed desired terminal aldehyde is used as

raw material for a broad range of products, e.g. synthetic materials, solvents or dyestuffs. The current industrial application of the hydroformylation reaction is limited to the conversion of short-chain olefins (<C8) due to the limited solubility of long-chain olefins in the aqueous catalyst phase (Haumann et al., 2002; Dwars et al., 2005; Desset et al., 2009). Therefore, in the last few years considerable efforts were made to develop novel catalyst-ligand complexes and solvent systems. It could be shown that high aldehyde yields at simultaneously high olefin conversions could be achieved e.g. with non-aqueous ionic liquids (Webb et al., 2003; Deshpande et al., 2011; Jakuttis et al., 2011), supercritical carbon dioxide (Guha et al., 2007; Subramaniam, 2010; Koeken et al., 2011b; Subramaniam and Akien, 2012; Ye et al., 2012) and combinations of those solvents (Haji and Erkey, 2002; Hintermair et al., 2007; Mokhadinyana et al., 2012). As a very promising alternative was demonstrated the application of thermomorphic multicomponent solvent (TMS) systems allowing to perform the reaction under homogeneous conditions at elevated temperature and to recover the catalyst in the polar phase formed after reaction by spontaneous phase separation at lower temperature (Brunsch and Behr, 2013). The potential has been recently shown for the isomerizing hydroformylation of trans-4-octene (Behr et al., 2005a; Behr et al., 2005b), the hydroaminomethylation (Behr and Roll, 2005; Neubert et al., 2016) and the hydroformylation of 1-dodecene (Brunsch and Behr, 2013; Markert et al., 2013).

For further development of such innovative reaction and solvent systems knowledge regarding the reaction mechanisms and the kinetics of hydroformylation is mandatory (Chaudhari et al., 2001; van Leeuwen and Claver, 2001; Murzin and Salmi, 2005). For this reason, various theoretical kinetic and mechanistic studies were carried out in the past for different solvent and catalyst-ligand systems. Empirical or semi-empirical reaction rate equations were derived and studied for the hydroformylation of 1-octene (Purwanto and Delmas, 1995; Deshpande et al., 1996; Shaharun et al., 2010) and 1-dodecene (Bhanage et al., 1997; Haumann et al., 2002; Yang et al., 2002; Zhang et al., 2002). Some recent publications provide mechanistic equations to quantify the hydroformylation rates of short-chain olefins (Murzin et al., 2010; Murzin et al., 2012) and long-chain olefins like 1-octene (Deshpande et al., 2011; Koeken et al., 2011a) and 1-decene (Divekar et al., 1994). However, focus was set in these studies primarily on the target reaction. Consecutive and side reactions were not described in depth. Furthermore, the well-known fact that such catalysts change their state as a function of the operating conditions (Behr, 2008) was not considered quantitatively.

Goal of this section is the development and validation of kinetic models for the hydroformylation of 1-dodecene performed in a thermomorphic solvent system using a rhodium catalyst with a suitable ligand. Following the catalytic cycle suggested recently (Markert et al., 2013) and well established GCCK approach (Helferich, 2004; Murzin and Salmi, 2005; Marin and Yablonsky, 2011), the relevant side reactions (isomerization and hydrogenations) had to be also quantified as well as the existence of different states of the applied Rh-catalyst. To achieve this goal a large amount of systematic batch experiments was carried out in a wide parameter range. Hereby different reactants were fed to the reactor in order to decouple the complex network. Advanced subset selection methods were applied to tackle the challenging model reduction and parameter estimation problems (section 2).

Preliminary the concrete reaction and solvent systems will be introduced in section 3.2. Then the catalytic cycle and the corresponding mechanistic models as well as the reduced model versions will be presented in section 3.2. Additionally, the test equipment and experimental procedures will be described in the section 3.3. The mathematical tools applied for model reduction and parameter estimation as well as the reactor model were already explained in section 2. Finally, for all key reactions of the network rate equations and corresponding parameters are provided and discussed in section 3.5.

### 3.1 Solvent system, ligand and reaction network

In order to allow an efficient recycling of the precious catalyst-ligand-complex the thermomorphic multicomponent solvent (TMS) system described in (Brunsch and Behr, 2013; Markert et al., 2013) was used. It consists of 20 wt.-% of the reactant 1-dodecene, 32 wt.-% of the polar solvent dimethylformamide (DMF) and 48 wt.-% of the additional non-polar component decane. The ternary-phase diagram, in particular the temperature dependence of the miscibility gap between DMF and decane, is reported in (Schäfer et al., 2012). This TMS system can be characterized as follows: At a reaction temperature above 85 °C a homogenous phase exists, whereas a cooling after the reaction causes a separation into two phases. Then the rhodium-ligand complex can be isolated in the polar DMF containing phase and recycled.

Based on results of (Markert et al., 2013) catalyst-ligand complexes consisting of the pre-catalyst  $\text{Rh}(\text{acac})(\text{CO})_2$ , and the ligand biphepos were applied. This catalyst provided the desired high *n/iso* ratios of the formed aldehydes at simultaneously high olefin conversions. It has been observed in extensive preliminary experiments (Markert et al., 2013) that the hydroformylation reactions are accompanied in a complex reaction network by isomerization and hydrogenation reactions. The product mixtures contained besides the desired linear aldehyde tridecanal, alkanes and also various isomers of dodecene and aldehydes. A simplification of the network was performed in (Markert et al., 2013) leading to the suggestion of two types of lumped isomers into the pseudo-components designated as “iso-dodecene” and “iso-aldehyde”, respectively. The six key reactions identified are summarized in fig. 3.1. The desired *n*-aldehyde (nAD) tridecanal is formed with a rate  $r_{\text{hf},b}$ . The undesired alkane (AL) dodecane is formed with rates  $r_{\text{hg},a}$  and  $r_{\text{hg},b}$ . The pseudo-components “iso-dodecene (iOL)” and “iso-aldehyde (iAD)” are formed with rates  $r_{\text{iso}}$ ,  $r_{\text{hf},a}$  and  $r_{\text{hf},c}$  respectively. These six reactions form the following four sub-networks (I-IV) of increasing complexity and the total network  $V_{\text{total}}$ :

Sub-network	Name	Abbreviation of involved reaction rates
• I	Isomerization of 1-dodecene	$r_{\text{iso}}$
• II	Hydrogenation of iso-dodecene	$r_{\text{iso}}$ , $r_{\text{hg},a}$
• III	Hydrogenation of 1-dodecene	$r_{\text{iso}}$ , $r_{\text{hg},a}$ , $r_{\text{hg},b}$
• IV	Hydroformylation of iso-dodecene	$r_{\text{iso}}$ , $r_{\text{hg},a}$ , $r_{\text{hg},b}$ , $r_{\text{hf},a}$
Total network (all 6 reactions)		
• $V_{\text{total}}$	Hydroformylation of 1-dodecene	$r_{\text{iso}}$ , $r_{\text{hg},a}$ , $r_{\text{hg},b}$ , $r_{\text{hf},a}$ , $r_{\text{hf},b}$ , $r_{\text{hf},c}$

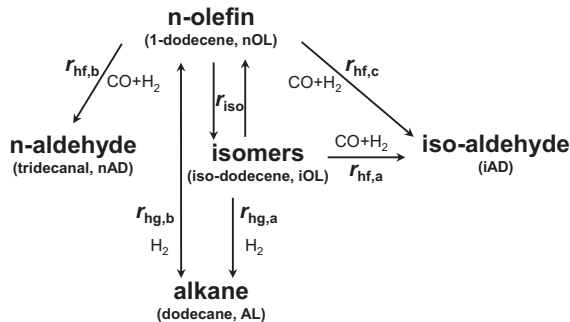


**Figure 3.1:** Reaction network of the hydroformylation of 1-dodecene considering isomerization ( $r_{iso}$ ), two hydrogenation ( $r_{hg,a}$ ,  $r_{hg,b}$ ) and three hydroformylation reactions ( $r_{hf,a}$ ,  $r_{hf,b}$ ,  $r_{hf,c}$ ) forming five subsets of reactions I-V<sub>total</sub> as postulated in (Markert et al., 2013; Kiedorf et al., 2014)

Following (Hu et al., 2011) a bottom-up approach to evaluate sequentially results of increasing complexity, starting with the smallest sub-network and ending with the complete network, was applied in this work to determine and validate reaction kinetic equations and corresponding parameters for all six reactions.

Based on a postulated catalytic cycle in a first stage mechanistic rate equations were derived for the hydroformylation, hydrogenation and isomerization reactions using techniques as already described in the section 2.1.

## 3.2 Catalytic cycle and mechanistic models

### 3.2.1 Catalytic cycle and the resting state of the catalyst species

Most of the few publications devoted to model the kinetics of the hydroformylation of long-chain olefins are based on applying semi-empirical or empirical rate expressions (Zhang et al., 2002) and side reactions like isomerization or hydrogenation are typically neglected (Divekar et al., 1994; Purwanto and Delmas, 1995; Deshpande et al., 1996; Purwanto et al., 1996; Bhanage et al., 1997; Deshpande et al., 1997; Yang et al., 2002; Zhang et al., 2002). Only a few recently published articles discuss the hydroformylation by means of mechanistic kinetic models (Murzin et al., 2010; Shaharun et al., 2010; Deshpande et al., 2011; Koeken et al., 2011a) (Murzin et al., 2012). These models are based on assuming a catalytic cycle, which describes the steps of the homogeneously catalyzed reactions including the involved specific catalyst species. Typically, and also in this work, catalytic cycles of the Wilkinson type are applied (Evans et al., 1968; van Leeuwen and Claver, 2001). The extended *Wilkinson* catalytic cycle analyzed in this work is depicted in fig. 3.2. It includes, besides the hydroformylation of the long-chain 1-olefin (nOL), as the essential side reactions isomerization to iso-dodecene (iOL) (already shown in fig. 2.2) and hydrogenation to alkanes (AL).

Common starting point for transforming the 1-olefin in the three different reaction cycles is the key species of the catalytic system indicated in fig. 3.2 as “catalyst in the resting state (rs)”. To quantify the amount of catalyst species and also other inactive Rh-

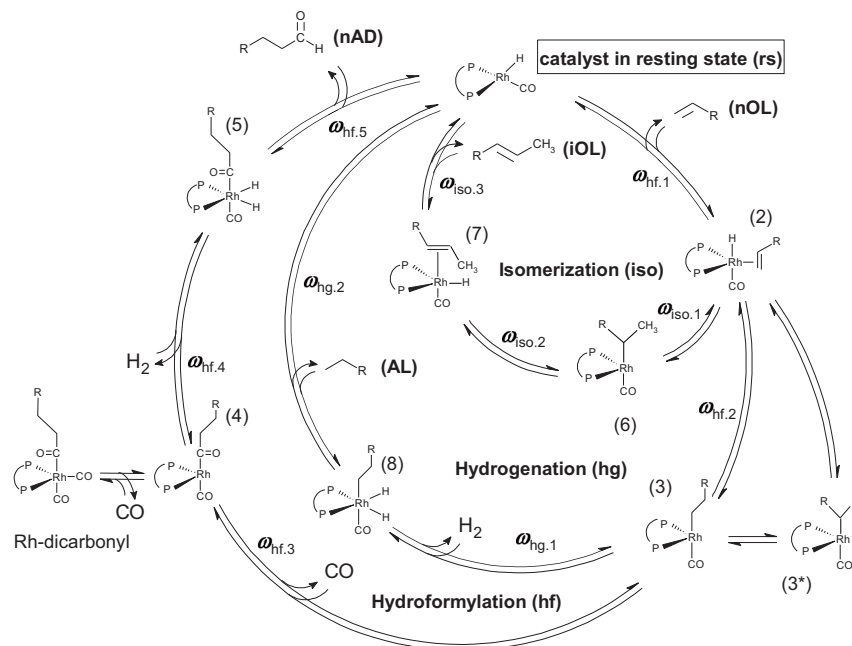


**Figure 3.2:** Potential mechanism and catalytic cycle for isomerization (iso), hydrogenation (hg) and hydroformylation (hf) of long-chain olefins. The frequencies of the specific reaction steps,  $\omega_{ij}$ , are used in deriving overall rate expressions applying the general approach (eqs. 2.3-2.6 for the isomerization and eqs. A.4 and A.8 for the hydrogenation and hydroformylation) (Evans et al., 1968; Kiedorf et al., 2014)

species outside the three main reaction cycles were considered. This will be discussed in fig. 3.3 in detail. Within the cycles of isomerization (iso), hydrogenation (hg) and hydroformylation (hf) the active resting state of the catalyst transforms into various intermediate states (2-8). Regarding species (3) the possibility of an alternative species (3\*) opening a second catalytic cycle which was discussed by (Markert et al., 2013) and is just indicated here. In fig. 3.2 also the possibility included that inactive Rh-dicarbonyl species are formed during hydroformylation, which leave the main cycle. The occurrence of such species was already verified using NMR-techniques (van Leeuwen and Claver, 2001; Kamer et al., 2004; Deshpande et al., 2011; Selent et al., 2011).

Catalytic cycle steps of the isomerization were already mentioned in section 2.1.1. The hydrogenation catalytic cycle starts with the olefin coordination at the catalyst species in resting state, too. At the formed  $\pi$ -complex (species 2) an insertion at the Rh-H bond to the alkyl-complex (species 3) happened. Afterwards an oxidative addition of  $H_2$  occur which form the di-hydrido-alkyl-complex (species 8). The catalytic cycle is closed with a reductive elimination of the alkane. The first two steps of the hydroformylation cycle are equal. Afterwards a CO insertion to the Rh-C bond occurs. This form the acyl-complex

(species 4). Following an oxidative addition of hydrogen forms the di-hydrido-rhodium-acyl-complex (species 5). The closing step of the hydroformylation cycle corresponds to the hydrogenation with a reductive elimination of aldehyde product (Evans et al., 1968; van Leeuwen and Claver, 2001; Deshpande et al., 2011; Markert et al., 2013; Kiedorf et al., 2014).

The catalyst in resting state as well as present inactive Rh-species are in equilibrium with one another. Potential inhibition rhodium based molecules which are already spectroscopic verified and described in literature are the Rh-dimer (Moasser et al., 1995; Bronger et al., 2004; Deshpande et al., 2011), the Rh-di-carbonyl (species 1) (Evans et al., 1968; Deshpande et al., 2011; Selent et al., 2011), the Rh-bis-chelate (Hamerla et al., 2013) and the Rh-tetra-carbonyl (Li et al., 2002; Hamerla et al., 2013) (fig. 3.3). These catalyst species were detected for different ligands and solvent systems. Because of a missing verification for the present system the catalyst pre-equilibrium network is reduced to the rhodium precursor  $\text{Rh}(\text{acac})(\text{CO})_2$ , the rhodium di-carbonyl, the rhodium dimer and the resting state. Moreover, only the catalyst in resting state is considered as active and selective for the isomerization, hydrogenation and hydroformylation of long-chain olefins (Evans et al., 1968; Carvajal et al., 2009).

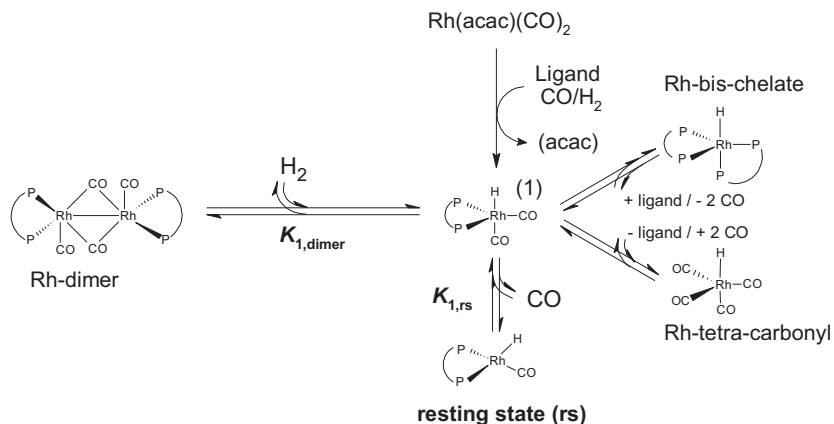


**Figure 3.3:** The preliminary formation of the active Rh-catalyst in the resting state (described by eqs. 3.1a-3.1d) is indicated. Possible species in the catalyst pre-equilibrium of the rhodium catalyzed isomerization, hydrogenation and hydroformylation of 1-dodecene (Kiedorf et al., 2014; Jörke et al., 2015b)

For quantification of the amount of catalyst present in the resting state (rs) the inhibition effect of carbon monoxide needs to be evaluated. Hereby, a quantification of the catalyst “pre-equilibrium” between species (1), the inactive dimer and the catalyst in the resting state (rs) must be done relating to the specific total mass of the supplied precious rhodium precursor  $\text{Rh}(\text{acac})(\text{CO})_2$ , which is assumed to be initially fully transformed into species (1). Thus, the following relation between the concentrations of the different Rh-containing

species holds:

$$c_{\text{Rh,precursor}} = c_{\text{cat,rs}} + c_{\text{cat,1}} + 2 \cdot c_{\text{cat,dimer}} \quad (3.1a)$$

By replacing the catalyst concentrations of the dimer and species (1) with the concentration of the catalyst in the resting state and two corresponding equilibrium constants  $K_{1,rs}$  and  $K_{1,dimer}$ , eq. 3.1b results.

$$c_{\text{Rh,precursor}} = c_{\text{cat,rs}} + \frac{c_{\text{cat,rs}} \cdot c_{\text{CO,li}}}{K_{1,rs}} + 2 \cdot \left( \frac{K_{1,dimer}}{c_{\text{H}_2,li}} \left( \frac{c_{\text{cat,rs}} \cdot c_{\text{CO,li}}}{K_{1,rs}} \right)^2 \right) \quad (3.1b)$$

Rearrangement provides eq. 3.1c, which describes the inhibiting influence of CO on the available amount of catalyst in the resting state.

$$c_{\text{cat,rs},1/2} = -\frac{c_{\text{H}_2,li} K_{1,rs} (K_{1,rs} + c_{\text{CO,li}})}{4K_{1,dimer} c_{\text{CO,li}}^2} \pm \left[ \left( \frac{c_{\text{H}_2,li} K_{1,rs} (K_{1,rs} + c_{\text{CO,li}})}{4K_{1,dimer} c_{\text{CO,li}}^2} \right)^2 + \frac{c_{\text{H}_2,li} K_{1,rs}^2 c_{\text{Rh,precursor}}}{2K_{1,dimer} c_{\text{CO,li}}^2} \right]^{1/2} \quad (3.1c)$$

Based on the two rhodium atoms in the rhodium dimer, a quadratic equation with two possible mathematical solutions occurs. A similar description for calculating the active catalyst concentration as a function of the CO and H<sub>2</sub> concentration in gas phase is given in (Jörke et al., 2015b). There only the first positive solution is considered. If in the total catalyst concentration balance (eq. 3.1a) the second rhodium atom in the rhodium dimer is neglected, the equation of the catalyst in resting state can be simplified to eq. 3.1d (Kiedorf et al., 2014).

$$c_{\text{cat,rs}} = \frac{c_{\text{Rh,precursor}}}{\left( 1 + K_{\text{cat},\alpha} \cdot c_{\text{CO,li}} + K_{\text{cat},\beta} \cdot c_{\text{CO,li}} / c_{\text{H}_2,li} \right)} \quad \text{with} \quad K_{\text{cat},\alpha} = \frac{1}{K_{1,rs}}, \quad K_{\text{cat},\beta} = \frac{K_{1,dimer}}{K_{1,rs}} \quad (3.1d)$$

A comparison of these two solutions is shown in fig. 3.4a-c. It is obviously, that the qualitative mathematical response for variations in the partial pressures of H<sub>2</sub> and CO as well as in the rhodium precursor concentration of the simplified function is strongly related to the positive quadratic solution. Based on this reason the catalyst equilibrium will be described by eq. 3.1d.

The concentration of the active catalyst in the resting state forms the starting point of the three catalytic sub-cycles (fig. 3.2) and will be incorporated later in the reactor mass balance (eq. 2.41).

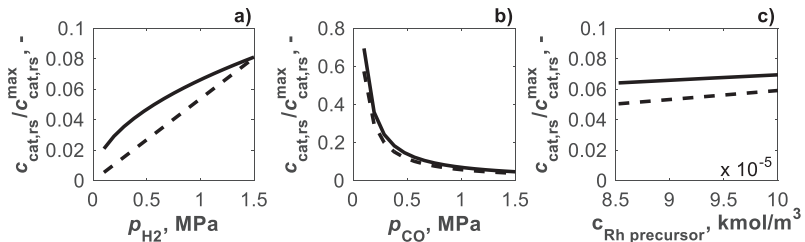


**Figure 3.4:** Comparison of the catalyst concentration in resting state of eq. 3.1c (solid line) and eq. 3.1d (dashed line) as a function of (a) hydrogen partial pressure ( $p_{\text{CO}} = 1$  MPa), (b) carbon monoxide partial pressure ( $p_{\text{H}_2} = 1$  MPa) and (c) the rhodium precursor concentration ( $p_{\text{CO}} = p_{\text{H}_2} = 1$  MPa)

Two different mechanistic approaches were applied in this section to derive rate expressions. Hereby, the common starting point is the catalyst in the resting state. It is quantitatively considered that the Rh present in this state can be transferred into species (2) to (8) (fig. 3.2). Not further considered were species (3\*) and the Rh-di-carbonyls.

### 3.2.2 Mechanistic approach to describe the rates in a network of reactions

The determination of mechanistic kinetics according to the GCCK approach (Helfferich, 2004; Murzin and Salmi, 2005) for the isomerization of 1-dodecene was introduced in section 2.1.1. The derivation of the corresponding overall kinetic rate equations for the other sub-cycles shown in fig. 3.2 describing the hydrogenation and hydroformylation can be performed in an analogous manner, leading finally to eqs. 3.5 and 3.9 given below. Details regarding the derivation of these expressions by the GCCK approach are provided in the appendix A.

The GCCK approach applied below leads to rate expressions, which contain a relative large number of free parameters. Thus, reduced models are attractive (see also section 2.2.3) and will be suggested and parameterized step by step based on experiments.

### 3.2.3 Reduced models with a single rate determining step

For the derivation of simplified mechanistic models often the assumption is made that one specific step in the catalytic cycle is the rate determining step (RDS).

Following a suggestion by (Deshpande et al., 2011), it will be considered below that the coordination of the olefin is rate determining for all the three sub-cycles of isomerization, hydrogenation and hydroformylation. In order to quantify the contributions of the sub-steps in a cycle the specifically involved catalyst species and their concentrations must be known. Hereby, the total amount of all catalyst species must be maintained and kept identical to the resting state amount. This is again illustrated for the isomerization in which the resting state (rs) and species (2), (6) and (7) are involved (fig. 3.2) bound by the following Rh-mass balance:

$$c_{\text{cat,tot,iso}} = c_{\text{cat,rs}} + c_{\text{cat,2}} + c_{\text{cat,6}} + c_{\text{cat,7}} \quad (3.2)$$

Then the reactant and catalyst species concentrations can be replaced by equilibrium constants for every non-rate determining step and inserted in the rate equation of the rate determining step. After rearranging and lumping the following reduced equation for the isomerization rate can be derived:

$$r_{\text{iso}} = \frac{k_{\text{iso}}(T) \cdot c_{\text{nOL}}}{(1 + K_{\alpha,\text{iso}} \cdot c_{\text{nOL}} + K_{\beta,\text{iso}} \cdot c_{\text{IOL}})} \quad (3.3)$$

This equation is obviously a reduced version of eq. 2.6 ( $K_{\text{eq,iso}} \rightarrow \infty$ ,  $K_{\text{v,iso}} = 0$ ).

Using the approach described, similar reduced rate equations can be derived for the hydrogenations and the hydroformylations (eqs. 3.6 and 3.10 below).

### 3.2.4 Reduced empirical models based on formal kinetics

An often applied significant model reduction can be achieved by formulating simple power laws. Assuming all reaction orders to be one and the possibility of either reversible or

irreversible overall reactions, empirical rate expressions can be formulated for the homogeneously catalyzed isomerization, hydrogenation and hydroformylation of 1-dodecene.

Examples for the corresponding expressions are eqs. 3.4, 3.7, 3.8, 3.11 and 3.12. The application of these strongly simplifying equations serves in this section essentially as a reference to evaluate the need for the more detailed approaches described before. They are further applied in cases where more detailed models could not be parameterized.

### 3.2.5 Summary of considered kinetic models

The following rate equations were applied and compared in the course of the work to sequentially analyze a large amount of experimentally determined batch reactor concentration profiles in order to quantify the kinetics of all five networks introduced above:

#### Isomerization (iso, sub-network I)

*“General Catalytic Cycle Kinetics (GCCK)” approach*

$$r_{\text{iso}} = \frac{k_{\text{iso}}(T) \cdot (c_{\text{nOL}} - c_{\text{IOL}} \cdot K_{\text{eq,iso}}^{-1})}{(1 + K_{\alpha,\text{iso}} \cdot c_{\text{nOL}} + K_{\beta,\text{iso}} \cdot c_{\text{IOL}} + K_{\gamma,\text{iso}})} \quad (2.6')$$

*Rate Determining Step (RDS) (section 3.2.3)*

$$r_{\text{iso}} = \frac{k_{\text{iso}}(T) \cdot c_{\text{nOL}}}{(1 + K_{\alpha,\text{iso}} \cdot c_{\text{nOL}} + K_{\beta,\text{iso}} \cdot c_{\text{IOL}})} \quad (3.3')$$

*Empirical*

$$r_{\text{iso}} = k_{\text{iso}}(T) \cdot (c_{\text{nOL}} - c_{\text{IOL}} \cdot K_{\text{eq,iso}}^{-1}) \quad (3.4)$$

#### Hydrogenation (hg, sub-network II and III)

*“General Catalytic Cycle Kinetics (GCCK)” approach*

$$r_{\text{hg,b}} = \frac{k_{\text{hg,b}} \cdot (c_{\text{nOL}} \cdot c_{\text{H}_2,\text{li}} - c_{\text{AL}} \cdot K_{\text{eq,hg,b}}^{-1})}{\left( 1 + K_{\alpha,\text{hg,b}} \cdot c_{\text{nOL}} + K_{\beta,\text{hg,b}} \cdot c_{\text{nOL}} \cdot c_{\text{H}_2,\text{li}} + K_{\gamma,\text{hg,b}} \cdot c_{\text{AL}} + K_{\delta,\text{hg,b}} \cdot c_{\text{H}_2,\text{li}} + K_{\epsilon,\text{hg,b}} \cdot c_{\text{AL}} \cdot c_{\text{H}_2,\text{li}} \right)} \quad (3.5)$$

*Rate Determining Step (RDS) (section 3.2.3)*

$$r_{\text{hg,b}} = \frac{k_{\text{hg,b}} \cdot c_{\text{nOL}} \cdot c_{\text{H}_2,\text{li}}}{(1 + K_{\alpha,\text{hg,b}} \cdot c_{\text{nOL}} + K_{\beta,\text{hg,b}} \cdot c_{\text{nOL}} \cdot c_{\text{H}_2,\text{li}})} \quad (3.6)$$

*Empirical*

$$r_{\text{hg,b}} = k_{\text{hg,b}} \cdot c_{\text{nOL}} \cdot c_{\text{H}_2,\text{li}} \quad (3.7)$$

$$r_{\text{hg,a}} = k_{\text{hg,a}} \cdot c_{\text{IOL}} \cdot c_{\text{H}_2,\text{li}} \quad (3.8)$$

#### Hydroformylation (hf, sub-network IV and the total network $V_{\text{total}}$ )

*“General Catalytic Cycle Kinetics (GCCK)” approach*

$$r_{\text{hf,b}} = \frac{k_{\text{hf,b}} \cdot (c_{\text{nOL}} \cdot c_{\text{H}_2,\text{li}} \cdot c_{\text{CO,li}} - c_{\text{nAD}} \cdot K_{\text{eq,hf,b}}^{-1})}{\left( 1 + K_{\alpha,\text{hf,b}} \cdot c_{\text{nOL}} + K_{\beta,\text{hf,b}} \cdot c_{\text{nOL}} \cdot c_{\text{CO,li}} + K_{\gamma,\text{hf,b}} \cdot c_{\text{nOL}} \cdot c_{\text{H}_2,\text{li}} \cdot c_{\text{CO,li}} + K_{\delta,\text{hf,b}} \cdot c_{\text{nAD}} + K_{\epsilon,\text{hf,b}} \cdot c_{\text{H}_2,\text{li}} \cdot c_{\text{CO,li}} \cdot c_{\text{nAD}} + K_{\zeta,\text{hf,b}} \cdot c_{\text{nOL}} \cdot c_{\text{H}_2,\text{li}} + K_{\eta,\text{hf,b}} \cdot c_{\text{H}_2,\text{li}} \cdot c_{\text{nAD}} + K_{\theta,\text{hf,b}} \cdot c_{\text{H}_2,\text{li}} + K_{\iota,\text{hf,b}} \cdot c_{\text{H}_2,\text{li}} \cdot c_{\text{CO,li}} + K_{\kappa,\text{hf,b}} \cdot c_{\text{CO,li}} \cdot c_{\text{nAD}} \right)} \quad (3.9)$$

*Rate Determining Step (RDS) (section 3.2.3)*

$$r_{\text{hf,b}} = \frac{k_{\text{hf,b}} \cdot c_{\text{nOL}} \cdot c_{\text{H}_2,\text{II}} \cdot c_{\text{CO,II}}}{\left(1 + K_{\alpha,\text{hf,b}} \cdot c_{\text{nOL}} + K_{\beta,\text{hf,b}} \cdot c_{\text{nOL}} \cdot c_{\text{CO,II}} + K_{\gamma,\text{hf,b}} \cdot c_{\text{nOL}} \cdot c_{\text{H}_2,\text{II}} \cdot c_{\text{CO,II}}\right)} \quad (3.10)$$

*Empirical*

$$r_{\text{hf,b}} = k_{\text{hf,b}} \cdot c_{\text{nOL}} \cdot c_{\text{H}_2,\text{II}} \cdot c_{\text{CO,II}} \quad (3.11)$$

$$r_{\text{hf,a}} = k_{\text{hf,a}} \cdot c_{\text{IOL}} \cdot c_{\text{H}_2,\text{II}} \cdot c_{\text{CO,II}} \quad (3.12)$$

### 3.3 Experimental equipment and procedures

The experimental set-up and procedures were designed and constructed by the author of this thesis at the Otto-von-Guericke University in Magdeburg.

#### 3.3.1 Reactor type

For the experimental investigation of the hydroformylation of 1-dodecene in a TMS system with DMF and decane a multi reactor system (MRS, *Parr Instruments*) was used to perform preliminary solubility measurements of the gaseous reactants and for systematic kinetic investigations. It consists of gas reservoirs for single gases and gas mixtures, the reactor unit and a control system. Six parallel reactors ( $V_{\text{seg}} = 0.105 \text{ l}$ ) can be fed separately from specific gas burettes. For each of the six reactors temperature and stirrer speed can be controlled separately. Further, each of these reactors has its own arrangements for sampling the liquid phase in discrete intervals via two valves. Additionally, it is possible to feed several gaseous or liquid components and gas mixtures, respectively. In fig. 3.5 is shown as an example a schematic illustration of one reactor with the corresponding gas reservoir and the sampling arrangement.

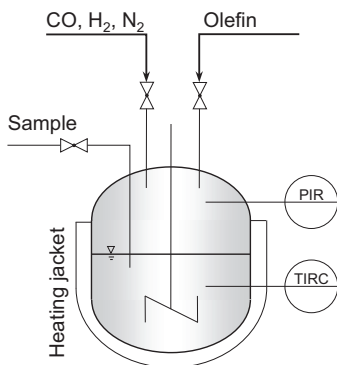


Figure 3.5: Schematic illustration of the used experimental reactor unit (*Parr Instrument*)

#### 3.3.2 Kinetic experiments

In a typical kinetic experiment DMF and decane,  $\text{Rh}(\text{acac})(\text{CO})_2$  and the ligand biphephos were charged into a beaker and mixed in an ultrasonic bath. Then, the solution was added

into an empty reactor and the agitator speed was adjusted to 1200 rpm. Subsequently, the reactor was evacuated and then flushed with the pre-treatment gas (see below) for five times. After another evacuation, the reactor was filled with nitrogen. Then the reactor was heated up to the reaction temperature. After reaching the desired value, 1-dodecene was added at ambient temperature as a short pulse using a syringe. While charging 1-dodecene the temperature of the reaction medium decreased but was stabilized by the controller within one minute. Finally, the gaseous reactants CO and/or H<sub>2</sub> were fed into the reactor until the desired total pressure was reached. With pressurization of the reactor the batch experiment started.

Each batch experiment lasted typically 1.5 hours. In this period approx.  $N_{sp} = 8$  samples were collected at discrete time steps and analyzed. Volume changes due to sampling were found to be negligible.

For the analysis of the six identified key reactions batch experiments were carried out in the temperature range 95–115 °C and in the total pressure range 0.5–2 MPa. The partial pressures of hydrogen and carbon monoxide and the 1-dodecene feed concentrations were changed in various steps. Effects of the carbon monoxide partial pressure on the rates of the isomerization ( $r_{iso}$ ), the hydrogenation ( $r_{hg,b}$ ) and the hydroformylation of 1-dodecene ( $r_{hf,b}$ ) were evaluated by changing the synthesis gas compositions in a broader range. Additionally, the hydroformylation and hydrogenation of an isomer mixture of various iso-dodecenes was investigated to consider specific reactions of the network individually.

The experimental program performed for five different temperatures and four total pressures consisted of:

- a) 18 ( $N_{exp,iso}$ ) experiments with 3 different initial olefin concentrations in nitrogen atmosphere and 5 additional variations of the CO pressure to study the isomerization (iso, sub-network I)
- b) 34 ( $N_{exp,hg}$ ) experiments with 3 different initial olefin concentrations and 3 variations of the syngas composition to study the hydrogenation (hg, sub-networks II and III)
- c) 42 ( $N_{exp,hf}$ ) experiments with 3 different initial olefin concentrations and 7 variations of the syngas composition to study the hydroformylation (hf, sub-network IV and total network  $V_{total}$ )

In addition to the mentioned experiments, several runs regarding the four sub-networks I-IV were repeated multiple times. Also for the total reaction system ( $V_{total}$ ) in particular for the reference temperature several repetitions were performed. An overview about the experimental program and the number of experiments carried out for each sub-network and the total network is shown in tab. 3.1.

### 3.3.3 Concentration analysis

The quantitative analysis of the liquid phase was realized by an off-line GC (*Agilent Series 6890*), equipped with a flame ionization detector and a 5 % Phenyl – 95 % methylpolysiloxane column (length 30 m, internal diameter 0.25 mm, film thickness 0.25 mm). Helium was used as carrier gas. Calibration was done using commercially available analytic standards for 1-dodecene, dodecane, decane and tridecanal with decanol as internal standard. No

**Table 3.1:** Summary of experimental program and number of specific experiments for each sub-network and the total network

	Isomerization		Hydrogenation		Hydroformylation	
	Sub-network I	Sub-network II	Sub-network III	Sub-network IV	V <sub>total</sub>	
Temperature and pressure variations $T = 95/100/105/110/115$ °C $p_{\text{tot}}^0 = 0.5/1.0/1.5/2.0$ MPa $p_{\text{CO}}^0 = 0/0.4/0.66/1.0/1.33/1.6/2.0$ MPa Variations of initial olefin concentration $c_{\text{nOL}}^0 = 0.80/0.87/1.05$ kmol·m <sup>-3</sup>	10	7	19	7	22	
Reproducibility tests	3	0	3	0	3	
	5	0	5	5	5	
<b>Total</b>	<b>18</b>	<b>7</b>	<b>27</b>	<b>12</b>	<b>30</b>	

standards were commercially available for both branched olefins (excluding 3-dodecene) and aldehydes. However, reliable quantification for all isomers was not possible. To have an estimation, response factors for the isomers of dodecene and aldehydes were taken to be equal to 1-dodecene and tridecanal, respectively. Therefore, the sum of the peak area of branched olefins and branched aldehydes with the corresponding calibration factors of 1-dodecene and the terminal aldehyde provides the concentration of the introduced pseudo components iso-dodecene, iOL, and iso-aldehyde, iAD, (Markert et al., 2013). Deviations in the carbon mass balance were for all samples taken in the experiments below 5 %.

## 3.4 Results of preliminary experiments

### 3.4.1 Initial investigation of gas solubilities

Besides the reaction rate models  $r_{fR}$  and the optimization parameter vector  $\Theta_{\text{opt}}$  therein, the solution of eqs. 2.41 and 2.42 further requires knowledge regarding the solubilities  $p_{j_c}^*$  and the mass transfer coefficients  $k_{\text{eff},j_c}$  of CO and H<sub>2</sub>, which were estimated based on the results of performed preliminary experiments following (Radhakrishnan et al., 1983; Deshpande et al., 1996; Purwanto et al., 1996; Bhanage et al., 1997). Thus, one of the MRS reactors was filled with a known volume of the TMS system decane/DMF/1-dodecene without catalyst, stirring rate at 1200 rpm was adjusted and the temperature was raised up to the desired value. After equilibration, the stirrer was stopped and the system was pressurized rapidly with one of the gaseous reactants. The liquid phase was then stirred again until a new equilibrium state occurred. If the pressure was constant the value was used to estimate the Henry parameters  $H_{j_c}$  (appendix B.3). These measurements were performed for the whole temperature reaction range considered in the kinetic experiments. The determined solubilities were correlated as follows:

$$p_{j_c}^* = c_{j_c,\text{li}}^* \cdot H_{j_c} \quad \text{with} \quad H_{j_c} = H_{j_c}^0 \cdot \exp\left(\frac{-E_{A,\text{sol},j_c}}{R \cdot T}\right) \quad (3.13)$$

The observed trends regarding hydrogen and carbon monoxide solubility as a function of

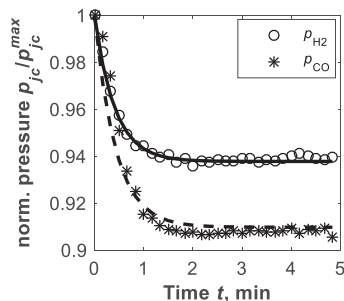


**Figure 3.6:** Experimental (symbols) and modeled (lines) data of the solubility measurement to determine eq. 3.13 of H<sub>2</sub> ( $p_{\text{tot}}^0 = p_{\text{H}_2}^0 = 1$  MPa) and CO ( $p_{\text{tot}}^0 = p_{\text{CO}}^0 = 1$  MPa) in decane/DMF/1-dodecene at  $T = 105$  °C

**Table 3.2:** Estimated parameters of eq. 3.13 for describing the solubility of H<sub>2</sub> and CO in the TMS (decane/DMF/1-dodecene) and for the mass transport coefficients  $k_{\text{eff},j,c}$  (eqs. 2.41-2.42).

Parameter	Unit	Value
$H_{\text{H}_2}^0$	MPa·m <sup>3</sup> ·kmol <sup>-1</sup>	905.37
$E_{A,\text{sol,H}_2}$	kJ·mol <sup>-1</sup>	10.173
$H_{\text{CO}}^0$	MPa·m <sup>3</sup> ·kmol <sup>-1</sup>	35500
$E_{A,\text{sol,CO}}$	kJ·mol <sup>-1</sup>	22.975
$k_{\text{eff,H}_2}$	min <sup>-1</sup>	2.44
$k_{\text{eff,CO}}$	min <sup>-1</sup>	2.31

partial pressure and temperature were formed to be comparable with data given by (Behr et al., 2004; Behr et al., 2005b).

The also recorded decreases of the pressure over time were subsequently used to estimate the mass transport coefficients  $k_{\text{eff},j,c}$  by matching the numerical solution of eqs. 2.41-2.42 (neglecting reactions,  $r_{jR} = 0$ ) to the experimental results.

The determined solubility parameters of eq. 3.13 and the estimated mass transport coefficients  $k_{\text{eff},j,c}$  are summarized in tab. 3.2. These expressions and values allowed describing the concentration profiles of CO and H<sub>2</sub> in a good agreement with experimental data as illustrated in fig. 3.6. Because of the rather small data basis acquired in these preliminary runs no further statistical evaluation regarding the quality of the  $H_{j,c}^0$ ,  $E_{A,\text{sol},j,c}$  and  $k_{\text{eff},j,c}$  was done and necessary.

### 3.4.2 Formation of active catalyst species

To follow the strategy of investigating all sub-networks independently it is essentially to start the isomerization, hydrogenations and hydroformylations with identical catalyst in the resting state (figs. 3.2 and 3.3).

The formation of the catalyst-ligand complex was studied in preliminary experiments to guarantee in all experiments defined initial conditions with respect to the catalyst state (van Leeuwen and Claver, 2001). Different pre-treatment strategies were evaluated experimentally varying the presence or absence of N<sub>2</sub>, CO, H<sub>2</sub> and synthesis gas (CO:H<sub>2</sub> = 1:1) and the formation time. Figure 3.7 illustrates the results of a hydroformylation after experiment formation of the catalyst complex in different gas atmospheres at the reference temperature of 105 °C. Preparing the complex in N<sub>2</sub> atmosphere a less active catalyst is formed or it is formed after an induction period during reaction. There is a significant reduction of the reaction rate if the catalyst formation was carried out in CO atmosphere. Thus, inactive Rh-species like Rh-dimers and Rh-dicarbonyl (fig. 3.3) are formed, so that

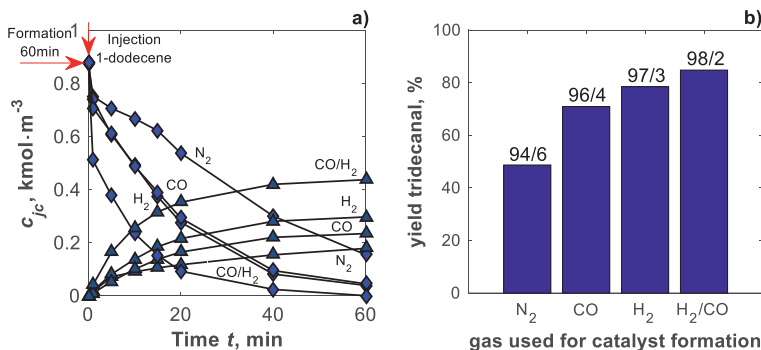


**Figure 3.7:** Gas influence during formation of the catalyst in resting state with subsequent hydroformylation of 1-dodecene (a) concentration profiles of 1-dodecene (diamond) and tridecanal (triangle) and (b) yield of tridecanal (eq. 1:3) and  $n/iso$ -aldehyde ratio (number on top of columns from eq. A6 in (Kiedorf et al., 2014)) after  $t = 60\text{min}$ ,  $p_{\text{cat}}^0 = 2\text{ MPa}$ ,  $p_{\text{CO}}^0 = p_{\text{H}_2}^0 = 1\text{ MPa}$  and  $T = 105\text{ }^\circ\text{C}$

the total mass of catalyst in resting state is reduced causing a lower yield of tridecanal (fig. 3.7b). Only a pre-treatment with synthesis gas provided the active catalyst in the resting state. The hydroformylation proceeded after this pre-treatment immediately (fig. 3.7a). No initial period of catalyst formation was observed compared to the cases with other formation gases. The highest amount of tridecanal was found with a formation using a stoichiometric synthesis gas ratio of  $p_{\text{CO}}:p_{\text{H}_2} = 1:1$  as illustrated in fig. 3.7b.

For the comparison and the evaluation of the four pre-treatment strategies the yield of tridecanal and the  $n/iso$  ratio of the composed aldehydes were used. The definitions are given in section 2.2.

The preparation of the catalyst in the resting state was carried out for one hour in synthesis gas (1:1) atmosphere, at a pressure of 0.3 MPa. Tests after two and three hours revealed the same catalytic behavior. In this way an identical and reproducible initial condition with respect to the catalyst amount and state were established for all kinetic measurement.

Following (Markert et al., 2013) the concentration of the precursor  $\text{Rh}(\text{acac})(\text{CO})_2$  was fixed for all experiments to be  $c_{\text{Rh,precursor}} = 8.76 \cdot 10^{-5}\text{ kmol}\cdot\text{m}^{-3}$  and the ligand:catalyst ratio was taken as 3.3 : 1  $\text{kmol}_L/\text{kmol}_{\text{cat}}$ .

### 3.5 Network analysis

In order to evaluate the general potential of the rhodium-biphephos catalyst in the applied TMS system and for illustrating the reaction courses, initially hydroformylation experiments were performed at boundary temperatures considered, namely  $95\text{ }^\circ\text{C}$  and  $115\text{ }^\circ\text{C}$ . The concentration profiles measured for all components are illustrated in fig. 3.8. Attractive  $n/iso$ -ratios ( $c_{\text{NAD}}/c_{\text{IAD}}$ ) of 55 at  $95\text{ }^\circ\text{C}$  and 39 at  $115\text{ }^\circ\text{C}$  were observed after a reaction time of 60 min indicating the potential of the applied catalyst and solvent system.

It can be recognized in fig. 3.8 that the consumption of the reactant 1-dodecene causes the formation of the desired terminal aldehyde tridecanal (nAL) as well as of other isomers,

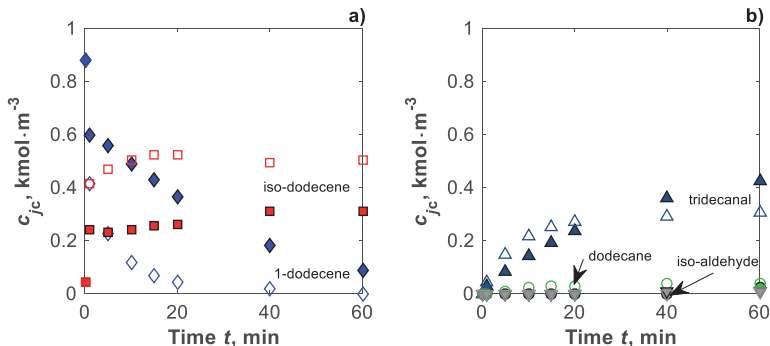


**Figure 3.8:** Experimentally determined concentration profiles of the total hydroformylation network ( $V_{\text{total}}$ ) of (a) 1-dodecene and iso-dodecene and (b) tridecanal, dodecane and iso-aldehyde at  $p_{\text{tot}}^0 = 2$  MPa,  $p_{\text{CO}}^0 = p_{\text{H}_2}^0 = 1$  MPa,  $T = 95$  °C (filled symbols) and  $T = 115$  °C (open symbols) (nOL  $\diamond$ , iOL  $\square$ , nAD  $\Delta$ , AL O, iAD  $\nabla$ )

which are lumped into the pseudo-component iso-dodecene (iOL). In particular, an isomerization of 1-dodecene proceeds. Iso-dodecene is the second main reaction product for the conditions considered. Furthermore, a smaller amount of the hydrogenation product dodecane and a very small amount of isomeric iso-aldehydes (iAD) could be detected. For the higher temperature (115 °C) the results reveal a significantly increased rate of the isomerization ( $r_{\text{iso}}$ ) relative to the desired hydroformylation ( $r_{\text{hf,b}}$ ).

These observations allow a first interpretation regarding relative activation energies. Obviously,  $E_{A,\text{iso}}$  seems to be larger than  $E_{A,\text{hf,b}}$ . Thus, less tridecanal can be formed at higher temperatures directly from the reactant 1-dodecene. Iso-dodecene is consumed in a series reaction and a significant amount of dodecane is produced via hydrogenation.

With respect to fig. 3.1, from the results of these first experiments could not yet be decided, which amount of dodecane is formed directly from 1-dodecene by hydrogenation with rate  $r_{\text{hg,b}}$  or by consecutive hydrogenation of formed iso-dodecene with rate  $r_{\text{hg,a}}$ . The same uncertainty remains regarding the two ways possible to form the small amount of observed iso-aldehyde considering a possible back-isomerization by the reversible reaction  $r_{\text{iso}}$  followed by  $r_{\text{hf,c}}$  (Behr et al., 2005b; Vogl et al., 2005).

In order to gain more quantitative insight, the models introduced before parameterization of the various model conditions is required.

### 3.5.1 Free parameters and estimation strategy

The three levels of rate expressions introduced in the rate equations (eqs. 2.6, 3.3-3.12) contain four types of parameters:

- Temperature dependent reaction rate constants  $k_R$ , which are described by a modified Arrhenius equation (eq. 2.23) with a reference temperature, preferentially in the middle of the interval of interest ( $T^{\text{ref}} = 105$  °C was used below).
- Reaction equilibrium constants  $K_{\text{eq},R}$ , which are related to the corresponding Gibbs energies of reaction  $\Delta G_{R,JR}$  (appendix A.4):

$$K_{\text{eq},jR} = \exp\left(\frac{-\Delta G_{R,jR}}{R \cdot T}\right) \quad (3.14)$$

- c) Numerous lumped inhibition constants  $K_{\text{q-k},jR}$  which should also follow an *Arrhenius* equation (eqs. 2.6, 3.3-3.12)
- d) Two temperature dependent equilibrium constants  $K_{\text{cat},\alpha}$  and  $K_{\text{cat},\beta}$  related to the different catalyst states (eq. 3.1d, fig. 3.3)

The reaction equilibrium constants  $K_{\text{eq}}$  of the hydrogenation and hydroformylation reactions could be calculated directly applying available *Gibbs* enthalpies of formation of the species involved using *Hess* law (Yaws, 1999) (see also appendix A). However, for the isomerization reaction no such data were available. For this reason the *Gibbs* enthalpy of isomerization  $\Delta G_{R,\text{iso}}$  has to be estimated additionally as a free parameter or calculated using the *Benson's* group increment theory (GIT) (Benson et al., 1969).

This shortcut method decomposes the considered molecule in individual parts and calculates the thermodynamic properties based on the several contributions. By this means fast and suitable approximations are possible. Additionally the method distinguishes between *cis*- and *trans*- conformations which is required in the isomerization analysis. The suitability of this method for homogeneous isomerization reaction network is already tested in (Jörke et al., 2015a; Jörke et al., 2016) for the isomerization of 1-decene and the corresponding *cis*- and *trans*- isomers. In this regard the equilibrium composition of the 1-decene isomerization network is predicted via this method and experimentally validated. In the present isomerization analysis, the *Gibbs* reaction enthalpy will be estimated at the kinetic experiments and calculated via *Benson's* GIT. Further the two *Gibbs* reaction enthalpies will be compared with each other.

To simplify the parameter estimation, the inhibition constants  $K_{jR}$  in eqs. 2.6, 3.3-3.12 and the catalyst equilibrium constants  $K_{\text{cat},\alpha}$  and  $K_{\text{cat},\beta}$  in eq. 3.1d were assumed to be constant in the relative small temperature range considered.

The mathematical framework described in the previous section was applied to reduce the derived mechanistic kinetic models and to determine the corresponding free parameters based on the results of the batch experiments carried out. Theoretically it is possible to analyze all reactions and all experiments together. However, estimating the relative large number of parameters is very difficult because of the possible occurrence of numerous local optima (Edgar and Himmelblau, 1988; Englezos and Kalogerakis, 2001; Hu et al., 2011; Marin and Yablonsky, 2011). To overcome this difficulty, as mentioned above, the four sub-networks for the isomerization of 1-dodecene (sub-network I;  $r_{\text{iso}}$ ), the hydrogenation of 1- and iso-dodecene (sub-networks III/II;  $r_{\text{hg},b}$  /  $r_{\text{hg},a}$ ), the hydroformylation of iso-dodecene (sub-network IV;  $r_{\text{hf},a}$ ) and the total network of the hydroformylation of 1-dodecene (network  $V_{\text{total}}$ :  $r_{\text{hf},b}$ ,  $r_{\text{hf},c}$ ) were analyzed sequentially.

### 3.5.2 Isomerization of 1-dodecene: sub-network I

Two sets of measured concentration profiles of the fed 1-dodecene and the exclusively formed pseudo-component iso-dodecene are given in fig. 3.9a for experiments carried out in nitrogen at 95 °C and 115 °C after forming the catalyst in resting state. The isomerization

rate  $r_{\text{iso}}$  is relatively high, especially at 115 °C. No hydrogenation or hydroformylation products could be detected. In additional experiments at 105°C the influence of CO on the isomerization was studied. The related inhibition effect is clearly visible in fig. 3.9b. It is due to backformation of the Rh-species (1) and inactive Rh-dimers indicated in fig. 3.3, which reduces the amount of the catalyst available in the resting state as described in eq. 3.1d. This issue will be discussed and quantified in more detail later in section 3.5.6, when the whole reaction system is analyzed and also used for process control and intensification.

In the introduced most general GCKK approach model equation quantifying the isomerization rate (eqs. 2.6 with eqs. 2.23 and 3.14), the kinetic parameters  $E_{A,\text{iso}}$  and  $k_{\text{iso},\infty}^{\text{ref}}$ , the equilibrium constant  $K_{\text{eq,iso}}$  with the *Gibbs* enthalpy of reaction and the inhibition constants  $K_{\alpha,\text{iso}}$ ,  $K_{\beta,\text{iso}}$  and  $K_{\gamma,\text{iso}}$  are unknown. Estimating these 6 parameters simultaneously using the results of all isomerization experiments performed without CO, led to a good description but provided partly very broad confidence intervals. The subsequently carried out singular value decomposition and the application of the threshold condition number of 1000 (eq. 2.35) revealed that the parameter  $K_{\gamma,\text{iso}}$  was identified as ill-conditioned and not essential for the parameter estimation. As a consequence, the general rate eq. 2.6 could be reduced.

#### Reduced GCKK approach for isomerization rate based on eq. 2.6

$$r_{\text{iso}} = \frac{k_{\text{iso},\infty}^{\text{ref}} \exp\left(\frac{-E_{A,\text{iso}}}{R} \cdot \left(\frac{1}{T} - \frac{1}{T^{\text{ref}}}\right)\right) \cdot \left(c_{\text{nOL}} - \frac{c_{\text{iOL}}}{K_{\text{eq,iso}}}\right)}{\left(1 + K_{\alpha,\text{iso}} \cdot c_{\text{nOL}} + K_{\beta,\text{iso}} \cdot c_{\text{iOL}}\right)} \quad (3.15)$$

An illustration of the agreement between experiments and model predictions using eq. 3.15 is given in fig.3.9 for one typical experiment.

The estimated isothermal *Gibbs* reaction enthalpy from 1-dodecene to the pseudo-component iso-dodecene amounts  $-11.1 \text{ kJ} \cdot \text{mol}^{-1}$ . Using the *Benson* increment group the-

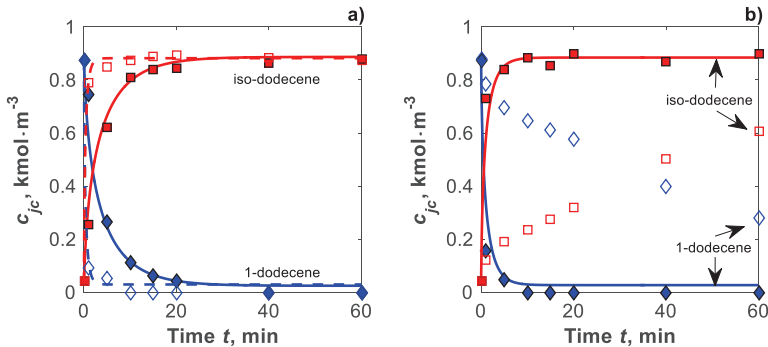


**Figure 3.9:** Isomerization of 1-dodecene (sub-network I,  $r_{\text{iso}}$ , eq. 3.15) (a) Temperature dependence  $p_{\text{tot}}^0 = p_{\text{N}_2}^0 = 0.1 \text{ MPa}$ ,  $T = 95 / 115 \text{ }^\circ\text{C}$ : model solid and dashed lines (nOL (blue), iOL (red)), experiment filled and open symbols (nOL  $\diamond$ , iOL  $\square$ ) and (b) CO dependence of the isomerization;  $p_{\text{tot}}^0 = 0.1 \text{ MPa}$ ,  $T = 105 \text{ }^\circ\text{C}$ ,  $p_{\text{CO}}^0 = 0/0.8 \text{ MPa}$ : (legend same as for a)

ory, the *Gibbs* formation enthalpy of each isomer can be approximated separately. The needed values for calculation of the *Gibbs* reaction enthalpy are given at standard conditions in table 3.3. The *Gibbs* enthalpy of formation literature value of 1-dodecene is 137.90 kJ·mol<sup>-1</sup> (Yaws, 1999) and is close to the calculated value via *Benson* method.

To calculate the isomer composition of the pseudo-component iso-dodecene at equilibrium conditions the following isomerization network is postulated (fig. 3.10). Consider all cis- and trans- conformations of dodecene, 23 isomerization reactions are assumed. Using the standard formation enthalpy and entropy of each isomer (tab. 3.3) and the corresponding heat capacity polynomial correlation, the free reaction enthalpies of these reactions can be calculated by means of the laws of *Hess* and *Kirchhoff* and the *Helmholtz* equation (Atkins and Paula, 2006).

The chemical equilibrium is determined using the non-stoichiometric formulation, which is based on a *Gibbs* energy minimization. Compared to the classical way, the computational effort is reduced significantly. Using this method  $N_E$  (number of different elements in the considered system) + 1 closing condition of non-linear equations have to be solved. The resulting equations are shown below.

$$0 = \frac{B_{j_E}}{n_{\text{tot}}} - \sum_{j_C=1}^{N_C} \beta_{j_E/j_C} \exp \left[ \frac{1}{\bar{R}T} \left( \sum_{j_E=1}^{N_E} \lambda_{j_E} \beta_{j_E/j_C} - \Delta G_{j_C}^0 - \bar{R}T \cdot \ln \left( \frac{P}{P^0} \right) - 1 \right) \right] \text{ with } j_E = 1 \dots N_E \quad (3.16)$$

$$0 = \sum_{j_C=1}^{N_C} \exp \left[ \frac{1}{\bar{R}T} \left( \sum_{j_E=1}^{N_E} \lambda_{j_E} \beta_{j_E/j_C} - \Delta G_{j_C}^0 - \bar{R}T \cdot \ln \left( \frac{P}{P^0} \right) - 1 \right) \right] - 1 \quad (3.17)$$

The equation system with respect to the *Lagrange* multipliers  $\lambda_{j_E}$  and the total molar amount  $n_{\text{tot}}$  can be solved using the *Levenberg-Marquardt* or the *trust-region-reflective* algorithm which are explained in detail in section 2.2.2.

The resulting equilibrium molar fraction of 1-dodecene and the corresponding isomers are shown in tab. 3.4 for three different temperatures.

Based on considering only neighbor interactions in *Benson* method, identical thermodynamically properties of cis-3/4/5-dodecene and trans-3/4/5-dodecene were observed. Accordingly, these calculated molar fractions are similar. Additionally, the trans-confor-

**Table 3.3:** Thermodynamic properties of 1-dodecene and the corresponding isomers

	$\Delta h_f^0$ , kJ·mol <sup>-1</sup>	$S^0$ , J·(mol·K) <sup>-1</sup>	$\Delta G_f^0$ , kJ·mol <sup>-1</sup>	$c_p$ (298 K), J·(mol·K) <sup>-1</sup>	$c_p$ (400 K), J·(mol·K) <sup>-1</sup>	$c_p$ (500 K), J·(mol·K) <sup>-1</sup>
1-d	-164.54	618.24	136.71	269.60	341.92	406.18
2-t	-177.17	614.79	126.11	269.80	340.08	403.88
2-c	-172.32	619.85	129.45	261.77	332.05	395.85
3-t	-177.42	613.83	126.15	267.54	339.70	404.18
3-c	-172.57	618.89	129.49	259.51	331.67	396.15
4-t	-177.42	613.83	126.15	267.54	339.70	404.18
4-c	-172.57	618.89	129.49	259.51	331.67	396.15
5-t	-177.42	613.83	126.15	267.54	339.70	404.18
5-c	-172.57	618.89	129.49	259.51	331.67	396.15
6-t	-177.42	608.07	127.87	267.54	339.70	404.18
6-c	-172.57	613.13	131.21	259.51	331.67	396.15

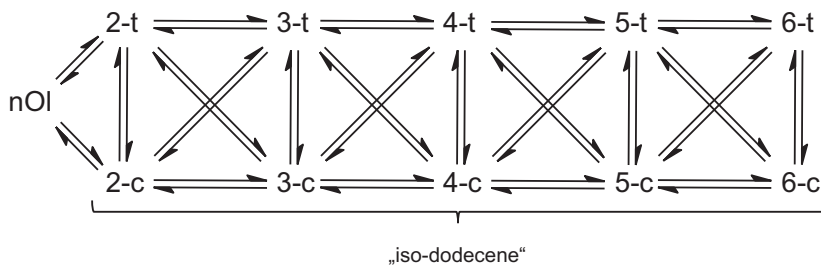
**Table 3.4:** Temperature dependent molar equilibrium fraction of 1-dodecene and the corresponding isomers

$T, ^\circ\text{C}$	$X_{\text{nOL}}$	$X_{2\text{-c}}$	$X_{2\text{-t}}$	$X_{3\text{-c}}$	$X_{3\text{-t}}$	$X_{4\text{-c}}$	$X_{4\text{-t}}$	$X_{5\text{-c}}$	$X_{5\text{-t}}$	$X_{6\text{-c}}$	$X_{6\text{-t}}$
50	0.003	0.052	0.172	0.051	0.169	0.051	0.169	0.051	0.169	0.026	0.085
100	0.006	0.062	0.166	0.060	0.159	0.060	0.159	0.060	0.159	0.030	0.080
150	0.009	0.070	0.160	0.066	0.151	0.066	0.151	0.066	0.151	0.033	0.076

mation is thermodynamically more favored than cis-. Thus, the trans-isomer molar fractions exceed the cis- amounts which is founded by repulsive substituent interactions (Schmuck, 2013; Smith, 2013). As the most favored isomer the 2-trans-dodecene is identified. The terminal olefin possesses the least molar fraction. These temperature independent observations are consistent with 1-decene isomerization equilibrium data (Jörke et al., 2015a; Jörke et al., 2016). A temperature rise leads to a slightly equilibrium shift to the terminal olefin. Consequential to support a possible back-isomerization higher reaction temperatures are required.

Using the molar fractions of all components of the isomerization network involved, the composition of the pseudo-component iso-dodecene at equilibrium conditions can be calculated. Thus, the thermodynamic properties of iso-dodecene result from the equilibrium composition and the single component thermodynamic data. The determined free reaction enthalpy of the isomerization of 1-dodecene to iso-dodecene and the isothermal estimated are shown in fig. 3.11a. On basis of quantum chemistry accurateness, a confidence interval of  $4 \text{ kJ}\cdot\text{mol}^{-1}$  can be assumed for the *Gibbs* reaction enthalpy calculated by *Benson* GIT. Thus, the estimated free reaction enthalpy is confirmed by this method. Consequently, the physical meaning of the estimated parameter was increased using the subset selection method.

The corresponding reaction equilibrium constants, calculated via eq. 3.14, are shown in fig. 3.11b. Compared to each other the estimated constant exceeds the calculated equilibrium constant in the whole temperature range considered. Accordingly, the 1-dodecene concentration on equilibrium condition is slightly underestimated. However, in the relevant reaction temperature range the differences are marginal. Additionally, based on large confidence intervals of the *Benson* GIT no precise calculations are possible. Based on these reasons in the following reaction kinetic analysis of the hydrogenation sub-networks and

**Figure 3.10:** Postulated isomerization equilibrium network of 1-dodecene consider cis- and trans- conformations (Markert et al., 2013; Jörke et al., 2015a)

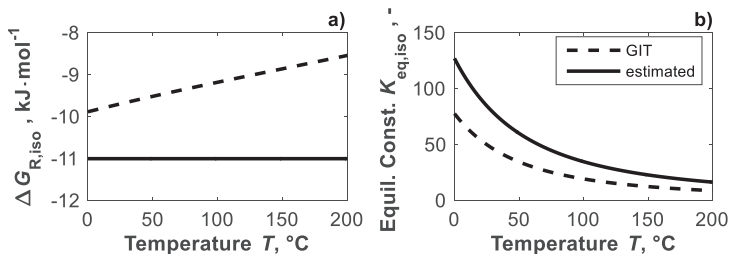


**Figure 3.11:** (a) At kinetic experiments estimated (solid line) and with *Benson* group increment theory (GIT) calculated (dashed line) *Gibbs* reaction enthalpy of the isomerization reaction of 1-dodecene to the pseudo-component iso-dodecene and (b) the resulting equilibrium constant of the isomerization

the total hydroformylation network the estimated isomerization *Gibbs* reaction enthalpy is used.

Therefore, the estimated 5 parameters of eqs. 3.14 and 3.15 were used subsequently in two ways. Except the pre-factor  $k_{iso,ref}$  all parameters were kept as found here in analyzing in the following steps larger sub-networks. Thus, e.g. the activation energy of the isomerization estimated to be  $E_{A,iso} = 137 \text{ kJ}\cdot\text{mol}^{-1}$  was fixed and further used like that. The other fixed values are given in the final overview provided in tab. 3.5 together with the confidence intervals. These intervals are relatively high indicating the remaining limits and uncertainties of this identification. In order to maintain the general structure of the model but to have some flexibility the obtained frequency factor  $k_{iso,ref} = 4.35 \cdot 10^{+3} \text{ m}^3 \cdot (\text{kg}_{cat} \cdot \text{min})^{-1}$  was used subsequently just as a starting value and was again readjusted, first during the analysis of experiments covering the next larger sub-network II of the hydrogenation of iso-dodecene and finally again in quantifying the complete reaction network  $V_{total}$  comprising all six reactions.

### 3.5.3 Hydrogenation of iso-dodecene: sub-network II

In a second step the rate of the iso-dodecene hydrogenation  $r_{hg,a}$  was quantified. A deeper understanding would require the consideration of all possible dodecene isomers. Due to the lack of pure isomers a representative mixture of isomers was prepared in a preliminary experiment in an available larger batch reactor (volume approx. 2 l described in (Markert et al., 2013)). This mixture, which contained also small amounts of dodecane was used as a lumped iso-dodecene feed fraction in experiments carried out in temperature and hydrogen pressure ranges of 95–105 °C and  $p_{H_2} = 0.5\text{--}1.5 \text{ MPa}$ . Figs. 3.12a and 3.12b illustrate the concentration profile of iso-dodecene and the formed hydrogenation product dodecane. There is only a relative small temperature and pressure effect in the considered ranges.

Due to the limited analysis regarding the isomer distribution only the simple empirical power law (eq. 3.8) was applied to analyze the results of the corresponding batch runs. The kinetic parameters ( $E_{A,hg,a}$  and  $k_{hg,a,ref}$ ) were estimated. As already discussed for the isomerization the estimated activation energy ( $E_{A,hg,a} = 102 \text{ kJ}\cdot\text{mol}^{-1}$ ) is fixed for the further

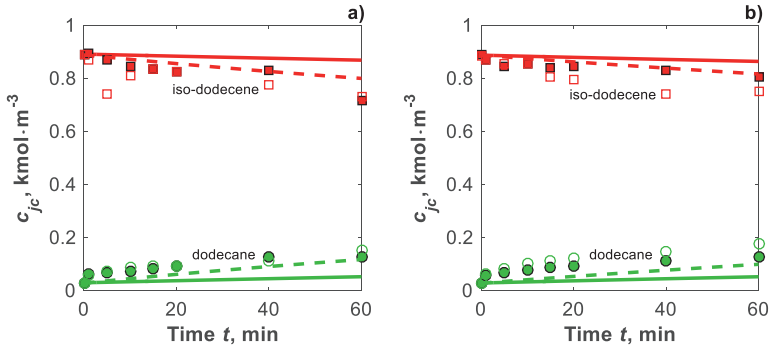


**Figure 3.12:** Hydrogenation of isomer mixture (sub-network II,  $r_{hg,a}$ , eq. 3.8) (a) Temperature dependence  $p_{H_2}^0 = p_{H_2}^\infty = 1$  MPa,  $T = 95 / 115$  °C: model solid and dashed lines (iOL (red), AL (green)), experiment filled and open symbols (iOL  $\square$ , AL  $\circ$ ) and (b) pressure dependence of the hydrogenation of isomers  $T = 105$  °C,  $p_{H_2}^0 = p_{H_2}^\infty = 0.5/1.5$  MPa: (legend same as for a)

analysis of the total network. The relative good quality of simulating  $r_{hg,a}$  with eq. 3.8 is illustrated fig.3.12. For the pre-exponential factor holds  $k_{hg,a,\infty}^{ref} = 1.59 \text{ m}^6 \cdot (\text{kg}_{cat} \cdot \text{min} \cdot \text{kmol})^{-1}$  which is used as initial value for parameter estimation in the next sub-network III which comprises in addition also the hydrogenation of 1-dodecene.

### 3.5.4 Hydrogenation of 1-dodecene: sub-network III

This sub-network contains the isomerization ( $r_{iso}$ ) and the subsequent hydrogenation ( $r_{hg,a}$ ) of the intermediate product iso-dodecene, respectively. Experiments were performed in the following ranges:  $T = 95\text{--}115$  °C,  $p_{H_2} = 0.5\text{--}2$  MPa and  $p_{H_2}:p_{CO} = 10:1, 16:1$ . Experimental concentration profiles of 1-dodecene, iso-dodecene and dodecane are given as points in fig. 3.13a for 95 °C and 115 °C at  $p_{H_2} = 1$  MPa and in fig. 3.13b for 105 °C at  $p_{H_2} = 0.5$  and 2 MPa. It can be seen that the consumption of the reactant 1-dodecene causes the formation of iso-dodecene and the hydrogenation product dodecane. In particular, the isomerization of 1-dodecene proceeds relatively fast and is the main reaction for these conditions. At 95 °C dodecane and iso-dodecene are primary products and the concentrations do not change much after 40 minutes. At the higher temperature of 115 °C the isomerization proceeds even faster compared to the hydrogenation. This is due to the relative higher activation energy of the isomerization. Thus, iso-dodecene is formed as the primary product at the beginning, before it is consumed to dodecane revealing the typical behavior of an intermediate product.

The results illustrated in fig. 3.13b shows that the hydrogenation rate increases with increasing pressure of hydrogen corresponding to a decreased isomerization rate. At  $p_{H_2} = 2$  MPa more dodecane is formed directly from the reactant 1-dodecene. For both pressures considered in fig. 3.13b the series reaction of iso-dodecene to dodecane takes place. However, a coupled mechanism of back-isomerization to 1-dodecene by  $r_{iso}$  and subsequent hydrogenation to dodecane by  $r_{hg,b}$  is imaginable (Vogl et al., 2005).

The influence of CO on the hydrogenation was investigated for ratios of  $p_{H_2}:p_{CO} = 10:1$  and 16:1. As observed before for the isomerization, the rates of hydrogenation were also reduced by the inhibiting effect of CO.

For quantification of the kinetics of the hydrogenation of 1-dodecene with  $r_{hg,b}$  all three models given by eqs. 3.5 (GCCK approach), 3.6 (RDS), and 3.7 (empirical) were applied. Hereby, the isomerization of 1-dodecene ( $r_{iso}$ , eq. 3.15) and the hydrogenation of iso-dodecene ( $r_{hg,a}$ , eq. 3.8) were described with the available parameters. The already estimated pre-exponential factors  $k_{iso,\infty}^{ref}$  and  $k_{hg,a,\infty}^{ref}$  were used as initial guesses. Consequently, the kinetic parameters ( $k_{hg,b,\infty}^{ref}$  and  $E_{A,hg,b}$ ) and equilibrium constants ( $K_{\alpha,hg,b} \dots K_{\epsilon,hg,b}$ ) are now the remaining free parameters and have to be estimated.

Parity plots of the measured and predicted concentrations of 1-dodecene and dodecane are given in fig. 3.13c-d. All models evaluated (GCCK approach, reduced GCCK, RDS and empirical) are able to describe the experimental reaction rates comparatively well. For

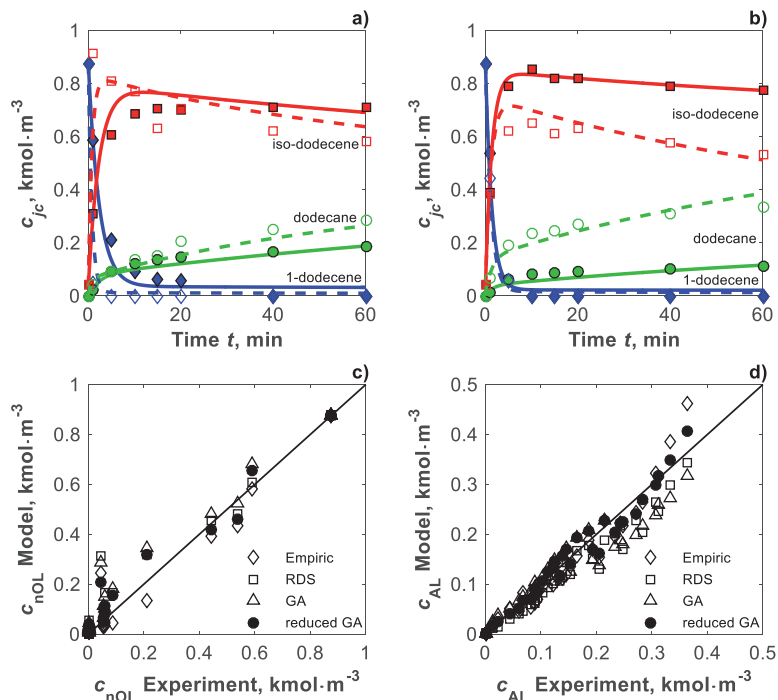


**Figure 3.13:** Hydrogenation of 1-dodecene (sub-network III,  $r_{hg,b}$ , eq. 3.18) (a) Temperature dependence  $p_{tot}^0 = p_{H_2}^0 = 1$  MPa;  $T = 95 / 115$  °C: model solid and dashed lines (nOL (blue), iOL (red)), AL (green)), experiment filled and open symbols (nOL  $\diamond$ , iOL  $\square$ , AL  $\circ$ ), (b) total pressure dependence of the hydrogenation  $T = 105$  °C;  $p_{tot}^0 = p_{H_2}^0 = 0.5/2$  MPa: (legend same as for a), (c) parity plot of the illustrated experiments for the concentration profile of 1-dodecene for all kinetic rate approaches and (d) parity plot of the illustrated experiments for the concentration profile of dodecane for all kinetic rate approaches (eqs. 3.5-3.7 and 3.18, parameter in tab. 3.5)

the GCCK approach (eq. 3.5) it was again not possible to estimate all 7 parameters in a way that they fulfill the criteria of statistical significance. Partly extreme large confidence intervals were found. As for the GCCK isomerization rate model a sensitivity analysis and a parameter reduction was performed leading to the following reduced GCCK equation:

**Reduced GCCK approach (based on eq. 3.5)**

$$r_{\text{hg,b}} = \frac{k_{\text{hg,b},\infty}^{\text{ref}} \exp\left(\frac{-E_{\text{A,hg,b}}}{\bar{R}} \cdot \left(\frac{1}{T} - \frac{1}{T^{\text{ref}}}\right)\right) \cdot \left(c_{\text{nOL}} \cdot c_{\text{H}_2,\text{II}} - \frac{c_{\text{AL}}}{K_{\text{eq,hg,b}}(T)}\right)}{\left(1 + K_{\text{a,hg,b}} \cdot c_{\text{nOL}} + K_{\text{V,hg,b}} \cdot c_{\text{AL}} + K_{\text{d,hg,b}} \cdot c_{\text{H}_2,\text{II}}\right)} \quad (3.18)$$

As mentioned before  $K_{\text{eq,hg,b}}$  can be calculated using eq. 3.14 with the following function for  $\Delta G_{\text{R,hg,b}}$  based on (Yaws, 1999).

$$\Delta G_{\text{R,hg,b}}(T) = -126.28 + 0.13 \cdot T + 6.80 \cdot 10^{-6} \cdot T^2 \quad (\text{kJ} \cdot \text{mol}^{-1}) \quad \text{with } T \text{ in K} \quad (3.19)$$

The experimental and accordingly calculated transients based on eq. 3.18 are in good agreement at different temperatures and for the hydrogen pressures considered (fig. 3.13a-b).

Excluding again the pre-factor  $k_{\text{hg,b},\infty}^{\text{ref}}$ , the activation energy  $E_{\text{A,hg,b}} = 76 \text{ kJ} \cdot \text{mol}^{-1}$  and all other kinetic parameters summarized in tab. 3.5 are kept constant. The  $k_{\text{iso},\infty}^{\text{ref}}$  value was reduced in this evaluation step compared to the value estimated initially by about 50 %. The three frequency factors  $k_{\text{iso},\infty}^{\text{ref}} = 2.30 \cdot 10^{+3} \text{ m}^3 \cdot (\text{kg}_{\text{cat}} \cdot \text{min})^{-1}$ ,  $k_{\text{hg,b},\infty}^{\text{ref}} = 398.40 \text{ m}^6 \cdot (\text{kg}_{\text{cat}} \cdot \text{min} \cdot \text{kmol})^{-1}$  and  $k_{\text{hg,a},\infty}^{\text{ref}} = 2.34 \text{ m}^6 \cdot (\text{kg}_{\text{cat}} \cdot \text{min} \cdot \text{kmol})^{-1}$  were used later as initial values in the subsequent analysis of the total network.

### 3.5.5 Hydroformylation of iso-dodecene: sub-network IV

The last independent sub-network investigated was the hydroformylation of iso-dodecene. Beside this reaction, the isomerization and the hydrogenation of 1- and iso-dodecene can occur simultaneously in the presence of CO and H<sub>2</sub>. The rates of these parallel-series reactions were quantified before and rate equations were available.

In the experiments the same mixture of olefin isomers was fed initially into the reactor as in the experiments carried out to hydrogenate iso-dodecene ( $r_{\text{hg,a}}$ ). Again temperature and total pressure ranges of 95–115 °C and  $p_{\text{tot}} = 1\text{--}2 \text{ MPa}$  were covered. The synthesis gas composition, i.e.  $p_{\text{H}_2}:p_{\text{CO}}$ , was varied between 1:2 and 2:1. In fig. 3.14 are depicted selected concentration profiles of the reactant iso-dodecene and the hydroformylation and hydrogenation products (tridecanal, iso-aldehyde and dodecane). Compared to the hydrogenation of iso-dodecene ( $r_{\text{hg,a}}$ ) a slight temperature dependence can be observed. Iso-dodecene is consumed only slightly. Iso-aldehyde is formed with a rate  $r_{\text{hf,a}}$  at 95 °C and 115 °C. The small amount of initially present dodecane in the feed remained nearly constant during the whole run. Obviously, tridecanal is the main reaction product especially at elevated temperatures and pressures. Thus, the reversible isomerization reaction ( $r_{\text{iso}}$ ) and the consecutive hydroformylation ( $r_{\text{hf,b}}$ ) occur in series as discussed also in (Behr et al., 2003; Vogl et al., 2005). Due to the high relative activation energy of the isomerization  $E_{\text{A,iso}}$  the influence of this reaction is particularly significant at elevated temperature as already mentioned above.

The pressure dependence of the tridecanal formation is illustrated in fig. 3.14b. The result reveals the fact, that the formation of tridecanal is reduced with increased total synthesis gas pressure connected with increased CO partial pressure. This observation is in good agreement with the results found for the isomerization sub-network. At higher CO partial pressures more inactive Rh-species are formed corresponding to a reduction of the amount of the active catalyst and an inhibition of the isomerization rate. Thus, for a high total pressure and a low reaction temperature the back-isomerization of iso-dodecene is suppressed and a lower amount of tridecanal is formed by the subsequent hydroformylation.

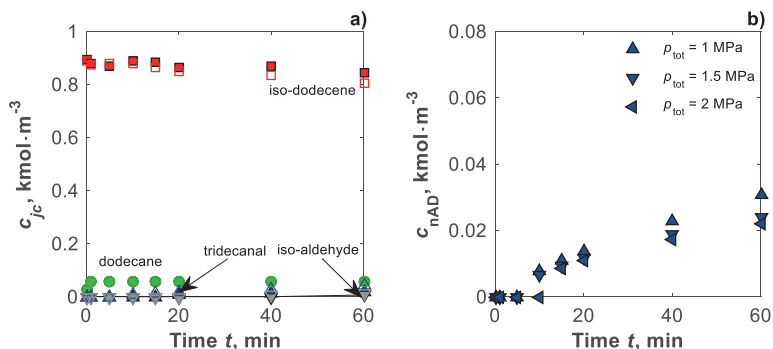


**Figure 3.14:** Hydroformylation of iso-dodecene (sub-network IV,  $r_{\text{hf},a}$ ): (a) Temperature dependence  $p_{\text{tot}}^0 = 2 \text{ MPa}$ ,  $p_{\text{CO}}^0 = p_{\text{H}_2}^0 = 1 \text{ MPa}$ ,  $T = 95 / 115 \text{ }^\circ\text{C}$ : experiment filled and open symbols (iOL  $\square$ , nAD  $\Delta$ , AL  $\circ$ , iAD  $\nabla$ ) and (b) total pressure dependence at  $p_{\text{tot}}^0 = 1\text{--}2 \text{ MPa}$ ,  $T = 115 \text{ }^\circ\text{C}$

Inspecting the results of the hydroformylation experiments with the olefin isomer mixture had to be concluded that the observed formation of tridecanal did not allow a reliable estimation of parameters quantifying the rate  $r_{\text{hf},a}$ . Thus, here the initially planned goal of decomposition of the reaction network failed. However, parameters  $E_{A,\text{hf},a}$  and  $k_{\text{hf},a,\text{ref}}$  of a simply power law approach (eq. 3.12) could be estimated during the final analysis of the total reaction network of the hydroformylation of 1-dodecene described in the following.

### 3.5.6 Hydroformylation of 1-dodecene: total network

Finally, the hydroformylation of 1-dodecene was investigated covering the complete network given in fig. 3.1. The total network is studied experimentally in the same temperature and synthesis gas total pressure ranges as before the sub-networks ( $T = 95\text{--}115 \text{ }^\circ\text{C}$ ,  $p_{\text{tot}} = 1\text{--}2 \text{ MPa}$ ). Additionally, the synthesis gas composition was varied:  $p_{\text{H}_2}:p_{\text{CO}} = 0:1; 1:4; 1:2; 2:1; 4:1$  and  $1:0$ .

The experimental results presented already in fig. 3.8 are repeated in figs. 3.15a and 3.15b, complemented now by the results of predictions using the final models and parameters to be discussed now. In addition, the also studied influence of the synthesis gas total pressure is shown in fig. 3.15c for the range  $p_{\text{tot}}^0 = 1\text{--}2 \text{ MPa}$ . At the lower total pressure (corresponding also to a lower CO partial pressure) the isomerization is the main reaction,

which forms iso-dodecene faster than the parallel hydroformylation forms the target tridecanal. For a higher total pressure of 2 MPa the isomerization rate is reduced and more tridecanal can be produced directly from 1-dodecene by  $r_{\text{hf},b}$ . Thus, with increasing total and CO partial pressure the isomerization rate is decreased as already illustrated in fig. 3.9b.

This is now the point to return the required quantification of the effect of the synthesis gas composition on the amount of active catalyst present in the resting state (eq. 3.1d). Fig. 3.15d shows the influence of the CO partial pressure measured at  $T = 105^\circ\text{C}$  and for  $p_{\text{tot}}^0 = 2\text{ MPa}$  (with hydrogen being the remainder) on the product composition after 60 min. The full range from pure hydrogen to pure carbon monoxide is covered. As discussed already above the hydrogenation and in particular the isomerization takes place if  $p_{\text{CO}}$  is zero. With increasing partial pressures of CO the isomerization rate  $r_{\text{iso}}$  and the hydrogenation rate  $r_{\text{hg},b}$  rate decrease gradually and the hydroformylation proceeds. The maximum

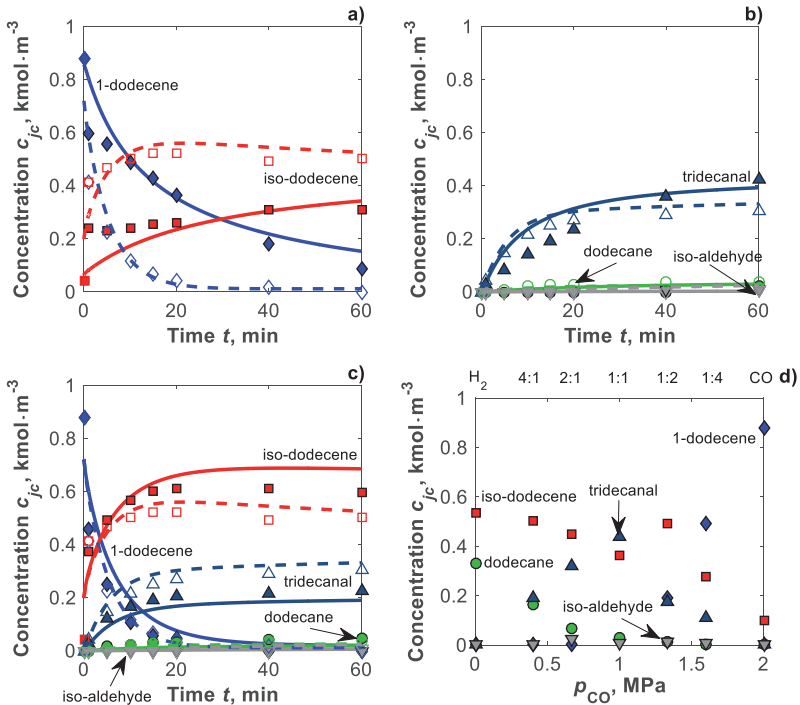


**Figure 3.15:** Hydroformylation of 1-dodecene (total network  $V_{\text{total}}$ ,  $r_{\text{hf},b}$ , eq. 3.20) (a and b) Temperature dependence  $p_{\text{tot}}^0 = 2\text{ MPa}$ ,  $p_{\text{CO}}^0 = p_{\text{H}_2}^0 = 1\text{ MPa}$ ,  $T = 95 / 115^\circ\text{C}$ : model solid and dashed lines (nOL (blue), iOL (red), nAD (dark blue), AL (green), iAD (grey)), experiment filled and open symbols (nOL  $\diamond$ , iOL  $\square$ , nAD  $\Delta$ , AL  $\circ$ , iAD  $\nabla$ ), (c) pressure dependence of the hydroformylation at  $T = 115^\circ\text{C}$ ,  $p_{\text{tot}}^0 = 1 / 2\text{ MPa}$ : (legend same as for a and b) and (d) Experimental observed effect of partial pressure CO and H<sub>2</sub> at the hydroformylation of 1-dodecene on the product spectrum at  $T = 105^\circ\text{C}$

amount of the desired hydroformylation product tridecanal formed by  $r_{\text{hf},b}$  was observed for the stoichiometric ratio  $\text{H}_2:\text{CO} = 1:1$ . If the CO partial pressure is further increased, the conversion of 1-dodecene is decreased, which reduces the extents of all reactions. For such CO rich conditions, the inactive Rh-dimers and Rh-dicarbonyl complexes shown in fig. 3.3 are formed (Kamer et al., 2004; Deshpande et al., 2011).

The pronounced and important effect of the syngas composition on the amount of catalyst in the resting state  $c_{\text{cat},rs}$  can be quantified using eq. 3.1d with the unknown equilibrium constants  $K_{\text{cat},\alpha}$  and  $K_{\text{cat},\beta}$ . Analyzing results of batch runs carried out with different syngas compositions, these two constants were now estimated together with the other still unknown kinetic parameters of the models describing the rates of the hydroformylation reactions. For the rates of the isomerization,  $r_{\text{iso}}$ , and the rates of the hydrogenations of iso- and 1-dodecene,  $r_{\text{hg},a}$  and  $r_{\text{hg},b}$ , eqs. 3.15, 3.8 and 3.18 were used. Hereby the pre-factors  $k_{\text{iso},\infty}^{\text{ref}}$ ,  $k_{\text{hg},a,\infty}^{\text{ref}}$  and  $k_{\text{hg},b,\infty}^{\text{ref}}$  determined before served just as initial guesses and were estimated again together with the free parameters of the hydroformylation kinetics described by eqs. 3.9-3.12 and 2.23, namely the activation energies  $E_{A,\text{hf},a}$ ,  $E_{A,\text{hf},b}$  and  $k_{\text{hf},a,\infty}^{\text{ref}}$ ,  $k_{\text{hf},b,\infty}^{\text{ref}}$  and the equilibrium constants  $K_{\alpha,\text{hf},a}, \dots, K_{\kappa,\text{hf},a}$ .

An estimation of the whole set of parameters using the general approach (eq. 3.9) was not satisfying, because many of the estimated parameters were identified as non-sensitive. Consequently, as for the isomerization and hydrogenation sub-networks, again a sensitivity analysis and a model reduction were performed. Applying eqs. 2.24-2.36 the following model equation (reduced GCCK approach), which contains just five free parameters was identified to describe the rate of the hydroformylation of 1-dodecene.

**Reduced GCCK approach (based on eq. 3.9):**

$$r_{\text{hf},b} = \frac{k_{\text{hf},b,\infty}^{\text{ref}} \exp\left(\frac{-E_{A,\text{hf},b}}{R} \cdot \left(\frac{1}{T} - \frac{1}{T^{\text{ref}}}\right)\right) \cdot c_{\text{nOL}} \cdot c_{\text{H}_2,\text{li}} \cdot c_{\text{CO,li}}}{\left(1 + K_{\alpha,\text{hf},b} \cdot c_{\text{nOL}} + K_{\delta,\text{hf},b} \cdot c_{\text{nAD}} + K_{\theta,\text{hf},b} \cdot c_{\text{H}_2,\text{li}}\right)} \quad (3.20)$$

The five parameters in eq. 3.20 were estimated together with the constants  $K_{\text{cat},\alpha}$  and  $K_{\text{cat},\beta}$  describing the catalyst equilibrium (eq. 3.1d) and parameters of a rate model for the in the previous chapter still not quantified hydroformylation of the iso-dodecene with the rate  $r_{\text{hf},a}$ . For the latter the simple empirical eq. 3.12 was used.

All estimated equilibrium and kinetic parameters are finally summarized in tab. 3.5 together with the parameters determined in the previous steps.

The quality of the description of the observed transients with the derived total model for the studied reaction network (figs. 3.1 and 3.2) is illustrated in fig. 3.15a-c. There is for the whole temperature and pressure range covered a relative good agreement between experimental results and predictions.

This is also illustrated by the parity plots of 1-dodecene and tridecanal concentrations given for several typical runs in fig. 3.16. In this figure are also given for comparison the corresponding parity plots for describing the rate of the 1-dodecene hydroformylation,  $r_{\text{hf},b}$ , with the complete GCCK model (eq. 3.9), with the simpler RDS approach based (eq. 3.10) and the empirical model (eq. 3.11) without presenting the related kinetic parameters and the corresponding larger confidence intervals. Although the differences are not so pro-

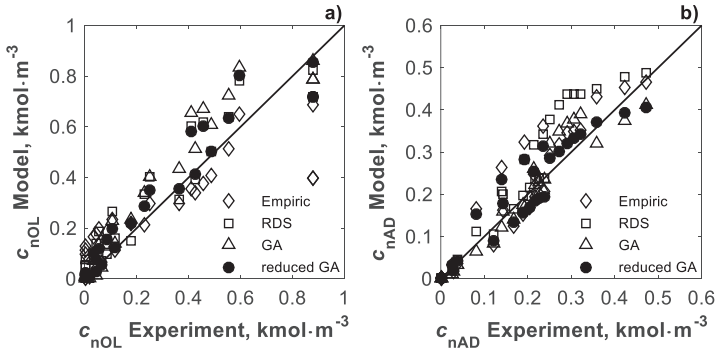


**Figure 3.16:** Parity plots for the evaluation of the total network  $V_{\text{total}}$  (eqs. 3.9-3.11 and 3.20, parameters in table 3.5) (a) of the presented experiments for the concentration profile of 1-dodecene for all kinetic rate approaches and (b) of the presented experiments for the concentration profile of tridecanal for all kinetic rate approaches

nounced, because of the systematically derived model using the reduced general approach should be clearly favored.

Fig. 3.17 shows finally the predicted effect of CO on the amount of active catalyst based on eq. 3.1d using the estimated two equilibrium constants as in tab. 3.5. It can be seen that for typical conditions used (namely  $p_{\text{tot}}^0 = 2$  MPa,  $p_{\text{H}_2}^0 = p_{\text{CO}}^0 = 1$  MPa,  $T = 105$  °C) only about 40 % of the total catalyst amount fed in the reactor are predicted to be in the resting state. However, this must be seen as a very rough estimation, because the  $K_{\text{cat},\alpha}$  and  $K_{\text{cat},\beta}$  values were estimated with quite high uncertainty together with several other parameters. A check of this unexpected low amount of active catalyst requires the application of additional measurements using NMR, Raman or IR-techniques.

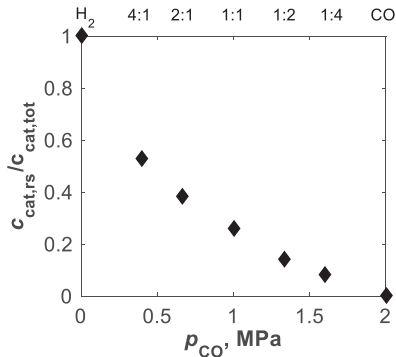


**Figure 3.17:** Effect on the active catalyst concentration in resting state;  $T = 105$  °C,  $p_{\text{tot}}^0 = 2$  MPa according eq. 3.1d and the parameter  $K_{\text{cat},\alpha}$  and  $K_{\text{cat},\beta}$  (table 3.5)

### 3.5.7 Evaluation of the overall approach followed and the kinetic parameters estimated

The applied strategy of analyzing sequentially sub-networks of increasing size should be in principle based on estimating on a higher level only a limited number of new parameters and to conserve completely the parameters determined on the lower level. Due to both unavoidable experimental and model errors this is a too optimistic approach. Accepting this limitation, essentially the most instructive activation energies were kept constant and, as noted above, the pre-exponential factors  $k_{j_c, \infty}^{\text{ref}}$  were updated on each higher level, using the values from the lower level just as initial estimated. An indicator of the overall consistency of the approach followed is the fact that the finally fixed pre-factors  $k_{\text{iso}, \infty}^{\text{ref}}$ ,  $k_{\text{hg}, \text{a}, \infty}^{\text{ref}}$ ,  $k_{\text{hg}, \text{b}, \infty}^{\text{ref}}$ ,  $k_{\text{hf}, \text{a}, \infty}^{\text{ref}}$ ,  $k_{\text{hf}, \text{b}, \infty}^{\text{ref}}$  are in the same order of magnitude as the values found earlier analyzing the corresponding smaller sub-networks. For example the frequency factor of the isomerization rate  $k_{\text{iso}, \infty}^{\text{ref}}$  evolves from initially  $4350 \text{ m}^3 \cdot (\text{kg}_{\text{cat}} \cdot \text{min})^{-1}$  (sub-network I) via  $2300 \text{ m}^3 \cdot (\text{kg}_{\text{cat}} \cdot \text{min})^{-1}$  (sub-network III) to the final value of  $696 \text{ m}^3 \cdot (\text{kg}_{\text{cat}} \cdot \text{min})^{-1}$  given in tab. 3.5. Besides the general errors mentioned, this shift in absolute values could be also ex-

**Table 3.5:** Summary of estimated parameters describing the network of reactions illustrated in figs. 3.1-3.3 via the reduced GCCK approach models.

Parameters	Unit	Value	95 % CI
<b>Catalyst equilibrium (eq. 3.1d)</b>			
$K_{\text{cat}, \alpha}$	$\text{m}^3 \cdot \text{kmol}^{-1}$	10.00	$\pm 20.5$
$K_{\text{cat}, \beta}$	-	1.01	$\pm 0.6$
<b>Isomerization (iso) I <math>r_{\text{iso}}</math> (eq. 3.15)</b>			
Frequency factor $k_{\text{iso}, \infty}^{\text{ref}}$	$\text{m}^3 \cdot (\text{kg}_{\text{cat}} \cdot \text{min})^{-1}$	$696.23^{(2)}$	$\pm 69.6$
Activation energy $E_{\text{A}, \text{iso}}$	$\text{kJ} \cdot \text{mol}^{-1}$	136.891	$\pm 39.7$
Gibbs-enthalpy $\Delta G_{\text{R}, \text{iso}}^{(1)}$	$\text{J} \cdot \text{mol}^{-1}$	$-1.1 \cdot 10^{+4}$	$\pm 2530.0$
$K_{\alpha, \text{iso}}$	$\text{m}^3 \cdot \text{kmol}^{-1}$	38.63	$\pm 97.4$
$K_{\beta, \text{iso}}$	$\text{m}^3 \cdot \text{kmol}^{-1}$	226.21	$\pm 47.5$
<b>Hydrogenation (hg) II/III <math>r_{\text{hg}, \text{a}}</math> (eq. 3.8) / <math>r_{\text{hg}, \text{b}}</math> (eq. 3.18)</b>			
Frequency factor $k_{\text{hg}, \text{b}, \infty}^{\text{ref}}$	$\text{m}^6 \cdot (\text{kg}_{\text{cat}} \cdot \text{min} \cdot \text{kmol})^{-1}$	$139.55^{(2)}$	$\pm 132.6$
Activation energy $E_{\text{A}, \text{hg}, \text{b}}$	$\text{kJ} \cdot \text{mol}^{-1}$	76.105	$\pm 19.8$
$K_{\alpha, \text{hg}, \text{b}}$	$\text{m}^3 \cdot \text{kmol}^{-1}$	2.66	$\pm 3.7$
$K_{\gamma, \text{hg}, \text{b}}$	$\text{m}^3 \cdot \text{kmol}^{-1}$	7.10	$\pm 6.9$
$K_{\delta, \text{hg}, \text{b}}$	$\text{m}^3 \cdot \text{kmol}^{-1}$	1.28	$\pm 1.5$
Frequency factor $k_{\text{hg}, \text{a}, \infty}^{\text{ref}}$	$\text{m}^6 \cdot (\text{kg}_{\text{cat}} \cdot \text{min} \cdot \text{kmol})^{-1}$	$0.70^{(2)}$	$\pm 12.9$
Activation energy $E_{\text{A}, \text{hg}, \text{a}}$	$\text{kJ} \cdot \text{mol}^{-1}$	102.260	$\pm 13.3$
<b>Hydroformylation (hf) IV/V <math>r_{\text{hf}, \text{a}}</math> (eq. 3.12) / <math>r_{\text{hf}, \text{b}}</math> (eq. 3.20)</b>			
Frequency factor $k_{\text{hf}, \text{b}, \infty}^{\text{ref}}$	$\text{m}^9 \cdot (\text{kg}_{\text{cat}} \cdot \text{min} \cdot \text{kmol}^2)^{-1}$	$5.00 \cdot 10^{+7}$	$\pm 1.7 \cdot 10^{+7}$
Activation energy $E_{\text{A}, \text{hf}, \text{b}}$	$\text{kJ} \cdot \text{mol}^{-1}$	113.080	$\pm 37.3$
$K_{\alpha, \text{hf}, \text{b}}$	$\text{m}^3 \cdot \text{kmol}^{-1}$	574.88	$\pm 2040.8$
$K_{\delta, \text{hf}, \text{b}}$	$\text{m}^3 \cdot \text{kmol}^{-1}$	3020.00	$\pm 8154.0$
$K_{\theta, \text{hf}, \text{b}}$	$\text{m}^3 \cdot \text{kmol}^{-1}$	$1.17 \cdot 10^{+4}$	$\pm 117.0$
Frequency factor $k_{\text{hf}, \text{a}, \infty}^{\text{ref}}$	$\text{m}^9 \cdot (\text{kg}_{\text{cat}} \cdot \text{min} \cdot \text{kmol}^2)^{-1}$	600.00	$\pm 864.0$
Activation energy $E_{\text{A}, \text{hf}, \text{a}}$	$\text{kJ} \cdot \text{mol}^{-1}$	120.844	$\pm 493.0$

<sup>1)</sup> related to  $K_{\text{eq}, \text{iso}}$  according to eq. 3.14

<sup>2)</sup> finally again adjusted in analyzing the whole network  $V_{\text{total}}$

plained by changes in the experimental conditions. E.g. the gas phase in the isomerization experiments differed from the gas phase in the hydroformylation experiments related to differences in the catalyst state, which is described only in a simplified way assuming the cycle shown in fig. 3.2 and the estimation of the resting state amount based on eq. 3.1d (fig. 3.3).

In further evaluating and interpreting the resulting set of parameters summarized in table 3.5, it should be also remembered that the reaction rate  $r_{\text{hf,c}}$  shown in fig. 3.1 as another possible pathway forming iso-aldehyde directly from the feed 1-dodecene cannot be fully excluded. It could be here expressed by a series reaction of initial isomerization with rate  $r_{\text{iso}}$  and subsequent hydroformylation of iso-dodecene with rate  $r_{\text{hf,a}}$  and, thus, was not further required for the mathematical description of the available batch run results.

The activation energy estimated for the isomerization ( $E_{\text{A,iso}} = 137 \text{ kJ}\cdot\text{mol}^{-1}$ ) is the highest found in the total network. This is confirmed by the observation that for the relative highest temperature isomerization is the dominating 1-dodecene consuming reaction. The activation energies of the two hydroformylation reactions of n-dodecene ( $E_{\text{A,hf,a}} = 113 \text{ kJ}\cdot\text{mol}^{-1}$ ) and iso-dodecene ( $E_{\text{A,hf,c}} = 121 \text{ kJ}\cdot\text{mol}^{-1}$ ) are lower. Consequently, with respect to selectivity, lower temperatures should be applied to suppress preliminary isomerization and support direct tridecanal formation. The two hydrogenation reactions of 1- and iso-dodecene are characterized by the lowest activation energies ( $E_{\text{A,hg,b}} = 76 \text{ kJ}\cdot\text{mol}^{-1}$  and  $E_{\text{A,hg,a}} = 102 \text{ kJ}\cdot\text{mol}^{-1}$ ). Altogether the total amount of alkane found is low for the selective hydroformylation catalyst used. Furthermore, comparing iso-dodecene and 1-dodecene as feeds the activation energies of the former are higher in both hydrogenation and hydroformylation. This fact can be explained by the specific steric hindrance provided by the ligand biphephos and/or by a coupled mechanism of back-isomerization and consecutive in-situ hydrogenation and hydroformylation to dodecane and iso-aldehyde, respectively.

Regarding the rather large confidence intervals of the parameters also given in table 3.5 should be noted that they are based on severe statistical evaluation. They indicated that caution is still required regarding interpretation of the postulated mechanisms.

It can be finally stated that the large amount of experimental and corresponding calculated results applying the models and parameters discussed are found to be in rather good agreement with respect to the individual sub-networks and the total network for the temperature and pressure range covered. Now they are available for application in reactor models.

## 3.6 Conclusions

In this section, the rhodium-catalyzed hydroformylation of 1-dodecene was studied as an example for a challenging homogeneously catalyzed reaction. Using a biphephos ligand and a thermomorphic multicomponent solvent system (olefin/decane/DMF), a broad range of temperatures, concentrations, total pressures and partial pressures of carbon monoxide and hydrogen was investigated. The complex reaction network consists of six main parallel-series reactions representing isomerization, hydrogenation and hydroformylation. In order to support estimating free parameters in rate equations for all identified reactions, the complete network was decomposed into four, progressively more complex sub-networks

with different intermediates as reactants. For the kinetic description detailed mechanistic models were derived based on a catalytic cycle including both active and inactive Rh-species. Reduced GCK approach models and the corresponding free parameters were identified by analyzing a large set of batch reactor runs using model reduction techniques based on singular value decomposition and subset selection methods. Following this sequential strategy, kinetic models and parameters could be determined for all sub-steps and the total network. The results provide valuable insight into the reaction progress of long-chain olefin hydroformylation in useful thermomorphic solvent systems. The overall model presented allows also describing quantitatively the effect of changes in the gas phase composition on the amount of the active catalyst. It was shown that the isomerization plays a key role in the total reaction network and reduces the terminal aldehyde yield. At elevated temperature, the isomerization reaction consumes relatively fast the reactant 1-dodecene and causes the formation of the undesired iso-aldehyde. Thus, this attractive hydroformylation process should be performed at lower temperature to avoid preliminary isomerization. The kinetic models developed in this work can be used to design and optimize new reactor concepts for this kind of homogeneously catalyzed multi-phase hydroformylation reactions.

The analysis performed for hydroformylation has proven that the systematic GCK approach can be applied successfully. In the following section, in order to further validate them, the kinetic models derived are used to predict the behavior of various operation modes capable to carry out the hydroformylation going beyond batch operation.

## 4 Application of Kinetic Models: Different Reactor Operations

In the previous section, the reaction kinetics of the homogeneously rhodium-biphephos catalyzed hydroformylation of 1-dodecene could be quantified. Reduced mechanistic kinetic models were derived for both the desired main reaction (eq. 3.20) and the most important side reactions (eqs. 3.15 and 3.18). Furthermore, relations were established which allow the calculation of the amount of the active catalyst present in the resting state as a function of the CO and H<sub>2</sub> concentrations in the liquid phase (eq. 3.1d).

In the present section, these reaction kinetics will be used to predict and to improve reactor performance in alternative operation modes beyond batch operation. The suitability of the reaction kinetics will be validated and partly adjusted considering semi-batch and continuous operation. Finally, a strategy based on recycling of unconverted 1-dodecene and formed iso-dodecene will be evaluated in a parametric study.

The results presented in this section were also acquired within a DFG-funded (SFB-TR 63) cooperation with the group of Prof. Sundmacher (Otto-von-Guericke University in Magdeburg), which resulted in the following publication:

B. Hentschel, G. Kiedorf, M. Gerlach, C. Hamel, A. Seidel-Morgenstern, H. Freund and K. Sundmacher, Model-Based Identification and Experimental Validation of the Optimal Reaction Route for the Hydroformylation of 1-Dodecene, *Industrial & Engineering Chemistry Research* 54 (6), 1755–1765, 2015

The author of this thesis contributed to this paper significantly by adjusting the kinetic parameters based on results of a large set of additional batch, semi-batch and dynamic experiments. The model-based identification of the ideal reaction route was done by B. Hentschel.

### 4.1 Experimental equipment and procedures

To analyze the hydroformylation of 1-dodecene in semi-batch, dynamic and continuous operation mode a pilot plant reactor unit from *Mettler Toledo* ( $V_{\text{seg,tot}} = 1.8$  l) was designed and constructed by J. Markert at the Otto-von-Guericke University in Magdeburg (fig. 4.1). The double wall stainless steel reactor can be operated at 10 MPa maximum total pressure and 150 °C reaction temperature. The pressure control concept was realized using an automatic pressure controller (*RCPress60, Mettler Toledo*), which enables several dosing concepts for the synthesis gas components CO and H<sub>2</sub> as well as the inert gas component N<sub>2</sub>. A gassing stirrer provides a fast ideal liquid and gas phase mixing compared to the magnetic stirrer of the multi reactor system (MRS, *Parr Instrument*) used in section 3. For continuous operation, additional HPLC-pumps (*Knauer*) and a fluid level control system including a phase separation unit with purge were installed to enable a continuous inlet and outlet fluid flux (CSTR-model), respectively. The dosing of the TMS system including the solved rhodium-biphephos catalyst is split in two pumps. Thus, a phase separation of the solvent system at the inlet flux at room temperature could be avoided (Markert et al., 2013; Hentschel et al., 2015).

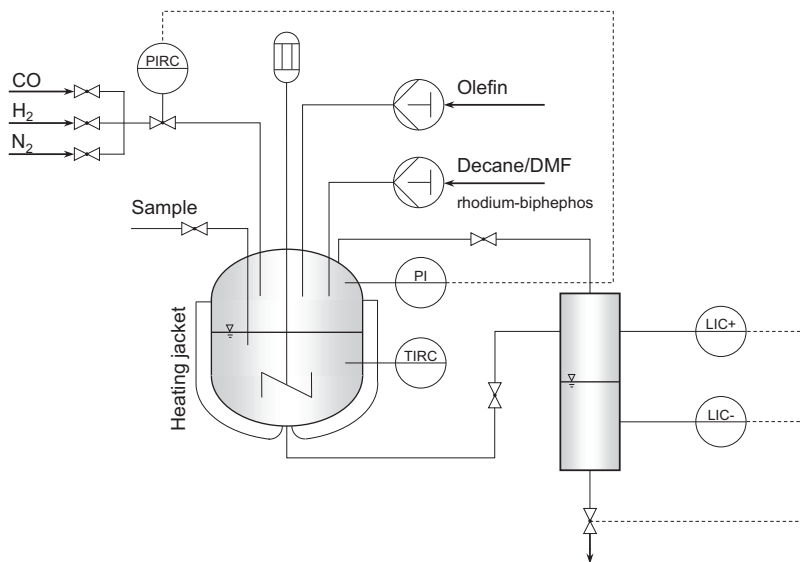


**Figure 4.1:** Schematic illustration of the pilot plant scale reactor calorimeter unit (*Mettler Toledo*) and continuous process equipment

The experimental procedure is close to the kinetic experiments in the MRS (*Parr Instrument*) (see also section 3.3.2). Before filling the reactor with the polar (DMF) and nonpolar (decane) components of the TMS system as well as the rhodium precursor and ligand biphephos, the reactor was flushed with  $N_2$  and evacuated several times to get inert conditions. The weighed masses (decane 343.8 g, DMF 229.8 g,  $Rh(acac)(CO)_2$   $8.49 \cdot 10^{-5}$  mol and biphephos  $2.8 \cdot 10^{-4}$  mol) correspond to the composition of the kinetic experiments in section 3. The catalyst pre-treatment was performed at 1.5 MPa synthesis gas pressure and the desired reaction temperature for at least 60 min. After the catalyst pre-treatment, the preheated reactant 1-dodecene ( $m_{nOL} = 142.8$  g and  $T = 60$  °C) was pulsed at the desired total pressure into the reactor unit using an additional pressure vessel, synthesis gas and the automatic pressure controller. The reaction has been started if the 1-dodecene was fed. The stirrer speed was set to 800 rpm and the samples were taken at discrete steps using a manually operated valve (Hentschel et al., 2015).

The concentration analysis of the reactants and products were realized using the off-line GC-TCD analytic which was already described in section 3.3.3.

## 4.2 Preliminary experiments

As aforementioned in section 3.4.1, gas solubilities and mass transfer coefficients have to be determined independently from hydroformylation experiments. While the effective mass transfer coefficient depends on stirrer, stirrer speed and reactor geometry, the thermodynamic equilibrium solubility of a gas component in a solvent system has to be determined

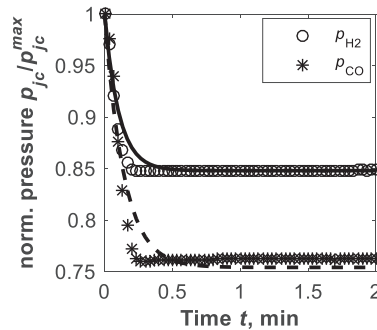
**Table 4.1:** Solubility parameters of synthesis gas components in the initial TMS system (eq. 3.13) and the corresponding effective mass transport coefficient (eq. 2.41-2.42) (Hentschel et al., 2015)

Component	$H_{j,c}^0$ , (MPa·m <sup>3</sup> )·kmol <sup>-1</sup>	$E_{A,sol,jc}$ , kJ·mol <sup>-1</sup>	$k_{eff,jc}$ , min <sup>-1</sup>
H <sub>2</sub>	6.64	-3.06	9.57
CO	7.39	-0.84	7.08

independently from the reactor unit. However, because of improving the experimental procedure and none kinetic limitations using a gassing stirrer the solubility and mass transport parameter of carbon monoxide and hydrogen are updated in tab. 4.1.

The experimental procedure was as follows. The reaction calorimeter was filled with the TMS system (see also section 4.1) neglecting rhodium catalyst and heated up at vacuum conditions to the desired temperature. After equilibration, the stirrer stopped and the system was pressurized rapidly with one of the gaseous reactants using the automatic pressure controller. After the desired total pressure is adjusted the stirrer starts again. The recorded pressure data are used to estimate the kinetic and equilibrium mass transfer parameters. The comparison of the single component modeled and experimental solubility data of hydrogen and carbon monoxide at 1 MPa total pressure and 105 °C, respectively, is presented in fig. 4.2.

However, the updated procedure is still error-prone regarding the gas phase pressurizing. Using the automatic pressure controller (fig. 4.1) to load the gas component the procedure is very slowly. Thus, during pressurizing the gas phase component can be solved in the TMS system without recording. Accordingly, the equilibrium gas solubility will be underestimated. Additionally, the temperature effect of the gas solubility is marginal. Based on this and the error-prone gas phase pressurizing the temperature depends of the gas solubility can be interpreted differently. Therefore, negative solubility activation energies are possible (compare  $E_{A,sol,jc}$  in tab. 3.2 and tab. 4.1). At future experiments an additional gas pressure vessel has to be used as accurately defined gas reservoir. Therefore, the needed time for gas pressurizing can be neglected in the error analysis.

**Figure 4.2:** Experimental (symbols) and modeled (lines) data of the solubility measurement in the reaction calorimeter to determine eq. 3.13 of H<sub>2</sub> ( $p_{tot}^0 = p_{H_2}^0 = 1$  MPa) and CO ( $p_{tot}^0 = p_{CO}^0 = 1$  MPa) in decane/DMF/1-dodecene at  $T = 105$  °C (estimated values in tab. 4.1)

### 4.3 Evaluation of different operation modes

Analyzing experimental data determined in a batch reactor an estimation of the kinetic parameters and the gas solubilities were performed in section 3. The resulting kinetic model described the hydroformylation of 1-dodecene for batch operation conditions in the experimentally covered pressure and temperature range quite well (see e.g. fig. 3.15). However, to design and optimize a process imposed by forced changes of the CO/H<sub>2</sub> atmosphere and temperature, an extrapolation of the derived kinetic model is required outside of the state space covered during the batch experiments. A test of applying the model for the prediction of an additionally performed semi-batch and forced dynamic experiments, not used for the parameter estimation, resulted in larger deviations between experimental data and the model prediction as illustrated in fig. 4.3. In particular, the iso-aldehyde production is overestimated generally. This mismatch based on the increased partial pressure of carbon monoxide at semi-batch conditions especially at an advanced reaction time in combination with a high iso-dodecene concentration. These conditions were not part of the previous batch experimental data.

For refining the kinetic model described in section 3, the general structure suggested previously was maintained (section 3, eqs. 3.1d, 3.8, 3.12, 3.15, 3.18 and 3.20). The additional information covers a larger range of experimental conditions which was applied to fit new model parameters better capable to predict higher concentrations of the gases dissolved in the liquid phase.

In order to cover the semi-batch and perturbed batch conditions it was necessary to introduce an exponent for the CO concentration  $n_{cat}$  in the catalyst pre-equilibrium calculation (eq. 3.1d). The revised equation is shown below.

$$c_{cat,rs} = \frac{C_{Rh,precursor}}{(1 + K_{cat,\alpha} \cdot c_{CO,ll}^{n_{cat}} + K_{cat,\beta} \cdot c_{CO,ll}^{n_{cat}} \cdot C_{H_2,ll}^{-1})} \quad (4.1)$$

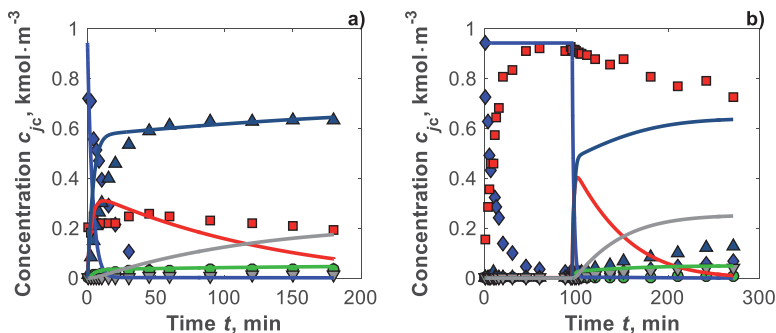


**Figure 4.3:** Experimental (symbols: nOL  $\blacklozenge$ , iOL  $\blacksquare$ , nAD  $\blacktriangle$ , AL  $\bullet$ , iAD  $\blacktriangledown$ ) and modeled (solid lines: original kinetic parameters from tab. 3.5, nOL (blue), iOL (red), nAD (dark blue), AL (green), iAD (grey)) concentration profiles over time of (a) semi-batch hydroformylation experiments of 1-dodecene in the reactor calorimeter ( $V_{seg,tot} = 1.8$  l) at  $T = 105$  °C and  $p_{tot} = 2$  MPa and (b) forced dynamic experiments with initial batch isomerization of 1-dodecene at  $T = 105$  °C and  $p_{CO}^0 = 1$  MPa and subsequent hydroformylation via perturbation with synthesis gas (1:1) up to  $p_{tot} = 2$  MPa and  $T = 115$  °C

The previously postulated catalyst pre-equilibrium included inactive Rh–dimers (fig. 3.3), as also described in (Moasser et al., 1995; Bronger et al., 2004; Deshpande et al., 2011). Based on the newly estimated exponent a more complex influence of CO and other catalyst species on the formation of the catalyst in resting state became apparent. Thus, during fitting the original parameter  $K_{\text{cat},\beta}$  was identified to be almost zero. As a consequence and in agreement with the observations of van Leeuwen (Bronger et al., 2004), no effect of inactive Rh-dimers could be deduced for the conditions investigated. To better understand this important aspect more detailed investigations of the catalyst pre-equilibrium with NMR-techniques or quantum chemistry calculations are necessary. Potential species were already introduced in fig. 3.3. Finally, to revise the model, a new reaction ( $r_{\text{hf},c}$ , see eq. 4.2 and fig. 3.1) was added and parameterized to accurately reproduce the formation of iso-aldehyde observed during semi-batch operation.

$$r_{\text{hf},c} = K_{\text{hf},c} \cdot c_{\text{nOL}} \cdot c_{\text{H}_2,\text{li}} \cdot c_{\text{CO,li}} \quad (4.2)$$

The refined parameters, which were estimated on semi-batch (fig. 4.5) and forced dynamic hydroformylation experiments (fig. 4.6), are listed in tab. 4.2, whereas the original parameters can be found in tab. 3.5. It should be emphasized that the confidence intervals of the refined parameters (the inhibition constants  $K_{\text{cat},\alpha-\beta}$  in eq. 4.1 and the frequency factors  $k_{\omega,jR}$  (eqs. 3.8, 3.12, 3.15, 3.18, 3.20 and 4.2) are much smaller than those of the original parameters. The parameter estimation was supported by the made additional assumptions, such as the introduction of a reaction order for CO and the incorporation of the direct formation of iso-aldehyde from 1-dodecene.

Simulations and a prove of applicability of the refined model (solid lines) are shown for batch, semi-batch, forced (perturbed) dynamic and continuous experimental data in figs. 4.4-4.7 and explained in more detail below.

**Table 4.2:** Revised kinetic parameters (eqs. 3.8, 3.12, 3.15, 3.18, 3.20, 4.1 and 4.2) for the hydroformylation of 1-dodecene reaction network (fig. 3.1)

Parameter	Unit	Value	95 % CI
<b>Catalyst equilibrium (eq. 4.1)</b>			
$K_{\text{cat},\alpha}$	$(\text{m}^3 \cdot \text{kmol}^{-1})^{n_{\text{cat}}}$	$3.041 \cdot 10^{+1}$	$\pm 2.557 \cdot 10^{+1}$
$K_{\text{cat},\beta}$	-	0	$\pm \text{inf}$
$n_{\text{cat}}$	-	0.644	$\pm 0.080$
<b>Isomerization <math>r_{\text{iso}}</math> (eq. 3.15)</b>			
Frequency factor $k_{\text{iso},\omega}^{\text{ref}}$	$\text{m}^3 \cdot (\text{kg}_{\text{cat}} \cdot \text{min})^{-1}$	$4.878 \cdot 10^{+3}$	$\pm 4.738 \cdot 10^{+2}$
<b>Hydrogenation <math>r_{\text{hg},a}</math> (eq. 3.8) / <math>r_{\text{hg},b}</math> (eq. 3.18)</b>			
Frequency factor $k_{\text{hg},b,\omega}^{\text{ref}}$	$\text{m}^6 \cdot (\text{kg}_{\text{cat}} \cdot \text{min} \cdot \text{kmol})^{-1}$	$2.724 \cdot 10^{+2}$	$\pm 4.608 \cdot 10^{+1}$
Frequency factor $k_{\text{hg},a,\omega}^{\text{ref}}$	$\text{m}^6 \cdot (\text{kg}_{\text{cat}} \cdot \text{min} \cdot \text{kmol})^{-1}$	$2.958 \cdot 10^{-2}$	$\pm 2.021$
<b>Hydroformylation <math>r_{\text{hf},a}</math> (eq. 3.12) / <math>r_{\text{hf},b}</math> (eq. 3.20) / <math>r_{\text{hf},c}</math> (eq. 3.20)</b>			
Frequency factor $k_{\text{hf},a,\omega}^{\text{ref}}$	$\text{m}^9 \cdot (\text{kg}_{\text{cat}} \cdot \text{min} \cdot \text{kmol}^2)^{-1}$	$3.702 \cdot 10^{+1}$	$\pm 3.901$
Frequency factor $k_{\text{hf},b,\omega}^{\text{ref}}$	$\text{m}^9 \cdot (\text{kg}_{\text{cat}} \cdot \text{min} \cdot \text{kmol}^2)^{-1}$	$4.904 \cdot 10^{+7}$	$\pm 6.824 \cdot 10^{+6}$
Frequency factor $k_{\text{hf},c,\omega}^{\text{ref}}$	$\text{m}^9 \cdot (\text{kg}_{\text{cat}} \cdot \text{min} \cdot \text{kmol}^2)^{-1}$	$3.951 \cdot 10^{+2}$	$\pm 4.296 \cdot 10^{+1}$
Activation energy $E_{A,\text{hf},c}$	$\text{kJ} \cdot \text{mol}^{-1}$	120.844 <sup>1)</sup>	-

<sup>1)</sup> activation energy adopt from  $E_{A,\text{hf},a}$  (see tab. 3.5)

### 4.3.1 Batch operation mode

In batch operation (fig. 4.4) no dosing of synthesis gas was performed during the experiments. Initially, no gas was solved in the liquid phase and the initial total pressure in the gas phase was set to 2 MPa with a  $H_2$  to CO ratio of 1. Due to the gradually vanishing driving forces the mass transfer into the liquid phase was slower than for semi-batch or perturbed batch operation mode discussed below. This fact was increased due to the application of a reactor system with a magnetic stirring bar in the kinetic experiments (section 3). This yielded to differences in the estimated  $k_{eff,jc}$  value for CO and  $H_2$  between the two sets of experiments (tab. 3.2 and tab. 4.1). A more detailed description of the reactor system and the experimental procedures can be found in section 3.3. Due to the batch operation, the pressure drops and  $H_2$  is gradually depleted, which reduces the extend of the hydroformylation reaction. In parallel, since the CO concentration in the liquid is comparatively low, there is no significant inhibition of the isomerization reaction, which lowers the selectivity with respect to tridecanal. Obviously, since the kinetic parameters reported in section 3 have been entirely obtained from batch experiments, the batch case could be predicted quite accurately in the covered range operating parameters. The experimental 1-dodecene concentration drop after one minute (fig. 4.4a) and the simultaneously iso-dodecene rise results from experimental procedure limits. Further studies use an improved synthesis gas pressurizing concept which reduces this effect to a minimum (Jörke et al., 2015a).

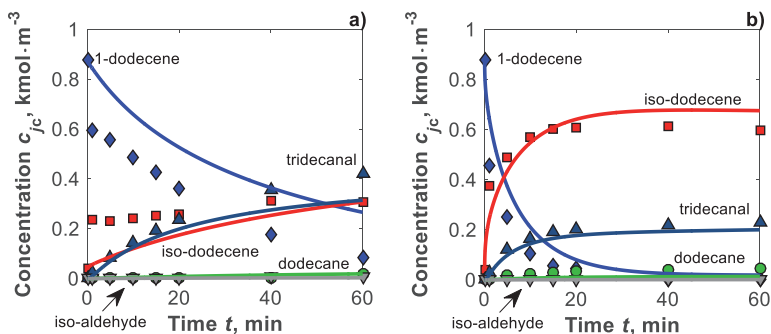


**Figure 4.4:** Experimental (symbols) and modeled (solid lines: revised kinetic parameters from tab. 4.2) concentration profiles over time of batch hydroformylation experiments of 1-dodecene in the multi reactor system ( $V_{seg} = 0.09$  l) at (a)  $T = 95$  °C;  $p_{tot} = 2$  MPa and (b)  $T = 115$  °C;  $p_{tot} = 1$  MPa

### 4.3.2 Semi-batch operation mode

In the semi-batch experiments (fig. 4.5) the same initial conditions were used as in the batch case, but the depletion of gas was compensated by dosing continuously stoichiometrically composed synthesis gas ( $J_{H_2}^{gas} = J_{CO}^{gas} = 0.5 \cdot J_{tot}^{gas}$ ), keeping a constant total pressure of 2 MPa. In this way, higher concentrations of gas in the liquid phase and therefore on the active catalyst could be maintained over the entire reaction time. The experimental data reveal that the isomerization is significantly reduced compared to batch oper-

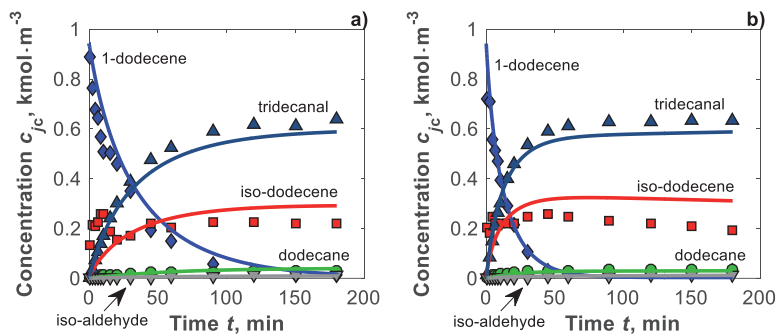


**Figure 4.5:** Experimental (symbols) and modeled (solid lines: revised kinetic parameters from tab. 4.2) concentration profiles over time of semi-batch hydroformylation experiments of 1-dodecene in the reaction calorimeter ( $V_{\text{seg}} = 1.8$  l) at (a)  $T = 95$  °C and  $p_{\text{tot}} = 2$  MPa and (b)  $T = 105$  °C and  $p_{\text{tot}} = 2$  MPa

ation. This can be well explained by the higher CO concentration in the liquid phase (see also fig. 3.15d) (Kiedorf et al., 2014). However, model predictions using the original parameter set overestimated the dynamics of the reaction system significantly (see also fig. 4.3). Also, the production of iso-aldehydes was overestimated. Since in the original batch experiments performed higher CO concentration in the liquid phase were present only for the short initial period, these experiments were characterized by a lack of information about the influence of higher CO concentrations on the reaction kinetics. Particularly, since all reactions were inhibited by CO, the inhibition constants in eq. 3.1d needed to be refined. The reported high confidence interval of  $K_{\text{cat},\alpha}$  in (Kiedorf et al., 2014) (tab. 3.5) clearly resulted from this missing information. Also, the overestimation of the iso-aldehyde formation can be explained with this fact.

### 4.3.3 Dynamic operation mode (perturbation experiments)

The additionally performed new perturbed experiments (fig. 4.6) are in principle two batch experiments carried out in series to re-parameterize the model regarding its CO sensitivity. During a first isomerization phase ( $\approx 100$  min), in which a pure CO atmosphere of 0.1 MPa (fig. 4.6a) or 0.3 MPa (fig. 4.6c) was applied, 1-dodecene was almost completely converted into iso-dodecenes. The subsequent hydroformylation phase was initiated via a perturbation with synthesis gas ( $J_{\text{H}_2}^{\text{gas}} = J_{\text{CO}}^{\text{gas}}$ ) up to 2 MPa. At the same time, the temperature was increased from 95 °C to 115 °C to enhance the rate of re-isomerization by shifting the chemical equilibrium. Using the original parameters, the model predicts a constant 1-dodecene concentration until the hydroformylation starts. According to eq. 3.1d the missing hydrogen led to a total deactivation of the active catalyst, and hence, the initial isomerization phase could not be reproduced (fig. 4.3b). Based on the experimental data acquired, a refinement of the reaction kinetics proposed by (Kiedorf et al., 2014) could be done to cover a wide range of operating conditions as needed for the process improvement studied in this work (fig. 4.6).

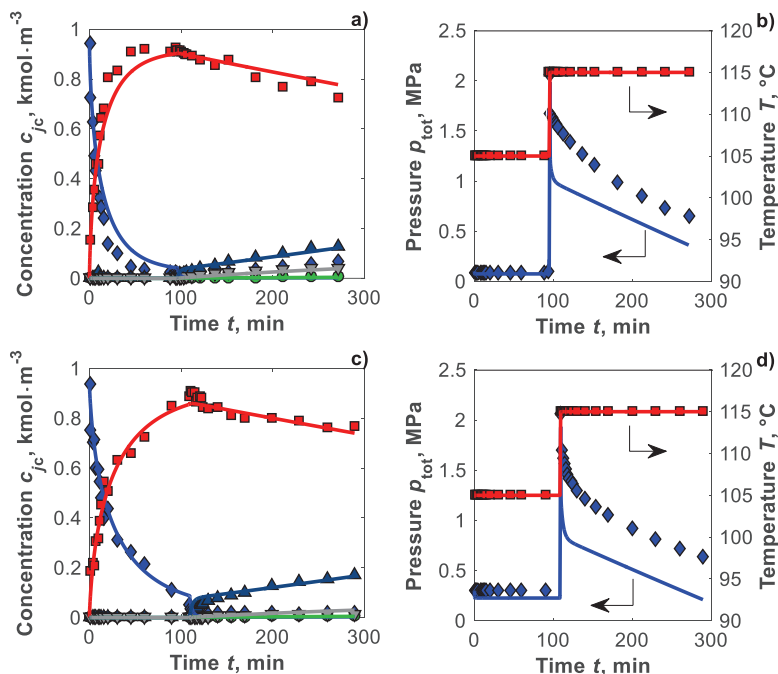


**Figure 4.6:** Experimental (symbols: nOL  $\diamond$ , iOL  $\blacksquare$ , nAD  $\blacktriangle$ , AL  $\bullet$ , iAD  $\nabla$ ) and modeled (solid lines: revised kinetic parameters from tab. 4.2, nOL (blue), iOL (red), nAD (dark blue), AL (green), iAD (grey)) concentration, pressure and temperature profiles over time of forced dynamic experiments with initial batch isomerization of 1-dodecene at  $T = 105$  °C and (a-b)  $p_{CO^0} = 1$  MPa and (c-d)  $p_{CO^0} = 3$  MPa and subsequent hydroformylation via perturbation with synthesis gas (1:1) up to  $p_{tot} = 2$  MPa and  $T = 115$  °C

#### 4.3.4 Continuous operation mode

For validation of the revised reaction kinetics and to appreciate the performance of a CSTR a continuous operated hydroformylation of 1-dodecene was performed. The experimental realization was already mentioned in section 4.1. Based on the previous batch, semi-batch and forced dynamic hydroformylation experiments the 60 min reaction time was transferred in an adequate CSTR residence time  $\tau$  (eq. 4.3).

$$\tau = \frac{V_{seg}}{\dot{V}_{tot}} = \frac{V_{seg,li}}{\dot{V}_{nOL+decane} + \dot{V}_{DMF+cat}} \quad (4.3)$$

By means of this equation and the available liquid reaction volume ( $V_{seg,li} = 0.9$  l) the volumetric fluxes of the nonpolar and polar part of the TMS system results in  $\dot{V}_{nOL+decane} = 7.63$  ml·min<sup>-1</sup> and  $\dot{V}_{DMF+cat} = 2.37$  ml·min<sup>-1</sup>, respectively. Based on the polarity the required catalyst/ligand complex was solved in the DMF inlet flux.

The continuous operation process (fig. 4.7) was initialized using the well-known batch

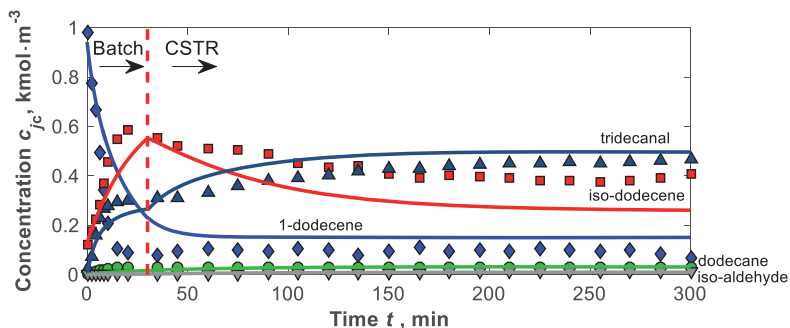


**Figure 4.7:** Validation of the revised reaction kinetic (tab. 4.2) in continuous operation mode using the reaction calorimeter ( $V_{\text{seg}} = 1.8$  l;  $T = 105$  °C;  $p_{\text{tot}} = 2$  MPa and  $\tau = 60$  min) with an initial batch process ( $t \leq 30$  min;  $T = 105$  °C;  $p_{\text{tot}} = 2$  MPa) (Hamel, 2016)

experimental setup for 30 min ( $T = 105$  °C and  $p_{\text{tot}} = 2$  MPa). Afterwards the system was transferred in a continuous process. Accordingly, after certain time continuous steady state conditions could be assumed.

The mathematical modeling was performed using the two phase CSTR partial pressure and concentration balances (eqs. 2.41-2.43) which were already introduced in section 2.3.1. Based on the experimental setup almost isothermal conditions were present. Corresponding to this, the energy balance was not solved. For analysis of the initial batch process, it becomes apparent, that the revised reaction kinetics clearly underestimate the isomerization of 1-dodecene ( $r_{\text{iso}}$ ) and the hydroformylation from 1-dodecene to tridecanal ( $r_{\text{hf,b}}$ ). The formation of the side products decane and iso-aldehyde can be described well. After switch to continuous conditions the system was transferred into the steady state. This dynamic can be described relatively well. However, because of missing the switchover point the absolute concentration values of 1-dodecene, iso-dodecene and tridecanal were not reached by the modeling. After 250 min overall reaction time experimental steady state conditions can be assumed. In this range the model predicted the steady state, too. But also in this connection the isomerization of 1-dodecene was underestimated by the reaction kinetic model. Accordingly, 1-dodecene and iso-dodecene were over- and underrate, respectively. Based on missing calibration response factors of the dodecene isomers for the GC analytic (see also section 3.3.3) the experimental isomer dodecene concentration description was inaccurate. Isomerization studies of the decene system offered differences in these response factors (Jörke et al., 2015a). Therefore, the measured gap of the iso-dodecene concentration was caused by analytic discrepancies, too. Further measured components can be reflected by the model description well. After 300 min the continuous experiment was terminated because of a limiting preparation and post-processing setup.

Based on these experimental data and the model prediction, it can be observed, that the revised reaction kinetic is able to describe the hydroformylation of 1-dodecene in a broad temperature and pressure range as well as in different operation modes. Accordingly, using the reaction kinetics several parametric studies can be performed to improve the reactor performance.

#### 4.4 Parametric study of feed variation

In all preliminary observations, the equilibrium limited isomerization was recognized as the main side reaction which reduces the process efficiency. Thus, to improve the reaction performance the forward isomerization of 1-dodecene has to prevent (see  $r_{iso}$  in fig. 3.1). The three main control settings of the isomerization properties are the reaction temperature, the total synthesis gas pressure and the partial pressure of hydrogen and carbon monoxide. Based on the estimated activation energies (see tab. 3.5,  $E_{A,iso} > E_{A,\dots}$ ) the specific adjustment of the reaction temperature is mostly promising. One another approach is to exploit the equilibrium composition of the terminal olefin and the corresponding isomers. If iso-dodecene is used as additional feed component the equilibrium dodecene composition can be shifted directly to 1-dodecene ( $nOL \leftrightarrow iOL$ ). Accordingly, the TMS system is extended by the iso-dodecene component. By means of the parametric study a suitable terminal olefin to isomer ratio will be determined to increase systematically the terminal aldehyde yield. For this purpose, in eq. 4.4 the molar inlet feed ratio of the isomer and terminal dodecene is introduced.

$$ratio = \frac{n_{iOL}^{in}}{n_{nOL}^{in}} \quad (4.4)$$

An inlet feed ratio of zero corresponds to the standard TMS system composition (section 3.1). To achieve the TMS system requirement, the total dodecene inlet concentration was set constant. Accordingly, the terminal inlet olefin concentration is decreased with an increased inlet ratio. Below the effect on the reaction performance of the three discussed control factors will be analyzed in detail.

In fig. 4.8 the complete olefin conversion consisting of 1- and iso-dodecene  $X_{OL}$ , the tridecanal selectivity and yield are shown as function of the inlet feed ratio and the reaction temperature. Obviously, the overall olefin conversion is decreased with increasing feed ratio. This is due to the reduced amount of more reactive terminal olefin at the feed position. At higher reaction temperatures the effect is decreased, because of the intensified re-isomerization of iso-dodecene.

The main product selectivity of tridecanal is shown in fig. 4.8b. Based on the additional isomer feed, the isomerization of 1-dodecene can be inhibited using the equilibrium com-

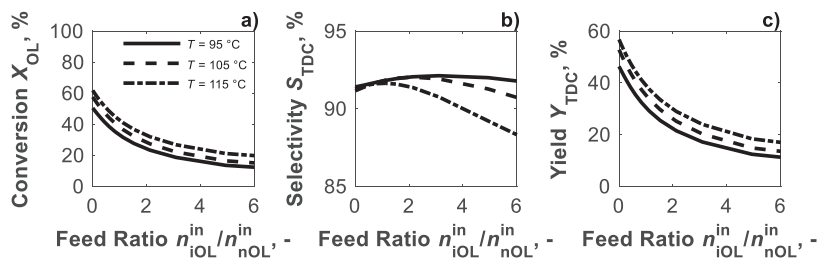


**Figure 4.8:** Steady state ( $t \geq 160$  h) CSTR performance parameter ((a) Terminal olefin conversion, (b) tridecanal selectivity and (c) tridecanal yield) as a function of the inlet feed ratio of iso-dodecene and 1-dodecene at three different reaction temperatures ( $p_{tot} = 1.8$  MPa)

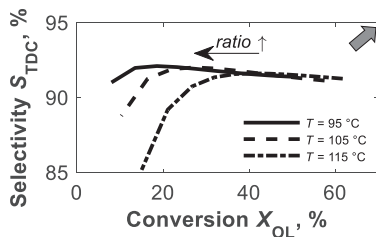


**Figure 4.9:** Steady state tridecanal selectivity as a function of the corresponding total olefin conversion for three different reaction temperatures ( $T = 95/105/115$  °C)

position. Consequentially the tridecanal selectivity is increased up to the maximum at a ratio of  $\approx 3$  at 95 °C. At higher reaction temperatures, the maximum is shifted to lower feed ratios. After passing the maximum the tridecanal selectivity is decreased. In this iso-dodecene concentration range, the production of iso-aldehydes is strongly supported and minimizes the main product.

Thus, at small inlet feed ratios a potential optimum can be expected. However, the decrease of the olefin conversion is much more pronounced than the selectivity increase. Accordingly, the product of conversion and selectivity, the tridecanal yield (fig. 4.8c) decreases strongly using an olefin mixture as feedstock. In the classical selectivity–conversion diagram (fig. 4.9) the effect is even more obviously. In this illustration, the optimal reaction performance is located marked using the grey arrow. For several investigated temperatures, the reaction performance is decreased at a simultaneously increasing feed ratio.

The effect of the total synthesis gas pressure in combination with the inlet feed ratio is shown in fig. 4.10. In the investigated pressure range no sufficiently performance changes can be observed. Only at lower feed ratios a trend to higher overall olefin conversion at higher total synthesis gas pressures is obvious.

Overall the effect of the inlet feed ratio in combination with a constant olefin concentration of the reaction performance is negative. As main reason the limited olefin conversion at higher feed ratios can be pronounced. Therefore, at the following feed variation

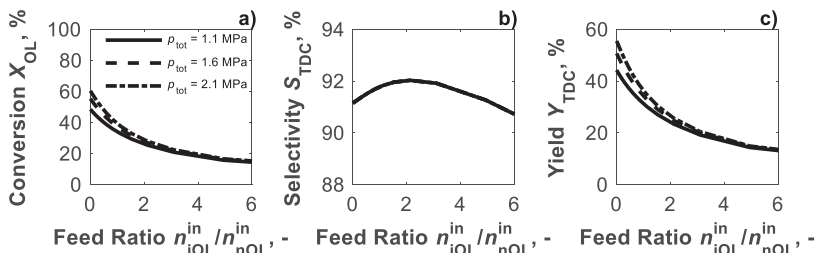


**Figure 4.10:** Steady state ( $t \geq 160$  h) CSTR performance parameter ((a) terminal olefin conversion, (b) tridecanal selectivity and (c) tridecanal yield) as a function of the inlet feed ratio of iso-dodecene and 1-dodecene at three different synthesis gas pressures ( $T = 105$  °C)

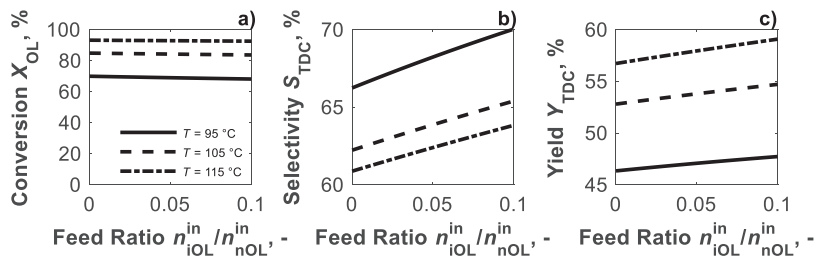


**Figure 4.11:** Steady state ( $t \geq 160$  h) CSTR performance parameter ((a) terminal olefin conversion, (b) tridecanal selectivity and (c) tridecanal yield) as a function of the inlet feed ratio of iso-dodecene and 1-dodecene at three different reaction temperatures ( $p_{tot} = 1.8$  MPa)

study the terminal olefin concentration was set constant. Accordingly, the total olefin concentration is increased by an increasing feed ratio. Hence, the feed ratio is varied only in a small range in order to keep the TMS system properties. The corresponding performance parameters are shown in fig. 4.11. During the terminal olefin conversion is nearly constant the tridecanal selectivity is clearly increased. Thus, a product yield optimization can be significantly observed. However, only a small variation in iso-dodecene inlet concentration is possible. Otherwise a new defined phase characteristic of the TMS system occurs.

Further optimization potential reveals the application of a recycle flux of none converted reactants and undesired isomerization product. First parametric studies were already done by (Hamel, 2016). In this regard, a maximum increase of the desired tridecanal yield of  $\approx 30$  % is observed.

## 4.5 Conclusions

In this section, the determined kinetic models of the rhodium catalyzed hydroformylation of 1-dodecene were applied. For this, an advanced experimental plant with the possibility of dosing the gas and liquid phase was realized. By means of this experimental plant the transferability of the kinetic parameters from batch experiments to semi-batch, forced dynamic and continuous operation modes was evaluated. The application of the kinetic parameters in more advanced operation modes turned out to be difficult and a modification of some parameters was performed. Hereby, an adjustment of the reaction rate constants was appropriate. Moreover, using the additional acquired experimental information an extension of the reaction network was performed by quantifying the hydroformylation of 1-dodecene to iso-aldehyde. The modified reaction kinetics were found to be able to describe the hydroformylation of 1-dodecene in a broad range of reaction temperatures, synthesis gas pressures, olefin concentrations and several operation modes.

Based on the modified extended reaction kinetics a parametric study was performed to evaluate the potential of selecting the initial TMS solvent composition. Using iso-dodecene as additional feed component in the TMS system the dodecene equilibrium composition can be affected. Thus, the undesired 1-dodecene isomerization can be reduced. If the overall inlet dodecene concentration is constant the loss in olefin conversion prevents

improving the reaction performance. However, if the terminal olefin concentration is constant and the isomer is added additionally to the TMS system an increase of the tridecanal yield can be realized.

The general concept followed in this thesis appears to be valuable to quantify the reaction kinetics of the homogeneously catalyzed hydroformylation of 1-dodecene. Using the adjusted kinetic parameter set, all operation modes studied could be described quite well.

In order to evaluate the possible application of the GCCK approach in heterogeneous catalysis an additional corresponding study was carried out. It was devoted to investigate the total oxidation of short-chain hydrocarbons. The results achieved are summarized in Part III.



**Part III**  
**Analysis of Heterogeneously**  
**Catalyzed Reactions**



## 5 Kinetics of the Total Oxidation of Short-Chain Hydrocarbons

The application of the GCCK approach was successfully demonstrated in Part II for the homogeneously catalyzed hydroformylation of 1-dodecene. In the following Part III, the GCCK approach will be applied to quantify the rates of heterogeneously catalyzed reactions. Analyzing such reactions, the transport of reactants and products has to be considered in kinetic modeling as well. Moreover, the identification of catalytic cycles is more difficult due to limited access to in-situ spectroscopic techniques. Therefore, the GCCK approach has been applied up to now rarely for heterogeneously catalyzed reactions. In order to demonstrate its corresponding potential, the total oxidations of gaseous short-chain hydrocarbons (ethylene and propylene) and carbon monoxide diluted in air carried out on a solid catalyst ( $\text{CrO}_x/\gamma\text{-Al}_2\text{O}_3$ ) will be studied in this section. Later in section 6, the periodic operation of the innovative and challenging Loop Reactor concept will be studied. Main goals are to demonstrate the potential of this reactor concept and to apply and to validate the determined kinetics of the ethylene and propylene total oxidation.

The results presented in this section regarding the reaction kinetic analysis were already published in the following two papers:

- 1) G. Kiedorf, T. Wolff, A. Seidel-Morgenstern and C. Hamel, Adsorption measurements on a  $\text{CrO}_x/\gamma\text{-Al}_2\text{O}_3$  catalyst for parameter reduction in kinetic analysis, *Chemical Engineering Science* 149, 266-276, 2016
- 2) G. Kiedorf, T. Wolff, A. Seidel-Morgenstern and C. Hamel, Kinetic analysis of the hydrocarbon total oxidation using individual measured adsorption isotherms, *Chemie Ingenieur Technik* 88 (11), 1746–1760, 2016

The author of this thesis contributed essentially to the results presented in these two papers. Regarding the first paper the contributions include the single and multi-component adsorption isotherm measurements and the parameter estimation. With respect to the second paper the contributions include the mechanistic reaction kinetic analysis of the partial and total oxidation of ethylene, propylene, mixtures of both and carbon monoxide on a chromium oxide supported catalyst both theoretically and experimentally.

Total oxidation reactions are used to purify exhaust streams from i.e. automotive engines and coal-fired power stations. Much effort has been dedicated to identify suitable catalysts for the total oxidation of volatile organic compounds (VOC) (Spivey, 1987; Hutchings and Taylor, 1999; Heynderickx et al., 2010a). Noble metal catalysts were proved to be most active for oxidation reactions (Spivey and Butt, 1992; Burgos et al., 2002). Platinum (Voltz et al., 1973; Herz and Marin, 1980; Burgos et al., 2002; Baylet et al., 2011) or palladium (Choudhary et al., 2002; Hurtado et al., 2004) are often applied as active metal components supported by  $\gamma\text{-Al}_2\text{O}_3$  particles or monoliths. Moreover, combinations of different metals are favorites (Nibbelke et al., 1998; Harmsen et al., 2000). Based on lower costs, higher stability and more unsusceptible against catalyst poisoning the trend is towards applying transition metal oxide catalysts (Spivey, 1987; Hutchings and Taylor, 1999; Liu et al., 2009; Gómez et al., 2014). As an active oxidation combination  $\text{CrO}_3$  (Spivey, 1987)

and vanadium based catalysts (Wang et al., 2000; Panizza et al., 2003; Nova et al., 2009) were identified. However, the suitability of a catalyst depends on the reactants as well. Hence, variable catalyst activity can occur (Yao, 1973; Bettahar et al., 1996). In this thesis, a  $\text{CrO}_x$  as active catalyst species is applied, supported by  $\gamma\text{-Al}_2\text{O}_3$ . Further specifications of the catalyst will be given in section 5.1.1.

For derivation of mechanistic rate models using the GCCK approach introduced in section 2.1 a catalytic cycle for the total oxidation reactions is needed. However, the identification of catalytic cycles in heterogeneous catalysis is hindered by missing in-situ spectroscopic techniques. Therefore, in heterogeneous catalysis as well as in this thesis the formulation of mechanistic rate approaches is based on well-established reaction mechanisms, such as e.g. the *Mars/van Krevelen* and *Eley/Rideal* mechanisms. Considering the assumptions used in deriving these reaction mechanisms, it can be shown that the resulting rate expressions form subsets of the general rate equations obtained from the *Christiansen* methodology. The selection of the appropriate reaction mechanism depends on the oxygen storage capacity of the active catalyst species. If no or only small lattice oxygen capacities available, adsorption–desorption mechanisms are often validated (Helfferrich, 2004; Baerns, 2006). If the catalyst species provide lattice oxygen, too, an oxidation–reduction mechanism can be observed (Mars and van Krevelen, 1954; Murzin, 2013). However, oxidation reactions consume lattice, adsorbed and gas phase oxygen, respectively (Yao, 1973; Heynderickx et al., 2010a; Gómez et al., 2014), which complicates the catalytic cycle identification even more. In literature were discussed different mechanisms of the total oxidation of short-chain olefins and carbon monoxide on a  $\text{CrO}_x$  catalyst (Yao, 1973; Murzin and Salmi, 2005). In (Yao, 1973)  $\alpha\text{-Cr}_2\text{O}_3$  with different morphological appearances was prepared and analyzed for the total oxidation of short-chain olefins, alkanes and carbon monoxide. In accordance to the adsorption measurements it was concluded that the investigated  $\text{Cr}_2\text{O}_3/\text{Si}$  catalyst offer no surface lattice oxygen for the total oxidation reaction mechanism. In contrast the authors of (Murzin and Salmi, 2005) illustrated that  $\text{Cr}_2\text{O}_3$  follows the MvK mechanism for the carbon monoxide oxidation. However, at special conditions experimental measured concentration profiles can be explained with several rate models (Kripylo et al., 1984; Redlingshöfer et al., 2003). The derivation of the mechanistic rate approaches used in this section was already presented in section 2.1.2 and will be additionally summarized in section 5.2.

Due to a large number of unknown kinetic parameters arising from the mechanistically based GCCK approach, mathematical model reduction techniques, as e.g. the subset selection method (section 2.2.3), or dedicated additional measurements are necessary. As aforementioned, in heterogeneous catalysis interphase transport phenomena of reactants and products have to be considered in kinetic modeling. Such single and multi-component phase equilibria from reactants and products between the fluid and solid catalyst phase can be measured separately. A successful application of separately measured phase equilibria within kinetic rate models was already presented by several authors (Pöpken et al., 2000; Yu et al., 2004; Corma and Ortega, 2005; Schmitt and Hasse, 2006; Al-Sabawi and Lasa, 2009). Thus, kinetic parameter estimation is simplified and the physical meaning of model parameters is conserved by separation kinetic and thermodynamic effects (Pöpken et al., 2000; Kiedorf et al., 2016a, 2016b). Individual measured single and competitive

adsorption isotherms of reactants and products will be performed in section 5.4.

The strategy of the reaction network decomposition as model reduction technique was successfully applied above for the homogeneously catalyzed hydroformylation (section 3.5). Considering the phases involved, this model reduction technique is suitable in heterogeneous catalysis as well. It will be applied in the reaction network analysis of the total oxidation of ethylene and propylene, respectively (section 5.5).

## 5.1 Catalyst characterization and reaction network

### 5.1.1 Catalyst preparation and characterization

The chrome-alumina catalyst used in the experimental setup was prepared and analyzed by Dr. T. Wolff at the Max Planck Institute in Magdeburg by wet impregnation technique. Chromium nitrate nanohydrate ( $\text{Cr}(\text{NO}_3)_3 \cdot 9\text{H}_2\text{O}$ , *Merck*) and chromium acetylacetonate ( $\text{Cr}(\text{C}_5\text{H}_7\text{O}_2)_3$ , *Merck*) with 99.99 % purity were used as precursor.  $\gamma$ -Alumina with spherical particles ( $d_p = 0.001 \text{ m}$ , *Sasol*) was used as porous support. The support was preheated at 120 °C for 24 h and impregnated with aqueous-acetone (1:1) of chromium precursor mixture of nitrate and acetylacetonate (12:1). This solution was kept in a roller mixer for 2 h. After removing rest solutions, the recovered solid was washed with deionized water, followed by drying at 50 °C for 24 h. Finally, the sample was calcinated at 700 °C for 8 h in air in a muffle furnace. The rate of heating was  $3 \text{ K} \cdot \text{min}^{-1}$ .

Chemical analysis of the total Cr was carried out by Inductively Coupled Plasma Optical Emission Spectroscopy (ICP-OES) using iCAP 6500 Duo (*Thermo Fisher*) system. The prepared fresh catalyst contained 1.0 wt.-% Cr and 38.4 wt.-% Al. After the period of experimental measurements, the chrome and alumina loadings were checked again and found to be constant. Thus, no release via gas phase occurred. Nitrogen physisorption isotherms were measured at -196 °C using a *Nova 2000e* (*Quantachrome*) analyzer. The sample was degassed for 24 h at 120 °C in vacuum. The specific surface area was calculated by BET and the pore diameter by BJH method (Alvarado Perea et al., 2013). The  $\text{CrO}_x/\gamma\text{-Al}_2\text{O}_3$  catalyst received a surface area of  $152.7 \text{ m}^2 \cdot \text{g}^{-1}$  and a pore diameter of 8.7 nm according to the  $\gamma\text{-Al}_2\text{O}_3$  support ( $157.7 \text{ m}^2 \cdot \text{g}^{-1}$  and 8.0 nm).

TPR profiles (fig. 5.1) were obtained on a BEL-CAT Catalyst Analyzer (*BEL Japan Inc.*) using 10 % hydrogen in argon. Basically, one reduction peak was apparent below 400 °C for the  $\text{CrO}_x/\gamma\text{-Al}_2\text{O}_3$  catalyst. It appears that this corresponds to  $\text{CrO}_3$ . The peak was slightly shifted from 430 to 340 °C. Further peaks of the  $\text{CrO}_x/\gamma\text{-Al}_2\text{O}_3$  catalyst in the TPR analysis were not observed. Accordingly, above 400 °C  $\text{Cr}_2\text{O}_3$  adsorption sites were present. Based on these measurements, the two oxidation states of chromium,  $\text{Cr}^{6+}$  and  $\text{Cr}^{3+}$ , can be observed.

In (Sattler et al., 2014) Raman and UV-Vis spectra of a  $\text{CrO}_x/\text{Al}_2\text{O}_3$  catalyst were investigated. Therefore, the additional  $\text{Cr}^{2+}$  and  $\text{Cr}^{5+}$  species were identified as active components in dehydrogenation reaction. Further the structure of the several present chrome centers was analyzed.  $\text{Cr}^{3+}$  was found as an isolated center stabilized by the catalyst support and in amorphous clusters. In this connection, it is pointed out that these clusters are invisible in the available XRD analysis (*X'Pert Pro diffractometer* by *PANalytik*). Crystalline structures were observed only at higher chromium loading. Accordingly, based on this

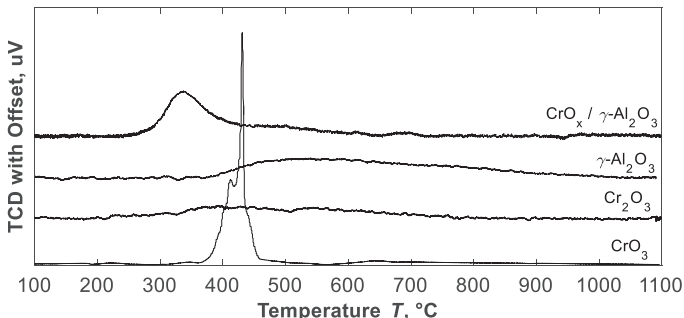


**Figure 5.1:** TPR profiles of the  $\text{CrO}_x/\gamma\text{-Al}_2\text{O}_3$  catalyst, the  $\gamma\text{-Al}_2\text{O}_3$  support material and the reference materials  $\text{Cr}_2\text{O}_3$  and  $\text{CrO}_3$ , the y-axis is shifted for the different profiles.

analysis the additional observed chrome species can be expected on the presented catalyst. A more detailed analysis of the presented catalyst will be forwent in this work. Rather the reaction kinetic analysis of the total oxidation of carbon monoxide, ethylene and propylene as single component inlet and ethylene and propylene in mixture will be the scope of this section.

### 5.1.2 Reaction network

The total oxidation reaction network postulated for the VOC system is presented in fig. 5.2a. The reaction network consider the total ( $r_1, r_3$ ) and partial ( $r_2, r_4$ ) oxidation reactions of the reactants ethylene and propylene, respectively (Hodnett, 2000). Furthermore, the product of the partial oxidation reaction, carbon monoxide, can be completely oxidized ( $r_5$ ) (Ayastuy et al., 2009). The thermal cracking reaction from propylene to ethylene ( $r_6$ ) (Van Damme et al., 1975; Lobera et al., 2008) were only observed in a range below 0.1 %. For that reason, this reaction is not quantified in this network analysis.

Analyzing the ethylene sub-network ( $r_3 = r_4 = 0$ ) kinetics temperature dependence (fig. 5.2b) showed that the ethylene integral conversion (eq. 2.16) below 300 °C was close to zero. If the temperature was increased the ethylene conversion was increased as well.

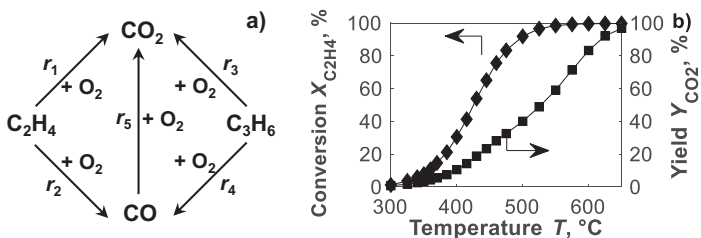


**Figure 5.2:** (a) Postulated reaction network for the total oxidation of ethylene and propylene and (b) Experimental conversion of  $\text{C}_2\text{H}_4$  (◆) and yield of  $\text{CO}_2$  (■) as a function of temperature for the ethylene sub-network ( $r_3 = r_4 = 0$ ) at  $x_{\text{C}_2\text{H}_4}^{\text{in}} = 1.00\%$ ,  $x_{\text{O}_2}^{\text{in}} = 20.90\%$  and  $W/F = 50 \text{ kg}_{\text{cat}} \cdot \text{s} \cdot \text{m}^{-3}$

Above 600 °C complete conversion was achieved. Complete conversion to carbon dioxide was achieved above 650 °C. In the range from 300 °C to 650 °C carbon monoxide can be detected as a product as well. Based on this knowledge, the kinetic analysis will be performed within this temperature range.

For analysis, the oxidation network will be decomposed in three sub-networks of different size and complexity. The analysis was started with the smallest and independent sub-network, the carbon monoxide oxidation ( $r_{1-r_4} = 0$ ). Further the complexity was increased and finalized at the complete network ( $r_{1-r_5} \neq 0$ ). The intermediate steps include the ethylene sub-network ( $r_{3-r_4} = 0$ ) and the propylene sub-network ( $r_{1-r_2} = 0$ ). For this approach, the experimental measurements were adapted at each sub-network. Finally, the transfer of the already estimated kinetic parameters at the sub-networks was reviewed at the complete network.

Sub-network	Name	Abbreviations of involved reaction rates
• I	Oxidation of CO	$r_5$
• II	Oxidation of C <sub>2</sub> H <sub>4</sub>	$r_1, r_2, r_5$
• III	Oxidation of C <sub>3</sub> H <sub>6</sub>	$r_3, r_4, r_5$
• Total reaction network	Oxidation of C <sub>2</sub> H <sub>4</sub> and C <sub>3</sub> H <sub>6</sub>	$r_1, r_2, r_3, r_4, r_5$

## 5.2 Catalytic cycle and mechanistic models

The kinetic analysis of the partial and total oxidation of ethylene, propylene and carbon monoxide will be performed for all studied reactants using the *Langmuir/Hinshelwood* (LH), the *Eley/Rideal* (ER) and the *Mars/van Krevelen* (MvK) mechanism. The derivation of the mechanistic ER and MvK kinetics using the GCKK approach were already presented in section 2.1.2. However, using the standard GCKK approach, only one catalyst species involved in the catalytic cycle can be handled. Therefore, this approach is not capable to generate the LH approach (Helfferich, 2004; Murzin and Salmi, 2005) (see also section 2.1). The derivation of this rate approach can be performed by the classical way in the appendix A.2 (Baerns, 2006). The LH reaction mechanism assumes that the surface reaction between the adsorbed components is rate determining and therefore the adsorption and desorption steps are in steady state. Thus, the reaction kinetics can be written as a function of the reactant surface concentrations. The applied reaction rate equation for the total oxidation reactions is presented in eq. 5.1. The research group of Marin (University Ghent) discussed also other steps of the catalytic cycle as rate determining and the corresponding rate equations (Heynderickx et al., 2010a).

$$r_{1-5}^{\text{LH}} = \frac{K_{1-5}^{\text{LH}}(T)(Kp)_{\text{O}_2}^{0.5}(Kp)_{\text{C}_2\text{H}_4/\text{C}_3\text{H}_6/\text{CO}} c_{\text{cat}}}{\left(1 + (Kp)_{\text{O}_2}^{0.5} + (Kp)_{\text{C}_3\text{H}_6} + (Kp)_{\text{C}_2\text{H}_4} + (Kp)_{\text{CO}} + (Kp)_{\text{CO}_2} + (Kp)_{\text{H}_2\text{O}}\right)^2} \quad (5.1)$$

Analyzing eq. 5.1, in addition to the rate determining surface reaction, oxygen dissociation on the catalyst species is assumed. If only one reactant adsorbs at the active catalyst species the LH reaction mechanism is reduced to the ER mechanism (see also fig. 2.3). The final mechanistic rate approach determined via the GCKK approach (section 2.1.2) is

presented in eq. 5.2. According to the LH mechanism, the ER reaction rate is inhibited product adsorption and oxygen dissociation at the catalyst active species is assumed.

$$r_{1-5}^{ER} = \frac{k_{1-5}^{ER}(T)(K_{O_2}P_{O_2})^{0.5}P_{C_2H_4/C_3H_6/CO}C_{cat}}{(1+(K_{O_2}P_{O_2})^{0.5}+K_{CO_2}P_{CO_2}+K_{H_2O}P_{H_2O})} \quad (5.2)$$

As aforementioned, the reactant oxidation via the MvK mechanism occurred using lattice surface oxygen. Afterwards, the reduced catalyst will be re-oxidized by gas phase oxygen. The final irreversible determined rate approach by the GCCK method (section 2.1.2) is presented in eq. 5.3.

$$r_{1-5}^{MvK} = \frac{k_{red}^+P_{C_2H_4/C_3H_6/CO}K_{ox}^+P_{O_2}}{(k_{red}^+P_{C_2H_4/C_3H_6/CO}+k_{ox}^+P_{O_2})} \quad (5.3)$$

For reaction kinetic analysis of the sub- and overall reaction network, all introduced rate approaches (eqs. 5.1-5.3) will be tested and ranked. The kinetic parameters of the best performed equations will be selected and sequentially transferred to the progressively larger sub-network and finally to the total network. The temperature dependence of the kinetic constants will be performed using a typical *Arrhenius* equation (eq. 2.21). For parameter estimation the modified *Arrhenius* approach by (Schwaab and Pinto, 2007) will be used (eq. 2.22). The individual quantification of the single component and competitive adsorption parameters will be performed in section 5.4.

### 5.3 Experimental equipment and procedures

The kinetic experiments were realized by the author of this thesis in a lab scale test facility (fig. 5.3) that consist of a gas supply, a furnace with an integrated quartz glass reactor, online FT-IR and a gas chromatograph analytic with a heated multi-position valve which enable a gas analysis of the reactants and products. The reactant feed gas was composed of ethylene (*Air Liquide* 3.0), propylene (*Westfalen Gas* 2.5) or carbon monoxide (*Linde* 2.0) in mixtures of air (technical grade) and nitrogen (*Air Liquide* 5.0). The total inlet flow was adjusted using mass flow controllers (*Bronkhorst*).

The tubular reactor (fused silica glass) with a length of 0.4 m and the inner diameter of 0.006 m was filled with 0.1827 g of the CrO<sub>x</sub>/γ-Al<sub>2</sub>O<sub>3</sub> powdered catalyst particles ( $d_p = 150\text{--}250 \mu\text{m}$ ) to avoid mass transport limitations proven in preliminary experiments. The catalyst bed was encased with inert particles (ZrO<sub>2</sub>/SiO<sub>2</sub>,  $d_p = 0.001\text{--}0.00125 \text{ m}$ , *Mühlmeier*), which was used as a pre-heating zone of the feed gas and to achieve an ideal mixture of the components in the gas phase. The reactor was embedded in a furnace (*HTM Reetz*). Thus, the temperature can be set between 25–1000 °C. The temperature was controlled by a thermocouple which was placed in the center of the catalyst bed. In addition, a thermocouple was positioned at the beginning and the end of the catalyst bed, respectively. By means of the three thermocouples a temperature profile across the catalyst bed can be estimated and calculated using a polynomial equation of second degree (appendix B.2).

The quantitative analysis of the gas composition was realized by a GC-TCD/MSD (*Agilent GC 6890*) system equipped with a two column configuration. Hydrocarbons and carbon dioxide were separated in the first column (*HP Plot Q*). The second column (*HP*

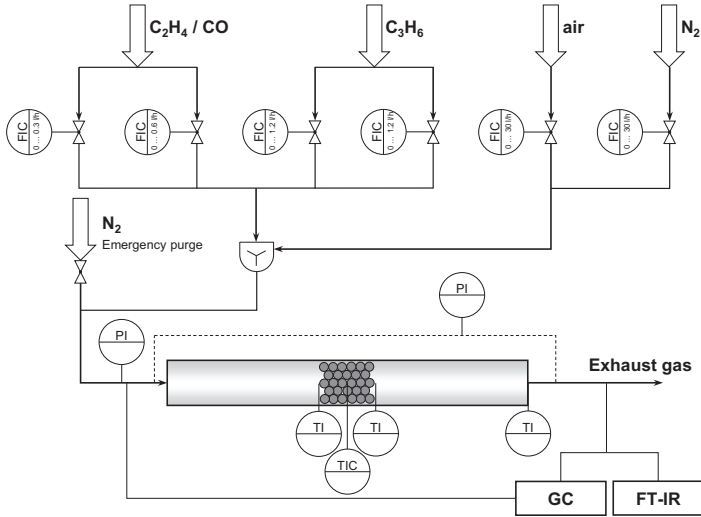


**Figure 5.3:** Process flow chart of the used kinetic experimental test facility including the gas supply, the furnace with an integrated quartz glass tubular reactor and the gas composition online analytic

*Molsieve*) separates the permanent gases and carbon monoxide. The detection occurred using a thermal conductivity detector (Klose et al., 2004; Hamel et al., 2008; Hamel et al., 2011).

The kinetic experiments were performed at a total volumetric flux (215 ml/min, STP 25°C) corresponding to a catalyst weight to volumetric flux ratio  $W/F$  of  $50 \text{ kg} \cdot \text{s} \cdot \text{m}^{-3}$ . The pressure drop of all kinetic experiments over the reactor length was less than 0.02 MPa and used as boundary conditions in the *Ergun*-equation (eq. 2.44) in the kinetic modeling. The kinetic experiments were done as function of the temperature ( $T = 300\text{--}650 \text{ }^\circ\text{C}$ ) and of the concentration of ethylene ( $x_{\text{C}_2\text{H}_4} = 0\text{--}1 \%$ ), propylene ( $x_{\text{C}_3\text{H}_6} = 0\text{--}1 \%$ ), carbon monoxide ( $x_{\text{CO}} = 0\text{--}1 \%$ ) and oxygen ( $x_{\text{O}_2} = 0\text{--}20.9 \%$ ). Each set of inlet concentration conditions and reaction temperatures was held for at least 0.5 h to obtain two gas samples at steady state conditions. Thus, the observed experimental data correspond to average values of at least two independent measurements.

To evaluate the experimental data, the carbon balance was analyzed for each data point. The error was  $\pm 5 \%$  and therefore within the accuracy of the used analytic GC measurement. Thus, additional side reactions or components cannot be observed. Furthermore, the catalyst activity regarding the oxidation reactions was found as constant in regularly time intervals.

The experimental program performed for the three above introduced different sub-networks and the complex total reaction network consist of

- a) **Sub-network I:** 360 steady state conditions at 20 different temperatures, 4 different inlet carbon monoxide concentrations and 7 different inlet oxygen concentrations.

- b) **Sub-network II:** 360 steady state conditions at 20 different temperatures, 4 different inlet ethylene concentrations and 7 different inlet oxygen concentrations.
- c) **Sub-network III:** 160 steady state conditions at 20 different temperatures, 4 different inlet propylene concentrations and 7 different inlet oxygen concentrations.
- d) **Total network:** 120 steady state conditions at 5 different ethylene to propylene mixture ratios at one inlet oxygen concentration.

#### 5.4 Preliminary determination of gas/solid adsorption equilibria

As aforementioned, in heterogeneous catalysis interphase transport phenomena of reactants and products which have to be considered in kinetic modeling will be measured separately in the following section. There, single component and competitive adsorption phase equilibria from reactants and products between the fluid reactant and solid catalyst phase will be studied in detail and further applied in the mechanistic kinetics.

This procedure was already successfully applied for the homogeneously and heterogeneously catalyzed acetic acid esterification by several authors (Pöpken et al., 2000; Yu et al., 2004; Schmitt and Hasse, 2006). There independent adsorption measurements of reactants and products were performed and subsequently integrated in the reaction kinetics. Adsorption equilibria of different hydrocarbons at zeolite supported catalysts were studied by several authors (Denayer and Baron, 1997; Denayer et al., 2003; Corma and Ortega, 2005; Al-Sabawi and Lasa, 2009). The aim of these authors was to identify the reactant concentrations at a broad range of temperatures at the catalyst surface and therefore the reactivity of the hydrocarbons and to determine adsorption isotherms. Analyzing these examples the kinetic parameter estimation was simplified and the physical meaning of model parameters was conserved by separation kinetic and thermodynamic effects (Pöpken et al., 2000; Kiedorf et al., 2016a, 2016b).

However, the performance of reactant adsorption measurements at highly active catalyst species turned out to be difficult. Unexpected cracking reactions at the desired temperature can occur. In order to eliminate these unexpected chemical reactions adsorption measurements were often realized at room temperature (Thamm et al., 1983; Murzin et al., 1997; Al-Sabawi and Lasa, 2009). Thus, the independent estimated adsorption parameters have to be extrapolated for the reaction kinetic analysis. Moreover, a catalyst species transformation based on the different temperatures can occur. Hence, the adsorption measurements cannot reflect the adsorption behavior at reaction conditions (Al-Sabawi and Lasa, 2009).

The aim of this section is to identify single gas and competitive adsorption isotherms of the present components of the ethylene and propylene total oxidation reaction network (fig. 5.2). Single component adsorption parameters will be estimated as function of temperature and gas phase concentration. Based on these data competitive isotherms will be predicted by using the *Multi-Langmuir* equation and the Ideal Adsorbed Solution (IAS) theory. Finally, some selected mixture adsorption isotherms of ethylene and propylene will be evaluated by experimental measurements.

### 5.4.1 Determination of single component adsorption isotherms

Many different procedures are existing to determine adsorption isotherms from experimental data. In literature it is distinguished between static and dynamic methods (Seidel-Morgenstern, 2004; Schmidt-Traub et al., 2012). Dynamic techniques are faster and more exact so it became most popular (Lisec et al., 2001; Seidel-Morgenstern, 2004; Andrzejewska et al., 2009). The most established one is the Frontal Analysis (FA) because of high accuracy. But also the elution and Frontal Analysis by characteristic points and the pulse method are used especially in liquid chromatography to determine adsorption isotherms (Duong, 1998; Seidel-Morgenstern, 2004; Andrzejewska et al., 2009).

Dynamic methods are based on the system response analysis of an inlet concentration step function of one component. A typical breakthrough curve and the theoretical scheme for the FA are shown in fig. 5.4a. Using this method, a known quantity of the analyzed component is admitted to a tube packed with the adsorption media, here the catalyst particles. The shaded area (fig. 5.4a) corresponds to the load capacity of the measured component for the corresponding partial pressure at a certain temperature and can be explained by an integral mass balance equation (eq. 5.4). To obtain the complete isotherm in a broad concentration range, several breakthrough curves have to be analyzed. Therefore, a "staircase" FA is suitable (fig. 5.4b) (Seidel-Morgenstern, 2004).

$$q_{j_{\text{step}}}(\rho_{j_{\text{step}}}^F) = q_{j_{\text{step}}}(\rho_{j_{\text{step}}}^I) + \frac{(t_R - t_0) \cdot (\rho_{j_{\text{step}}}^F - \rho_{j_{\text{step}}}^I)}{\bar{R} \cdot T \cdot F \cdot t_0} \quad \text{with} \quad F = \frac{1 - \varepsilon}{\varepsilon} \quad (5.4)$$

The loading of a step  $q_{j_{\text{step}}}(\rho^F)$  (fig. 5.4a) is the amount adsorbed at the equilibrium as a function of the partial pressure  $\rho^F$  of the measured component at the inlet position, temperature  $T$  and the void fraction  $\varepsilon$  of the catalyst bed. Furthermore,  $t_0$  corresponds to the hold-up time of the experimental plant and  $t_R$  to the retention time of the breakthrough curve. The calculation of the retention time can be done by different methods. Guiochon et al. recapitulated the application of the inflection point of the curve or the half-height of the whole step as retention time (Gritti and Guiochon, 2003; Andrzejewska et al., 2009). In this work, the first statistical mathematical moment was used to calculate the center (point of gravity) of the breakthrough curve (Baerns, 2006). The key assumption for this

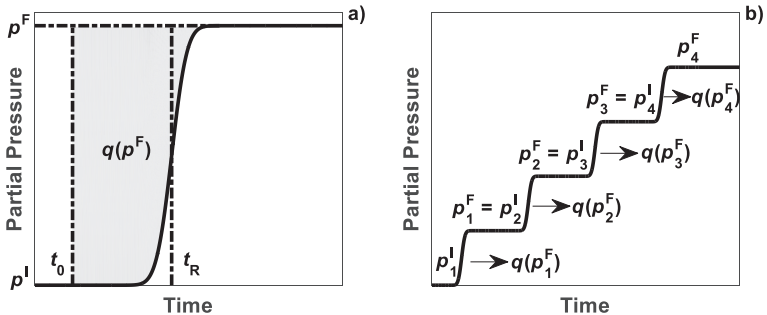


**Figure 5.4:** (a) Typical trend of breakthrough curves for the adsorption of one component in frontal analysis between the initial and feed pressure,  $p^I$  and  $p^F$  and (b) breakthrough curves of FA by increasing the inlet partial pressure

kind of formulation of the mass balance (eq. 5.4) in FA is that the amount of the adsorbed component has to be in a lower range. Thus, a diluted system is considered. In high concentrated systems, the change in the volumetric flux has to be taken into account. The partial pressure will be increased intermittently so that the system response of each step can be analyzed separately (James and Phillips, 1954; Seidel-Morgenstern and Guiochon, 1993; Lisec et al., 2001; Andrzejewska et al., 2009). In this work, only diluted systems will be analyzed ( $x_{jc} \leq 4\%$ ). Accordingly, changes of the volumetric flux can be neglected.

To describe the relationship between coverage of a particular gas and its partial pressure the *Henry's law* and the *Langmuir* adsorption models are commonly used. The corresponding expressions are shown in eqs. 5.5 and 5.6, respectively.

$$\begin{array}{ll} \textbf{Henry-model} & \textbf{Langmuir-model} \\ q_{H,jc}(p_{jc}) = H_{jc}(T) \cdot p_{jc} & q_{L,jc}(p_{jc}) = q_{jc}^{\text{sat}}(T) \frac{K_{jc}(T) \cdot p_{jc}}{1 + K_{jc}(T) \cdot p_{jc}} \end{array} \quad (5.5) \quad (5.6)$$

Where  $H_{jc}$  is the *Henry* constant,  $K_{jc}(T)$  the temperature dependent adsorption constant and  $q_{jc}^{\text{sat}}$  the monolayer saturation capacity of the *Langmuir* isotherm. The linear *Henry* model is limited to diluted concentrations of the adsorbed species in the bulk phase. If the constraints are not available non-linear models (e.g. *Langmuir*) should be used. This concept assumes identical binding energies of all adsorbed components at all surface sites (Duong, 1998; Schmidt-Traub et al., 2012). Added no interactions between the adsorbed components are accepted. However, the surface of a catalyst particle offers an energetically heterogeneity based on the catalytic active species and the supporting material. For considering such heterogeneity adsorption surfaces, binary adsorption isotherm models exist (eqs. 5.7 and 5.8) (Nicoud and Seidel-Morgenstern, 1996). In these cases, the total amount of the load capacity yields from sum of each term (Duong, 1998; Chorkendorff and Niemantsverdriet, 2003; Yu et al., 2004; Murzin and Salmi, 2005; Andrzejewska et al., 2009).

$$\textbf{Bi-Langmuir-model} \\ q_{bi-L,jc}(p_{jc}) = q_{1,jc}^{\text{sat}}(T) \frac{K_{1,jc}(T) \cdot p_{jc}}{1 + K_{1,jc}(T) \cdot p_{jc}} + q_{2,jc}^{\text{sat}}(T) \frac{K_{2,jc}(T) \cdot p_{jc}}{1 + K_{2,jc}(T) \cdot p_{jc}} \quad (5.7)$$

$$\textbf{Henry-Langmuir-model} \\ q_{H-L,jc}(p_{jc}) = H_{jc}(T) \cdot p_{jc} + q_{jc}^{\text{sat}}(T) \frac{K_{jc}(T) \cdot p_{jc}}{1 + K_{jc}(T) \cdot p_{jc}} \quad (5.8)$$

To describe a broad range of the adsorption behavior in temperature, basis for the kinetic experiments, an *Arrhenius* approach (eq. 5.9) with the adsorption energy  $\Delta h_{\text{ads},jc}$  for the different parameters can be used (Duong, 1998).

$$K_{jc} = K_{jc,\infty} \cdot \exp\left(\frac{\Delta h_{\text{ads},jc}}{RT}\right) \quad (5.9)$$

The effect of the temperature of the *Henry*- (eq. 5.5) and *Langmuir* (eq. 5.6) models and the combination of both (eq. 5.8) are shown schematically in fig. 5.5a-c.

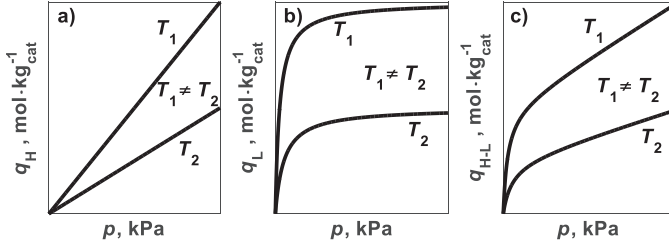


**Figure 5.5:** (a) Henry adsorption isotherms for two different temperatures (eq. 5.5), (b) Langmuir adsorption isotherms for two different temperatures (eq. 5.6) and (c) Bi-adsorption isotherm model with a Henry- and a Langmuir term (eq. 5.8)

### 5.4.2 Determination of mixture adsorption isotherms

In real reaction networks and also for the considered one (see fig. 5.2), more than one component is present. Thus, mixture adsorption isotherms are necessary to determine more exactly adsorption parameters. The default routine to estimate multi-component adsorption equilibria is to predict them from single component adsorption isotherms. For this purpose, several theories had been published (Suwanayuen and Danner, 1980; Duong, 1998). One general approach is the *Multi-Langmuir* equation (eq. 5.10) which is only thermodynamically consistent with identical saturation load capacities of each component. The saturation capacity and the adsorption constants of the components will be derived from single component data (Čermáková et al., 2008).

$$q_{j_c} = q_{j_c}^{\text{sat}} \frac{K_{j_c} p_{j_c}}{1 + \sum_{j_c=1}^{N_c} K_{j_c} p_{j_c}} \quad (5.10)$$

The most famous method to describe mixture adsorption isotherms using single component isotherm data is the IAS theory (Landa et al., 2013; Santori et al., 2014). Originally developed by (Myers and Prausnitz, 1965) several modifications also for computing are existing (Radke and Prausnitz, 1972; Duong, 1998; Landa et al., 2013).

This theory is based on the equilibrium of the ideal gas and the adsorbed phase. Related to this, the adsorbed phase is considered as an ideal solution and follows *Raoult's* law. The set-up of the following algebraic equations have to be solved simultaneously (Radke and Prausnitz, 1972; Seidel-Morgenstern and Guiochon, 1993; Worch, 2012).

$$\sum_{j_c=1}^{N_c} \frac{p_{j_c}}{p_{j_c}^*(p_{j_c}, T)} = 1 \quad (5.11)$$

$$\pi_{\text{mix}} = \frac{\bar{R} \cdot T}{A} \int_{p_0}^{p_{j_c}^*} \frac{q_{j_c}(p_{j_c}^*)}{p_{j_c}^*} dp_{j_c}^* \quad (5.12)$$

$$q_{j_c}^{\text{tot}} = \sum_{j_c=1}^{N_c} q_{j_c} = \left[ \sum_{j_c=1}^{N_c} \frac{p_{j_c}}{p_{j_c}^* \cdot q_{j_c}^*(p_{j_c}^*)} \right]^{-1} \quad (5.13)$$

$$q_{j_c} = q_{j_c}^{\text{tot}} \cdot \frac{p_{j_c}}{p_{j_c}^* (\pi_{\text{mix}}, T)} \quad j_c = 1, \dots, N_c \quad (5.14)$$

The fictitious partial pressure  $p_{j_c}^*$  represents the amount of the pure component  $j_c$  which possess the spreading pressure of the mixture  $\pi_{\text{mix}}$ . This value has to be calculated by the implicit eqs. 5.12 and 5.13 and needs numerical methods. Subsequent the load capacity of component  $j_c$  in the mixture follows eq. 5.14 using the total load capacity  $q_{j_c}^{\text{tot}}$ .

If the saturation capacities of the mixture components are equal, the IAS theory is thermodynamically consistent. Thus, also for markedly different saturation capacities a solution for the IAS theory can be reached (Seidel-Morgenstern and Guiochon, 1993).

### 5.4.3 Experimental equipment and methods for adsorption isotherms

In order to estimate the adsorption equilibria, the test facility in combination with the online fast FT-IR analytic which was already introduced in section 5.3 (fig. 5.3) was used. The accurate volumetric fluxes of the measured components (ethylene (*Air Liquide* 3.0), propylene (*Westfalen* 2.5), carbon dioxide (*Westfalen* 2.0), carbon monoxide (*Linde* 2.0) and oxygen (compressed air) and the dilute gas nitrogen (*Air Liquide* 5.0) were set by mass flow controllers (*Bronkhorst*) as described in section 5.3.

The tubular reactor (stainless steel) with a length of 0.4 m and the inner diameter of 0.008 m was filled with 0.0134 kg of the  $\text{CrO}_x/\gamma\text{-Al}_2\text{O}_3$  catalyst particles. The reactor tube was embedded in a furnace (*HTM Reetz*). Thus, the temperature can be set between 25 – 1000 °C. The control of the temperature occurred by a thermocouple which was placed in the center of the catalyst bed. A flow through FT-IR from *Gasmet* (cell length 5.0 m) realized the analysis of the composition of the gas mixture. The calibration of the analytic was carried out with different gases and in different concentrations consisting of the measured component and diluted in nitrogen, which was mixed by the mass flow controllers. Thus, for each component several reference spectra were received for the completely measured range.

In order to obtain water adsorption measurements an additional vaporizer is required. Because of missing suitable equipment, the corresponding adsorption parameters of water will be estimated at kinetic measurements.

The hold-up time  $t_0$  of the measured component of the reaction plant was carried out exemplary for all components with carbon dioxide. For these measurements, the catalyst particles were replaced by an inert material  $\alpha\text{-Al}_2\text{O}_3$  ( $d_p = 0.001$  m) at a constant particle volume. These particles offered a surface area, which was below the detection limit of the equipment used. Therefore, the predicted adsorption of the gas components can be neglected.

The total volumetric flux of the adsorption experiment was  $0.03 \text{ m}^3 \cdot \text{h}^{-1}$ . At first only nitrogen was pressurized at the reactor. If the nitrogen volumetric flux was constant, the reactor was heated up at the desired temperature. The experiment started, if the measured component was added at the entrance of the reactor. Therefore, the mass flow of the component was increased to the desired amount. Simultaneously, the flux of nitrogen was decreased. Thus, the total volumetric flux was set constant. The start-up behavior of the

mass flow controller achieved 90 % of the set value after one second. Hence, a comparable pressure application for all steps in the FA and all components were obtained. The next step was set manually if the previous concentration was reached at the outlet of the reactor (steady state) (fig. 5.4b).

A controlled desorption/regeneration of the “catalyst bed” occurred in two steps. First, the reactor was heated up at least over 500 °C. At this temperature, the reactor was pressurized with air. Consequently, the adsorbed components were total oxidized. After regeneration with oxygen, the catalyst was controlled desorbed with nitrogen for at least 12 h. After this time, the concentration of the measured component was below the detection limit of the used FT-IR analytic. Thus, reproducible conditions for each experiment were adjusted.

#### 5.4.4 Single component adsorption measurements

##### Selection of adsorption model

A schematic multi-step breakthrough curve of the FA was already given in fig. 5.4b. As a result of the experimental observed breakthrough curve of carbon dioxide, the load capacity is illustrated as a function of the partial pressure ( $p_{\text{CO}_2} = 1\text{--}4$  kPa) in fig. 5.6a. The first step resulted in the highest retention time and in this regard in the highest increase of the load capacity. The further steps were very similar related to the retention time and resulted in a further continuous increase in  $q_{\text{CO}_2}$  ( $p_{\text{CO}_2} = 0.1\text{--}2.5$  kPa). This trend suggests a non-linear isotherm (Seidel-Morgenstern, 2004). The corresponding experimental adsorption isotherm shape is given in fig. 5.6a and b. To analyze the kind of the adsorption isotherm, different models were parameterized and compared to the experimental data. At first in fig. 5.6a, the typical *Henry* (eq. 5.16) and *Langmuir* (eq. 5.17) adsorption models were estimated, respectively. However, the experimental data cannot be described sufficiently by assuming one adsorption site only. The *Henry* isotherm model (fig. 5.6a) offers huge deviations especially at low carbon dioxide partial pressures. Applying the *Langmuir* model (fig. 5.6b) the experimental data reflection was improved. Nevertheless, the lower concentration range is still missing in the model description. A further improvement can be achieved by a *Bi-Langmuir* model (eq. 5.7 and fig. 5.6b). Thus, the total experimental concentration range is described well. However, the application of this model complicated the parameter estimation, because of linear dependencies between the parameters. In order to avoid these complications, the model can be obviously simplified from *Bi-Langmuir* to a *Henry–Langmuir* model (eq. 5.8 and fig. 5.6b) (Nicoud and Seidel-Morgenstern, 1996). Using this model reduction, no loss in accurateness was achieved. Moreover, the confidence intervals of the estimated parameters were decreased. Based on these results, all obtained single component adsorption isotherm data will be described by a *Henry–Langmuir* model (eq. 5.8). The comparison of experimental and modeled adsorption isotherms for the other components will be presented in the appendix C.

Two different adsorption sites are required to characterize the adsorption behavior. As aforementioned in section 5.1 two chromium oxide species were observed and further species are possible (Sattler et al., 2014). Additionally, the support material  $\gamma\text{-Al}_2\text{O}_3$  offered an adsorption capacity as well. A classification of these adsorption sites to the correspond-

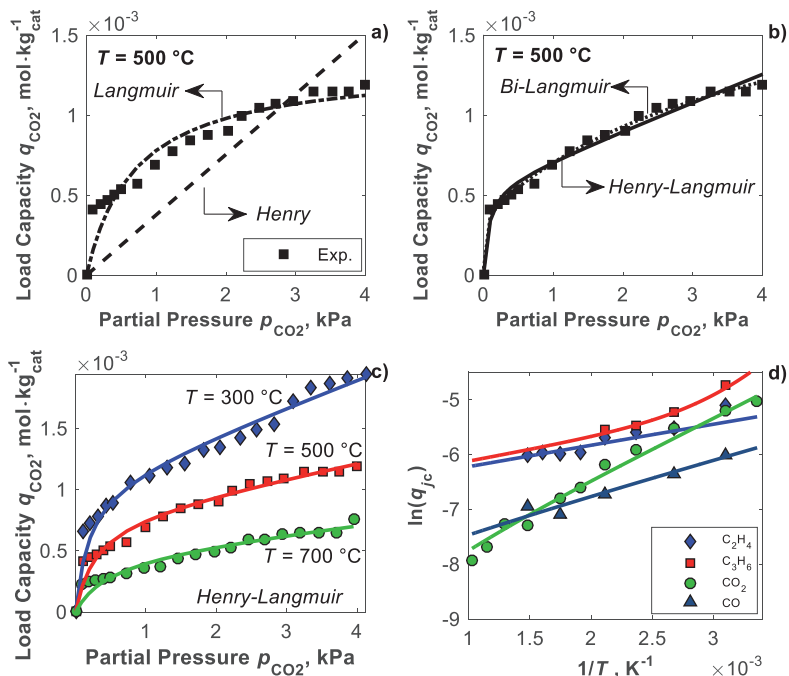


**Figure 5.6:** (a-b) Experimental measured adsorption isotherm of CO<sub>2</sub> (symbols) at 500 °C in comparison of different modeled adsorption isotherms (H model (eq. 5.5), L model (eq. 5.6), BI-L model (dotted line, eq. 5.7), H–L model (solid line, eq. 5.8)); (c) experimental determined CO<sub>2</sub> load capacities for three different temperatures (symbols) in comparison with the simulated *Henry–Langmuir* adsorption isotherm (line) (300°C blue, 500°C red, 700°C green) and (d) Logarithmized total load capacity of all measured components versus the inverse temperature at a constant partial pressure ( $p_{jc} = 1$  kPa)

ing model requires an individual adsorption measurement of each component at several catalyst species. Based on the surface ratio of each species the load capacity amount of the gas phase component can be calculated. Accordingly, the identification of the corresponding adsorption site to the isotherm model is complicated and not part of this work.

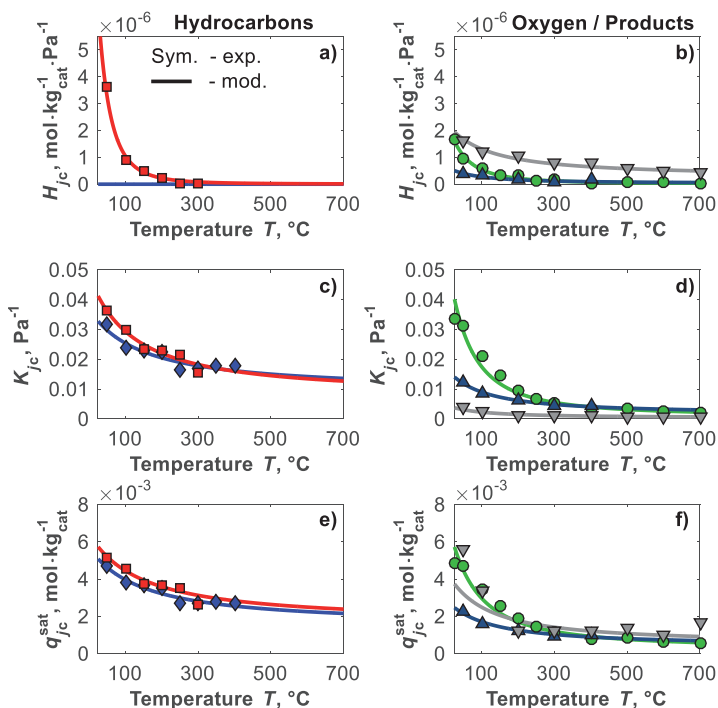
**Temperature dependence**

Figure 5.6c illustrates the experimental load capacity data (symbols) of carbon dioxide at three different temperatures ( $T = 300/500/700$  °C). A temperature increase led to a decrease of the total load capacity  $q_{CO_2}$ . Consequently, at each temperature the adsorption isotherm parameters were estimated separately.

In fig. 5.6d are illustrated the logarithmized experimental and modeled (eq. 5.8 with single gas component parameter from table 5.1) single gas load capacities  $q_{jc}$  of all measured components versus the inverse temperature at a constant partial pressure ( $p_{jc} = 1$  kPa). This plot reveals the overall load capacity of all components in comparison to each

other. It can be observed, that at low temperatures propylene offers the highest values with respect to the *Henry* and *Langmuir* adsorption. The further order is carbon dioxide, ethylene, oxygen and carbon monoxide. With increasing temperature, the load capacity of all components at the catalyst particles decreases. The strongest effect possesses carbon dioxide. Thus, carbon dioxide provides the highest heat of adsorption followed by propylene, oxygen, carbon monoxide and ethylene. Based on the different heat of adsorptions the order of the components changes at possible reaction temperatures. If the load capacities are extrapolated to 500 °C, the new order follows ethylene, propylene, oxygen, carbon monoxide and carbon dioxide. The several gradients multiplied with the universal gas constant can be seen in table 5.1.

**Adsorption isotherm model parameters** The adsorption parameters obtained from the estimations at each temperature are plotted as a function of temperature in fig. 5.7a-f. As aforementioned with increasing temperature the load capacity of CO<sub>2</sub> decreased. Accordingly, the adsorption parameters decrease (fig. 5.7b, d and f). Similar char-



**Figure 5.7:** Temperature depends of the estimated parameter of the different adsorption isotherms: (a-b) *Henry* constant of the linear term; (c-d) adsorption constant of the *Langmuir* term and (e-f) saturation of the load capacity of *Langmuir* term; symbols corresponds to the estimated parameter of the single adsorption isotherms, lines are modeled data of the *Arrhenius* approach (eq. 5.9); ethylene (◆); propylene (■); carbon dioxide (●); carbon monoxide (▲) and oxygen (▼)

**Table 5.1:** Summary of single component adsorption parameters of the *Henry–Langmuir* models (eq. 5.8)

Parameters	Frequency factor	Unit	95 % CI	Sorption enthalpy, $\text{kJ}\cdot\text{mol}^{-1}$	95 % CI	$\Delta\bar{h}_{\text{ads}}$ $\text{kJ}\cdot\text{mol}^{-1}$
$H_{\text{C}_2\text{H}_4}$	0	$\text{mol}\cdot\text{kg}_{\text{cat}}^{-1}\cdot\text{Pa}^{-1}$	$\pm$ inf %	0	$\pm$ inf %	
$K_{\text{C}_2\text{H}_4}$	$9.201\cdot 10^{-3}$	$\text{Pa}^{-1}$	$\pm$ 11 %	3.148	$\pm$ 16 %	3.223
$q_{\text{C}_2\text{H}_4}^{\text{sat}}$	$1.477\cdot 10^{-3}$	$\text{mol}\cdot\text{kg}_{\text{cat}}^{-1}$	$\pm$ 7 %	3.063	$\pm$ 11 %	
$H_{\text{C}_3\text{H}_6}$	$7.231\cdot 10^{-10}$	$\text{mol}\cdot\text{kg}_{\text{cat}}^{-1}\cdot\text{Pa}^{-1}$	$\pm$ 63 %	22.582	$\pm$ 22 %	
$K_{\text{C}_3\text{H}_6}$	$7.531\cdot 10^{-3}$	$\text{Pa}^{-1}$	$\pm$ 17 %	4.215	$\pm$ 16 %	6.843
$q_{\text{C}_3\text{H}_6}^{\text{sat}}$	$1.620\cdot 10^{-3}$	$\text{mol}\cdot\text{kg}_{\text{cat}}^{-1}$	$\pm$ 12 %	3.130	$\pm$ 16 %	
$H_{\text{CO}_2}$	$7.189\cdot 10^{-9}$	$\text{mol}\cdot\text{kg}_{\text{cat}}^{-1}\cdot\text{Pa}^{-1}$	$\pm$ 18 %	13.408	$\pm$ 7 %	
$K_{\text{CO}_2}$	$6.390\cdot 10^{-4}$	$\text{Pa}^{-1}$	$\pm$ 20 %	10.263	$\pm$ 10 %	10.392
$q_{\text{CO}_2}^{\text{sat}}$	$2.159\cdot 10^{-4}$	$\text{mol}\cdot\text{kg}_{\text{cat}}^{-1}$	$\pm$ 14 %	8.124	$\pm$ 8 %	
$H_{\text{CO}}$	$2.023\cdot 10^{-7}$	$\text{mol}\cdot\text{kg}_{\text{cat}}^{-1}\cdot\text{Pa}^{-1}$	$\pm$ 18 %	4.745	$\pm$ 16 %	
$K_{\text{CO}}$	$2.192\cdot 10^{-3}$	$\text{Pa}^{-1}$	$\pm$ 6 %	5.431	$\pm$ 5 %	5.719
$q_{\text{CO}}^{\text{sat}}$	$4.770\cdot 10^{-4}$	$\text{mol}\cdot\text{kg}_{\text{cat}}^{-1}$	$\pm$ 11 %	4.714	$\pm$ 10 %	
$H_{\text{O}_2}$	$2.700\cdot 10^{-7}$	$\text{mol}\cdot\text{kg}_{\text{cat}}^{-1}\cdot\text{Pa}^{-1}$	$\pm$ 8 %	4.895	$\pm$ 8 %	
$K_{\text{O}_2}$	$3.155\cdot 10^{-4}$	$\text{Pa}^{-1}$	$\pm$ 24 %	6.113	$\pm$ 17 %	5.823
$q_{\text{O}_2}^{\text{sat}}$	$4.926\cdot 10^{-4}$	$\text{mol}\cdot\text{kg}_{\text{cat}}^{-1}$	$\pm$ 41 %	5.023	$\pm$ 54 %	

acteristics can be also seen for the other components. Only the temperature dependency is differentially expressed.

It becomes apparent, that the temperature dependence of the *Henry* coefficient of propylene is obviously greater than from all other components (see fig. 5.7a and b). Thereby, it appears that at high temperatures the linear *Henry* term decreases rapidly until the influence disappears completely. For the second olefin ethylene, this parameter was estimated completely to zero. For the oxidation products carbon monoxide, carbon dioxide and the reactant oxygen the *Henry* coefficient possesses lower temperature dependence. The effect of the linear *Henry* term of the products disappears with increasing temperature as well. Only for oxygen, the linear part is still available at higher temperature conditions.

The temperature dependence on the adsorption constant  $K_{\text{f}_c}$  is shown in in fig. 5.7c and d. The highest temperature effect revealed carbon dioxide. Again, at potential reaction conditions the parameter decreases at the range of the second product carbon monoxide. The temperature dependence of the olefins is similar compared to each other. At low temperatures, the parameter of propylene exceeds ethylene. With increasing temperature, the parameter is passed by ethylene. However, the parameter dimensions are very similar. Furthermore, based on cracking reactions ( $T > 300 - 400$  °C) on the catalyst particles the experimental adsorption measurements of ethylene and propylene were extrapolated at the higher temperatures. In contrast oxygen offered nearly no effect with respect to the temperature. Furthermore, the adsorption constant of oxygen was very small in general compared to the other measured components.

The saturation capacity of the *Langmuir* approach of the alkenes (fig. 5.7e) on the

CrO<sub>x</sub>/γ-Al<sub>2</sub>O<sub>3</sub> catalyst possessed similar dimensions. In addition, the range of the products and the reactant oxygen (fig. 5.7f) was very similar compared to the olefins. For this reason, no displacement effects at the catalyst surface will be expected in mixture conditions. Therefore, the reactants (see reaction network fig. 5.2a) can be simultaneously adsorbed at the catalyst surface and can be reacted to completion.

All separately estimated parameters can be reflected by the *Arrhenius* approach (eq. 5.9) very well. The corresponding parameters with the associated 95 % confidence intervals are shown in table 5.1. The calculated errors are for the frequency factors maximal ± 63 % and for the sorption enthalpies ± 54 %. The large error in the frequency factors of the *Henry* parameters from ethylene and propylene result from there small values. It can be observed, that the influence of the *Henry* term completely disappeared at higher temperatures. Thus, at reaction conditions the assumption of *Langmuir* adsorption of all reactants and products will be promising.

**Simplified adsorption isotherm model** As aforementioned, the application of more realistic but sophisticated phase equilibrium models for single and competitive adsorption behavior are computational intensive. Using the IAS theory an implicit expression of the adsorption phase equilibria is obtained (eqs. 5.11-5.14), which have to be solved by numeric optimization methods (section 2.2.2). Based on this reason, simplified adsorption models are attractive in kinetic modeling. Due to complexity, simple explicit *Langmuir* expressions for single component adsorption behavior can be used. In fig. 5.6 the adsorption isotherm of carbon dioxide was already analyzed using both the *Langmuir* and the more complex *Henry-Langmuir* adsorption model. Applying the *Langmuir* model, only the lower concentration range was missing in the model description. Moreover, the additional *Henry*-term, which compensates this deviation, disappeared for the measured hydrocarbons at the oxidation reaction temperatures (see also fig. 5.2b). Accordingly, the model deviation remains small by using the simple *Langmuir* model. Therefore, all single component adsorption data will be described by this simple adsorption isotherm model (eq. 5.6) as well.

**Table 5.2:** Summary of single component adsorption parameters of the *Langmuir* model (eq. 5.6)

Parameters	Frequency factor	Unit	95 % CI	Sorption enthalpy, kJ·mol <sup>-1</sup>	95 % CI
$K_{C_2H_4}$	$6.990 \cdot 10^{-1}$	Pa <sup>-1</sup>	± 41 %	- 13.397	± 15 %
$q_{C_2H_4}^{sat}$	$4.472 \cdot 10^{-4}$	mol·kg <sub>cat</sub> <sup>-1</sup>	± 29 %	7.688	± 15 %
$K_{C_3H_6}$	$2.371 \cdot 10^{-1}$	Pa <sup>-1</sup>	± 66 %	- 7.103	± 61 %
$q_{C_3H_6}^{sat}$	$4.472 \cdot 10^{-4}$	mol·kg <sub>cat</sub> <sup>-1</sup>	± 29 %	7.688	± 15 %
$K_{CO_2}$	$1.355 \cdot 10^{-3}$	Pa <sup>-1</sup>	± 11 %	4.182	± 14 %
$q_{CO_2}^{sat}$	$1.934 \cdot 10^{-4}$	mol·kg <sub>cat</sub> <sup>-1</sup>	± 14 %	9.935	± 7 %
$K_{CO}$	$7.868 \cdot 10^{-4}$	Pa <sup>-1</sup>	± 29 %	4.665	± 35 %
$q_{CO}^{sat}$	$8.657 \cdot 10^{-4}$	mol·kg <sub>cat</sub> <sup>-1</sup>	± 14 %	3.517	± 18 %
$K_{O_2}$	$1.416 \cdot 10^{-5}$	Pa <sup>-1</sup>	± 17 %	3.440	± 27 %
$q_{O_2}^{sat}$	$2.520 \cdot 10^{-2}$	mol·kg <sub>cat</sub> <sup>-1</sup>	± 8 %	2.572	± 16 %

The comparison of experimental and modeled adsorption isotherms for each component will be presented in the appendix C. The corresponding estimated parameters are shown in table 5.2 including the associated 95 % confidence intervals.

### 5.4.5 Prediction and validation of mixture adsorption isotherms

Based on the postulated total oxidation reaction network of ethylene and propylene (fig. 5.2), a complex gas mixture consists of reactants and products. Therefore, competitive adsorption isotherm data are required. As discussed above the prediction occurs via IAS theory (eqs. 5.11–5.14) using the estimated single component parameters of the *Henry-Langmuir* model (eq. 5.8 and tab. 5.1) and via the simple *Multi-Langmuir* model (eq. 5.10) applying the estimated parameters from the *Langmuir* model (eq. 5.6 and tab. 5.2). As model competitive adsorption system, the feed mixture (ethylene/propylene) is taken into account to investigate the prediction of the adsorption behavior. Based on the identical saturation load capacity (tab. 5.2) also the *Multi-Langmuir* model is thermodynamically consistent. Would be extend the gas composition with the products the thermodynamically consistent is not be ensured.

Figure 5.8 illustrates predicted competitive adsorption isotherms of (a) ethylene in the presence of propylene and (b) reversed, respectively. Starting with the modeled single component isotherms the experimental data can be described via the *Henry-Langmuir* model (eq. 5.8) very well. Especially the propylene isotherm offered an agreement at all. Merely the first sharp increase of the ethylene isotherm possessed small deviations. The *Langmuir* model (eq. 5.6) offered higher deviations, especially with increasing of the partial pressures. Based on identical load capacities estimated for ethylene and propylene via the *Langmuir* model, the saturation of the load capacity of propylene was underestimated using the *Multi-Langmuir* model.

With addition of the competitive component, the predicted isotherms of both models for the components were nearly similar. The calculations revealed that with a first increase

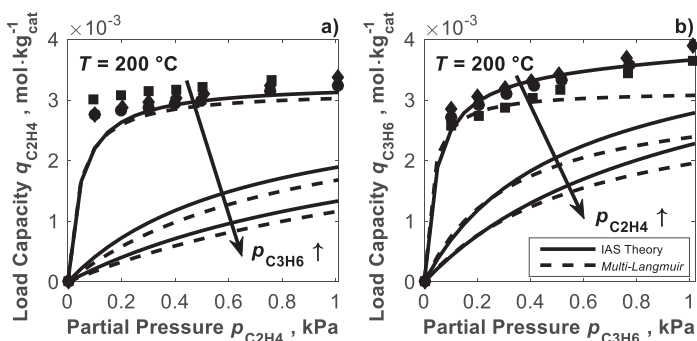


**Figure 5.8:** Predicted competitive adsorption isotherms via IAS theory (solid lines) and via *Multi-Langmuir* (dashed lines) in comparison to measured load capacities (symbols) at  $T = 200\text{ °C}$  for (a) ethylene at different partial pressures of propylene ( $\blacklozenge / \blacksquare / \bullet$   $p_{\text{C}_3\text{H}_6} = 0 / 0.5 / 1.0\text{ kPa}$ ) and (b) propylene at different partial pressures of ethylene ( $\blacklozenge / \blacksquare / \bullet$   $p_{\text{C}_2\text{H}_4} = 0 / 0.5 / 1.0\text{ kPa}$ )

in the partial pressure of the second component the load capacity decreased strongly. Mostly, the first sharp gradient was decreased. The influence in a further increase of the competitive component declined.

However, the predicted adsorption behavior of the IAS theory or *Multi-Langmuir* model cannot be validated by the experimental measurements. It seemed that for the concentration range with respect to component considered (diluted system  $\sum X_{jc} \leq 2\%$ ) no mixture effect for ethylene and propylene was obviously. Only slight deviations in the adsorption isotherms were pronounced. This was probably due to the fact of slightly deviations in the experimental equipment and procedure. A possible reason of the simulation fail is the space requirement of the molecules. The *Langmuir* model possesses the assumption of a monolayer at the sorbent. Because of the similar structure of ethylene and propylene the possibility exist of a multi-layer at the catalyst particles. In addition, another perpendicular orientation of the molecules at the sorbent is conceivable. Thus, the space requirement was decreased.

In fig. 5.9 the temperature effect of the load capacity is given in connection to the partial pressures of ethylene and propylene. It can be observed, that the temperature dependence of  $q_{C_{2H_4}}$  (see fig. 5.9a) at a constant partial pressure of ethylene and propylene for both models is marginal. Furthermore, it seems that the ethylene effect also with increasing temperature decreases. In contrast, the influence of the temperature on the load capacity of propylene (see fig. 5.9b) is in spite of the addition of ethylene for both models very pronounced. Additionally, the differences of the quantified models increase at higher temperatures. During the deviation between the IAS theory and the *Multi-Langmuir* model in the load capacity of ethylene is nearly constant. In contrast, the prediction of the higher load capacity of propylene switches below  $145\text{ }^\circ\text{C}$  for  $p_{C_{3H_6}} = 1\text{ kPa}$  and  $180\text{ }^\circ\text{C}$  for  $p_{C_{3H_6}} = 0.5\text{ kPa}$  from the IAS theory to the *Multi-Langmuir* model. Again, also for  $q_{C_{3H_6}}$  the influence of the partial pressure decreases with increasing temperature. However, the deviations between the predicted and experimental data, which was already suggested in fig. 5.8, are very high.

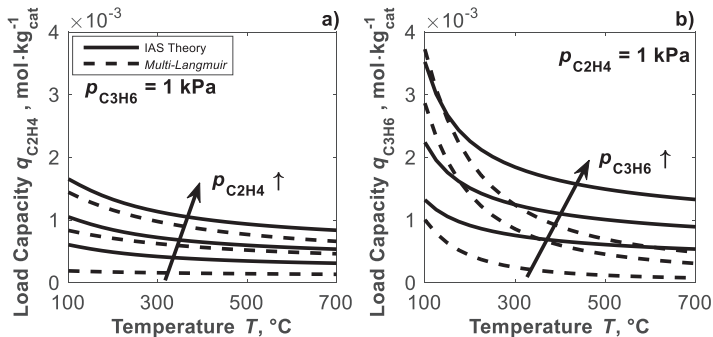


**Figure 5.9:** Predicted load capacities via IAS theory (solid lines) and via *Multi-Langmuir* (dashed lines) as a function of temperature and different partial pressures for (a)  $p_{C_{2H_4}} = 0.1 / 0.5 / 1.0\text{ kPa}$  and a constant partial pressure of propylene ( $p_{C_{3H_6}} = 1\text{ kPa}$ ) and (b)  $p_{C_{3H_6}} = 0.1 / 0.5 / 1.0\text{ kPa}$  and a constant partial pressure of ethylene ( $p_{C_{2H_4}} = 1\text{ kPa}$ )

However, with a further increase of the partial pressure of the competitive component ( $\sum X_{i,c} \geq 4\%$ ) the IAS theory and the *Multi-Langmuir* model works very well. In fig. 5.10 are shown the experimental and the predicted load capacities of ethylene at a constant partial pressure of propylene ( $p_{C_3H_6} = 4$  kPa) (fig. 5.10a) and propylene at a constant partial pressure of ethylene ( $p_{C_2H_4} = 4$  kPa) (fig. 5.10b) at a temperature of 200 °C. Only small deviations between the models and the experimental data can be observed. Especially the load capacity of ethylene is described at all partial pressures investigated experimentally. The prediction of the propylene load capacity offers a small gap mainly at low partial pressures. If the propylene concentration is increased, the IAS theory slightly overestimated the experimental data during the *Multi-Langmuir* model describes this part excellent. For higher temperatures model validation is more complicated due to the occurrence of cracking reactions.

Consequently, the IAS theory and the *Multi-Langmuir* model describe the competitive adsorption at higher partial pressures only, where such effects are pronounced experimentally. For kinetic modeling (section 5.5) of the total oxidation of hydrocarbon concentrations e.g. describing mixtures of VOC, the prediction of the competitive adsorption isotherm can be performed via the *Multi-Langmuir* model. Therefore, the estimated parameters of the single component adsorption data are sufficient.

However, a benefit-cost analysis related to the complex IAS theory should be done. As explicit shown the simple *Multi-Langmuir* model describes the experimental data at high concentrations sufficient as well. In the part where this theory failed also the IAS theory cannot predict the data.

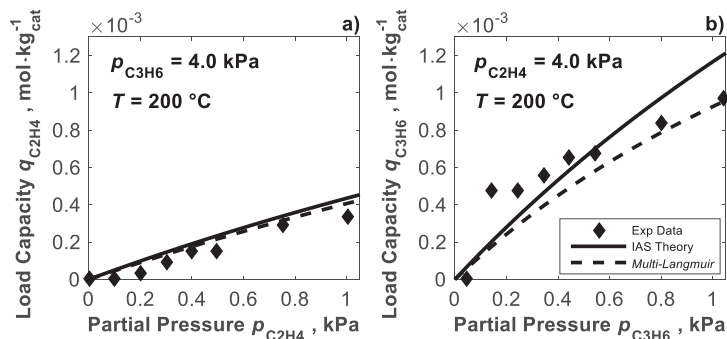


**Figure 5.10:** Predicted competitive adsorption isotherms via IAS theory (solid line) and via *Multi-Langmuir* (dashed line) versus measured load capacities (diamond) at  $T = 200$  °C for (a) ethylene at 4 kPa partial pressure of propylene and (b) propylene at 4 kPa partial pressure of ethylene

#### 5.4.6 Conclusions regarding additional adsorption investigation

In this section, the adsorption behavior of reactants and products (except water) of the total oxidation network of ethylene and propylene including the intermediate CO on a  $\text{CrO}_x/\gamma\text{-Al}_2\text{O}_3$  catalyst was studied. Therefore, single component adsorption isotherms in a

broad temperature range were investigated experimentally. For the mathematical description, different adsorption models were parameterized. The adsorption parameter estimation for all components was based on a bi-adsorption isotherm model consisting of a *Langmuir* and *Henry* term. The temperature dependence of the parameters was depicted by an *Arrhenius* approach. Thus, the experimental adsorption isotherms can be reflected within in the researched area very well. In addition, all single component data were used to parameterize a *Langmuir* adsorption model. This model possessed especially at low temperature small gaps. With increasing temperature, the linear effect of the *Henry* term decreased for propylene, carbon dioxide and carbon monoxide strongly. Thus, at potential reaction temperatures the *Langmuir* model described the adsorption behavior sufficient as well.

Afterwards, the competitive adsorption isotherms from ethylene and propylene were predicted via the IAS theory and the *Multi-Langmuir* model. It can be observed, that the effect of the shape of the isotherm based on the added component was preliminary strong and with a further increase of the partial pressure the influence decrease. Based on mean deviations between the investigated models the effort of the extensive IAS theory in the investigated concentration range (diluted system) was unnecessary. Only at the present of a more complex high concentrated mixture behavior the IAS theory was suitable.

Thus, for kinetic modeling of the total oxidation reaction network, the estimated adsorption parameters at the single component measurements can be applied. In assistance of the estimated adsorption parameter the kinetic parameters can be estimated independently without any correlations and consequently with low confidence intervals.

In general, this section illustrated the general need in more quantitative descriptions of multi-component adsorption equilibria in the frame of formulating reliable rate expressions in heterogeneous catalysis!

## 5.5 Kinetic investigation and network analysis

As aforementioned in section 5.1.2 the reaction network analysis is based on the network decomposition strategy as successful applied in the homogeneously catalyzed hydroformylation of 1-dodecene (section 3.5). First the smallest sub-network (CO oxidation) will be studied. Afterwards the reaction network complexity will be increased step by step. Therefore, all estimated parameters will be transferred in the next sub-network.

### 5.5.1 Carbon monoxide oxidation: sub-network I

For the reaction kinetics analysis of the total oxidation of carbon monoxide three different rate approaches (eqs. 5.1-5.3) were determined and quantified as discussed in section 5.2. To avoid parameter correlation and for improving the comparability of the rate approaches the adsorption constants of the ER and LH mechanism were already estimated independently from the occurring reaction in section 5.4 (Pöpken et al., 2000). As presented the competitive adsorption behavior can be described via *Multi-Langmuir* adsorption isotherms. Thus, the adsorption parameters from table 5.2 will be used without any modification in kinetic analysis. Based on the diluted system ( $x_{\text{CO}} \leq 1\%$ ) and the low exo-

thermal heat energy of the CO total oxidation ( $\Delta h_{R,5}(T = 500^\circ\text{C}) = -283 \text{ kJ}\cdot\text{mol}^{-1}$  (Yaws, 1999)) the kinetic experiments can be considered as isothermal.

To obtain a reliable kinetic equation the temperature dependence of the reaction rates was determined for four different carbon monoxide ( $x_{\text{CO}} = 0.25\text{--}1.00\%$ ) and five oxygen ( $x_{\text{O}_2} = 1.00\text{--}20.90\%$ ) inlet molar ratios. The temperature was varied between  $300\text{--}650^\circ\text{C}$ . The comparison of experimental and modeled data concerning the three approaches is given in fig. 5.11. Several measured reaction temperatures are illustrated at the molar inlet ratios of carbon monoxide and oxygen of  $1.0\%$  (shortage) and  $20.9\%$  (excess), respectively. The catalyst weight to total volumetric flux ratio was  $50 \text{ kg}_{\text{cat}}\cdot\text{s}\cdot\text{m}^{-3}$ . It is obvious that with increasing reaction temperature the conversion of carbon monoxide increased. The performance of the catalyst presented at  $300^\circ\text{C}$  a CO conversion close to zero. Above  $450^\circ\text{C}$  the conversion was clearly emerging. Complete conversion of CO was reached at  $625^\circ\text{C}$ .

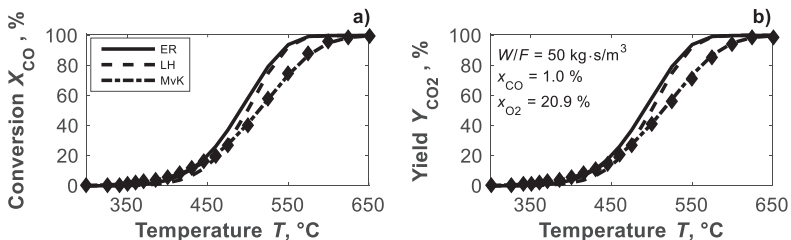


**Figure 5.11:** Experimental (symbols) and modeled (lines) steady state performance parameter (a) conversion of CO and (b) yield of  $\text{CO}_2$  of the CO oxidation (sub-network I) as a function of temperature and different reaction rate approaches

The adsorption-based reaction mechanisms overestimated the experimental conversion and carbon dioxide yield data. In contrast, the reduced MvK approach (eq. 2.14) reflected the data in an excellent way (fig. 5.11). In this connection, the estimated kinetic parameters are shown in table 5.3. The activation energies of the approaches differ strongly from  $97.5 \text{ kJ}\cdot\text{mol}^{-1}$  (MvK) up to  $169 \text{ kJ}\cdot\text{mol}^{-1}$  (LH). This is reflected in fig. 5.11, as well. The gradients of the adsorption-based rate approaches were too stiff. However, the difficulty was not the temperature dependency. Rather the dependency of the reaction rate on the reactant components cannot be described by the ER and LH model. In contrast, the activation energy of the suitable MvK approach was close to literature data. In (Liu and Flytzanistephanopoulos, 1995) an activation energy of  $91 \text{ kJ}\cdot\text{mol}^{-1}$  at a  $\text{CuO-Cr}_2\text{O}_3/\gamma\text{-Al}_2\text{O}_3$  catalyst for a semi-

**Table 5.3:** Estimated kinetic parameters of the total oxidation of CO and the corresponding 95 % confidence intervals (rate approaches from eqs. 5.1-5.3)

Approach	Frequency factor $k_{e,s}$	Unit	95 % CI	$E_{A,5}$ ( $\text{kJ}\cdot\text{mol}^{-1}$ )	95 % CI
ER ( $k_5$ )	$7.437\cdot 10^{+6}$	$\text{mol}\cdot(\text{kg}_{\text{cat}}\cdot\text{s}\cdot\text{Pa})^{-1}$	$\pm 3.749\cdot 10^{+6}$	159.161	$\pm 3.312$
LH ( $k_5$ )	$2.433\cdot 10^{+10}$	$\text{mol}\cdot(\text{kg}_{\text{cat}}\cdot\text{s})^{-1}$	$\pm 1.411\cdot 10^{+10}$	161.334	$\pm 3.816$
MvK ( $k_{\text{red},5}^+$ )	$1.579\cdot 10^{+1}$	$\text{mol}\cdot(\text{kg}_{\text{cat}}\cdot\text{s}\cdot\text{Pa})^{-1}$	$\pm 1.473$	97.141	$\pm 0.587$
MvK ( $k_{\text{ox},5}^+$ )	$7.350\cdot 10^{-5}$	$\text{mol}\cdot(\text{kg}_{\text{cat}}\cdot\text{s}\cdot\text{Pa})^{-1}$	$\pm 4.851\cdot 10^{-6}$	0	$\pm \text{inf}$

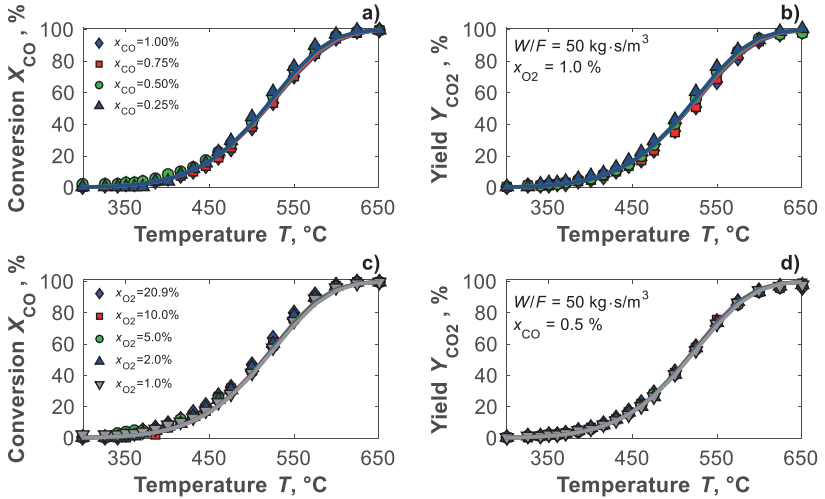


**Figure 5.12:** Experimental (symbols) and modeled (lines) steady state performance parameter (a and c) conversion of CO and (b and d) yield of  $\text{CO}_2$  of the CO oxidation (sub-network I) as a function of temperature and (a and b) different CO inlet concentrations and (c and d) different  $\text{O}_2$  inlet concentrations

empirical ER approach was presented. Thus, the carbon monoxide oxidation at a chromium based catalyst can be described by a MvK mechanism (Murzin and Salmi, 2005).

In order to illustrate the suitability of the MvK the comparison of the experimental performance parameters and the modeled data are shown in fig. 5.12 for a wide carbon monoxide and oxygen inlet concentration range. Fig. 5.12a-b and c-d reveal the individual effect of carbon monoxide and oxygen, respectively. During the temperature dependence of the performance parameter was obviously, the effect of the partial pressures was insignificant. This can be explained by oxygen excess conditions for all experimental data observed. In addition, during parameter estimation the activation energy of the oxidation step was estimated to be zero (see tab. 5.3). Accordingly, the re-oxidation step of the catalyst species of the MvK mechanism (fig. 2.4) seemed to be not rate determining.

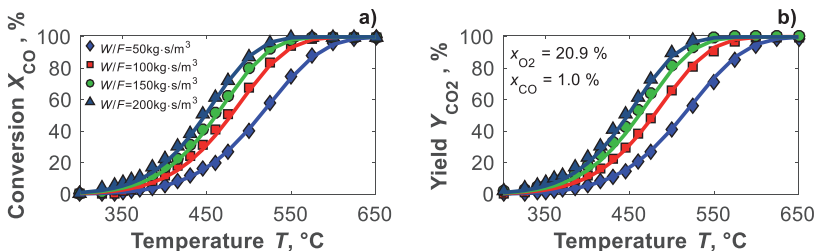


**Figure 5.13:** Experimental (symbols) and modeled (lines) steady state performance parameter (a) conversion of CO and (b) yield of  $\text{CO}_2$  of the CO oxidation (sub-network I) as a function of temperature and different residence times

In fig. 5.13 is shown the influence of the catalyst weight to total volumetric flux ratio. The description of this effect is not part of the kinetic rate equation but rather of the reactor model. This was already introduced in section 2.3.2. Accordingly, the experimental measured CO conversion and CO<sub>2</sub> yield with a  $W/F$  ratio of 100, 150 and 200 kg<sub>cat</sub>·s·m<sup>-3</sup> were predicted very well by the reactor model itself. If the  $W/F$  ratio increases, the total volumetric flux decreases and hence the residence time increases. Consequentially the CO conversion and CO<sub>2</sub> yield increases at further constant conditions.

In the next steps of the more complex reaction network (II and III) analyses the already estimated kinetic parameter of reaction 5 (see fig. 5.2 and tab. 5.3) will be fixed. Thus, finally all parts and the total network can be described by the quantified kinetic approaches.

### 5.5.2 Ethylene oxidation: sub-network II

In the second sub-network the total ( $r_1$ ) and partial ( $r_2$ ) oxidation of ethylene were quantified. The experimental observation of the ethylene oxidation presented for the selected inlet conditions ( $X_{C_2H_4} = 1\%$ ;  $X_{O_2} = 20.9\%$ ) show that the ethylene conversion (fig. 5.14a) increases from 300 °C from close to zero to 100 % at 550 °C. The resulting products were carbon monoxide and carbon dioxide. Further components were not observed by the GC equipment. The experimental carbon monoxide yield (fig. 5.14b) increased between 300 °C and 500 °C from zero to maximum 50 %. A further temperature increase supported the total oxidation of CO (see also sub-network I; section 5.5.1). Thus, the yield decreased to zero at 650 °C. The experimental yield of carbon dioxide (fig. 5.14c) increased continuously from zero to 100 % in the temperature range considered.

The kinetic parameter estimation procedure by network decomposition of ethylene and propylene oxidation in the sub-networks for the adsorption-based approaches was limited by the equilibrium adsorption constant of water. Due to unsuitable equipment, these individual adsorption measurements and the corresponding parameter estimation are missing in section 5.4. In literature (Sup Song et al., 2001; Auer and Thyron, 2002) the gaseous water adsorption at transition metal oxides was described as strongly pronounced. Accordingly, the inhibition effect by water adsorption on the active catalyst species in resting state was apparent for all reaction rates in an analogous manner. Based on this, the parameter estimation of the remaining sub-networks followed simultaneously on the experimental data.

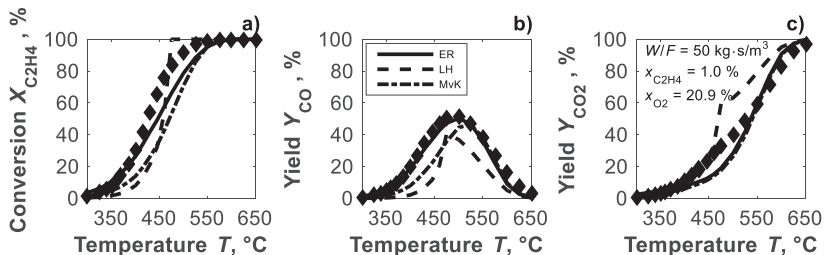


**Figure 5.14:** Experimental (symbols) and modeled (lines) steady state performance parameters (eqs. 2.16–2.18) of the C<sub>2</sub>H<sub>4</sub> oxidation (sub-network II) as a function of temperature and different reaction rate approaches, (a) conversion of C<sub>2</sub>H<sub>4</sub>, (b) yield of CO and (c) yield of CO<sub>2</sub>

In previous articles, several kinetic rate approaches were investigated to describe the total oxidation of short-chain olefins and alkanes. Starting with empirical (Yao, 1973; Haber and Turek, 2000; Sup Song et al., 2001) and semi-empirical rate laws (Sup Song et al., 2001; Auer and Thyron, 2002) up to ER (Liu and Flytzanistephanopoulos, 1995; Sup Song et al., 2001), LH (Heynderickx et al., 2010a; Benard et al., 2013) and MvK (Haber and Turek, 2000; Heynderickx et al., 2010b) approaches. Dependent on the active catalyst species and the reactant different approaches were suitable. In recently published articles spectroscopic techniques were used to identify active catalyst sites and analyze oxidation mechanisms reliable on a copper-cerium oxide catalyst (Menon et al., 2012; Zhang et al., 2012) and CrO<sub>x</sub> catalyst (Sattler et al., 2014).

In this work, the applied reaction rate models were the LH (eq. 5.1), the ER (eq. 5.2) and the MvK (eq. 5.3) mechanism as discussed before. The partial and total oxidation reactions of each reactant were described by the same mechanism. Based on parameter correlations for estimating the temperature dependence on the reaction and adsorption behavior of water, the adsorption equilibrium parameter was estimated independent from temperature. A similar effect of correlated parameters in temperature depends was observed for the isomerization of 1-dodecene (section 3.5.2). The re-oxidation step of the catalyst species by gaseous oxygen for a MvK mechanism is independent of the catalyst reduction step. Accordingly, the reaction cycle step constant  $k_{ox}^*$  of the CO oxidation can be transferred to the ethylene and propylene oxidation, respectively. The estimated kinetic parameters of the several reaction rate approaches of sub-network II are listed in table 5.4. A comparison of the modeled temperature dependence for the performance parameters of the different reaction rate approaches is shown in fig. 5.14. Additionally, the experimental measured data are presented.

The suitability of the derived rate approaches was evaluated differently. The trend of the performance parameters as a function of temperature was reflected by all models. Nevertheless, the activation energies of the LH approaches exceeded all other studied mechanisms (tab. 5.4). Thus, the corresponding ethylene conversion was under and over-estimated at low and high temperatures by LH, respectively. Additionally, the yields of CO and CO<sub>2</sub> possessed major deviations. This was reflected by the MvK approach, too. Especially the yield of CO was widely underestimated. The most suitable approach for the description of the ethylene oxidation was the ER mechanism. Accordingly, gas phase eth-

**Table 5.4:** Estimated kinetic parameters of the total and partial oxidation of C<sub>2</sub>H<sub>4</sub> and the corresponding 95 % confidence intervals (rate approaches from eqs. 5.1-5.3)

Approach	Frequency factor $k_{\infty}$	Unit	95 % CI	$E_A$ kJ·mol <sup>-1</sup>	95 % CI
ER ( $k_1$ )	<b>3.151·10<sup>-1</sup></b>	mol·(kg <sub>cat</sub> ·s·Pa) <sup>-1</sup>	<b>± 2.211·10<sup>-1</sup></b>	<b>56.836</b>	<b>± 3.546</b>
LH ( $k_1$ )	5.323·10 <sup>+8</sup>	mol·(kg <sub>cat</sub> ·s) <sup>-1</sup>	± 4.134·10 <sup>+8</sup>	118.430	± 3.293
MvK ( $k_{red,1}$ )	4.436·10 <sup>-3</sup>	mol·(kg <sub>cat</sub> ·s·Pa) <sup>-1</sup>	± 4.884·10 <sup>-3</sup>	50.168	± 4.855
ER ( $k_2$ )	<b>1.160·10<sup>+4</sup></b>	mol·(kg <sub>cat</sub> ·s·Pa) <sup>-1</sup>	<b>± 2.527·10<sup>+3</sup></b>	<b>110.685</b>	<b>± 1.299</b>
LH ( $k_2$ )	9.257·10 <sup>+11</sup>	mol·(kg <sub>cat</sub> ·s) <sup>-1</sup>	± 7.044·10 <sup>+11</sup>	165.834	± 3.422
MvK ( $k_{red,2}$ )	3.565·10 <sup>+2</sup>	mol·(kg <sub>cat</sub> ·s·Pa) <sup>-1</sup>	± 2.173·10 <sup>+2</sup>	112.256	± 2.940
ER / LH ( $K_{H2O}$ )	<b>3.518·10<sup>-10</sup></b>	Pa <sup>-1</sup>	<b>± 3.608·10<sup>-8</sup></b>	<b>0</b>	<b>± inf</b>

ylene reacts directly with the adsorbed oxygen catalyst species complex. Such characteristics of transition metal oxide catalysts for the total oxidation of short-chain alkanes and olefins had been observed in (Veldsink et al., 1995; Angelidis and Tzitzios, 1999; Auer and Thyron, 2002). The comparison of the estimated activation energy of the total oxidation with literature data offered some deviations. In (Yao, 1973) 90 kJ·mol<sup>-1</sup> for the ethylene oxidation on a commercialized Cr<sub>2</sub>O<sub>3</sub> catalyst were observed.

In order to clarify the suitability of the ER mechanism, in fig. 5.15 the temperature dependence of the performance parameters is shown in a wide ethylene and oxygen concentration range. First the ethylene partial pressure dependence is investigated (see fig. 5.15a-c). For this purpose, the ethylene molar inlet feed ratio was varied between 0.25–1.00 %. Further inlet conditions were set constant ( $x_{O_2} = 20.9\%$ ;  $W/F = 50 \text{ kg}_{\text{cat}} \cdot \text{s} \cdot \text{m}^{-3}$ ). With increasing ethylene concentration, the conversion slightly decreased at a constant reaction temperature. Accordingly, the yield of CO and CO<sub>2</sub> decreased marginal. This was related to the required longer residence time of a larger quantity of ethylene. The effect of the increasing released heat of reaction with increased ethylene concentration can only be notified above 450 °C and was considered in the kinetic modeling as well.

Second the effect of the oxygen inlet concentration is studied in fig. 5.15d-f at a constant ethylene molar inlet ratio ( $x_{C_2H_4} = 1.0\%$ ). Based on oxygen excess conditions the concentration decreased to the point of oxygen deficiency. The first decrease in oxygen affected the performance parameter marginally. Only below stoichiometric conditions the influence was obvious. It is clear that the oxygen concentration limits the ethylene conversion (fig. 5.15d). As a result, the yield of CO increased (fig. 5.15e) and the yield of CO<sub>2</sub>

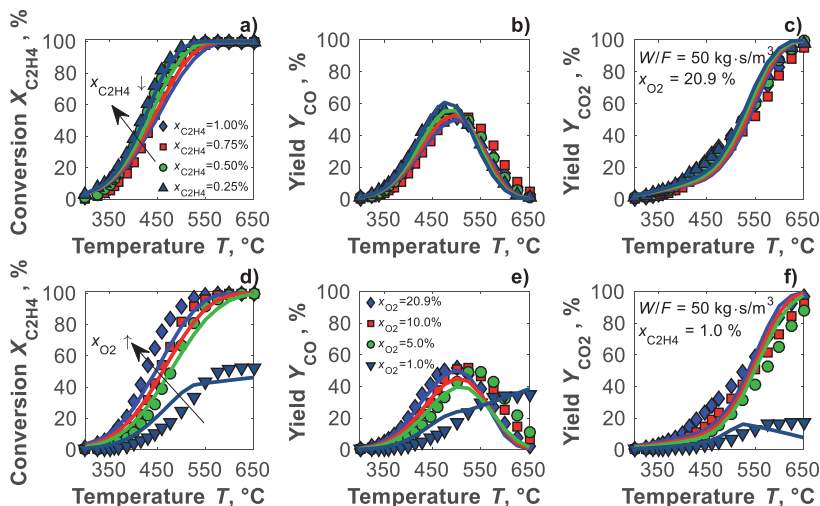


**Figure 5.15:** Experimental (symbols) and modeled (lines) steady state performance parameters (eqs. 2.16–2.18) of the C<sub>2</sub>H<sub>4</sub> oxidation (sub-network II) as a function of temperature (a and d) conversion of C<sub>2</sub>H<sub>4</sub>, (b and e) yield of CO and (c and f) yield of CO<sub>2</sub> and (a-c) different C<sub>2</sub>H<sub>4</sub> inlet concentrations and (d-f) different O<sub>2</sub> inlet concentrations

(fig. 5.15f) decreased strongly at high reaction temperatures, respectively. This behavior was reflected by the ER kinetic model as well.

Also in the ethylene sub-network, the effect of residence time is studied individually (see fig. 5.16a-c). As aforementioned, this is part of the reactor model and cannot be reflected by the reaction kinetics. The investigation was performed by constant inlet molar ratios ( $X_{O_2} = 20.9\%$ ;  $X_{C_2H_4} = 1.0\%$ ). The catalyst weight to total volumetric flux ratio was varied between 50 and 150  $\text{kg}_{\text{cat}} \cdot \text{s} \cdot \text{m}^{-3}$ . Expectedly, with an increased residence time, the conversion of ethylene increased, too. This resulted in higher CO and CO<sub>2</sub> yields at constant reaction temperatures. Generally, the applied reactor model reflected the experimental data well. Nevertheless, the yield of CO was underestimated and CO<sub>2</sub> overestimated at low and high temperatures, respectively. However, the trend was obvious.

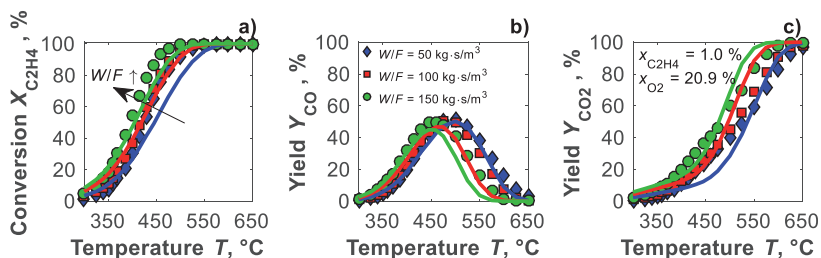


**Figure 5.16:** Experimental (symbols) and modeled (lines) steady state performance parameter (eqs. 2.16-2.18) of the C<sub>2</sub>H<sub>4</sub> oxidation (sub-network II) as a function of temperature and different residence times (a) conversion of C<sub>2</sub>H<sub>4</sub>, (b) yield of CO and (c) yield of CO<sub>2</sub>

### 5.5.3 Propylene oxidation: sub-network III

The sub-network III contains the total ( $r_3$ ) and partial ( $r_4$ ) oxidation reaction of propylene as well as the previously estimated oxidation of CO ( $r_5$ ). The quantification of the reaction rates was performed in an analogous manner to the ethylene sub-network II. The required adsorption equilibrium constant of water ( $K_{H_2O}$ ) for the adsorption-based reaction rate approaches was already introduced in section 5.5.2. The re-oxidation constant ( $k_{ox^+}$ ) of the MvK approach was already estimated in sub-network I. The comparison of the quantified rate models and the corresponding experimental data of one inlet feed composition ( $X_{C_3H_6} = 0.5\%$ ;  $X_{O_2} = 20.9\%$ ;  $W/F = 50 \text{ kg}_{\text{cat}} \cdot \text{s} \cdot \text{m}^{-3}$ ) is shown in fig. 5.17 a-c. The associated kinetic parameters and their 95 % confidence intervals of several rate approaches are given in table 5.5.

The experimentally observed performance parameters and dependencies on reaction temperature and reactant concentrations were analog to the ethylene oxidation. Based on the chain length of propylene the oxidation reactivity was increased compared to ethylene (Yao, 1973). Additionally, the total oxidation enthalpy of reaction was clearly increased. Calculated values of reaction  $r_1$  and  $r_3$  are  $\Delta h_{R,1}(T = 500^\circ\text{C}) = -1322 \text{ kJ} \cdot \text{mol}^{-1}$  and  $\Delta h_{R,3}(T = 500^\circ\text{C}) = -1925 \text{ kJ} \cdot \text{mol}^{-1}$ , respectively (see fig. 5.2a) (Yaws, 1999). Accordingly, the temperature control process along the catalyst bed was more complicated. The maximum observed temperature range was amounted to 80 °C at 8 mm catalyst bed length.

Based on this reason, the experimental data of the propylene oxidation were restricted to either small propylene or oxygen concentration, respectively.

The comparison of the estimated rate approaches revealed that the ER and LH mechanism reflect the experimental example data well (fig. 5.17a-c). The predicted values of the LH approach were in agreement with the yield of CO and CO<sub>2</sub>. However, the observed boundary range offered large deviation. The performance of the MvK mechanism faded compared to the others. Accordingly, the ER approach was used to describe the whole experimental data set of the propylene total and partial oxidation. Compared to literature data the activation energy of the total oxidation of propylene was estimated in a similar dimension. In (Zahn, 2012) a value of  $128.4 \pm 17.2 \text{ kJ}\cdot\text{mol}^{-1}$  for an empiric power law approach on a Cu-CrO<sub>x</sub>/γ-Al<sub>2</sub>O<sub>3</sub> catalyst and in (Yao, 1973)  $101 \text{ kJ}\cdot\text{mol}^{-1}$  on a Cr<sub>2</sub>O<sub>3</sub> catalyst were reported.

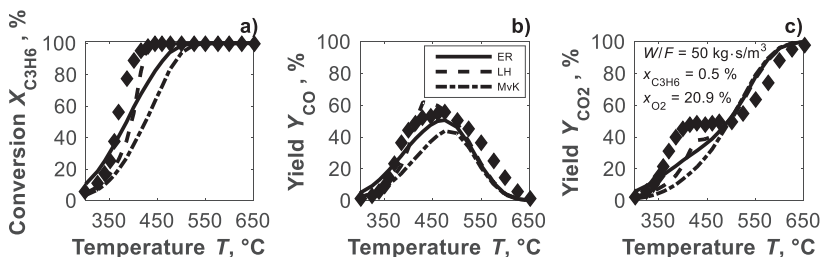


**Figure 5.17:** Experimental (symbols) and modeled (lines) steady state performance parameter (eqs. 2.16-2.18) (a) conversion of C<sub>3</sub>H<sub>6</sub>, (b) yield of CO and (c) yield of CO<sub>2</sub> of the C<sub>3</sub>H<sub>6</sub> oxidation (sub-network III) as a function of temperature and different reaction rate approaches

In fig. 5.18a-f a comparison of experimental and modeled performance parameter for a broad propylene and oxygen concentration range is shown. At a constant oxygen inlet molar fraction ( $x_{\text{O}_2} = 1.0 \%$ ), the propylene feed concentration was varied between  $x_{\text{C}_3\text{H}_6} = 0.25\text{--}1.0 \%$  (see fig. 5.18a-c). With increasing propylene partial pressure, the steady state conversion decreased at constant residence time conditions ( $W/F = 50 \text{ kg}_{\text{cat}}\cdot\text{s}\cdot\text{m}^{-3}$ ). At the same time the yield of CO and CO<sub>2</sub> decreased, too. In kinetic modeling the effect can be reflected as well. Nevertheless, the yield of CO and CO<sub>2</sub> was strongly underestimated and overestimated for the minimal propylene concentration studied, respectively.

**Table 5.5:** Estimated kinetic parameters of the total and partial oxidation of C<sub>3</sub>H<sub>6</sub> and the corresponding 95 % confidence interval (rate approaches from eqs. 5.1-5.3)

Approach	Frequency factor $k_{\infty}$	Unit	95 % CI	$E_A$ kJ·mol <sup>-1</sup>	95 % CI
ER ( $k_3$ )	$3.112\cdot 10^{+2}$	mol·(kg <sub>cat</sub> ·s·Pa) <sup>-1</sup>	$\pm 4.002\cdot 10^{+2}$	<b>86.156</b>	$\pm 5.462$
LH ( $k_3$ )	$1.368\cdot 10^{+5}$	mol·(kg <sub>cat</sub> ·s) <sup>-1</sup>	$\pm 9.261\cdot 10^{+4}$	73.234	$\pm 3.259$
MvK ( $k_{\text{red},3^+}$ )	$1.371\cdot 10^{+1}$	mol·(kg <sub>cat</sub> ·s·Pa) <sup>-1</sup>	$\pm 3.020\cdot 10^{+1}$	90.343	$\pm 7.545$
ER ( $k_4$ )	<b><math>7.807\cdot 10^{+3}</math></b>	<b>mol·(kg<sub>cat</sub>·s·Pa)<sup>-1</sup></b>	<b><math>\pm 6.335\cdot 10^{+3}</math></b>	<b>101.741</b>	<b><math>\pm 3.940</math></b>
LH ( $k_4$ )	$9.757\cdot 10^{+6}$	mol·(kg <sub>cat</sub> ·s) <sup>-1</sup>	$\pm 4.401\cdot 10^{+6}$	94.409	$\pm 2.121$
MvK ( $k_{\text{red},4^+}$ )	8.839	mol·(kg <sub>cat</sub> ·s·Pa) <sup>-1</sup>	$\pm 12.816$	83.595	$\pm 5.836$

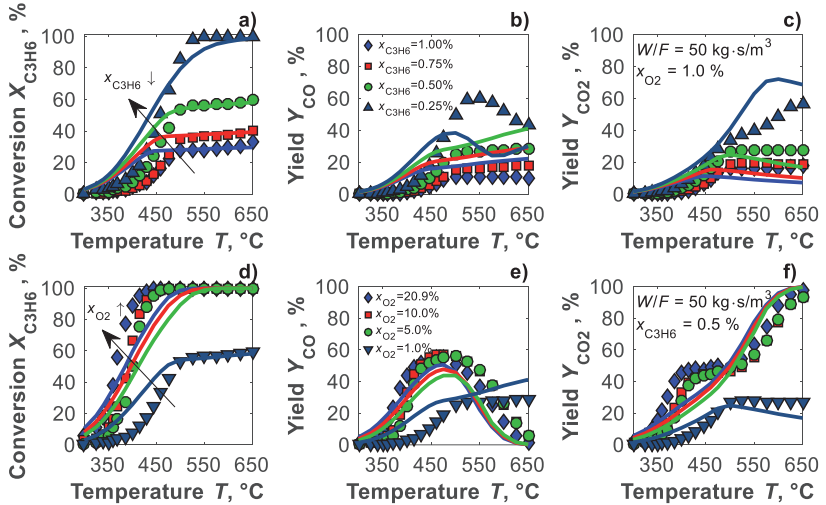


**Figure 5.18:** Experimental (symbols) and modeled (lines) steady state performance parameters (eqs. 2.16-2.18) of the  $C_3H_6$  oxidation (sub-network III) as a function of temperature, (a and d) conversion of  $C_3H_6$ , (b and e) yield of CO and (c and f) yield of  $CO_2$  and (a-c) different  $C_3H_6$  inlet concentrations and (d-f) different  $O_2$  inlet concentrations

The effect of the oxygen concentration (see fig. 5.18d-f) was only visible below stoichiometric conditions. This was obvious at the limited propylene conversion. The corresponding yield of CO and  $CO_2$  was affected by the oxygen limitation, too. However, at this point the kinetic modeling cannot reflect the experimental data. At oxygen excess conditions the performance parameters were only slightly affected. With an increased oxygen concentration, the propylene conversion increased, too. The corresponding yield of CO and  $CO_2$  first increased equivalent. At higher reaction temperatures, the following total oxidation of CO ( $r_5$ ) was also supported. This led to a strong decreased CO yield.

The investigation of the residence time effect on the sub-network III was performed at  $x_{C_3H_6} = 0.5\%$  and  $x_{O_2} = 20.9\%$  as inlet composition. Based on the experimental plant

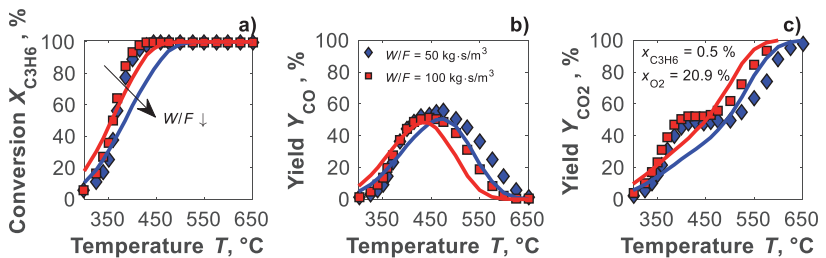


**Figure 5.19:** Experimental (symbols) and modeled (lines) steady state performance parameters (eqs. 2.16-2.18) of the  $C_3H_6$  oxidation (sub-network III) as a function of temperature and different residence times, (a) conversion of  $C_3H_6$ , (b) yield of CO and (c) yield of  $CO_2$

limitation the catalyst weight to total volumetric flux ratio was varied between 50 and 100  $\text{kg}_{\text{cat}} \cdot \text{s} \cdot \text{m}^{-3}$ . The comparison of the experimental and modeled performance parameter is shown in fig. 5.19a-c. As aforementioned in sub-network I and II, respectively, with increase in residence time the conversion of propylene increases, too. The modeled effect was much more pronounced as experimentally validated. This can be observed for the yield of CO and CO<sub>2</sub> as well.

### 5.5.4 Evaluation of the total oxidation reaction network

In the previous analysis of the three sub-networks all reaction kinetic parameters had been estimated (see bold parameters in tab. 5.3-5.5). Thus, in the following section the reaction kinetic will be validated at mixture conditions which were not considered during parameter estimation. Therefore, no additional parameter estimation will be done. The validation occurred at oxygen excess ( $x_{\text{O}_2} = 20.9\%$ ) and a catalyst weight to total volumetric flux ratio of 50  $\text{kg}_{\text{cat}} \cdot \text{s} \cdot \text{m}^{-3}$ . Often inhibition effects based on competitive adsorption of the reactants were reported in literature (Ertl et al., 2008; Zahn, 2012). To analyze the mutual retardation of the hydrocarbon oxidation in mixtures first the ethylene inlet concentration was set constant and the propylene molar ratio was varied between 0 and 0.75%. The experimental and modeled performance parameters are shown in fig. 5.20.

The opposite variation ( $x_{\text{C}_3\text{H}_6} = \text{const.} = 0.25\%$  and ethylene molar ratio was varied between 0 and 0.75%) is illustrated in fig. 5.21.

It is obvious that mutual retardation occurred for both cases. Only the magnitude was differently pronounced. The conversion of the reactants for several conditions revealed

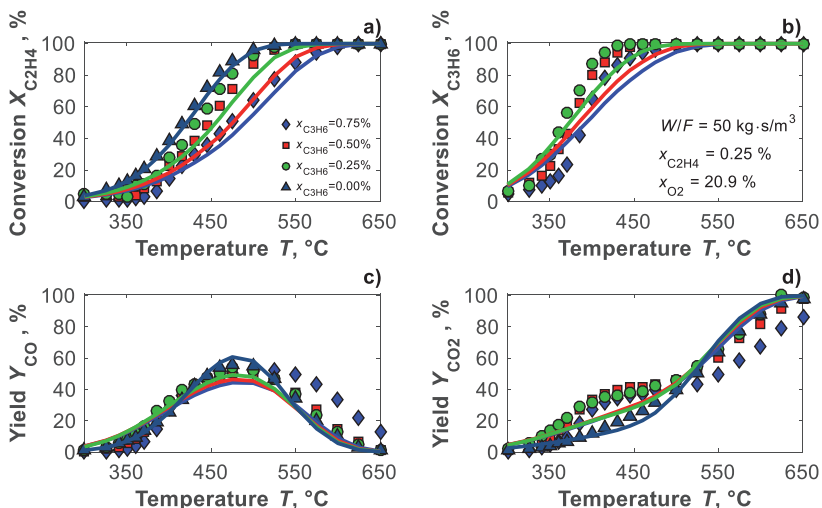


**Figure 5.20:** Experimental (symbols) and modeled (lines) steady state performance parameters (eqs. 2.16-2.18) (a) conversion of C<sub>2</sub>H<sub>4</sub>, (b) conversion of C<sub>3</sub>H<sub>6</sub>, (c) yield of CO and (d) yield of CO<sub>2</sub> of the total oxidation network as a function of temperature for a-d: different C<sub>3</sub>H<sub>6</sub> inlet concentrations at a constant O<sub>2</sub> ( $x_{\text{O}_2} = 20.9\%$ ) and C<sub>2</sub>H<sub>4</sub> ( $x_{\text{C}_2\text{H}_4} = 0.25\%$ ) inlet concentrations

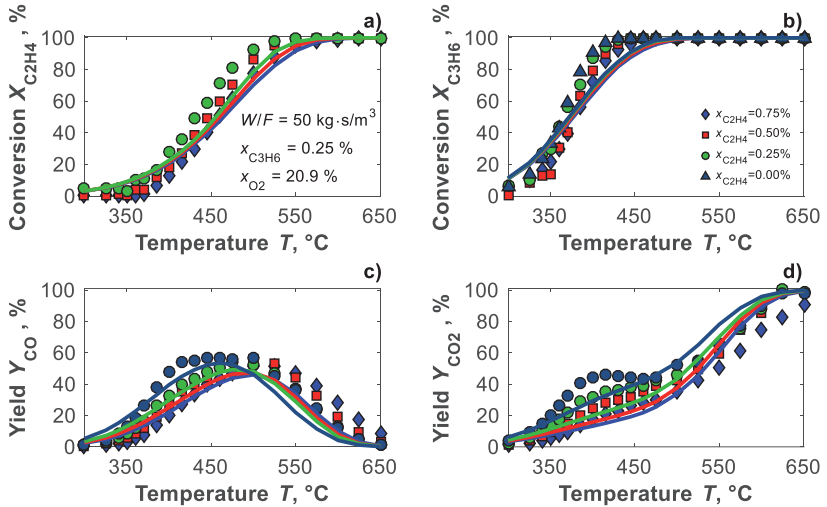


**Figure 5.21:** Experimental (symbols) and modeled (lines) steady state performance parameter (a) conversion of  $C_2H_4$ , (b) conversion of  $C_3H_6$ , (c) yield of  $CO$  and (d) yield of  $CO_2$  of the total oxidation network as a function of temperature for different  $C_2H_4$  inlet concentrations at a constant  $O_2$  ( $x_{O_2} = 20.9\%$ ) and  $C_3H_6$  ( $x_{C_3H_6} = 0.25\%$ ) inlet concentrations

that the ethylene oxidation was strongly inhibited by propylene addition. Vice versa only a marginal effect could be observed. This was already determined at the competitive adsorption measurements of ethylene and propylene (section 5.4). In this connection, the *Multi-Langmuir* adsorption model reflected the competitive adsorption behavior for the active catalyst sites well (fig. 5.10). By including the individual estimated single component adsorption parameter in the ER kinetic approach the effect and also the order of the magnitude can be reflected by the kinetic model as well (see fig. 5.20 and fig. 5.21). This reaction order and the corresponding inhibition effects of the hydrocarbon oxidation was already observed by several transition metal oxide catalysts (Moro-Oka et al., 1967; Yao, 1973). For the yield of  $CO$  and  $CO_2$  the effect of the competitive component adsorption can be studied in detail. Whereas the yield of  $CO$  and according to these the partial oxidation reactions ( $r_2$  and  $r_4$ ) were only slightly effected. The yield of  $CO_2$  increases significantly with an increase of the competitive component at lower reaction temperatures.

Based on the estimated activation energy values of the partial and total oxidation reactions the reaction pathway can be analyzed. Obviously, the total oxidation of the hydrocarbons is energetic favored. The corresponding activation energies ( $E_{A,1} = 57 \text{ kJ}\cdot\text{mol}^{-1}$  and  $E_{A,3} = 86 \text{ kJ}\cdot\text{mol}^{-1}$ ) are significantly smaller as of the partial oxidation ( $E_{A,2} = 111 \text{ kJ}\cdot\text{mol}^{-1}$  and  $E_{A,4} = 102 \text{ kJ}\cdot\text{mol}^{-1}$ ). Thus, the main part of the produced carbon dioxide amount results directly from the total oxidation. Consider the activation energy of the carbon monoxide oxidation ( $E_{A,5} = 97 \text{ kJ}\cdot\text{mol}^{-1}$ ) only high temperatures yields in complete conversion. Regarding the hydrocarbon chain length, the activation energy of the total oxidation is increased for longer molecules. In contrast the activation energy of the partial oxidation is

decreased. The calculated 95 % confidence intervals of the estimated parameters are mostly in a significant range. Especially the confidence intervals of the activation energies are less than 11 %.

## 5.6 Conclusions

This section described results of investigating the kinetics of the heterogeneously catalyzed partial and total oxidation reactions of ethylene, propylene, mixture of both and carbon monoxide on a  $\text{CrO}_x/\gamma\text{-Al}_2\text{O}_3$  catalyst. The mentioned reactions proceed in a rather wide range of temperatures and partial pressures. Mechanistic rate equations were determined by using the GCCK approach.

In heterogeneous catalysis, detailed information about catalytic cycles and the typically large number of species involved are usually missing. Therefore, the determination of mechanistic rate models is typically based on well-established reaction simplified mechanisms, such as e.g. the *Mars/van Krevelen* and the *Eley/Rideal* approach. Considering the assumptions used in deriving these reaction mechanisms, it can be shown that the corresponding rate expressions form subsets of the general rate equations obtainable from the *Christiansen* methodology.

Studying multi-phase systems additional information regarding phase equilibria of the reactants and products have to be considered in kinetic modeling. In order to support the parameter estimation and to describe the adsorption behavior of the components involved, *Langmuir* adsorption isotherm models are often applied. Using these models, the single component adsorption behavior could be characterized quite well. By means of the *Multi-Langmuir* model, based exclusively on the parameters of the single component isotherms, the competitive adsorption behavior of ethylene and propylene mixtures could be predicted. If more realistic but sophisticated phase equilibrium models for description of competitive adsorption behavior are needed, the IAS theory can be suggested. Using this theory, thermodynamic consistent adsorption models of reactants and products within kinetic modeling can be obtained. This theory was applied in this work as well. Single component adsorption isotherm models consisting of a *Henry* and *Langmuir* term were quantified for all studied components. By means of the IAS theory, the competitive adsorption behavior of ethylene and propylene mixtures could be predicted. However, the obtained implicit set of expressions have to be solved numerically. Therefore, the subsequent kinetic analysis could be carried out using the *Langmuir* adsorption isotherm models. Using these additionally determined adsorption parameters within the kinetic analysis, a more profound description of the reaction rates was feasible by separating kinetic and thermodynamic effects.

The subsequent kinetic analysis of the total oxidation reaction network occurred considering three different sub-networks. In order to describe the experimental data, several postulated mechanistic kinetics were tested and ranked. The best performed kinetic models were selected and transferred to the progressively larger sub-network and finally to the total network. All sub-networks and the total reaction network could be well described by using one set of kinetic models and parameters. Based on this analysis, the carbon mon-

oxide oxidation corresponds to the *Mars/van Krevelen* mechanism in agreement with (Murzin and Salmi, 2005) and the hydrocarbon partial and total oxidation reactions to the *Eley/Rideal* approach, where the hydrocarbons react from gas phase with adsorbed oxygen in agreement with (Yao, 1973). A validation of the parameterized reaction model was done by analyzing several inlet mixtures of ethylene and propylene in a broad temperature and concentration range. Based on the competitive adsorption results mutual retardation of both reactants was predicted by the kinetic modeling and indeed observed experimentally.

The general kinetic concept followed in this thesis, namely the GCCK approach, as a starting concept to formulate kinetic models could be successfully applied for the heterogeneously catalyzed total and partial oxidation reactions.

In the following final section 6, the challenging innovative multi fixed-bed Loop Reactor concept will be studied both theoretically and experimentally. Besides evaluating its potential, the above described reaction kinetics will be applied and validated.



## 6 Application of Kinetic Models: Multi Fixed-Bed Loop Reactor

In the previous section, mechanistic reaction kinetic models were derived via the GCKK approach and parameterized based on experimental data for the heterogeneously catalyzed partial and total oxidation of ethylene, propylene, mixtures of both and carbon monoxide on a chromium oxide supported catalyst (section 2.1 and 5.5).

The aim of this section is to investigate the periodic operation of the attractive Loop Reactor (LR) concept both theoretically and experimentally and to validate the determined reaction kinetics of the oxidation reactions.

Applying very detailed mechanistic kinetic models as obtained from the GCKK approach in combination with rigorous Loop Reactor models, high performance computing is required. In order to identify general LR characteristics, the accuracy of the detailed model is unnecessary. Therefore, to study the LR concept theoretically a single and multi-reactant simulation study is performed in section 6.3 using simplified power law kinetic models suggested in the literature (Haynes and Caram, 1994). In a second part of this section will be shown the experiments performed in this work (section 6.4) and a model based analysis of the LR concept (section 6.5). As reaction system, the total oxidation of ethylene and propylene in air on a  $\text{CrO}_x/\gamma\text{-Al}_2\text{O}_3$  catalyst will be studied.

Simulation results will be generated using a more detailed reactor model, which is explained in detail in appendix B.5.

Finally, results of a parametric study are presented which evaluate a dosing strategy capable to further increase the LR operation window.

### 6.1 Principle and history of the Loop Reactor

The purification of industrial volatile organic compound (VOC) exhaust streams requires special attention in order to observe the strict emission standards (Brinkmann et al., 1999). Frequently, harmful environmental components are diluted in air or nitrogen. Thus, the total oxidation of these components ( $\Delta H_R < 0$ ) requires a significant amount of thermal energy to preheat the whole stream especially including inerts to the ignition temperature  $T_{\text{ign}}$  (Brinkmann et al., 1999). Based on this reason the idea of an autothermal process was investigated in the seventies in the 20<sup>th</sup> century. The first concept was given by *Matros* (Boreskov et al., 1977; Matros, 1977).

The so-called Reverse Flow Reactor (RFR) concept uses one adiabatic catalytic fixed bed which can be streamed in both directions. If cold feed gas enters the preheated packed bed the reactants heated up to ignition temperature and total oxidation occurs. Consequently, an exothermal reaction front is created and moves in flow direction. Depending on the exothermal heat release, an additional leading thermal front is generated, which heats up the catalyst bed again. If the fronts reach the end of the reactor, the flow direction is reversed. Thus, the high temperature zone area enclosed by the exothermal reaction and the leading thermal front can be captured within the reactor and ignited cyclic steady state conditions are obtained (Silveston and Hudgins, 2012). The main field of application

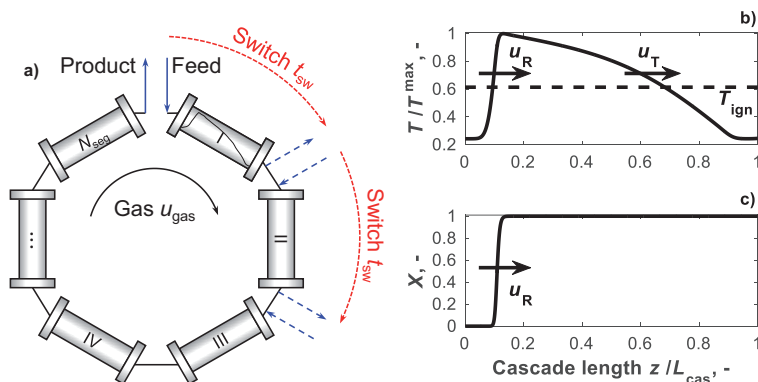


**Figure 6.1:** (a) Principle of the Loop Reactor based on exploiting a periodically operated reactor cascade of  $N_{\text{seg}}$  catalytic fixed beds and switching in- and outlet port positions in the gas flow direction, (b) the resulting temperature and (c) conversion profiles including for illustration the traveling exothermal reaction ( $u_R$ ) and temperature ( $u_T$ ) fronts in the middle of switching period (Zahn, 2012)

of this concept is the VOC destruction (Eigenberger and Nieken, 1994; Nieken et al., 1994; Fissore et al., 2005; Barresi et al., 2007; Silveston and Hudgins, 2012). Other commercial applications are  $\text{NO}_x$  reduction, the mitigation of methane in coal mine and the catalytic decomposition of  $\text{N}_2\text{O}$  to the abatement of greenhouse gas emissions (Silveston and Hudgins, 2012). However, the RFR concept offers an unbalanced catalyst bed using and a slip of unconverted reactants directly after flow reversal (Sheintuch and Nekhamkina, 2005). Therefore, a STAR reactor concept was introduced, that operates in a fully transient mode and combines the autothermal RFR operation and constant outlet concentrations (Vanden Bussche and Froment, 1996).

Another promising and innovative reactor concept is the Loop Reactor (LR) (fig. 6.1a). The theoretical principle was first introduced by (Haynes and Caram, 1994). For a successful process an adiabatic reactor cascade of at least two segments ( $N_{\text{seg}} \geq 2$ ) is assumed. Exactly as the RFR operation, cold feed gas enters the first segment, heats up to ignition temperature  $T_{\text{ign}}$  and reaction occurs. The formed exothermal reaction front moves in flow direction by the shift of cold feed gas. After passing completely the segment I, the feed and outlet port position is shifted into flow direction following the reaction front. Thus, the formerly cold first segment is switched at the end of the reactor cascade and the hot exhaust gas can heat up the segment again. This periodic process attempts to trap a self-sustained exothermic front and allows an autothermal operation. At cyclic steady state conditions two fronts are formed, the exothermal reaction front and the leading thermal front (fig. 6.1b). Based on the catalytic fixed bed, gas phase properties and adiabatic temperature rise different front velocities can be observed ( $u_R$  and  $u_T$  in fig. 6.1b-c). The periodic switching of the ports mimics a discrete countercurrent movement of the phases involved, which is well-known in the Simulated Moving Bed chromatography (Seidel-Morgenstern et al., 2008).

To maintain stable ignited conditions in the LR several aspects have to be considered.

For the determination of suitable front velocities and the suitable switching times  $t_{sw}$  have to be identified. Additionally, unexpected ignition behaviors as well as the front dynamics for processing mixtures have to be investigated. To reduce the computing effort needed simplified reactor models and approximations were introduced. In (Sheintuch and Nekhamkina, 2004, 2005) limits of the exploitable switching velocities are studied using an asymptotic model  $N_{seg} \rightarrow \infty$ . In (Nekhamkina and Sheintuch, 2008) are discussed an approximate rotating pulse solution and the corresponding switching stability limits and maximum temperatures. Another simplified model was presented by (Zahn, 2012). Inspired by Simulated Moving Bed modeling. A True Moving Bed Reactor model (eq. 2.52) was used to study the effect of switching time, inlet temperature, heat loss and heat capacity of the catalyst bed on temperature and conversion patterns and maximum temperatures. Based on this model a bifurcation analysis was applied to identify various switching domains.

An important application field of the autothermal reactor concept is VOC destruction. For this field are presented several model-based and experimental studies of the LR configuration (Haynes and Caram, 1994; Barresi et al., 1999; Brinkmann et al., 1999; Fissore and Barresi, 2002; Madai and Sheintuch, 2008; Zahn, 2012; Madai et al., 2017). New fields of application are given by (Velardi and Barresi, 2002; Fissore et al., 2003). In these studies, the equilibrium limited were investigated the methanol synthesis and the production of synthesis gas by a combination of partial oxidation and steam reforming, respectively.

In the next sections at first a preliminary parametric study of the LR concept is presented. To reduce the computational efforts the simplified power law reaction kinetic model published by (Haynes and Caram, 1994) will be taken. Single and multi-component mixtures were considered as the feed. Subsequently, the total oxidation of ethylene and propylene (see section 5) is used to study the LR more systematically. For this an experimental evaluation of the autothermal total oxidation is performed in a special newly developed pilot plant. Selected experimental data were compared with modeled data using the already introduced LR model (eqs. 2.48-2.51) and the derived kinetic models (eqs. 5.2-5.3 and tab. 5.2-5.5).

## 6.2 Characterization of the Loop Reactor

To maintain ignited conditions in the LR system an understanding of front propagation is indispensable. Typically, spatio-temporal temperature as well as concentration patterns were suggested in fig. 6.1b-c. Based on the mean positions and the shapes of the velocities of the thermal,  $u_T$ , and exothermic reaction front,  $u_R$ , the time for switching between the several inlet and outlet ports of the reactor cascade can be adjusted. The basis for the determination of the front velocities are the mass and the energy balances already introduced in eqs. 2.48 and 2.50. The final approximations of the thermal front and the exothermic reaction front velocities is given in eq. 6.1 and 6.2, respectively. A more detailed derivation of traveling front velocities is given in appendix B.7.

$$u_T \approx \frac{\varepsilon(\rho c_p)_{gas}}{(1-\varepsilon)(\rho c_p)_{cat}} u_{gas} \quad \text{with} \quad (\rho c_p)_{gas} \ll (\rho c_p)_{cat} \quad (6.1)$$

$$u_R = \left( 1 - \frac{\Delta T_{ad}}{T^{max} - T^{in}} \right) u_T \quad \text{with} \quad \Delta T_{ad} = \frac{(-\Delta h_R) c_{j_c}^0}{(\rho c_p)_{gas} (-v_{j_c})} \quad (6.2)$$

Based on eq. 6.1 the thermal non-reactive front velocity  $u_T$  is characterized by a lower velocity compared to the velocity of gas phase (Zahn, 2012). Upon changes of the fluid phase and/or the catalyst support the thermal front velocity can be altered. If heat dispersal is considered, the maximum temperature is decreased due to smearing the front shape. However, the mean velocity always corresponds to eq. 6.1. An similar analytical solution is also available for the more complex boundary conditions of an open-open system (Westertep et al., 1993; Zahn, 2012).

Eq. 6.2 describes the velocity of the exothermic reaction front. Disturbances can be affect the shape and position of the reaction front (Zahn, 2012). The ideal formulation of the reaction front illustrates that at steady state conditions ( $u_R = 0$ ) the maximum temperature corresponds to the adiabatic temperature rise. Furthermore, at non steady state conditions ( $u_R > 0$ )  $T^{max} - T^{in}$  increases. This temporal temperature increase can be explained by larger reactant amounts at the reaction front present in section 6.3.2. If  $u_R$  corresponds to  $u_T$ , eq. 6.2 possesses a singularity. An opposite behavior is to be expected for an exothermic reaction front velocity smaller than zero (Zahn, 2012).

Based on these front velocity characterizations, open and closed loop control concepts can be developed as described below.

### 6.2.1 Definition of switching times

As aforementioned, the time between the switching operations from one inlet port to the next have to correspond to the thermal and exothermic reaction front velocity, respectively (fig. 6.1). A reduced switching time  $\gamma$  can be defined as the ratio of the thermal front to switching velocity (eq. 6.3) (Haynes and Caram, 1994; Zahn, 2012).

$$\gamma = \frac{u_T}{u_{sw}} = \frac{u_T \cdot t_{sw}}{L_{seg}} \quad (6.3)$$

Using eq. 6.1 to substitute the thermal front velocity the equation of the reduced switching time can be written as follows (eq. 6.4).

$$\gamma = \frac{\varepsilon (\rho c_p)_{gas} u_{gas}}{(\rho c_p)_{bulk}} \frac{u_{gas}}{L_{seg}} t_{sw} \quad (6.4)$$

Using this definition, a  $\gamma = 1$  corresponds to a reduced switching time directly adjusted to the thermal front (Haynes and Caram, 1994). If  $\gamma$  is increased, the switching time  $t_{sw}$  also increases and vice versa. Bounds for stable ignited conditions in terms of a fast and slow switching regime can be directly deduced from the exothermic reaction and thermal front velocities, respectively (Nekhamkina and Sheintuch, 2008).

Based on eq. 6.4, suitable switching times can be determined for an open loop controlled process (also called as non-feedback controller). This concept will be applied in the single and multi-reactant simulation study of the LR concept, presented in section 6.3. In experimental reality, the determination of suitable switching times is more complex due to uncertainties in the reactor and kinetic models. Open loop control, applying predefined

switching times, is therefore not appropriate (Zahn et al., 2011). For this reason, closed loop control is attractive. The concept applied is explained below.

### 6.2.2 Definition of control concepts

Suitable controller concepts for the switching time has to ensure cyclic stable ignited conditions for the LR operation. Changes in the switching time beyond these stable ignited conditions leads to reactor extinction. Moreover, robustness to concentration and total volumetric flux perturbations as well as short start-up behavior are controller requirements (Zahn et al., 2011). Several theoretical studies of advanced control concepts for the LR were introduced and experimental validated. For example, Fissore et al. suggested an observer design for the catalytic reduction of  $\text{NO}_x$  (Fissore et al., 2007). The group of Sheintuch investigated a control concept based on several sensors (Sheinman and Sheintuch, 2009; Smagina and Sheintuch, 2009). Using these sensors, the front position is reconstructed using a parabola. In addition, the front velocity is estimated via a proportional and PI controller. However, an optimal number of sensors has not been reported, yet (Zahn et al., 2011).

A promising Multi-sensor controller concept is suggested by (Zahn et al., 2011). The basic idea of this closed loop control concept is to monitor the exothermal reaction front position at the sensor locations. This is realized by one thermocouple installed at the end of each reactor segment. The switching operation is triggered if a certain temperature setpoint  $T_{sw}$  has been reached from top to down. This means, that the exothermal reaction front leaves the active reactor segment and enter the following. Accordingly, the formerly active segment is switched at the end of the reactor cascade and will be prepared for next operation again. Using this closed loop controller concept robust operation for the start-up procedure and cyclic steady state can be achieved. For this reason, the experimental investigation of the single and multi-component feed (section 6.4) is realized using the Multi-sensor controller concept.

## 6.3 Simulation studies using simplified kinetics

In order to study and illustrate the characteristics of the LR concept as front velocities and maximum observed temperatures, a detailed simulation study is presented. Therefore, several variations of gas and catalyst phase properties as well as inlet conditions and reactant species are realized. Based on these results the following experimental study of the LR concept can be focused directly on the obtained main setting parameters. Accordingly, the model study is used to prepare the experimental design.

Applying very detailed mechanistic kinetic models as obtained from the GCCK approach (section 2.1.2 and 5) in combination with rigorous Loop Reactor models, high performance computing is required. To reduce the computational effort, the simulation study for single and multi-reactant inlet is realized using simplified power law kinetics (section 6.3.1). Using such power law kinetics, the ordinary differential equation system consisting of the mass and energy balances can be solved by efficient and fast solving algorithms as available in the used simulation software *MatLab*<sup>®</sup>.

The application of the full kinetic models, obtained from the GCCK approach (section 5), and the validation of this more detailed model is realized only on selected experimental Loop Reactor data (section 6.5).

### 6.3.1 Simplified kinetics and reactor model

The simple power laws used in the simulation study (eq. 6.5) are adopted from (Haynes and Caram, 1994; Sheintuch and Nekhamkina, 2005). The used kinetic parameters for the single reactant inlet are shown in tab. 6.1. The kinetic parameters used for the multi-component feed (section 6.3.3) are summarized later in tab. 6.2.

$$r_{jR} = k_{x,jc} \exp\left(\frac{-E_{A,jc}}{R \cdot T}\right) c_{jC}^0 (1 - X_{jC}) \quad (6.5)$$

The simplified one dimensional mass and homogeneous energy balance is shown in eq. 6.6 and 6.7, respectively (Haynes and Caram, 1994).

$$c_{jC}^0 \frac{\partial X_{jC}}{\partial t} = -u_{gas} c_{jC}^0 \frac{\partial X_{jC}}{\partial Z} + \sum_{jR=1}^{N_R} V_{jC,jR} r_{jR} \quad (6.6)$$

$$(\rho c_p)_{cat} \frac{\partial T}{\partial t} = -\varepsilon u_{gas} (\rho c_p)_{gas} \frac{\partial T}{\partial Z} + \lambda_{eff} \frac{\partial^2 T}{\partial Z^2} + \varepsilon \sum_{jR=1}^{N_R} (-\Delta h_{R,jR}) r_{jR} \quad (6.7)$$

The physical gas and solid catalyst properties are independent from temperature and summarized in tab. 6.1. Additional no axial mass dispersal is considered.

**Table 6.1:** Top: standard conditions adopted for simplified model (eq. 6.5-6.7) in the parametric study (Haynes and Caram, 1994). Bottom: range of the varied reaction kinetic parameters and physical properties

Parameter	Value	Parameter	Value	Parameter	Value
$c_1^0, \text{mol} \cdot \text{m}^{-3}$	0.3	$k_{x,1}, \text{s}^{-1}$	29732	$E_{A,1}, \text{kJ} \cdot \text{mol}^{-1}$	66.512
$(\rho c_p)_{gas}, \text{J} \cdot \text{m}^{-3} \cdot \text{K}^{-1}$	500	$\varepsilon, -$	0.45	$\lambda_{eff}, \text{J} \cdot \text{m}^{-3} \cdot \text{s}^{-1} \cdot \text{K}^{-1}$	2.06
$(\rho c_p)_{bulk}, \text{J} \cdot \text{m}^{-3} \cdot \text{K}^{-1}$	$2 \cdot 10^6$	$u_{gas}, \text{m} \cdot \text{s}^{-1}$	1	$\Delta h_{R,1}, \text{kJ} \cdot \text{mol}^{-1}$	-206
$N_{seg}, -$	3	$L_{seg}, \text{m}$	0.45		
$c_1^0, \text{mol} \cdot \text{m}^{-3}$	0.05 – 0.30			$E_{A,1}, \text{kJ} \cdot \text{mol}^{-1}$	51.512 – 81.512
$N_{seg}, -$	2 – inf			$u_{gas}, \text{m} \cdot \text{s}^{-1}$	0.5 – 2.0
$(\rho c_p)_{gas}, \text{J} \cdot \text{m}^{-3} \cdot \text{K}^{-1}$	400 – 600			$(\rho c_p)_{bulk}, \text{J} \cdot \text{m}^{-3} \cdot \text{K}^{-1}$	$1 \cdot 10^6$ – $3 \cdot 10^6$
$\lambda_{eff}, \text{J} \cdot \text{m}^{-3} \cdot \text{s}^{-1} \cdot \text{K}^{-1}$	1.06 – 3.06				

### 6.3.2 Single reactant simulation study

The single component feed simulation study of the LR concept was devoted to analyze the general performance. The predicted values, such as maximum temperatures, do not correspond to the experimental data. Therefore, the reactor temperature profiles will be normalized with the maximum obtained temperature. Analogously, the concentration profiles are presented using the reactant conversion (eq. 2.16).

### General temperature and conversion pattern

As aforementioned in order to attain an ignited cyclic steady state the system has to be preheated over the ignition temperature one time. Afterwards the catalytic fixed bed works as an integral heat exchanger heating up the cold feed gas to the desired ignition requirement. Meanwhile, the reactor entrance is cooling down. Depending on the total volumetric flux and the adiabatic temperature rise the maximum temperature increases above initial condition. This start-up behavior is shown for the temperature and conversion in fig. 6.2a and b.

The further trend of the temperature and conversion profiles for an increasing tact number  $N_{\text{lact}}$  is presented in fig. 6.2c and d. It is obvious that the high temperature range is decreased up to cyclic steady state conditions. Accordingly, the reaction takes place in the small exothermic reaction front only (fig. 6.2d), where the conversion is abrupt rose. The remaining catalyst bed is used as heat exchanger only. If the initial conditions are revised, a changed start-up behavior is possible (Zahn, 2012). Furthermore, it becomes apparent using the open loop control concept (section 6.2.1) that a large amount of  $N_{\text{lact}}$  is necessary to obtain steady state conditions. In the present example, the  $N_{\text{lact}}$  is close to 100. The shown temperature and conversion profiles in fig. 6.2c-d are in the middle of the switching time exclusively.

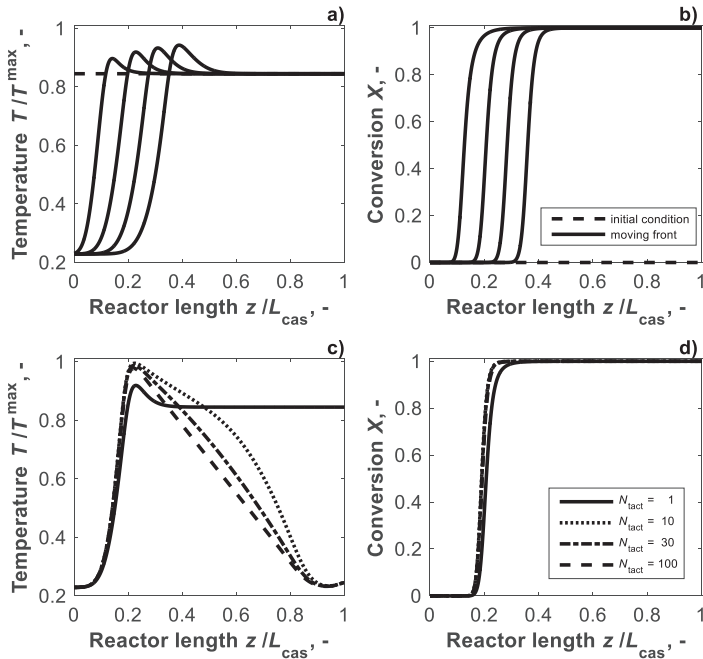


**Figure 6.2:** (a and c) Temperature and (b and d) conversion profile across the normalized reactor length in the middle of switching period for (a and b) within the first tact and (c and d) for increasing tact amount (parameters adopted from tab. 6.1)

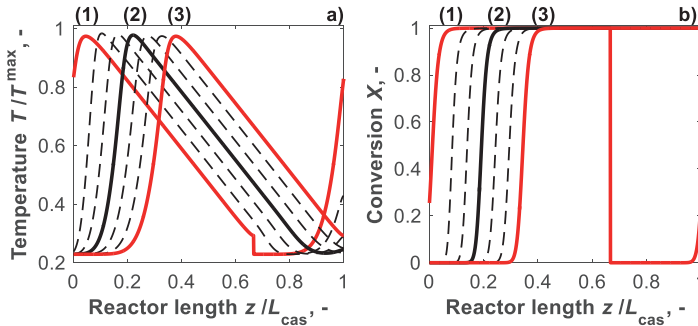


**Figure 6.3:** (a) Temperature and (b) conversion profile across the normalized reactor length at (1) initial, (2) middle and (3) end of switching period (parameters adopted from tab. 6.1)

In fig. 6.3a-b the cyclic steady state temperature and conversion pattern across the normalized reactor length over one switching period is shown, respectively. The red profiles (1 and 3) correspond to the initial and end of the switching period. In addition, snapshots of several intermediate and the half of the period are given. The initial profile is interrupted among the second and third reactor. The last segment, first reactor of the preceding period, offers a remaining preheated zone area at the outlet position. The range in front of this zone is loaded with unconverted reactant. Over time the typical temperature bell shape can be developed (profile in the middle of switching period). At that time the exothermic reaction front is located in the first and the leading thermal front in the last segment. Finalizing the switching period, the thermal front is close to leaving the reactor outlet, while the exothermic reaction front is transferred in the second segment. In the next step the inlet position is switched and the tact starts again (see also fig. 6.1a) (Zahn, 2012).

During the inlet properties are set constant, the product flux composition and temperature varies within the circulation as illustrated in fig. 6.4a-b. Based on the periodic switching operation, sawtooth-like temperature outlet signals can be obtained (Zahn, 2012). Zahn also presented, that the mean outlet temperature in perfectly adiabatic reactor represents the adiabatic temperature rise (Zahn, 2012). If a radial heat transfer resistances are considered the mean outlet temperature value is differed.

The conversion (fig. 6.4b) is decreased directly after switching operation. As aforementioned a plug of unconverted reactant is flushed in the beginning of the cycle. The so-called “slip” can be decreased by optimizing the switching time. This will be studied below.

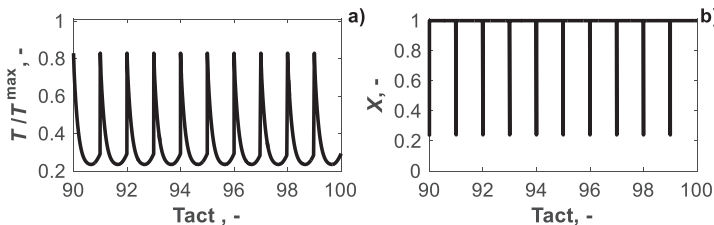


**Figure 6.4:** (a) Temperature and (b) conversion profile at the reactor outlet position as function of the reaction time at cyclic steady state conditions (parameters adopted from tab. 6.1)

### Effect of reactor segment number

In this section, the effect of the number of reactor segments is studied. To get comparable conditions each reactor segment length is corrected to obtain a constant catalyst amount. Based on a total catalyst fixed bed length of five meter the reactor segment number is increased from 2 up to infinite. For the calculation of the limiting case of an infinite reactor amount, the TMBR model is used which was already introduced in section 2.3.3. As aforementioned in this model the discrete switching of the in- and outlet ports between the reactor segments is replaced by a constant countercurrent flux of the solid catalyst phase. Thus, the solid phase velocity has to be adjusted to the open loop controlled switching time in the SMBR model (see also eq. 6.4). Therefore, (Zahn, 2012) suggested the following expression (eq. 6.8).

$$\gamma = \frac{u_{\text{gas}} (\rho c_p)_{\text{gas}}}{u_s (\rho c_p)_{\text{cat}}} \quad (6.8)$$

The cyclic steady state temperature and conversion profiles at half of the switching time are shown in fig. 6.5a-b. The used normalized switching time is one. The remaining unlisted parameters are taken from tab. 6.1. Independent from the reactor segment number the exothermic reaction and leading thermal front is formed. Only the position has changed. Based on a decreasing reactor segment length the switching time is decreased as well. However, the front velocities are not affected. Accordingly, the steady state profiles at half of the switching time are closer to the reactor cascade inlet. The limiting case is presented by the TMBR model which offers a standing wave. Different switching times lead to equivalent results (Zahn, 2012).

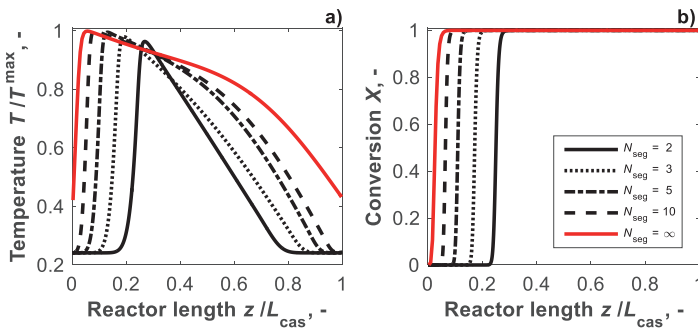


**Figure 6.5:** (a) Temperature and (b) conversion profile in the middle of switching period for increasing amount of reactor segments at  $\gamma = 1$ . Infinite reactor segment number corresponds to the TMBR model (eqs. 2.48 and 2.52) (remaining parameters adopted from tab. 6.1)

### Effect of switching time

The effect of the most important setting parameter, the switching time, on the fronts is studied in the following. The analysis is basically divided into open and closed loop control. Further, the operation limitations of stable ignited conditions will be presented.

**Open loop control** The open loop control process uses a fixed switching time, which is correlated to the exothermal reaction front velocity. Detailed information were presented in section 6.2.1. Simulated results of the temperature and conversion pattern at half of the switching time for the open loop control are shown in fig. 6.6a-b. The gradient of the exothermic reaction front is preserved. Only the front is marginal shifted to the entrance or outlet position as function of the switching time, respectively (fig. 6.6a). However, the maximum temperature increases with switching time up to the maximum value at  $\gamma = 1.02$  is reached (fig. 6.7). Based on this fact, high switching velocities are suitable to reduce the maximum temperature. A further increase of the switching time causes a slightly decrease of the maximum temperature (Nekhamkina and Sheintuch, 2008). If axial thermal dispersion is neglected, the maximum temperature at stable ignited conditions is independent from switching time (Zahn, 2012). Thus, the effect on the educt conversion is nonexistent (fig. 6.6b). Rather the shape of the leading thermal front changes obviously. Larger switching time values lead to a broadened high temperature zone. Accordingly, the steepness of the thermal front increases.

The slip of the reactor outlet is significantly affected by the switching time. The cyclic steady state reactor cascade outlet properties of the fastest ( $\gamma = 0.98$ ) and slowest ( $\gamma = 1.05$ ) switching are shown in fig. 6.8. For the first condition, the temperature profile increases rapidly shortly after switching, followed by a decrease to the inlet temperature. This corresponds to the switch of the ports directly within the exothermic reaction front. Afterwards, the remaining reaction front is flushed out at the outlet position. Compared to this, the slow switching proceeding offers an advanced front moving. Accordingly, the temperature peak after switching operation is decreased. However, the subsequently temperature flush is followed by a temperature rise. This results from leaving of the leading thermal front at the reactor outlet.

The corresponding conversion slip at the switching operation offers a different magnitude for the investigated times. The fast switching regime spares more heated catalyst phase of the first reactor segment in the switching operation. Accordingly, less unconverted reactant is flushed out. Based on this, faster switching reduces the slip. In (Zahn,

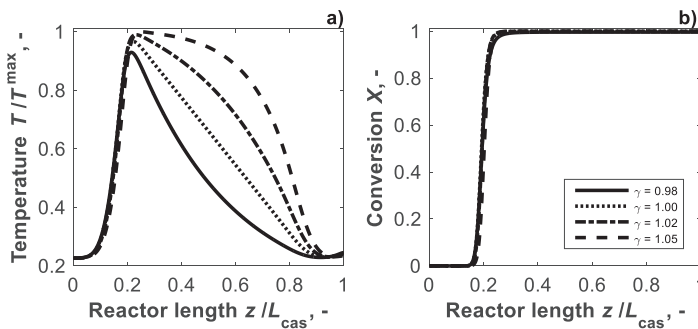


**Figure 6.6:** (a) Temperature and (b) conversion profile in the middle of switching period for different normalized switching times  $\gamma$  (eq. 6.4) in open loop control (section 6.2.1) (parameters adopted from tab. 6.1)

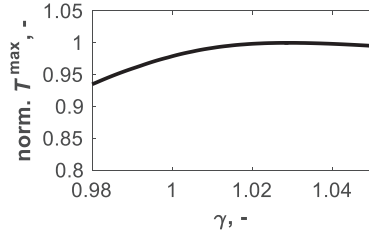


**Figure 6.7:** Simulated maximum reactor temperature as function of normalized switching time  $\gamma$  (eq. 6.4) using the TMBR model including axial thermal dispersion

2012) reaction conditions are identified without any slip. However, if switching is too fast, the leading thermal front did not enter the next segment and extinction occurred.

**Closed loop control** The closed loop Multi-sensor control concept is characterized by a feedback of a temperature signal at the end of each reactor segment. It was suggested in (Zahn et al., 2011). The switching operation is triggered if the temperature set-point  $T_{sw}$  has been passed from top to down. Accordingly, the variation of the temperature set-point effects the switching time. A high set-point corresponds to fast switching and vice versa. A more detailed description of the applied Multi-sensor approach is presented in section 6.2.2.

The calculated cyclic steady state temperature and conversion profiles in the middle of the switching period as a function of the temperature set-point compared to the standard open loop control switching time ( $\gamma = 1.00$ ) are shown in fig. 6.9. Basically, similar characteristics can be observed. The use of low temperature set-points leads to protracted periods. Accordingly, a broad hot zone area including sharp reaction and thermal fronts are obviously. A rising control temperature causes a decrease of the switching time. In this case, the leading thermal front is flattened out and the exothermic reaction front is shifted to the entrance. Additionally, the maximum temperature is affected by this variation similar to fig. 6.7. However, the set-point has to be chosen close to the maximum temperature to reach the standard switching time in open loop control process. Accordingly, the experimental investigation, using this control concept, is focused on the slow switching regime.

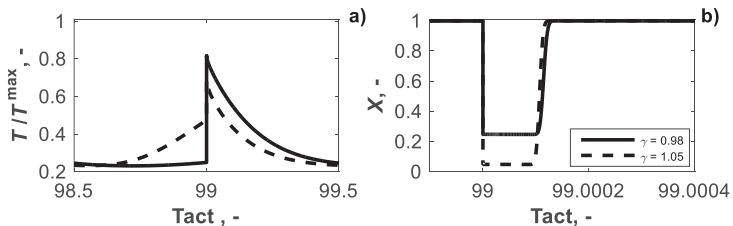


**Figure 6.8:** Conversion profile as function of reaction time to illustrate the slip of unconverted reactants for open and closed loop control concepts (section 6.2)

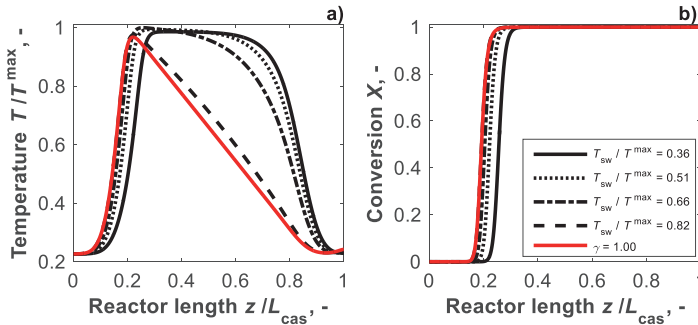


**Figure 6.9:** (a) Temperature and (b) conversion profile in the middle of switching period for different closed loop control switching temperatures ( $T_{\text{sw}}$ ) compared to open loop controlled operation ( $\gamma = 1$ ) (parameter adopted from tab. 6.1)

### Effect of residence time

Temporal dependent fluctuations in the total volumetric flux are common practice in industrial plants. Independent from desired or undesired perturbations huge effects can occur. To maintain an ignited cyclic steady state in the LR cascade the results have to be investigated more closely. As aforementioned, changes in total volumetric flux have to be adjusted by the switching time (Brinkmann et al., 1999; Madai and Sheintuch, 2008; Zahn, 2012). In open loop control eq. 6.4 is suitable. Referred to this equation the gas phase velocity and switching time are inversely proportional. Calculated cyclic steady state temperature and conversion profiles as function of the residence time are presented in fig. 6.10. To keep  $\gamma$  constant ( $\gamma = 1.00$ ) the switching time  $t_{\text{sw}}$  is adjusted every time (section 6.2.1). Obviously, the maximum temperature as well as the exothermic reaction front steepness is strongly decreasing, if the residence time is increased. The flattening of the leading thermal front results from maximum temperature reduces. Similar experimental results were given by (Madai and Sheintuch, 2008; Zahn, 2012).

The decrease in residence time is limited by mass and energy transport phenomena.

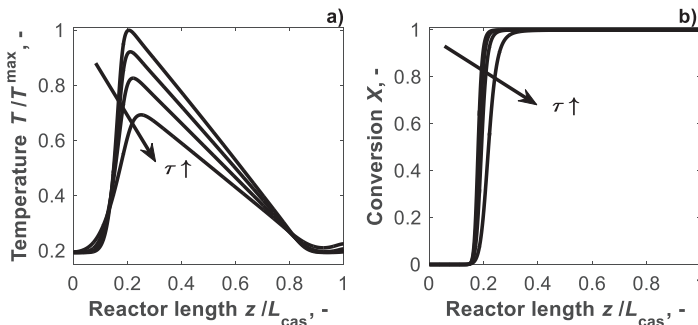


**Figure 6.10:** (a) Temperature and (b) conversion profile in the middle of switching period for increasing residence time (eq. 4.3,  $\tau = 0.25-1$  s) (parameter adopted from tab. 6.1)

If transport limitations reduce the total conversion and the corresponding reaction energy release, extinction can occur (Brinkmann et al., 1999).

Dependent on the shape of the exothermic reaction front the reactant conversion is also affected. Based on sharpness and maximum temperature the front is shifted to the entrance or outlet position, respectively.

### Effect of gas phase

The above described analysis of the LR principle was focused on investigation of reactor amount, switching and residence time, respectively. In the following, the emphasis was placed on the study of the reactant. Therefore, the inlet concentrations as well as physical gas phase properties are varied. The effect of different reactants in the LR concept is described below.

**Initial concentration** The cyclic steady state profiles of the reaction temperature and reactant conversion in the middle of switching period as function of the adiabatic temperature rise  $\Delta T_{ad}$  are presented in fig. 6.11. Using eq. 6.2  $\Delta T_{ad}$  is varied in a range of 82–144 K. Further parameters as well as the normalized switching time  $\gamma$  (eq. 6.13) are set constant and adopted from tab. 6.1.

As already known, an increase of the reactant inlet concentration leads to a steeper temperature rise within the exothermic reaction front. Moreover, an increase of the maximum temperature can be observed (Silveston and Hudgins, 2012). However, in LR principle the maximum temperature does not correspond to the adiabatic temperature rise (Brinkmann et al., 1999; Sheintuch and Nekhamkina, 2005). Based on the steeper temperature rise the total reactant conversion is shifted to the entrance. The leading thermal front is nearly unaffected by variations of the adiabatic temperature rise.

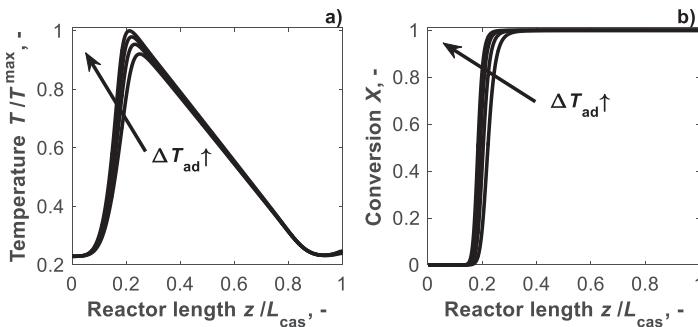


**Figure 6.11:** (a) Temperature and (b) conversion profile in the middle of switching period for increasing adiabatic temperature rise (part of eq. 6.2,  $\Delta T_{ad} = 82\text{--}144$  K) (parameters adopted from tab. 6.1)

**Physical properties** In this part, the effect of the inert gas phase component is studied. As aforementioned, the LR concept is introduced as a method to purify lean waste gas streams. Accordingly, a large percentage of the gas phase offer inert behavior. Mostly, the exhaust gases are mixed in air or directly in nitrogen. Thus, only small changes will be

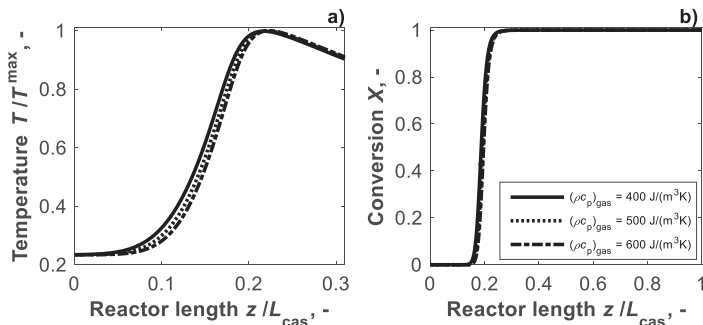


**Figure 6.12:** (a) Temperature and (b) conversion profile in the middle of switching period for different inert gas components (parameters adopted from tab. 6.1)

expected. In fig. 6.12 the calculated temperature and conversion profiles are presented as function of the gas phase heat capacity and density  $(\rho c_p)_{\text{gas}}$ . Based on marginal changes of the calculated temperature profiles, the leading thermal fronts are omitted in the presented data. However, the exothermal reaction front offers an effect. A rise of the gas phase heat capacity or density leads to an increase of the desired thermal energy to heat up the reactant to ignition temperature. Thus, the heating transfer area has to be increased. Consequently, the front is shifted to the reactor outlet. Based on the marginal shift of the exothermic reaction front the conversion front is shifted as well. The gradient increase of the exothermal reaction front is attended by a small maximum temperature rise. However, as aforementioned in eq. 6.1 the gas phase heat capacity is by orders of magnitude smaller than of the catalyst. Accordingly, possible control potential by the inert gas phase is marginal.

**Reactant species** In the following, the effect of the used reactant is discussed in detail. In order to present the results, the activation energy  $E_A$  is varied in the range from 51.5 to 81.5 kJ·mol<sup>-1</sup>. This corresponds to the estimated parameters of the full kinetic model (GCCK approach in section 5) of the ethylene (56.8 kJ·mol<sup>-1</sup>) and propylene (86.2 kJ·mol<sup>-1</sup>) total oxidation on a CrO<sub>x</sub>/γ-Al<sub>2</sub>O<sub>3</sub> catalyst, respectively. The corresponding calculated temperature and conversion profiles are presented in fig. 6.13. Obviously, the maximum temperature is increased strongly with the activation energy. This effect is already apparent in the rough estimation of the ignition temperature (dashed lines in fig. 6.13a, calculated by eq. B.42) (Zahn, 2012). Based on this, the ignition temperature is increased up to 30 percent. This change is directly transferred to the maximum temperature. Thus, the point where total conversion is reached is shifted to reactor outlet. However, the position of the exothermal reaction front is not affected. Based on the maximum temperature increase the leading thermal front offers a steeply rising.

The previous analysis of the LR concept illustrates that the most exercise of influence is given by the reactant and the corresponding quantified reaction kinetic. Accordingly, the determination of the reaction kinetics and consequently section 5 gain in importance. This aspect of a reaction mixture of clearly different ignition temperatures and the corresponding effect on each other is the main focus in section 6.3.3.

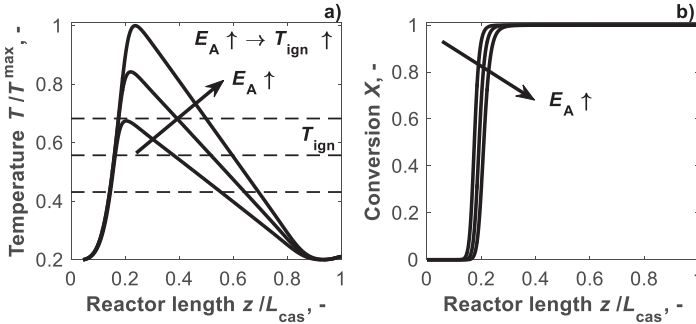


**Figure 6.13:** (a) Temperature and (b) conversion profile in the middle of switching period for different VOC components ( $E_A = 51\text{--}81 \text{ kJ}\cdot\text{mol}^{-1}$  in eq. 6.5) (parameter adopted from tab. 6.1), dashed lines in (a) correspond to ignition temperatures  $T_{\text{ign}}$  calculated by eq. B.42 (appendix B.6)

### Effect of catalyst and support

In this section, the focus is on the heat conduction and capacity of the solid catalyst phase and the corresponding support material, respectively. Usually, to avoid hot spots in the reactor fixed bed the catalyst is diluted by the limited surface material,  $\alpha\text{-Al}_2\text{O}_3$  (Brinkmann et al., 1999). Compared to the catalyst support  $\gamma\text{-Al}_2\text{O}_3$  the inert material  $\alpha\text{-Al}_2\text{O}_3$  offer a higher density and heat capacity (Yaws, 1999). Independent from catalytic activity the heat transfer and thermal conductivity of these two limit cases is studied below. Therefore, in fig. 6.14 the calculated temperature and conversion profiles of the heat capacity and heat conductivity variation is shown, respectively.

The main advantage of the LR concept is that the heat transfer between the gas and solid phase is optimized (Barresi et al., 1999). Thus, additional heat exchanger units can be omitted (Fissore et al., 2003). The heat transfer between the phases involved, is a function of the dimensionless Reynolds and Prandtl number (Verein Deutscher Ingenieure, 2006). Based on this, the variation of the heat capacity does not affect the heat transfer kinetic and accordingly the shape of the exothermal reaction and leading thermal front, respectively. Moreover, the adiabatic temperature rise depends on reactant and reaction properties only (part of eq. 6.2). Accordingly, the maximum temperature is constant in this study (fig. 6.14a). However, the variation of the solid phase heat capacity includes changes in switching time (eq. 6.4). This behavior is expressed in the derivation of the front velocities (eqs. 6.1 and 6.2). For the presented results, the range of the switching times correspond to 37–111 min. In case of an experimental validation or industrial application such fluctuations of the catalyst and inert particle distribution have to be considered (Zahn, 2012). Depending on the magnitude of the fluctuations, different switching times of the reactor segments can be observed.

The variation of the catalyst support or inert material is attended by a modification of the effective heat conductivity of the solid phase. The results of this modification are shown in fig. 6.14c-d. An increase of the effective heat conductivity leads to smearing of the exothermal reaction front and a corresponding reduction of the maximum temperature. Further the gradient of the leading thermal front is decreased as well.

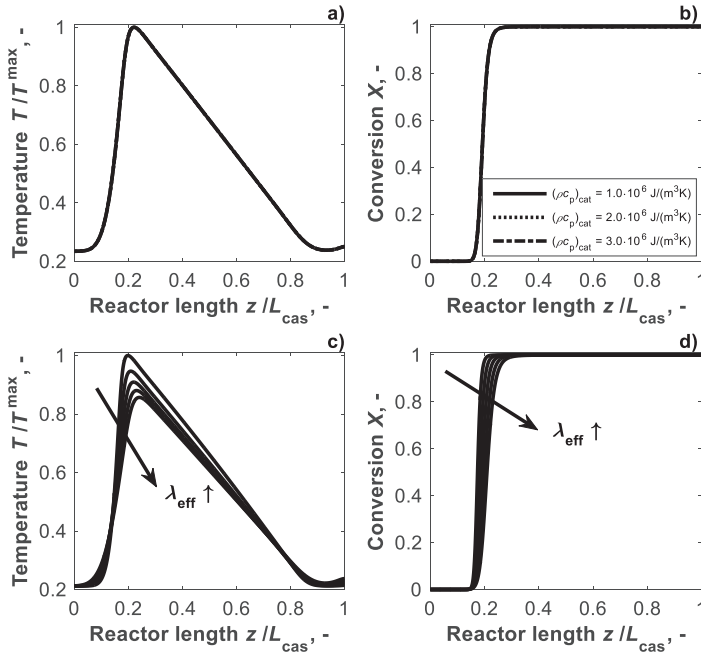


**Figure 6.14:** (a and c) Temperature and (b and d) conversion profile in the middle of switching period for (a and b) different catalyst support materials using a constant normalized switching time ( $\gamma = 1.00$ ; further parameter adopted from tab. 6.1) and for (c and d) increasing effective heat conductivity of the bulk material

Using a single reactant inlet, the LR concept could be demonstrated successfully. However, the small operation window of stable ignited conditions is limited by several factors as characterized in the presented study. Accordingly, the switching time has to be adjusted on the reaction properties (residence time and catalyst support). Additionally, the maximum temperature, which is limited by the experimental equipment, is affected by residence time, initial reactant concentration and the reactant component. As assumed in eq. 6.1 the influence of the inert gas phase properties is insignificant.

### 6.3.3 Multi reactant simulation study

In the following section, the theoretical LR simulation study is continued for a multi-reactant inlet. Therefore, the inlet gas phase is extended by a second reactant. Using an industrial reactant mixture, the determination of the optimal switching time to achieve total conversion of all reactants requires background knowledge of the reaction kinetics and the LR concept. The simplified power law reaction kinetic model of this additional feed gas is presented by eq. 6.5. The used kinetic parameters for both components are shown in tab 6.2. The reaction constants  $k_{\infty, jR}$  and the activation energies  $E_{A, jR}$  correspond to the minimum and maximum value investigated in the single component model study (tab. 6.1).

**Table 6.2:** Kinetic parameters of the second reactant, remaining parameters adopted from tab. 6.1

Parameter	Value	Parameter	Value	Parameter	Value
$\Delta h_{R,1}$ , kJ·mol <sup>-1</sup>	-141	$k_{\infty,1}$ , s <sup>-1</sup>	2973	$E_{A,1}$ , kJ·mol <sup>-1</sup>	51.512
$\Delta h_{R,2}$ , kJ·mol <sup>-1</sup>	-206	$k_{\infty,2}$ , s <sup>-1</sup>	29732	$E_{A,2}$ , kJ·mol <sup>-1</sup>	81.512

First results of this study are already presented in section 6.3.2. Based on educt reactivity and thermodynamic reaction properties the formed temperature and component conversion profiles vary strongly (fig. 6.13). In (Zahn, 2012) a bifurcation analysis of the LR operation using a binary mixture revealed different, nonuniform temperature profiles. The explanation is given by different exothermal reaction front velocities (see also eq. 6.2). Based on these velocities, two distinct operation isola of stable cyclic ignited conditions as function of the switching time are formed, one for each reactant. Operating in the higher temperature operation isola, complete conversion for all reactants is achieved. Using the low temperature switching time isola as operating conditions the second reactant offers incomplete conversion. Between these operation windows complex dynamic behavior can be observed. Furthermore, the inlet mixture ratio as well as the total flow-rate are setting parameters to affect the LR operation.

To transfer these results to the present study different inlet concentrations as function of the normalized switching time  $\gamma$  are shown in fig. 6.15. The upper row illustrates temperature and conversion profiles which are calculated using  $c_1^{\text{in}} = 0.25 \text{ mol}\cdot\text{m}^{-3}$  and  $c_2^{\text{in}} = 0.05 \text{ mol}\cdot\text{m}^{-3}$  as inlet concentrations, respectively. In the second row the ratio of the inlet

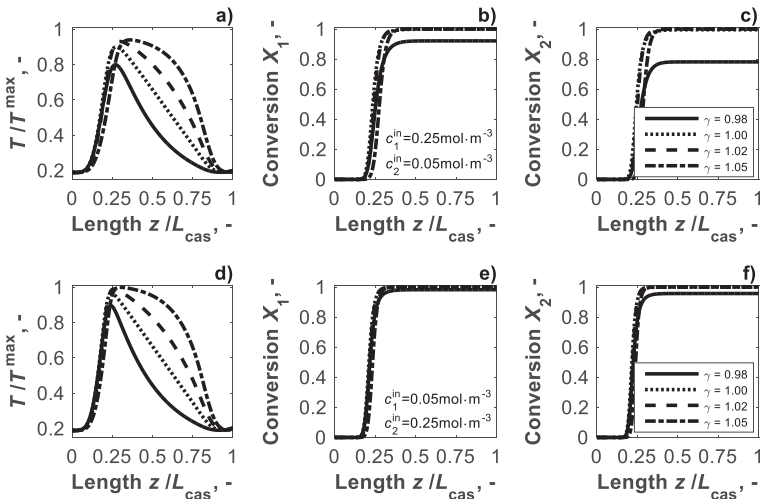


**Figure 6.15:** Cyclic steady state profiles of (a and d) normalized temperature ( $T^{\text{max}} = 1578 \text{ K}$ ), (b and e) conversion of component 1 and (c and f) conversion of component 2 as function of varies switching times  $\gamma$  in open loop control (section 6.2.1); (a-c)  $c_1^{\text{in}} = 0.25 \text{ mol}\cdot\text{m}^{-3}$  and  $c_2^{\text{in}} = 0.05 \text{ mol}\cdot\text{m}^{-3}$  and (d-f)  $c_1^{\text{in}} = 0.05 \text{ mol}\cdot\text{m}^{-3}$  and  $c_2^{\text{in}} = 0.25 \text{ mol}\cdot\text{m}^{-3}$  (further parameters adopted from tabs. 6.1-6.2)

component concentrations is the other way around. Compared to the single component calculations in fig. 6.13 the total inlet concentration is set to be constant. It is obviously, that for the first set of inlet conditions especially in the fast switching regime total conversion of the second component is not achieved (fig. 6.15c). A further increase of the switching velocity leads to an extinction of both reactants. Based on (Zahn, 2012) the fast switching regime operates in the low temperature operation isola. The maximum temperature for this switching time corresponds to 80 % of the absolute maximum temperature (fig. 6.15a). If the inlet concentration of the second component is increased the LR operates in the higher temperature isola (fig. 6.15d). Accordingly, total conversion of both components can be observed. Besides independent from inlet mixture ratio the shape of the reactor temperature as function of the normalized switching time  $\gamma$  corresponds to single reactant analysis (fig. 6.13 in section 6.3.2).

The second part of the multi-component feed LR analysis focuses on the total inlet reactant concentration variation ( $c_{tot}^{in} = 0.05-0.30 \text{ mol}\cdot\text{m}^{-3}$ ). Therefore, in fig. 6.16a-c the reactor behavior as function of component 1 is presented. The second component inlet concentration and the normalized switching time are set constant ( $c_2^{in} = 0.05 \text{ mol}\cdot\text{m}^{-3}$  and  $\gamma = 1.00$ ). In fig. 6.16d-f the inlet concentration of component 2 is varied and component 1 is fixed ( $c_1^{in} = 0.05 \text{ mol}\cdot\text{m}^{-3}$ ). Remember, the frequency factor, the activation energy and the reaction enthalpy of  $r_1$  are decidedly lower compared to the second reaction (tab. 6.2). Accordingly, the reactivity and the produced thermal energy of the first reaction are lower

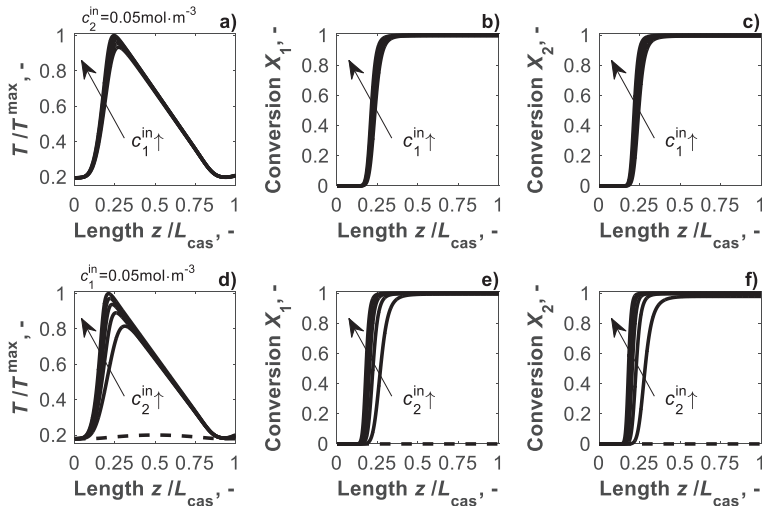


**Figure 6.16:** Cyclic steady state profiles of (a and d) normalized temperature, (b and e) conversion of component 1 and (c and f) conversion of component 2 for (a-c) as function of the inlet concentration of component 1  $c_1^{in} = 0.00-0.25 \text{ mol}\cdot\text{m}^{-3}$  and constant component 2 inlet concentration ( $c_2^{in} = 0.05 \text{ mol}\cdot\text{m}^{-3}$ , further parameters adopted from tabs. 6.1 and 6.2) and (d-f) as function of the inlet concentration of component 2  $c_2^{in} = 0.00-0.25 \text{ mol}\cdot\text{m}^{-3}$  and constant component 1 inlet concentration ( $c_1^{in} = 0.05 \text{ mol}\cdot\text{m}^{-3}$ , further parameters adopted from tabs. 6.1 and 6.2)

as well. Thus, it can be mentioned for analyzing the first row of fig. 6.16 a small amount of component 2 is sufficient to get stable ignited conditions. If the inlet concentration of component 1 is increased only a marginal effect for the maximum temperature or exothermal reaction front shift can be observed. Based on this knowledge it can be concluded that the system operates in the higher temperature isola, where total conversion of all reactants is obtained.

Analyzing the second row (fig. 6.16d-f) the inlet concentration ratio of the reactants is switched. Obviously, using only component 1 as feed, extinction occurred (dashed line in fig. 6.16d). If the feed concentration of component 2 is increased, the maximum temperature is increased as well. Thus, stable ignited periodic operation is possible. However, for the low inlet concentration range total conversion of both reactants is not achieved. Accordingly, for these inlet conditions the LR system operates in the lower temperature isola.

Based on these calculations it can be concluded, that an additional reactant, which offers a higher ignition temperature, in feed mixture is totally oxidized as well, profit from the exothermal heat energy release of the main reactant. However, in the opposite the exothermal energy release is too low and total conversion is not achieved for the second reactant. To avoid this, the second component has to be in excess (Zahn, 2012). Thus, consider these results in the aspect of the industrial exhaust gas purification in the LR concept, complex reactant gas mixtures are feasible to total oxidized autothermal.

## 6.4 Experimental results of hydrocarbon total oxidation using LR concept

In this section, the extensive LR performance results obtained theoretically for single and multi-component feed using a simplified kinetic model will be transferred into an experimental investigation. As a real VOC system, the total oxidation of ethylene and propylene on a  $\text{CrO}_x/\gamma\text{-Al}_2\text{O}_3$  catalyst is used (fig. 5.2 in section 5).

At first the developed experimental pilot plant is introduced. It is an extension of the plant described in (Zahn, 2012).

Then experimental results of the LR concept using the total oxidation of hydrocarbons will be discussed. The main focus is on achieving stable ignited conditions for different reactant species, reactant inlet concentrations and total residence time.

### 6.4.1 Experimental Loop Reactor equipment

The experimental pilot plant was designed and constructed at the Max Planck Institute (MPI) in Magdeburg. The set-up was installed in the course of this thesis project in close cooperation with the electronic and mechanical workshops from the MPI.

The test facility was subdivided in three parts. The gas supply unit provides the VOC example reactants ethylene (purity 99.95 %) and propylene (purity 99.5 %) diluted in air (technical grade) or nitrogen (purity 99.995 %). A second feed gas stream for an improved dosing concept between the reactor segments was available (Feed 2 in fig. 6.17). For the second feed gas two other VOC example gases were provided. To expand the reactant mixture, the second stream could be fed at the main inlet position as well. The individual component streams were adjusted using mass flow controller types *F-201CV-100* (hydro-

carbons), *F-201AV-50K* (air) and *F-201C-FBC* (nitrogen) from *Bronkhorst* (appendix D).

The reactor part consisted of two segments as shown in fig. 6.17. An additional fixed-bed was filled with  $\alpha\text{-Al}_2\text{O}_3$  (not shown) and used as preheating system for an appropriate start-up behavior (see also section 6.3.2). The specified process line of several operation modes was controlled by nine on-off valves and presented in tab. 6.3. The thermal coupling in the LR concept requires temperature-resistant pneumatic valves (Y104 and Y204 in fig. 6.17, series U from *Swagelok*,  $T^{\text{max}} = 648\text{ }^\circ\text{C}$ ) between the reactor segments. The valves in front and behind the reactor cascade operate in a temperature range below  $80\text{ }^\circ\text{C}$ , respectively.

The designed operation modes are listed in tab. 6.3. The first three were already introduced in (Zahn, 2012) and corresponds to the standard cyclic LR operation in a two bed configuration. At the preheating procedure the gas flows through the preheater and subsequent the reactor cascade. Following, the cyclic operation starts with the cold feed on R1 and the product outlet on R2. If the exothermal reaction front is leaving the first segment, the position is switched. The advanced LR operation includes the additional reactant dosing between the reactors to stabilize the cyclic ignited operation. The additional feed is introduced using the valves Y103 and Y203, respectively. Further information of the improved dosing concept to the area of application is presented in a parametric study in appendix B.5.

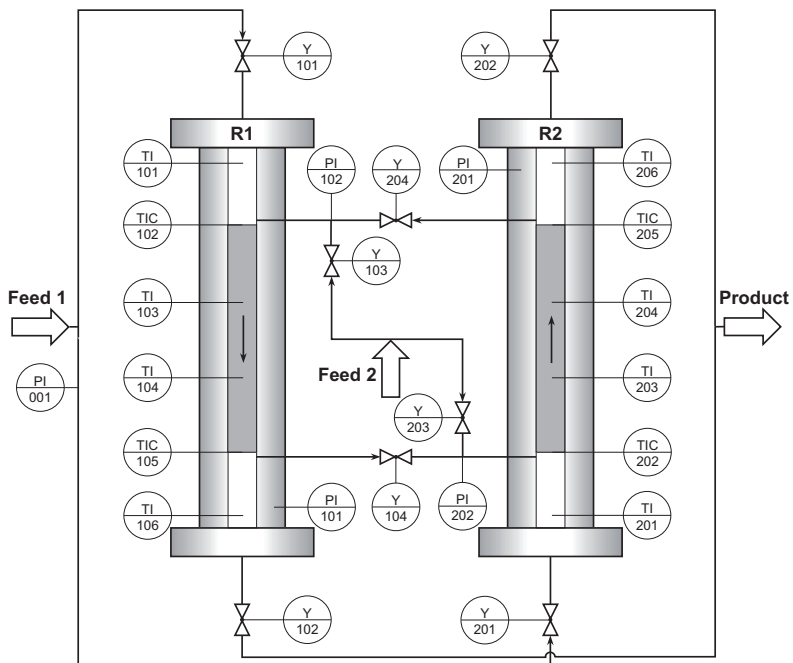


**Figure 6.17:** Schematic illustration of the process flow diagram of the reactor part of the constructed pilot Loop Reactor plant

**Table 6.3:** Valve assignment of several operation modes of the constructed pilot LR plant adopted from (Zahn, 2012)

Operation mode	Y001	Y101	Y102	Y103	Y104	Y201	Y202	Y203	Y204
preheating	1	0	0	0	1	0	1	0	0
Without additional dosing (Feed 2 = 0 in fig 6.17)									
Feed on R1	0	1	0	0	1	0	1	0	0
Feed on R2	0	0	1	0	0	1	0	0	1
With additional dosing (Feed 2 $\neq$ 0 in fig 6.17)									
Feed on R1	0	1	0	1	0	0	1	1	0
Feed on R2	0	0	1	0	1	1	0	0	1

To ensure adiabatic behavior of the reactor segments several studies of static (Klerk, 2005) and dynamic (Fissore et al., 2005; Hevia et al., 2006; Zahn, 2012) operations were already presented. In this work, the reactor segment consisted of a double jacket contain an evacuated jacket volume to minimize radial heat conduction controlled by PI101 and PI201 (fig. 6.17), respectively. Energy losses were reduced using a flexible ceramic canvas heat shield (3M™ Nexte™), which was fixed on a steel grid. Further insulation was achieved by stone wool within the void between the radiation shield and the reactor over-jacket. Thus, the ratio of reactor length ( $L_{seg} = 0.45$  m), inner diameter ( $d_{seg} = 0.025$  m) and catalyst particle size ( $d_p = 0.001$  m) was adjusted with respect to the pressure drop and maldistribution at the reactor wall according to (Winterberg and Tsotsas, 2000). The pressure drop of each reactor and the corresponding absolute pressure was monitored by pressure transmitters (series *BTE*, *Tetra Tec*). The catalyst bed was fixed by metal sieves. Close to these sieves the connection lines between the reactors were placed in order to increase the distance to the flanges to reduce the effect of the dynamics of the temperature fronts. These lines were as short as possible and heated to compensate heat losses of the flanges and high temperature valves (Y104 and Y204 in fig. 6.17). To avoid an oversized energy input, the temperature controller of the heating band (Co. *Horst*) adjusted the out- and inlet temperature of the reactors, respectively. Based on the cyclic heating and cooling of the fixed-bed thermal forces had to be considered. To avoid a structural damage of the reactor pipe, these forces were taken up by a bellow. To minimize the effect on the moving fronts the bellow was installed outside the catalytic fixed-bed on top of the inner reactor pipe.

To exploit the complete reactor length and improve the moving front observation, large inert heat transfer sections on the reactor entrance, which were described in (Brinkmann et al., 1999) were omitted. Each reactor segment was filled with 0.165 kg  $\text{CrO}_x/\gamma\text{-Al}_2\text{O}_3$  catalyst particles ( $d_p = 0.001$  m) encased by 0.02 m inert material ( $\alpha\text{-Al}_2\text{O}_3$ ) at in- and outlet position to prevent catalyst discharge, respectively. The observation of the moving temperature fronts along the catalyst fixed-bed was realized by stainless steel thermocouples of 0.001 m diameter in the center of the bed. To avoid radial heat bridges the thermocouples were installed from the reactor bottom. Accordingly, different lengths were inserted. The accurateness of the sensor position depends on the length and amounts to  $\pm 0.003$  m. However, using this method experimental error introduced by axially non-uniform maldistribution, heat conduction and undesired side reaction can occur (Zahn, 2012).

The third part of the experimental plant consisted of the analytics implemented. The quantitative analysis of the gas composition was realized by a FT-IR from *Gasmet* (cell length 5.0 m) which was already introduced in section 5.4.2. In addition, a gas chromatograph (*Agilent 6890 GC*) combined with a mass spectrometer (*Agilent 5973 MS*) was used. The setup GC-MS analytic can be referred in section 5.3. The gas phase sampling was done by on-off magnet valves (*6011 Bürkert*) and mass flow controller type *F-201C-FBC* from *Bronkhorst* at several positions in the experimental plant. Thus, total reactant conversion and product yield of each reactor segment can be observed. In order to reduce the dead volume and product condensate within the sampling system, 1/16" heated lines were installed. The corresponding schematic illustration of the analytic unit is given in the appendix D.

In order to purify exposed exhaust gases from the LR and analytic system a catalytic post-combustion reactor was installed (not shown in fig. 6.17). This reactor was filled with a platinum catalyst and works at 450 °C. The reaction temperature was set using heating sleeves from *Horst* and monitored by several thermocouples. For a sufficient air supply an additional air flux was given by a mass flow controller from *Bürkert* (*type 8712* with profibus) (Hamel, 2008).

The system control of the experimental LR plant was realized by a *Siemens SIMATIC PCS7* system. This system was able to control the installed thermocouples, the gas phase flow-rates and the valve positions. Additionally, the data recording and safety as well as pre-processing and post processing procedures can be implemented. Thus, the already introduced open and closed loop switching control concepts (Barresi et al., 1999; Brinkmann et al., 1999; Zahn et al., 2011) of the LR system was realized (see also section 6.2).

#### 6.4.2 Experimental observed periodic operation

In fig. 6.18 are illustrated experimentally observed temporal temperature profiles. The inlet volumetric flow-rate was set to  $\dot{V}_{\text{tot}} = 825 \text{ l}\cdot\text{h}^{-1}$  at ambient temperature. This corresponded for  $m_{\text{cat}} = 0.165 \text{ kg}$  to a catalyst weight to volumetric flux ratio of  $W/F = 720 \text{ kg}_{\text{cat}}\cdot\text{s}\cdot\text{m}^{-3}$ . The inlet molar ratio of propylene was set  $x_{\text{C}_3\text{H}_6}^{\text{in}} = 0.4 \%$ . Cyclic steady state operation was controlled by the closed loop controller concept adopted from (Zahn et al., 2011). The closed loop control concept applied was based on the Multi-Sensor approach (section 6.2.2). To remember, at the end of each reactor fixed bed one thermocouple (TIC105 and TIC205) was installed. If the temperature set-point ( $T_{\text{sw}} = 400 \text{ °C}$ ) has been reached from top to down, the switch of the inlet and outlet ports were triggered. Thus, robustness and a fast start-up procedure were achieved (Brinkmann et al., 1999; Zahn et al., 2011).

The duration of the start-up phase (approx. 5.5 h) is illustrated in fig. 6.18a. In this time, the reactor cascade entrance is heated up above 400 °C. Within the first reactor segment a temperature difference from entrance to outlet position of 60 °C was observed. Afterwards, periodic operation was initiated. The cyclic steady state was attained approximately after 15 switches. Within this initial operation, the closed loop controlled switching time was decreased from 55 to 32 minutes for the first reactor segment (fig. 6.19a). During the preheating procedure, the entrance of the first segment was heating up as well. Thus, the first tacts were affected by heating release of the segment shell. Accordingly, based

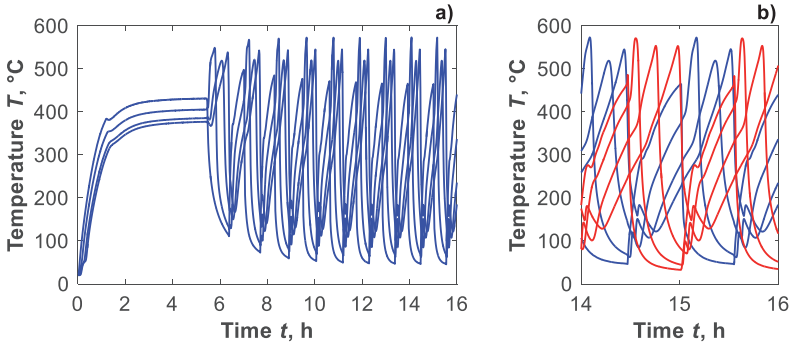


**Figure 6.18:** Closed loop reactor operation (section 6.2.2): (a) Temperature signals of reactor 1 (TI102-105) for start-up behavior and periodic operation and (b) temperature signals of reactor 1 (blue lines, TI102-105) and reactor 2 (red lines, TI202-205) within two reactor cycles

on this none ideal adiabatic condition, the exothermic reaction front was smearing. Consequently, the switching time was increased during the maximum temperature was decreased, respectively. The cyclic steady state maximum temperature was reached after seven tacts and close to 575 °C for both segments (fig. 6.19b). The different obtained maximum temperatures inside one and the same segment within one tact can be explained by the thermocouple positions. During the segment filling procedure, it was attempt to place the measuring points directly in the catalyst bed center. However, because of mechanical stress of the thermocouples this precision is not warranted.

The transfer of the time dependent temperature signals (fig. 6.18) to spatial profiles is illustrated in fig. 6.20. Based on thermocouple positions inside the catalyst fixed bed, the upper diagram represents the reaction temperature along the reactor cascade within the 40th switching period. The feed position is in front of the first reactor (see arrow at  $z/L_{\text{cas}} = 0$ ). The pipe distance between the reactors is excluded. In order to follow the front moving, several snapshots (every 10 min) of the temperature profile are shown ( $t_0 < t_1 < t_2 < t_3 < t_{\text{end}}$ ). The relatively sharp exothermic reaction front was moving inside the first segment and offered a maximum temperature of close to 575 °C. Simultaneously, the leading thermal front heated up again the second segment. If the feed position was switched (see arrow at  $z/L_{\text{cas}} = 0.5$ ) the exothermic reaction front was moving through the second seg-

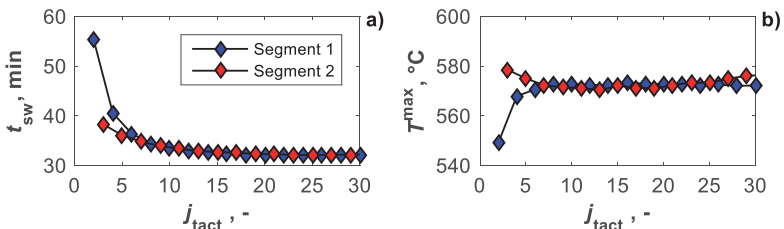


**Figure 6.19:** Temporal course of (a) experimental observed switching time for closed loop control (section 6.2.2) and (b) the maximum temperature of reactor one and two for increasing tact index

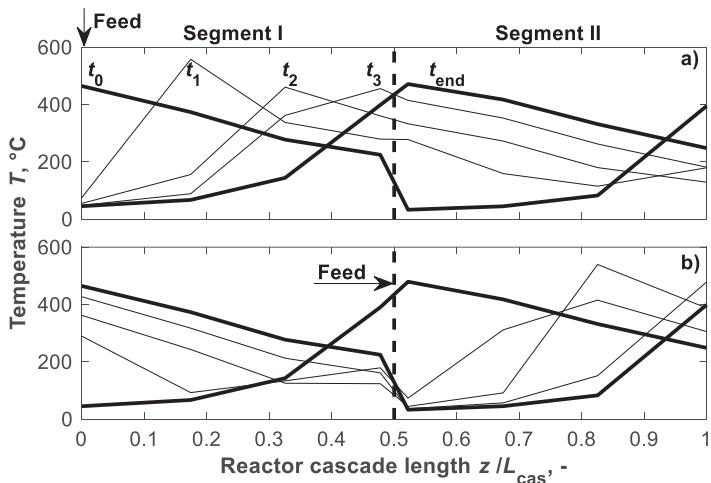


**Figure 6.20:** Closed loop reactor operation (section 6.2.2): temperature profiles as function of the reactor cascade length for two switching periods. Snapshots are shown every 10 min ( $t_0 < t_1 < t_2 < t_3 < t_{end}$ ). (a) feed on the first segment ( $z/L_{cas} = 0$ ) and (b) feed on second reactor segment ( $z/L_{cas} = 0.5$ )

ment and the first reactor was heated up again (lower diagram in fig. 6.20).

The characteristic properties of the observed temperature profiles are in agreement to the model study (section 6.3). A self-sharpening exothermal reaction front as well as a dispersive leading thermal front can be observed. The experimental front velocities of the first reactor segment were determined to  $2.36 \text{ cm} \cdot \text{min}^{-1}$  for the thermal front and  $1.41 \text{ cm} \cdot \text{min}^{-1}$  for the exothermal reaction front. Based on these front velocities the thermal regeneration is considerably faster than the reaction is in progress. Thus, cyclic stable ignited conditions are adjusted. Experimental front velocity fluctuations between the reactor segments can be explained by different void fractions. If the void fraction is increased the front velocity increases as well (Zahn, 2012).

As mentioned in section 6.4.1 heat losses at the connection pipe and the high temperature valve between the reactor segments could not be avoided experimentally. To reduce and compensate this energy loss diverse strip heater were installed. However, the temperature profiles offered a kink at the interface between the reactors and the transfer of the leading thermal front to the next segment was hindered. Further experimental uncertainties occurred in the non-ideality of the thermal insulation of the reactor segments and axial as well as radial heat dispersion in the catalyst fixed bed.

### 6.4.3 Single component feed gas: ethylene or propylene

The experimental investigation of oxidizing a single reactant was realized using propylene or ethylene as reactant and air as oxidizing agent in the feed gas mixture. To maintain stable ignited conditions, the closed loop control concept was applied ( $T_{sw} = 400 \text{ °C}$ ) (section 6.2.2). Further reaction conditions were adopted from section 6.4.1. Based on the

obtained modeled results in section 6.3 several aspects were evaluated experimentally, namely the influences of residence time, initial concentration and feed component.

### Residence time

Following the theoretical analysis given in section 6.3 the variation of the total volumetric flow-rate is studied in fig. 6.21. There experimental observed temperature profiles as well as maximum temperature and average switching time are shown. The volumetric flow-rate was varied in the range between  $500 \text{ l}\cdot\text{h}^{-1}$  and  $1000 \text{ l}\cdot\text{h}^{-1}$ . The inlet molar ratio of propylene was set constant to 0.4 %. As expected the switching time was adjusted to the corresponding volumetric flux by the closed loop controller concept (fig. 6.21a). Based on the exothermal reaction front velocity calculation (eq. 6.2)  $u_R$  was directly proportional to  $u_{\text{gas}}$ . Accordingly, if the gas velocity was doubled the front velocity was doubled as well. Thus, the experimental observed switching time (see also controller concept in section 6.2.2) was halved. This is seen in fig. 6.21a.

Similar to the theoretical results the maximum temperature of the reaction front was decreased by increasing residence time (fig. 6.21b-c). However, the observed effect was smaller pronounced as predicted in the feasible study (see also fig. 6.10). The reason for the deviations from theoretical prediction can be explained with non-ideal adiabatic reactor behavior. The model study did not include heat losses over the reactor segment length and especially between the segments. Moreover, these heat losses by thermal radiation increase by the fourth cube with temperature. Correspondingly, the maximum temperature raise with total volumetric flux increase is reduced.

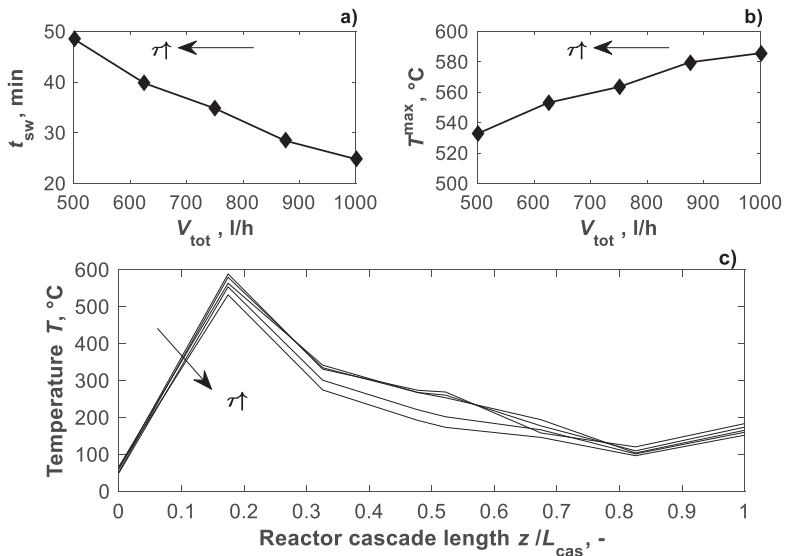


**Figure 6.21:** (a) Experimental observed cyclic steady state switching time  $t_{sw}$ , (b) maximum temperature  $T^{max}$  and (c) temperature profiles along the reactor cascade (exothermal reaction front directly positioned at T103 (see also fig. 6.17)) for different total flow-rates in closed loop control of the first segment as function of the total flow-rate ( $\chi_{C_3H_6}^{in} = 0.40\%$ ;  $T_{sw} = 400^\circ\text{C}$ )

Depending on the maximum temperature the leading thermal front is more or less flattened with a residence time increase (fig. 6.21c).

**Inlet concentration** The experimental series of different propylene molar inlet are shown in fig. 6.22. The propylene molar inlet ratio  $x_{C_3H_6}^{in}$  was varied between 0.35 % and 0.5 %. The total volumetric flux was set constant at  $750 \text{ l}\cdot\text{h}^{-1}$ . Each set of inlet conditions was fixed for at least 24 hours. As expected the adiabatic temperature rise led to an increase of the maximum temperature of the exothermal reaction front (fig. 6.22b-c). This was accompanied by largely increased switching times ranging from about 35 min up to 45 min for segment 1 (fig. 6.22a). As illustrated in eq. 6.11 the increased adiabatic temperature rise decreased the exothermal reaction front velocity, which required larger switching times in closed loop reactor control. Using propylene molar ratios below 0.4 % reactor extinction occurred (dashed line fig. 6.22c).

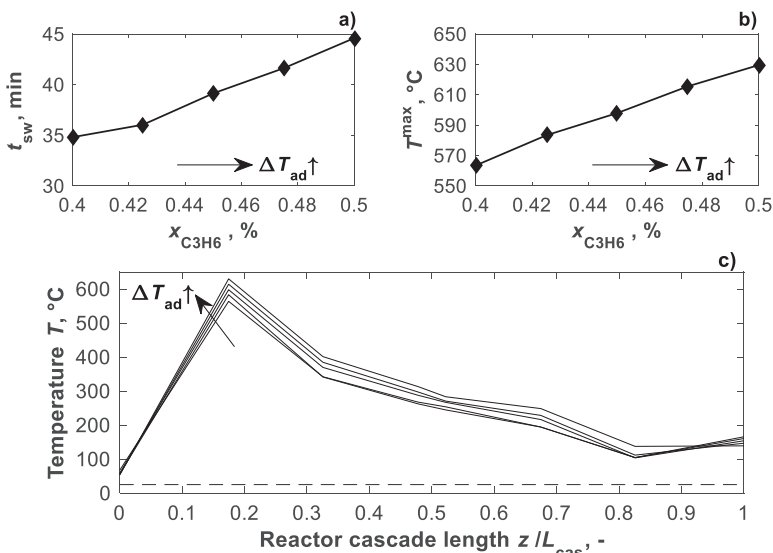


**Figure 6.22:** (a) Experimental observed cyclic steady state switching time  $t_{sw}$ , (b) maximum temperature  $T^{max}$  and (c) temperature profiles along the reactor cascade (exothermal reaction front directly positioned at T103 (see also fig. 6.17)) for different propylene inlet concentrations, in closed loop control as function of the inlet propylene molar ratio  $x_{C_3H_6}^{in}$  ( $\dot{V}_{tot}^{in} = 750 \text{ l}\cdot\text{h}^{-1}$ ;  $W/F = 790 \text{ kg}\cdot\text{s}\cdot\text{m}^{-3}$ ;  $T_{sw} = 400 \text{ }^\circ\text{C}$ )

**Reactant species** Analyzing the simulation study for single component feed the most pronounced influence at the reactor cascade was due to the reactant oxidized. As shown above the modeled maximum temperature increased for higher activation energies (fig. 6.13). Based on these results, in fig. 6.23 experimental observed temperature profiles of ethylene and propylene as single reactant inlet are presented, respectively. For comparison, each reactant inlet concentration was set 0.6 % at a total volumetric flux of

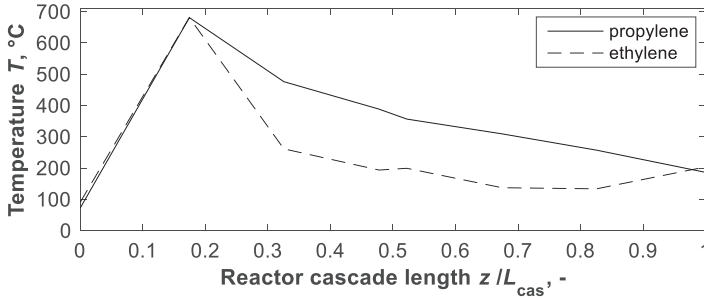


**Figure 6.23:** Experimental observed cyclic steady state temperature profiles along the reactor cascade (exothermal reaction front directly positioned at T103 (see also fig. 6.17)) in closed loop control of the first segment for ethylene (dashed line) and propylene (solid line) as inlet component ( $x_{ic}^{in} = 0.6\%$ ;  $V_{tot}^{in} = 750 \text{ l}\cdot\text{h}^{-1}$ ;  $W/F = 790 \text{ kg}\cdot\text{s}\cdot\text{m}^{-3}$ ;  $T_{sw} = 400 \text{ }^\circ\text{C}$ )

$750 \text{ l}\cdot\text{h}^{-1}$ . As expected the temperature profile shapes were almost identical for both reactants. However, the model predicted maximum temperature increase was unverifiable. The experimental observed difference was below  $1 \text{ }^\circ\text{C}$  and corresponded to the measuring error of the applied thermocouple. In contrast the comparison of the observed reaction front velocity possessed clear differences. Provided that the maximum temperature  $T^{\max}$  was constant, eq. 6.2 offers that the reaction front velocity  $u_R$  decreases, if the adiabatic temperature rise  $\Delta T_{ad}$  is increased. Accordingly, the adjusted switching time (closed loop control with  $T_{sw} = 400 \text{ }^\circ\text{C}$ ) for propylene ( $t_{sw} \approx 62 \text{ min}$ ) was obviously higher than for ethylene ( $t_{sw} \approx 30 \text{ min}$ ). Based on these values the reaction front velocity for the ethylene inlet was twice as big as for the propylene inlet. However, if similar gas phase properties (reactants were diluted in air) and total flux conditions were assumed, the predicted reaction front velocity ratio by eq. 6.2 was less than the experimental observed value. This phenomenon is explained by non-ideal adiabatic reactor segment behavior. Additional energy accumulation effects of the reactor shell distort the observed front velocities. Independently from reactant gas the controller concept enabled an ignited cyclic steady state operation.

Considering the thermal front velocities, no differences were obtained. These velocities depend only on the gas phase velocity and physical properties of the gas phase and solid catalyst phase. These parameters were almost constant. However, because of different reaction front velocities, the thermal front was far ahead and a broadened high temperature zone was occurred for the propylene feed.

#### 6.4.4 Mixture feed gas: ethylene and propylene

The LR performance is shown for mixture feed concentrations and the total flow-rate in fig. 6.24. The first row (fig. 6.24a) displays the thermocouple signal T1103 which was placed on the second position within the first reactor segment (see also fig. 6.17). Considering the time dependent temperature profile, changes in front velocity and maximum temperature can be observed. The second and third row (fig. 6.24b-c) illustrates the set inlet conditions

of the total flow-rate and the propylene and ethylene concentrations, respectively. The last row (fig. 6.24d) shows the adjusted switching time by the controller output.

The long time experiment was carried out over 4.5 days. After preheating the reactor cascade (first 5 hours) the reactant inlet concentrations of ethylene and propylene were varied at a constant total volumetric flow-rate. This first part started with a propylene molar ratio of 0.5 % at  $750 \text{ l}\cdot\text{h}^{-1}$  ( $x_{\text{C}_2\text{H}_4} = 0$ ). Following the propylene inlet concentration was step-wise decreased while the ethylene inlet concentration was step-wise increased. At the second part the reactant inlet concentrations were set constant ( $x_{\text{C}_3\text{H}_6} = 0.3 \%$  and  $x_{\text{C}_2\text{H}_4} = 0.25 \%$ ) and the total flow-rate was varied step-wise ( $V_{\text{tot}} = 500\text{--}1000 \text{ l}\cdot\text{h}^{-1}$ ). Each inlet condition set of these two parts was hold for 10 hours.

**Inlet concentration** As aforementioned, within the first part of the long time experiment, the reactant inlet concentrations were varied at a constant total volumetric flow-rate. As a result, the maximum temperature inside the catalytic fixed bed was increased with the ethylene molar fraction. The adjusted switching times by the controller concept became smaller revealing a higher exothermal reaction front velocity. (Zahn, 2012) explained this

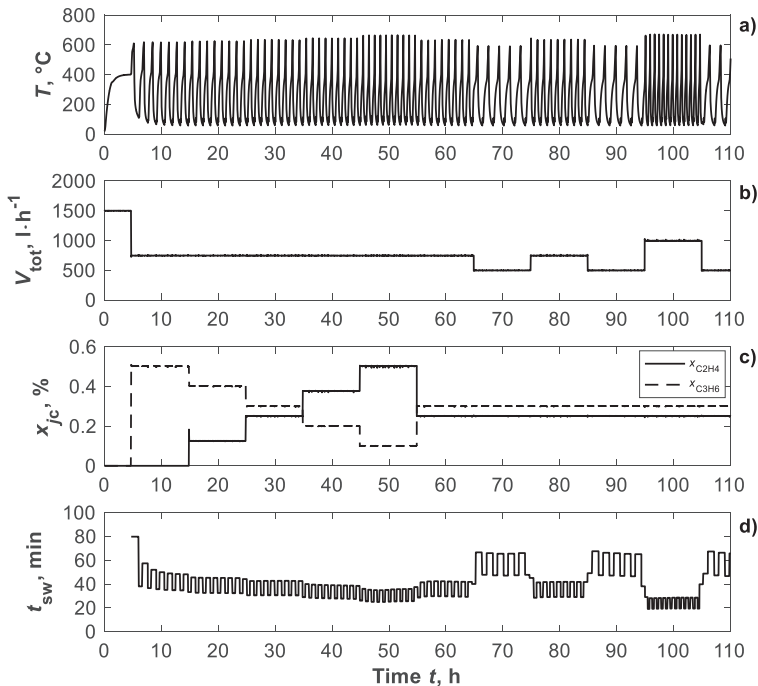


**Figure 6.24:** Experimental study LR performance by step wise input variation of reactant inlet concentration (ethylene/propylene mixture) and total flow-rate: (a) experimental observed temperature signal T1103 (see fig. 6.17), (b) total flow-rate, (c) ethylene and propylene inlet molar ratio and (d) switching time

phenomenon by reaction kinetics. As found before in the reaction kinetic analysis (section 5), the total oxidation of ethylene was much slower than the propylene oxidation. Accordingly, a decreased reaction rate led to a higher exothermal reaction front velocity and a maximum temperature increase. This phenomenon was already seen in the comparison of the different reactant species. In this connection, the switching time of ethylene as reactant was found to be approximately half of the switching time of propylene at otherwise constant conditions (section 6.4.3). This difference between the reactant species illustrates the importance of the detailed reaction kinetic analysis. Moreover, significant deviations between the reactor segments were observed. The switching time of the first segment was obviously larger than of the second segment. This can be explained by different front velocities within the segments caused by different void fractions.

Considering the controller performance, a stable ignited cyclic steady state operation for the complete mixture inlet concentration spectrum was observed. Large input steps in the feed concentration could be handled. However, the differences between the reactant species were marginal. The effect of more complex reactant mixtures could not be evaluated in the course of this thesis.

**Residence time** After 55 hours the reactant inlet concentrations were set constant and the total flow-rate was varied systematically. As already shown in the simulation (section 6.3) and the single reactant experimental study (section 6.4.3), an increased flow-rate pushed the exothermal reaction front as well as the leading thermal front faster through the cascade segments, respectively. Accordingly, the adjusted switching time by the controller concept was decreased by higher volumetric flow-rates. The effect of different switching times of the segments, caused by the different void fractions, was increased for the higher flow-rates. Compared to the mixture inlet concentration analysis the effect of the total flow-rate relating to the switching time and the maximum temperature was much more pronounced. This relation has to be considered in continuing experimental study.

Despite of the changes in the total flow-rate, the overall performance of the relatively simple controller applied can be positive evaluated. Stable ignited operation could be maintained over a longer time.

## 6.5 Validation of detailed kinetic model using single feed propylene

For a more detailed analysis of the experimentally observed temperature and conversion profiles of the LR concept, the simplified reactor and kinetic models used in section 6.3, are not sufficient. Therefore, to further quantify and characterize the experimental data, the detailed kinetic model of the total oxidation reactions determined via the GCCK approach (section 2.1 and 5) was applied. Moreover, deviations from adiabatic conditions due to energy losses and temperature dependent physical properties were considered in a more detailed reactor model. Hereby, the energy losses between the cascade segments, which were compensated by heating, were neglected. The set of equations forming the applied pseudo-homogeneous mass and energy balances as well as temperature dependent component properties are not given here. They are summarized in appendix B.4. The

use of this extended model was more time consuming. The computational effort of one switching period amounts approximately 10 hours.

To evaluate the model, in fig. 6.25 is given just one example of cyclic steady state LR operation ( $x_{C_3H_6}^{in} = 0.45\%$ ;  $\dot{V}_{tot}^{in} = 750\text{ l}\cdot\text{h}^{-1}$ ;  $W/F = 790\text{ kg}\cdot\text{s}\cdot\text{m}^{-3}$ ;  $T_{sw} = 400\text{ }^\circ\text{C}$ ). There the experimental and modeled temperature profiles are compared at one-third of the switching period (feed on  $z/L_{cas} = 0$ ). The modeled profiles are in qualitative agreement with the experimental data. A steep reaction front and a sharp decline of the leading thermal front within the first segment could be observed. Additional energy accumulation of the reactor pipe led to smearing of the experimental formed temperature fronts. Therefore, the base point of the temperature and reaction front differed from the model prediction. This was seen at the remaining reaction front at the cascade outlet directly after switching operation as well. For that, the experimental observed temperature at the outlet position was rising again. Further the maximum temperature of the reaction front was about  $90\text{ }^\circ\text{C}$  over-estimated.

To improve the model prediction, the LR model has to be stated more precisely. In addition to the catalytic fixed-bed, the reactor shell offered an energy accumulation as well. Therefore, the inlet gas mixture was preheated by the reactor shell before the exothermal reaction front was reached by the reactants. Thus, the experimental obtained exothermal reaction front was smeared which includes a reduced observed maximum temperature. Further simulation work should include more sophisticated rigorous reactor models.

About the transient start up period required to reach the constant pattern state of the exothermal reaction front no information can be provided here. Based on constructional limits the first thermocouple was positioned after one-third of the catalyst fixed bed. At this point the constant pattern state was already reached. This observation was in agreement with literature observations (Zahn, 2012).

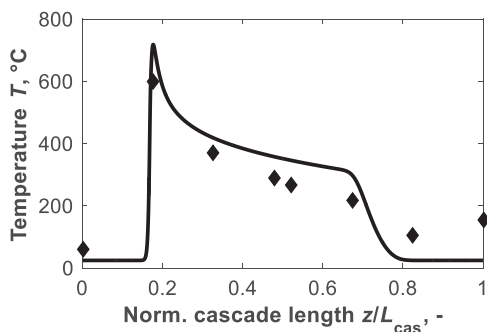


**Figure 6.25:** Comparison of experimental observed (symbols) and modeled (line) cyclic steady state temperature profiles along the reactor cascade in closed loop control operation for propylene as inlet component (exothermal reaction front directly positioned at T103 (see also fig. 6.17);  $x_{C_3H_6}^{in} = 0.45\%$ ;  $\dot{V}_{tot}^{in} = 750\text{ l}\cdot\text{h}^{-1}$ ;  $W/F = 790\text{ kg}\cdot\text{s}\cdot\text{m}^{-3}$ ;  $T_{sw} = 400\text{ }^\circ\text{C}$ )

## 6.6 Conclusions

The aim of this section was to investigate theoretically and experimentally the periodic operation of the challenging multi fixed-bed Loop Reactor concept for the oxidation of ethylene and propylene (section 5).

The multi fixed-bed Loop Reactor aims at trapping the exothermal reaction front in a reactor cascade by shifting the feed position into flow direction. Thus, an autothermal operation, in which the inlet flux is introduced at ambient temperature, can be achieved. To characterize the LR concept for single reactant inlet and industrial more relevant mixtures, a simulation study was realized. To reduce the computational effort at first a simplified reaction kinetic model was adopted from (Haynes and Caram, 1994). To reveal the reaction and temperature front velocities as well as the expected maximum temperature within the reactor cascade the segment number, switching time of the inlet and outlet ports, residence time and gas and catalyst phase properties are varied in a suitable range. The most significant effect on the maximum temperature is achieved by the chosen reactant. Accordingly, in an experimental validation, the reactant mixture composition has to be analyzed carefully. Further, to enable an ignited cyclic steady state operation the switching time  $t_{sw}$  has to be adjusted on external circumstances. Therefore, the closed loop control concept was applied (Zahn et al., 2011) and suitable switching temperatures  $T_{sw}$  were studied.

The second part of this section described the experiments performed in this work and present a model based analysis of the LR concept. To perform the experiments a new pilot plant unit was set-up and the total oxidations of ethylene and propylene in air were used (section 5). The corresponding reaction kinetic models were determined before as described in section 5 using the GCCK approach (section 2.1). Periodic operation of a two bed LR experimental plant was investigated. Systematic experiments of reactant inlet concentration and total volumetric flux variations in closed loop control reveal the domain of ignited reactor states. Simulation results using an augmented reactor model showed a good qualitative agreement with experimental observed data. Further improvements of reactor modeling should be done by more rigorous reactor models. Moreover, the total oxidation of mixtures of ethylene and propylene was studied. Larger feed fraction of ethylene leads to a faster reaction front, which is compensated by adjusting smaller switching times of the control concept. The multi reactant experiments of the LR concept also revealed, that for the observed ethylene and propylene mixtures the reactor control does not pose larger problems.

Finally, the full kinetic model of the total oxidation network of propylene determined by the GCCK approach (section 2.1 and section 5) was used together with a more detailed reactor model taking into account heat losses in order to predict experimental LR performance. The modeled temperature profile was in qualitative agreement with the experimental observed data. A steep reaction front and a sharp decline of the leading thermal front within the first reactor segment could be observed. However, deviations from adiabatic conditions due to energy accumulation of the reactor pipe lead to broadening of the experimental formed temperature fronts. This phenomenon was not in the reactor model

and therefore could not be predicted by the simulations. Further model predictions are required using more detailed rigorous reactor models.

# **Part IV**

## **Summary**



## 7 Overall Conclusions and Outlook

### 7.1 Overall conclusions

This thesis contributed to four problems of large relevance for chemical reaction engineering. At first, a powerful classical theoretical tool for analyzing reaction networks and quantifying reaction kinetics was described and reevaluated in order to promote its wider application. This concept was then applied in two different case studies in order to demonstrate its potential for quantifying rates in two industrially important fields of catalysis, namely homogeneous and heterogeneous catalysis. The last section of this thesis provided a contribution to future reactor technology. A challenging new dynamic reactor operation concept exploiting a periodically connection of several reactor segments was investigated both theoretically and experimentally.

#### **Analysis of reaction mechanisms and kinetics**

The design and optimization of chemical reactors requires reliable models capable to describe the kinetics of the reactions of interest in a broad concentration and temperature range. The frequently applied addition of catalysts in the same or another phase (homogeneous or heterogeneous catalysis) makes quantitative descriptions rather difficult.

Due to the complexity of the kinetics of simultaneously occurring reactions frequently simple empirical rate expressions are applied, as e.g. power laws. They can capture main features of the reaction kinetics and are in some cases in good agreement with available experimental data. However, due to their simplicity there are clear limitations of such non-mechanistic rate equations. Consequently, extrapolations beyond the range of measurements are highly uncertain.

In this thesis a very general and widely applicable methodology was first reviewed and subsequently applied in different case studies. The concept was first suggested by *Christiansen* already in the 1930's (Christiansen, 1931, 1935, 1953). More recently, it was "rediscovered", reviewed and evaluated by several authors (Helfferich, 2004; Murzin and Salmi, 2005; Marin and Yablonsky, 2011). The approach was designated in this thesis as "General Catalytic Cycle Kinetics (GCCK)". It is not based on the frequently applied concept of identifying in early stage rate determining steps in order to reduce the model. In contrast, it assumes pseudo-first order rate laws for all elementary steps and includes explicitly just one catalyst species. More than one catalyst species involved in the catalytic cycle cannot be handled by the standard GCCK approach. Nevertheless, a large number of unknown kinetic parameters arises, which have to be estimated based on experimental data. Hereby, there are frequently correlations between parameters, which inhibits their identification. This is the main reason, why the approach has been applied so far only rarely, mainly to analyze homogeneously catalyzed reactions. It has not reached wider recognition and acceptance.

After introducing the general framework, concepts were introduced and discussed mainly devoted to reduce the sizes of the models originating from the GCCK approach. The ill-posed inverse parameter estimation problems were treated in this thesis by means of reaction network decomposition and mathematical model reduction techniques. In order

to identify subsets of sensitive kinetic parameters, a model reduction technique based on singular value decomposition combined with a rank revealing QR factorization was applied. Using the strategy of the reaction network decomposition and the model reduction technique, the calculated confidence intervals of the estimated kinetic and catalyst equilibrium parameters could be significantly decreased for the examples considered.

Based on this theoretical introduction, in the next sections of this thesis two challenging example reaction networks coming from both homogeneous and heterogeneous catalysis are considered. In these two case studies, experimental data were readily available or were newly acquired in the course of this work. To accomplish the desired derivation of reduced mechanistic kinetic rate equations, beside the kinetic models, also suitable models were needed to describe the laboratory reactors used to generate the experimental data basis.

The description of the methods and of the tools for application and the successful demonstration and validation of the general GCK approach provided in this thesis should encourage its wider use.

### **Application of the GCK approach in homogeneous catalysis**

The rhodium-biphenos catalyzed hydroformylation of 1-dodecene with synthesis gas was investigated as a challenging and relevant example for a homogeneously catalyzed reaction. This reaction was carried out in a thermomorphic multi-component solvent system (olefin/decane/DMF). The network analysis was based on experiments performed in a broad range of temperatures, total pressures and partial pressures of carbon monoxide and hydrogen, respectively. The derivation of mechanistic kinetic rate models for the hydroformylation, hydrogenation and isomerization of 1-dodecene was based on the widely accepted *Wilkinson* catalytic cycle. Quantification of hydrogen and carbon monoxide gas solubilities was based on separate experiments and a two phase mass transfer model. The corresponding model parameters were estimated analyzing experimental data obtained in a batch reactor. The formation of the active catalyst in the resting state, i.e. the initial point of the catalytic cycles considered for the main and the side reactions, was described by a rhodium equilibrium balance approach. To correlate the amount of observed inactive catalytic species (e.g. a rhodium dimer) a function of partial pressures of hydrogen and carbon monoxide and of the rhodium precursor concentration was derived. The required equilibrium constant of the catalyst formation step could be also estimated based on experimental kinetic data. To reduce the number of parameters in the models the less important rates of the consecutive hydroformylation and hydrogenation reactions of iso-dodecene were described in a simplified manner by empirical power laws.

Since the simultaneous estimation of a large number of kinetic parameters is difficult due to numerous local optima, a reaction network analysis was performed first sequentially for four sub-networks with increasing complexity and only finally for the total network. The kinetic parameters estimated for the sub-networks were transferred to the progressively larger sub-network. The free parameters of the additionally required reactor models were identified by analyzing batch reactor runs. In order to identify subsets of sensitive kinetic parameters, the subset selection method was applied. The final set of kinetic parameters

was able to describe the main and most important side reactions in a broad range of temperatures, total pressures and partial pressures of hydrogen and carbon monoxide as well as concentrations of the active catalyst in the resting state.

The determined reaction kinetic models were applied and evaluated in different operating modes, namely batch, semi-batch, perturbed batch and continuous operation. The extrapolation of the estimated set of kinetic parameters in operation modes beyond batch runs failed. Only after modifying some reaction rate parameters, including the carbon monoxide order in the catalyst equilibrium equation as well as in eq. 4.2 the hydroformylation of 1-dodecene to iso-aldehyde, the kinetic models were able to describe experimental results observed using other operating modes, including continuous stirred tank reactor data. Finally, the reaction kinetic models were used to identify an optimal strategy for dosing the terminal olefin and the corresponding isomers in order to improve the yield with respect to the terminal aldehyde. Altogether, the derived and quantified mechanistic kinetic rate model is seen to be appropriate to design and optimize new reactor and process concepts for this type of homogeneously catalyzed multi-phase hydroformylation reactions.

The hydroformylation reaction network analysis performed has proven that the GCCK approach could be applied successfully for this example originating from homogeneous catalysis.

### **Application of the GCCK approach in heterogeneous catalysis**

Studying multi-phase systems additional phase equilibrium data of reactants and products have to be considered in kinetic modeling. Therefore, the GCCK approach was applied so far only rarely for heterogeneous reactions. In order to demonstrate its corresponding potential, the partial and total oxidations of ethylene, propylene, mixtures of both and carbon monoxide on a  $\text{CrO}_x/\gamma\text{-Al}_2\text{O}_3$  catalyst were studied. The mentioned reactions proceed in a broad range of temperatures and partial pressures.

The derivation of mechanistic rate models using the GCCK approach provides in general rate equations without any assumptions. The formulation of mechanistic rate approaches is in heterogeneous catalysis typically based on established reaction mechanisms, such as e.g. the *Mars/van Krevelen* and *Eley/Rideal* mechanisms. Considering the assumptions used in deriving these reaction mechanisms, it can be shown that the resulting rate expressions form subsets of the general rate equations obtained from the *Christiansen* methodology.

In order to support the parameter estimation, the kinetic and thermodynamic effects were separated in this work by acquiring experimentally additional phase equilibrium data. Single component adsorption isotherms were measured for all reactants and products in a broad temperature and concentration range. The quantification of the experimental adsorption isotherms occurred using the conventional *Langmuir* adsorption model. In this way the single component adsorption behavior could be characterized quite well. By means of the *Multi-Langmuir* model, based exclusively on the parameters of the single component isotherms, the competitive adsorption behavior of ethylene and propylene mixtures could be predicted as well. Using these separately determined adsorption parameters within the kinetic analysis, a more profound description of the reaction rates was feasible by separating kinetic and thermodynamic effects. This kinetic study of the partial and

total oxidation of carbon monoxide, ethylene and propylene occurred considering three different sub-networks. In order to describe the experimentally observed performance parameters, several postulated mechanistic kinetics were tested and ranked. The kinetic parameters of the best performed equations were selected and transferred to the progressively larger sub-network and finally to the total network. All sub-networks and the total reaction network could be well described by using one set of kinetic parameters. Based on this analysis, the carbon monoxide oxidation corresponds to the *Mars/van Krevelen* mechanism and the hydrocarbon partial and total oxidation reactions to the *Eley/Rideal* approach, where the hydrocarbons react from gas phase with adsorbed oxygen. The validation of the parameterized reaction model occurred by analyzing several inlet mixtures of ethylene and propylene in a broader temperature and concentration range. Based on the competitive adsorption results mutual retardation of both reactants was predicted by the kinetic modeling and indeed observed experimentally.

The total oxidation reaction network analysis performed has proven that the GCK approach combined with established reaction mechanisms could be applied successfully for the quantification of heterogeneously catalyzed reactions.

### Validation of Loop Reactor concept

In section 6 the periodic operation of a challenging multi fixed-bed Loop Reactor (LR) was investigated. The study was also used to validate the ethylene and propylene total oxidation kinetic models determined by the GCK approach. By means of trapping self-sustained exothermal reaction fronts inside the multi fixed-bed LR an autothermal, energy efficient operation can be obtained, in which the inlet mixture can be introduced at ambient temperature. The desired function is achieved by shifting the feed position in the direction of the flow when the reaction front leaves the currently active reactor segment. In this way, extinction can be avoided and continuous operation can be achieved.

As general characterization of the LR concept, a simulation study for single component and multi-component feeds was performed. Since the simulation of the rigorous reactor model in combination with detailed mechanistic kinetic models is numerically very expensive, at first simplified reaction kinetic models were adopted as available in the literature (Haynes and Caram, 1994). To understand the reaction and temperature front velocities as well as the maximum temperature within the reactor cascade, the most relevant operating and reactor parameters were varied in a wide range. A potentially high impact on the maximum temperature of the multi fixed-bed Loop Reactor is related to the type of reactants. To prepare the experimental investigations, the reactant mixture composition was analyzed systematically. To maintain an ignited cyclic steady state, the switching time  $t_{sw}$  has to be adjusted. Therefore, the closed loop control concept suggested in (Zahn et al., 2011) was applied.

The second part of section 6 described a challenging experimental study performed in this work. As in the model study, as the reaction system the total oxidation of ethylene and propylene in air on a  $\text{CrO}_x/\gamma\text{-Al}_2\text{O}_3$  catalyst was considered. Hereby the periodic LR operation was investigated using a two bed configuration. Systematic experiments of the LR operation using closed loop control revealed the domain of ignited reactor states as

function of the reactant inlet concentrations and the total volumetric fluxes. Simulation results using an extended reactor model and the mechanistic kinetic models determined via the GCCK approach (section 5) gave a relative good qualitative agreement with respect to the temperature profiles. The lack of exactly describing the maximum temperature is due to experimental uncertainties regarding the non-perfect adiabatic reactor behavior. Further improvements of reactor modeling should be done essentially implementing a more detailed reactor model. The experiments of totally oxidizing mixtures of ethylene and propylene generated increased reaction front velocities for larger fractions of the less reactive reactant ethylene. This issue could be compensated by applying smaller switching times as generated by the Multi-sensor control concept. However, if the reaction rates of the reactant mixture differ significantly, more complex ignition-extinction operation can be expected (Zahn, 2012) and further validation is needed.

## 7.2 Suggestions for further activities

- 1) The large potential of the “General Catalytic Cycle Kinetics” approach based on the *Christiansen’s* methodology could be demonstrated with respect to the derivation and parametrization of mechanistic rate models both for homogeneously and heterogeneously catalyzed reactions of different complexity. Further application of this powerful and elegant concept and the tools available is recommended. Extensions are seen in quantifying rates of enzymatic reactions (see also appendix A.3).
- 2) The Rh-catalyzed hydroformylation of long chain olefins is possible in thermomorphic solvents (TMS) that allow for efficient recovery of the precious catalysts. This concept should be further exploited considering renewable resources as feedstocks. The required kinetic models can be determined using the approach followed in this thesis.
- 3) Due to complexity of single and multi-component phase equilibria in heterogeneous catalysis frequently *Langmuir* expressions are applied. More realistic but sophisticated phase equilibrium models for single and competitive adsorption behavior are so far rarely used. Therefore, the Ideal Adsorbed Solution (IAS) theory is suggested to describe thermodynamic consistent competitive adsorption behavior of reactants and products within kinetic modeling.
- 4) The Loop Reactor is seen as an attractive energy efficient concept capable to perform efficiently heterogeneously catalyzed total oxidation reactions. Future investigations are recommended to apply this concept also for other reactions, e.g. hydrogenations.



## References

- Agar, D.W., Ruppel, W., 1988. Multifunktionale Reaktoren für die heterogene Katalyse. *Chemie Ingenieur Technik* 60 (10), 731–741. 10.1002/cite.330601003.
- Al-Sabawi, M., Lasa, H. de, 2009. Kinetic modeling of catalytic conversion of methylcyclohexane over USY zeolites: Adsorption and reaction phenomena. *AIChE J.* 55 (6), 1538–1558. 10.1002/aic.11825.
- Alvarado Perea, L., Wolff, T., Veit, P., Hilfert, L., Edelmann, F.T., Hamel, C., Seidel-Morgenstern, A., 2013. Alumino-mesostructured Ni catalysts for the direct conversion of ethene to propene. *Journal of Catalysis* 305, 154–168. 10.1016/j.jcat.2013.05.007.
- Andrzejewska, A., Kaczmarski, K., Guiochon, G., 2009. Theoretical study of the accuracy of the pulse method, frontal analysis, and frontal analysis by characteristic points for the determination of single component adsorption isotherms. *Journal of chromatography. A* 1216 (7), 1067–1083. 10.1016/j.chroma.2008.12.021.
- Angelidis, T.-N., Tzitzios, V., 1999. A comparative kinetic study of CH<sub>4</sub> oxidation by NiO/Al<sub>2</sub>O<sub>3</sub>, Pt/Al<sub>2</sub>O<sub>3</sub> and NiO-Pt/Al<sub>2</sub>O<sub>3</sub> catalysts, in: Froment, G.F., Waugh, K.C. (Eds.), *Reaction Kinetics and the Development of Catalytic Processes*, vol. 122. Elsevier, pp. 341–348.
- Atkins, P., Paula, J. de, 2006. *Physikalische Chemie*, 4th ed. Wiley-VCH, Weinheim.
- Auer, R., Thyron, F.C., 2002. Kinetics of the Total Oxidation of Methane over a La<sub>0.9</sub>Ce<sub>0.1</sub>CoO<sub>3</sub> Perovskite Catalyst. *Ind. Eng. Chem. Res.* 41 (4), 680–690. 10.1021/ie0104924.
- Ayastuy, J.L., Gurbani, A., González-Marcos, M.P., Gutiérrez-Ortiz, M.A., 2009. Kinetics of Carbon Monoxide Oxidation over CuO Supported on Nanosized CeO<sub>2</sub>. *Ind. Eng. Chem. Res.* 48 (12), 5633–5641. 10.1021/ie9001603.
- Baerns, M., 2004. *Basic principles in applied catalysis*. Springer-Verlag, Berlin, New York.
- Baerns, M., 2006. *Technische Chemie*. Wiley-VCH-Verlag, Weinheim.
- Barresi, A.A., Baldi, G., Fissore, D., 2007. Forced Unsteady-State Reactors as Efficient Devices for Integrated Processes: Case Histories and New Perspectives. *Ind. Eng. Chem. Res.* 46 (25), 8693–8700. 10.1021/ie070477k.
- Barresi, A.A., Vanni, M., Brinkmann, M., Baldi, G., 1999. Control of an autothermal network of nonstationary catalytic reactors. *AIChE J.* 45 (7), 1597–1602. 10.1002/aic.690450722.
- Barz, T., López Cárdenas, Diana C., Arellano-Garcia, H., Wozny, G., 2013. Experimental evaluation of an approach to online redesign of experiments for parameter determination. *AIChE J.* 59 (6), 1981–1995. 10.1002/aic.13957.
- Bates, D.M., Watts, D.G., 2007. *Nonlinear regression analysis and its applications*. Wiley, New York.
- Baylet, A., Capdeillayre, C., Retailleau, L., Valverde, J.L., Vernoux, P., Giroir-Fendler, A., 2011. Parametric study of propene oxidation over Pt and Au catalysts supported on sulphated and unsulphated titania. *Applied Catalysis B: Environmental* 102 (1-2), 180–189. 10.1016/j.apcatb.2010.11.040.

- Behr, A., 2008. *Angewandte homogene Katalyse*. Wiley-VCH Verlag GmbH & Co. KGaA, Weinheim.
- Behr, A., Henze, G., Obst, D., Turkowski, B., 2005a. Selection process of new solvents in temperature-dependent multi-component solvent systems and its application in isomerising hydroformylation. *Green Chem.* 7 (9), 645. 10.1039/B508032K.
- Behr, A., Obst, D., Schulte, C., Schosser, T., 2003. Highly selective tandem isomerization–hydroformylation reaction of trans-4-octene to n-nonanal with rhodium-BIPHEPHOS catalysis. *Journal of Molecular Catalysis A: Chemical* 206 (1-2), 179–184. 10.1016/S1381-1169(03)00461-8.
- Behr, A., Obst, D., Turkowski, B., 2005b. Isomerizing hydroformylation of trans-4-octene to n-nonanal in multiphase systems: acceleration effect of propylene carbonate. *Journal of Molecular Catalysis A: Chemical* 226 (2), 215–219. 10.1016/j.molcata.2004.10.030.
- Behr, A., Roll, R., 2005. Hydroaminomethylation in thermomorphic solvent systems. *Journal of Molecular Catalysis A: Chemical* 239 (1-2), 180–184. 10.1016/j.molcata.2005.06.020.
- Beller, M., Cornils, B., Frohning, C.D., Kohlpaintner, C.W., 1995. Progress in hydroformylation and carbonylation. *Journal of Molecular Catalysis A: Chemical* 104 (1), 17–85. 10.1016/1381-1169(95)00130-1.
- Beller, M., Renken, A., van Santen, R.A., 2012. *Catalysis: From principles to applications*. Wiley-VCH Verlag GmbH & Co. KGaA, Weinheim.
- Bellman, R., Åström, K.J., 1970. On structural identifiability. *Mathematical Biosciences* 7 (3-4), 329–339. 10.1016/0025-5564(70)90132-X.
- Benard, S., Baylet, A., Vernoux, P., Valverde, J.L., Giroir-Fendler, A., 2013. Kinetics of the propene oxidation over a Pt/alumina catalyst. *Catalysis Communications* 36, 63–66. 10.1016/j.catcom.2013.03.001.
- Benson, S.W., Cruickshank, F.R., Golden, D.M., Haugen, G.R., O'Neal, H.E., Rodgers, A.S., Shaw, R., Walsh, R., 1969. Additivity rules for the estimation of thermochemical properties. *Chem. Rev.* 69 (3), 279–324. 10.1021/cr60259a002.
- Bettahar, M., Costentin, G., Savary, L., Lavalley, J., 1996. On the partial oxidation of propane and propylene on mixed metal oxide catalysts. *Applied Catalysis A: General* 145 (1-2), 1–48. 10.1016/0926-860X(96)00138-X.
- Bhanage, B.M., Divekar, S.S., Deshpande, R.M., Chaudhari, R.V., 1997. Kinetics of hydroformylation of 1-dodecene using homogeneous HRh(CO)(PPh<sub>3</sub>)<sub>3</sub> catalyst. *Journal of Molecular Catalysis A: Chemical* 115 (2), 247–257. 10.1016/S1381-1169(96)00289-0.
- Boreskov, G.K., Matros, Y.S., Kiselev, O.V., Bunimovich, G.A., 1977. Performance of Heterogeneous Catalytic Process in Unsteady State. *Doklady Akademii Nauk SSSR* 237, 160–163.
- Börner, A., Franke, R., 2016. *Hydroformylation: Fundamentals, processes, and applications in organic synthesis*. Wiley-VCH Verlag GmbH & Co, Weinheim.
- Brinkmann, M., Barresi, A.A., Vanni, M., Baldi, G., 1999. Unsteady state treatment of very lean waste gases in a network of catalytic burners. *Catalysis Today* 47 (1-4), 263–277. 10.1016/S0920-5861(98)00307-1.
- Bronger, R.P., Bermon, J.P., Herwig, J., Kamer, P.C., van Leeuwen, Piet W.N.M., 2004. Phenoxaphosphino-Modified Xantphos-Type Ligands in the Rhodium-Catalysed Hydroformylation of Internal and Terminal Alkenes. *Advanced Synthesis & Catalysis* 346 (7), 789–799. 10.1002/adsc.200404066.

- 
- Brun, R., Reichert, P., Künsch, H.R., 2001. Practical identifiability analysis of large environmental simulation models. *Water Resour. Res.* 37 (4), 1015–1030. 10.1029/2000WR900350.
- Brunsch, Y., Behr, A., 2013. Temperature-controlled catalyst recycling in homogeneous transition-metal catalysis: minimization of catalyst leaching. *Angewandte Chemie (International ed. in English)* 52 (5), 1586–1589. 10.1002/anie.201208667.
- Burghardt, A., Berezowski, M., Jacobsen, E.W., 1999. Approximate characteristics of a moving temperature front in a fixed-bed catalytic reactor. *Chemical Engineering and Processing: Process Intensification* 38 (1), 19–34. 10.1016/S0255-2701(98)00067-1.
- Burgos, N., Paulis, M., Mirari Antxustegi, M., Montes, M., 2002. Deep oxidation of VOC mixtures with platinum supported on Al<sub>2</sub>O<sub>3</sub>/Al monoliths. *Applied Catalysis B: Environmental* 38 (4), 251–258. 10.1016/S0926-3373(01)00294-6.
- Carvajal, M.Á., Kozuch, S., Shaik, S., 2009. Factors Controlling the Selective Hydroformylation of Internal Alkenes to Linear Aldehydes. 1. The Isomerization Step. *Organometallics* 28 (13), 3656–3665. 10.1021/om801166x.
- Čermáková, J.Ř., Marković, A., Uchytíl, P., Seidel-Morgenstern, A., 2008. Single component and competitive adsorption of propane, carbon dioxide and butane on Vycor glass. *Chemical Engineering Science* 63 (6), 1586–1601. 10.1016/j.ces.2007.11.021.
- Chaudhari, R., Seayad, A., Jayasree, S., 2001. Kinetic modeling of homogeneous catalytic processes. *Catalysis Today* 66 (2-4), 371–380. 10.1016/S0920-5861(00)00633-7.
- Chorkendorff, I., Niemantsverdriet, J.W., 2003. *Concepts of modern catalysis and kinetics*. Wiley-VCH, Weinheim [Germany].
- Choudhary, T., Banerjee, S., Choudhary, V., 2002. Catalysts for combustion of methane and lower alkanes. *Applied Catalysis A: General* 234 (1-2), 1–23. 10.1016/S0926-860X(02)00231-4.
- Christiansen, J.A., 1931. Ein Versuch zur Anwendung der Methode der stationären Geschwindigkeiten auf die Reaktion  $\text{CH}_3\text{OH} + \text{H}_2\text{O} \rightarrow 3\text{H}_2 + \text{CO}_2$ . *Zeitschrift für Physikalische Chemie* 1931A (Supplement). 10.1515/zpch-1931-s108.
- Christiansen, J.A., 1935. Einige Bemerkungen zur Anwendung der BODENSTEIN sehen Methode der stationären Konzentrationen der Zwischenstoffe in der Reaktionskinetik. *Zeitschrift für Physikalische Chemie* 1935 (Supplement), 303.
- Christiansen, J.A., 1953. The Elucidation of Reaction Mechanisms by the Method of Intermediates in Quasi-Stationary Concentrations. *Advances in Catalysis* 5 (C), 311–353.
- Cintrón-Arias, A., Banks, H.T., Capaldi, A., Lloyd, A.L., 2009. A sensitivity matrix based methodology for inverse problem formulation. *Journal of Inverse and Ill-posed Problems* 17 (6). 10.1515/JIIP.2009.034.
- Corma, A., Ortega, F., 2005. Influence of adsorption parameters on catalytic cracking and catalyst decay. *Journal of Catalysis* 233 (2), 257–265. 10.1016/j.jcat.2005.04.023.
- Danckwerts, P.V., 1953. Continuous flow systems. *Chemical Engineering Science* 2 (1), 1–13. 10.1016/0009-2509(53)80001-1.
- Denayer, J.F., Martens, J.A., Jacobs, P.A., Thybaut, J.W., Marin, G.B., Baron, G.V., 2003. Influence of the zeolite composition on the hydro-isomerisation and hydrocracking of alkanes on Pt/USY zeolites: modelling of the reaction kinetics using an adsorption–reaction approach. *Applied Catalysis A: General* 246 (1), 17–28. 10.1016/S0926-860X(02)00665-8.

- Denayer, J.F.M., Baron, G.V., 1997. Adsorption of normal and branched paraffins in faujasite zeolites NaY, HY, Pt/NaY and USY. *Adsorption* 3 (4), 251–265. 10.1007/BF01653628.
- Deshpande, R., Purwanto, Delmas, H., Chaudhari, R.V., 1997. Effect of pH on rate and selectivity behavior in biphasic hydroformylation of 1-octene. *Journal of Molecular Catalysis A: Chemical* 126 (2-3), 133–140. 10.1016/S1381-1169(97)00103-9.
- Deshpande, R.M., Kelkar, A.A., Sharma, A., Julcour-Lebigue, C., Delmas, H., 2011. Kinetics of hydroformylation of 1-octene in ionic liquid-organic biphasic media using rhodium sulfoxantphos catalyst. *Chemical Engineering Science* 66 (8), 1631–1639. 10.1016/j.ces.2010.12.040.
- Deshpande, R.M., Purwanto, Delmas, H., Chaudhari, R.V., 1996. Kinetics of Hydroformylation of 1-Octene Using  $[\text{Rh}(\text{COD})\text{Cl}]_2$  -TPPTS Complex Catalyst in a Two-Phase System in the Presence of a Cosolvent. *Ind. Eng. Chem. Res.* 35 (11), 3927–3933. 10.1021/ie960047m.
- Desset, S.L., Cole-Hamilton, D.J., 2009. Carbon dioxide induced phase switching for homogeneous-catalyst recycling. *Angewandte Chemie (International ed. in English)* 48 (8), 1472–1474. 10.1002/anie.200804729.
- Desset, S.L., Reader, S.W., Cole-Hamilton, D.J., 2009. Aqueous-biphasic hydroformylation of alkenes promoted by “weak” surfactants. *Green Chem.* 11 (5), 630. 10.1039/b822139a.
- Divekar, S.S., Bhanage, B.M., Deshpande, R.M., Gholap, R.V., Chaudhari, R.V., 1994. Selectivity in hydroformylation of 1-decene by homogeneous catalysis. *Journal of Molecular Catalysis* 91 (1), L1-L6. 10.1016/0304-5102(94)00045-X.
- Duong, D.D., 1998. Adsorption analysis: Equilibria and kinetics. Imperial College Press, London.
- Dwars, T., Paetzold, E., Oehme, G., 2005. Reactions in micellar systems. *Angewandte Chemie (International ed. in English)* 44 (44), 7174–7199. 10.1002/anie.200501365.
- Edgar, T.F., Himmelblau, D.M., 1988. Optimization of chemical processes. McGraw-Hill, New York.
- Eigenberger, G., Nieken, U., 1994. Catalytic cleaning of polluted air: reaction engineering problems and new solutions. *International chemical engineering* 34 (1), 4–16.
- Englezos, P., Kalogerakis, N., 2001. Applied parameter estimation for chemical engineers. M. Dekker, New York.
- Ergun, S., 1952. Fluid Flow through Packed Columns. *Journal of Chemical Engineering Progress* 48 (2), 89–94.
- Ergun, S., Orning, A.A., 1949. Fluid Flow through Randomly Packed Columns and Fluidized Beds. *Ind. Eng. Chem.* 41 (6), 1179–1184. 10.1021/ie50474a011.
- Ertl, G., Knözinger, H., Schüth, F., Weitkamp, J. (Eds.), 2008. Handbook of Heterogeneous Catalysis. Wiley-VCH Verlag GmbH & Co. KGaA, Weinheim, Germany.
- Evans, D., Osborn, J.A., Wilkinson, G., 1968. Hydroformylation of alkenes by use of rhodium complex catalysts. *J. Chem. Soc., A*, 3133. 10.1039/J19680003133.
- Fang, J., Jana, R., Tunge, J.A., Subramaniam, B., 2011. Continuous homogeneous hydroformylation with bulky rhodium catalyst complexes retained by nano-filtration membranes. *Applied Catalysis A: General* 393 (1-2), 294–301. 10.1016/j.apcata.2010.12.011.

- 
- Fang, J., Jin, H., Ruddy, T., Pennybaker, K., Fahey, D., Subramaniam, B., 2007. Economic and Environmental Impact Analyses of Catalytic Olefin Hydroformylation in CO<sub>2</sub>-Expanded Liquid (CXL) Media. *Ind. Eng. Chem. Res.* 46 (25), 8687–8692. 10.1021/ie070405t.
- Fink, M., Attarian, A., Tran, H., 2007. Subset selection for parameter estimation in an HIV model. *Proc. Appl. Math. Mech.* 7 (1), 1121501–1121502. 10.1002/pamm.200700319.
- Fissore, D., Barresi, A.A., 2002. Comparison between the Reverse-Flow Reactor and a Network of Reactors for the Oxidation of Lean VOC Mixtures. *Chem. Eng. Technol.* 25 (4), 421–426. 10.1002/1521-4125(200204)25:4<421:AID-CEAT421>3.0.CO;2-K.
- Fissore, D., Barresi, A.A., Baldi, G., 2003. Synthesis Gas Production in a Forced Unsteady-State Reactor Network. *Ind. Eng. Chem. Res.* 42 (12), 2489–2495. 10.1021/ie0205748.
- Fissore, D., Barresi, A.A., Baldi, G., Hevia, M.A.G., Ordóñez, S., Díez, F.V., 2005. Design and testing of small-scale unsteady-state afterburners and reactors. *AIChE J.* 51 (6), 1654–1664. 10.1002/aic.10430.
- Fissore, D., Pisano, R., Barresi, A.A., 2007. Observer design for the Selective Catalytic Reduction of NO<sub>x</sub> in a loop reactor. *Chemical Engineering Journal* 128 (2-3), 181–189. 10.1016/j.cej.2006.09.026.
- Frank-Kamenetskii, D.A., 1959. *Stoff- und Wärmeübertragung in der chemischen Kinetik.* Springer-Verlag, Berlin.
- Freund, H., Sundmacher, K., 2008. Towards a methodology for the systematic analysis and design of efficient chemical processes. *Chemical Engineering and Processing: Process Intensification* 47 (12), 2051–2060. 10.1016/j.cep.2008.07.011.
- Freund, H.-J., Meijer, G., Scheffler, M., Schlögl, R., Wolf, M., 2011. CO oxidation as a prototypical reaction for heterogeneous processes. *Angewandte Chemie (International ed. in English)* 50 (43), 10064–10094. 10.1002/anie.201101378.
- Freund, H.-J., Nilius, N., Risse, T., Schauermann, S., 2014. A fresh look at an old nanotechnology: catalysis. *Physical chemistry chemical physics: PCCP* 16 (18), 8148–8167. 10.1039/c3cp55231d.
- Froment, G.F., Bischoff, K.B., 1990. *Chemical reactor analysis and design*, 2nd ed. Wiley, New York.
- Giese, M., Rottschäfer, K., Vortmeyer, D., 1998. Measured and modeled superficial flow profiles in packed beds with liquid flow. *AIChE J.* 44 (2), 484–490. 10.1002/aic.690440225.
- Gómez, D.M., Galvita, V.V., Gatica, J.M., Vidal, H., Marin, G.B., 2014. TAP study of toluene total oxidation over a Co<sub>3</sub>O<sub>4</sub>/La-CeO<sub>2</sub> catalyst with an application as a washcoat of cordierite honeycomb monoliths. *Physical chemistry chemical physics: PCCP* 16 (23), 11447–11455. 10.1039/c4cp00886c.
- Grah, A., 2004. *Entwicklung und Anwendung modularer Software zur Simulation und Parameterschätzung in gaskatalytischen Festbettreaktoren.* Dissertation Martin-Luther-Universität Halle-Wittenberg.
- Gritti, F., Guiochon, G., 2003. New thermodynamically consistent competitive adsorption isotherm in RPLC. *Journal of Colloid and Interface Science* 264 (1), 43–59. 10.1016/S0021-9797(03)00332-1.
- Guha, D., Jin, H., Dudukovic, M.P., Ramachandran, P.A., Subramaniam, B., 2007. Mass transfer effects during homogeneous 1-octene hydroformylation in -expanded solvent: Modeling and experiments. *Chemical Engineering Science* 62 (18-20), 4967–4975. 10.1016/j.ces.2006.12.029.

- Haber, J., Turek, W., 2000. Kinetic Studies as a Method to Differentiate between Oxygen Species Involved in the Oxidation of Propene. *Journal of Catalysis* 190 (2), 320–326. 10.1006/jcat.1999.2764.
- Haji, S., Erkey, C., 2002. Investigation of rhodium catalyzed hydroformylation of ethylene in supercritical carbon dioxide by in situ FTIR spectroscopy. *Tetrahedron* 58 (20), 3929–3941. 10.1016/S0040-4020(02)00246-6.
- Hamel, C., 2008. Experimentelle und modellbasierte Studien zur Herstellung kurzketziger Alkene sowie von Synthesegas unter Verwendung poröser und dichter Membranen, 1st ed. Docupoint-Verl., Magdeburg.
- Hamel, C., 2016. Beeinflussung der Produktselektivität homogener und heterogener katalysierter Reaktionen. Habilitation, Magdeburg.
- Hamel, C., Tóta, Á., Klose, F., Tsotsas, E., Seidel-Morgenstern, A., 2008. Analysis of single and multi-stage membrane reactors for the oxidation of short-chain alkanes—Simulation study and pilot scale experiments. *Chemical Engineering Research and Design* 86 (7), 753–764. 10.1016/j.cherd.2008.03.025.
- Hamel, C., Wolff, T., Subramaniam, P., Seidel-Morgenstern, A., 2011. Multicomponent Dosing in Membrane Reactors Including Recycling—Concept and Demonstration for the Oxidative Dehydrogenation of Propane. *Ind. Eng. Chem. Res.* 50 (23), 12895–12903. 10.1021/ie2001692.
- Hamerla, T., Rost, A., Kasaka, Y., Schomäcker, R., 2013. Hydroformylation of 1-Dodecene with Water-Soluble Rhodium Catalysts with Bidentate Ligands in Multiphase Systems. *ChemCatChem* 5 (7), 1854–1862. 10.1002/cctc.201200744.
- Harmsen, J., Hoebink, J., Schouten, J.C., 2000. Transient Kinetic Modeling of the Ethylene and Carbon Monoxide Oxidation over a Commercial Automotive Exhaust Gas Catalyst. *Ind. Eng. Chem. Res.* 39 (3), 599–609. 10.1021/ie990614g.
- Haumann, M., Koch, H., Hugo, P., Schomäcker, R., 2002. Hydroformylation of 1-dodecene using Rh-TPPTS in a microemulsion. *Applied Catalysis A: General* 225 (1-2), 239–249. 10.1016/S0926-860X(01)00869-9.
- Haus, U.-U., Michaels, D., Seidel-Morgenstern, A., Weismantel, R., 2007. A method to evaluate the feasibility of TMB chromatography for reduced efficiency and purity requirements based on discrete optimization. *Computers & Chemical Engineering* 31 (11), 1525–1534. 10.1016/j.compchemeng.2007.01.001.
- Haynes, T.N., Caram, H.S., 1994. The simulated moving bed chemical reactor. *Chemical Engineering Science* 49 (24), 5465–5472. 10.1016/0009-2509(94)00383-1.
- Hefferich, F.G., 2004. Kinetics of multistep reactions, 2nd ed. Elsevier, Amsterdam, Boston.
- Hentschel, B., Kiedorf, G., Gerlach, M., Hamel, C., Seidel-Morgenstern, A., Freund, H., Sundmacher, K., 2015. Model-Based Identification and Experimental Validation of the Optimal Reaction Route for the Hydroformylation of 1-Dodecene. *Ind. Eng. Chem. Res.* 54 (6), 1755–1765. 10.1021/ie504388t.
- Herz, R.K., Marin, S.P., 1980. Surface chemistry models of carbon monoxide oxidation on supported platinum catalysts. *Journal of Catalysis* 65 (2), 281–296. 10.1016/0021-9517(80)90306-1.
- Hevia, M.A.G., Ordóñez, S., Díez, F.V., 2006. Effect of wall properties on the behavior of bench-scale reverse flow reactors. *AIChE J.* 52 (9), 3203–3209. 10.1002/aic.10920.
- Heynderickx, P.M., Thybaut, J.W., Poelman, H., Poelman, D., Marin, G.B., 2010a. Kinetic modeling of the total oxidation of propane over CuO-CeO<sub>2</sub>/γ-Al<sub>2</sub>O<sub>3</sub>. *Applied Catalysis B: Environmental* 95 (1-2), 26–38. 10.1016/j.apcatb.2009.11.018.

- 
- Heynderickx, P.M., Thybaut, J.W., Poelman, H., Poelman, D., Marin, G.B., 2010b. The total oxidation of propane over supported Cu and Ce oxides: A comparison of single and binary metal oxides. *Journal of Catalysis* 272 (1), 109–120. 10.1016/j.jcat.2010.03.006.
- Hintermair, U., Zhao, G., Santini, C.C., Muldoon, M.J., Cole-Hamilton, D.J., 2007. Supported ionic liquid phase catalysis with supercritical flow. *Chemical communications* (Cambridge, England) (14), 1462–1464. 10.1039/B616186C.
- Hirschfelder, J.O., Curtiss, C.F., Bird, R.B., 1964. *Molecular theory of gases and liquids*. Wiley-VCH, New York.
- Hodnett, B.K., 2000. *Heterogeneous catalytic oxidation: Fundamental and technological aspects of the selective and total oxidation of organic compounds*. John Wiley, New York.
- Hong, Y.P., Pan, C.-T., 1992. Rank-revealing QR factorizations and the singular value decomposition. *Math. Comp.* 58 (197), 213. 10.1090/S0025-5718-1992-1106970-4.
- Hu, W., Lowry, B., Varma, A., 2011. Kinetic study of glycerol oxidation network over Pt–Bi/C catalyst. *Applied Catalysis B: Environmental*. 10.1016/j.apcatb.2011.05.015.
- Hurtado, P., Ordóñez, S., Sastre, H., Díez, F.V., 2004. Development of a kinetic model for the oxidation of methane over Pd/Al<sub>2</sub>O<sub>3</sub> at dry and wet conditions. *Applied Catalysis B: Environmental* 51 (4), 229–238. 10.1016/j.apcatb.2004.03.006.
- Hutchings, G.J., Taylor, S.H., 1999. Designing oxidation catalysts. *Catalysis Today* 49 (1–3), 105–113. 10.1016/S0920-5861(98)00414-3.
- Jakuttis, M., Schönweiz, A., Werner, S., Franke, R., Wiese, K.-D., Haumann, M., Wasserscheid, P., 2011. Rhodium-phosphite SILP catalysis for the highly selective hydroformylation of mixed C<sub>4</sub> feedstocks. *Angewandte Chemie (International ed. in English)* 50 (19), 4492–4495. 10.1002/anie.201007164.
- James, D.H., Phillips, C.S.G., 1954. The chromatography of gases and vapours. Part III. The determination of adsorption isotherms. *J. Chem. Soc.*, 1066. 10.1039/JR9540001066.
- Janssen, M., Wilting, J., Müller, C., Vogt, D., 2010. Continuous rhodium-catalyzed hydroformylation of 1-octene with polyhedral oligomeric silsesquioxanes (POSS) enlarged triphenylphosphine. *Angewandte Chemie (International ed. in English)* 49 (42), 7738–7741. 10.1002/anie.201001926.
- Jörke, A., Kohls, E., Triemer, S., Seidel-Morgenstern, A., Hamel, C., Stein, M., 2016. Resolution of structural isomers of complex reaction mixtures in homogeneous catalysis. *Chemical Engineering and Processing: Process Intensification* 102, 229–237. 10.1016/j.cep.2016.01.001.
- Jörke, A., Seidel-Morgenstern, A., Hamel, C., 2015a. Isomerization of 1-decene: Estimation of thermodynamic properties, equilibrium composition calculation and experimental validation using a Rh-BIPHEPHOS catalyst. *Chemical Engineering Journal* 260, 513–523. 10.1016/j.cej.2014.09.015.
- Jörke, A., Triemer, S., Seidel-Morgenstern, A., Hamel, C., 2015b. Kinetic Investigation Exploiting Local Parameter Subset Selection: Isomerization of 1-Decene using a Rh-Biphephos Catalyst. *Chemie Ingenieur Technik* 87 (6), 713–725. 10.1002/cite.201400148.
- Joshi, M., 2007. *Statistical analysis of models and parameters in chemical and biochemical reaction networks*. Logos-Verl, Berlin.

- Kamer, P., van Rooy, A., Schoemaker, G.C., van Leeuwen, P., 2004. In situ mechanistic studies in rhodium catalyzed hydroformylation of alkenes. *Coordination Chemistry Reviews* 248 (21-24), 2409–2424. 10.1016/j.ccr.2004.06.006.
- Kiedorf, G., Hoang, D.M., Müller, A., Jörke, A., Markert, J., Arellano-Garcia, H., Seidel-Morgenstern, A., Hamel, C., 2014. Kinetics of 1-dodecene hydroformylation in a thermomorphic solvent system using a rhodium-biphenos catalyst. *Chemical Engineering Science* 115, 31–48. 10.1016/j.ces.2013.06.027.
- Kiedorf, G., Wolff, T., Seidel-Morgenstern, A., Hamel, C., 2016a. Adsorption measurements on a  $\text{CrO}_x/\gamma\text{-Al}_2\text{O}_3$  catalyst for parameter reduction in kinetic analysis. *Chemical Engineering Science* 149, 266–276. 10.1016/j.ces.2016.04.040.
- Kiedorf, G., Wolff, T., Seidel-Morgenstern, A., Hamel, C., 2016b. Kinetic Analysis of the Hydrocarbon Total Oxidation Using Individually Measured Adsorption Isotherms. *Chemie Ingenieur Technik* 88 (11). 10.1002/cite.201600043.
- Kiselev, O.V., Matros, Y.S., 1980. Propagation of the combustion front of a gas mixture in a granular bed of catalyst. *Combust Explos Shock Waves* 16 (2), 152–157. 10.1007/BF00740193.
- Klerk, A. de, 2005. Adiabatic Laboratory Reactor Design and Verification. *Ind. Eng. Chem. Res.* 44 (25), 9440–9445. 10.1021/ie050212a.
- Klose, F., Joshi, M., Hamel, C., Seidel-Morgenstern, A., 2004. Selective oxidation of ethane over a  $\text{VO}_x/\gamma\text{-Al}_2\text{O}_3$  catalyst – investigation of the reaction network. *Applied Catalysis A: General* 260 (1), 101–110. 10.1016/j.apcata.2003.10.005.
- Koch, W., Holthausen, M.C., 2001. *A chemist's guide to density functional theory*, 2nd ed. Wiley-VCH, Weinheim, New York.
- Koeken, A., van den Broeke, L., Deelman, B.-J., Keurentjes, J., 2011a. Full kinetic description of 1-octene hydroformylation in a supercritical medium. *Journal of Molecular Catalysis A: Chemical* 346 (1-2), 1–11. 10.1016/j.molcata.2011.06.012.
- Koeken, A.C., van den Broeke, L., Benes, N.E., Keurentjes, J., 2011b. Triphenylphosphine modified rhodium catalyst for hydroformylation in supercritical carbon dioxide. *Journal of Molecular Catalysis A: Chemical* 346 (1-2), 94–101. 10.1016/j.molcata.2011.06.014.
- Körkel, S., 2002. *Numerische Methoden für Optimale Versuchsplanungsprobleme bei nichtlinearen DAE-Modellen*. Dissertation, Heidelberg.
- Kripylo, P.H.K., Klose, D., Khuat Minh, T., 1984. Mechanism and Selectivity in the Oxidation of Propene to Acrolein on Bi/Mo-Oxide Catalysts. *Chemische Technik (Leipzig)* 36 (2), 58–61.
- Kumar, K.V., Porkodi, K., Rocha, F., 2008. Langmuir–Hinshelwood kinetics – A theoretical study. *Catalysis Communications* 9 (1), 82–84. 10.1016/j.catcom.2007.05.019.
- Landa, H.O.R., Flockerzi, D., Seidel-Morgenstern, A., 2013. A method for efficiently solving the IAST equations with an application to adsorber dynamics. *AIChE J* 59 (4), 1263–1277. 10.1002/aic.13894.
- Lauschke, G., Gilles, E.D., 1994. Circulating reaction zones in a packed-bed loop reactor. *Chemical Engineering Science* 49 (24), 5359–5375. 10.1016/0009-2509(94)00291-6.
- Levenberg, K., 1944. A Method for the Solution of Certain Problems in Least Squares. *Quart. Appl. Math.* 2, 164–261.
- Levenspiel, O., 1999. *Chemical reaction engineering*, 3rd ed. Wiley, New York.

- 
- Li, C., Widjaja, E., Chew, W., Garland, M., 2002. Rhodium Tetracarbonyl Hydride: The Elusive Metal Carbonyl Hydride. *Angew. Chem. Int. Ed.* 41 (20), 3785–3789. 10.1002/1521-3773(20021018)41:20<3785:AID-ANIE3785>3.0.CO;2-O.
- Lisec, O., Hugo, P., Seidel-Morgenstern, A., 2001. Frontal analysis method to determine competitive adsorption isotherms. *Journal of Chromatography A* 908 (1-2), 19–34. 10.1016/S0021-9673(00)00966-3.
- Liu, Q., Wang, L.-C., Chen, M., Cao, Y., He, H.-Y., Fan, K.-N., 2009. Dry citrate-precursor synthesized nanocrystalline cobalt oxide as highly active catalyst for total oxidation of propane. *Journal of Catalysis* 263 (1), 104–113. 10.1016/j.jcat.2009.01.018.
- Liu, W., Flytzanistephanopoulos, M., 1995. Total Oxidation of Carbon-Monoxide and Methane over Transition Metal Fluorite Oxide Composite Catalysts. *Journal of Catalysis* 153 (2), 317–332. 10.1006/jcat.1995.1133.
- Ljung, L., 1999. *System identification: Theory for the user*, 2nd ed. Prentice Hall PTR, Upper Saddle River, NJ.
- Lobera, M.P., Téllez, C., Herguido, J., Menéndez, M., 2008. Transient kinetic modelling of propane dehydrogenation over a Pt–Sn–K/Al<sub>2</sub>O<sub>3</sub> catalyst. *Applied Catalysis A: General* 349 (1-2), 156–164. 10.1016/j.apcata.2008.07.025.
- Luss, D., Sheintuch, M., 2005. Spatiotemporal patterns in catalytic systems. *Catalysis Today* 105 (2), 254–274. 10.1016/j.cattod.2005.02.043.
- Madai, A.Y., Nekhamkina, O., Sheintuch, M., 2017. What is the leanest stream to sustain a nonadiabatic loop reactor: Analysis and methane combustion experiments. *AIChE J* 63 (6), 2030–2042. 10.1002/aic.15580.
- Madai, A.Y., Sheintuch, M., 2008. Demonstration of loop reactor operation. *AIChE J.* 54 (9), 2413–2422. 10.1002/aic.11551.
- Marin, G.B., Yablonsky, G.S., 2011. *Kinetics of chemical reactions: Decoding complexity*. Wiley-VCH Verlag, Weinheim, Germany.
- Markert, J., Brunsch, Y., Munkelt, T., Kiedorf, G., Behr, A., Hamel, C., Seidel-Morgenstern, A., 2013. Analysis of the reaction network for the Rh-catalyzed hydroformylation of 1-dodecene in a thermomorphic multicomponent solvent system. *Applied Catalysis A: General* 462-463, 287–295. 10.1016/j.apcata.2013.04.005.
- Marquardt, D.W., 1963. An Algorithm for Least-Squares Estimation of Nonlinear Parameters. *Journal of the Society for Industrial and Applied Mathematics* 11 (2), 431–441. 10.1137/0111030.
- Mars, P., van Krevelen, D.W., 1954. Oxidations carried out by means of vanadium oxide catalysts. *Special Supplement to Chemical Engineering Science* 3, 41–59.
- Matros, Y.S., 1977. Perspective Applications of the Unsteady-State Processes in Catalytic Reactors. *Journal of D.I. Mendeleev Chemical Society* 22, 576–580.
- Menon, U., Poelman, H., Bliznuk, V., Galvita, V.V., Poelman, D., Marin, G.B., 2012. Nature of the active sites for the total oxidation of toluene by CuOCeO<sub>2</sub>/Al<sub>2</sub>O<sub>3</sub>. *Journal of Catalysis* 295, 91–103. 10.1016/j.jcat.2012.07.026.
- Moasser, B., Gladfelter, W.L., Roe, D.C., 1995. Mechanistic Aspects of a Highly Regioselective Catalytic Alkene Hydroformylation using a Rhodium Chelating Bis(phosphite) Complex. *Organometallics* 14 (8), 3832–3838. 10.1021/om00008a034.
- Mokhadinyana, M., Desset, S.L., Williams, D Bradley G, Cole-Hamilton, D.J., 2012. Cooperative ligand effects in phase-switching homogeneous catalysts. *Angewandte Chemie (International ed. in English)* 51 (7), 1648–1652. 10.1002/anie.201108200.

- Moré, J.J., Sorensen, D.C., 1983. Computing a Trust Region Step. *SIAM J. Sci. and Stat. Comput.* 4 (3), 553–572. 10.1137/0904038.
- Moro-Oka, Y., Morikawa, Y., Ozaki, A., 1967. Regularity in the catalytic properties of metal oxides in hydrocarbon oxidation. *Journal of Catalysis* 7 (1), 23–32. 10.1016/0021-9517(67)90004-8.
- Müller, I., Kiedorf, G., Runne, E., Seidel-Morgenstern, A., Hamel, C., 2017. Synthesis, Kinetic Analysis and Modeling of Galacto-Oligosaccharides Formation. *Biochemical Engineering Journal*.
- Murzin, D., 2013. *Engineering catalysis*. Walter de Gruyter GmbH, Berlin.
- Murzin, D., Salmi, T., 2005. *Catalytic Kinetics*. Elsevier, Amsterdam.
- Murzin, D.Y., 2010. Size-dependent heterogeneous catalytic kinetics. *Journal of Molecular Catalysis A: Chemical* 315 (2), 226–230. 10.1016/j.molcata.2009.09.016.
- Murzin, D.Y., Bernas, A., Salmi, T., 2010. Kinetic modelling of regioselectivity in alkenes hydroformylation over rhodium. *Journal of Molecular Catalysis A: Chemical* 315 (2), 148–154. 10.1016/j.molcata.2009.06.023.
- Murzin, D.Y., Bernas, A., Salmi, T., 2012. Mechanistic model for kinetics of propene hydroformylation with Rh catalyst. *AIChE J.* 58 (7), 2192–2201. 10.1002/aic.12746.
- Murzin, D.Y., Salmi, T., Smeds, S., Laatikainen, M., Mustonen, M., Paatero, E., 1997. Toluene and methylcyclohexane adsorption on nickel catalysts. *Reaction Kinetics and Catalysis Letters* 61 (2), 227–236. 10.1007/BF02478377.
- Myers, A.L., Prausnitz, J.M., 1965. Thermodynamics of mixed-gas adsorption. *AIChE J.* 11 (1), 121–127. 10.1002/aic.690110125.
- Nekhamkina, O., Sheintuch, M., 2008. Approximate design of loop reactors. *Chemical Engineering Science* 63 (20), 4924–4934. 10.1016/j.ces.2007.09.019.
- Neubert, P., Meier, I., Gaide, T., Behr, A., 2016. Additive-Free Palladium-Catalysed Hydroamination of Piperylene with Morpholine. *Synthesis* 48 (14), 2287–2293. 10.1055/s-0035-1560438.
- Nibbelke, R.H., Nievergeld, A.J., Hoebink, J.H., Marin, G.B., 1998. Development of a transient kinetic model for the CO oxidation by O<sub>2</sub> over a Pt/Rh/CeO<sub>2</sub>/γ-Al<sub>2</sub>O<sub>3</sub> three-way catalyst. *Applied Catalysis B: Environmental* 19 (3-4), 245–259. 10.1016/S0926-3373(98)00076-9.
- Nicoud, R.M., Seidel-Morgenstern, A., 1996. Adsorption Isotherm: Experimental Determination and Application to Preparative Chromatography. *Isolation and Purification* 2, 165–200.
- Nieken, U., Kolios, G., Eigenberger, G., 1994. Fixed-bed reactors with periodic flow reversal: Experimental results for catalytic combustion. *Catalysis Today* 20 (3), 335–350. 10.1016/0920-5861(94)80130-4.
- Nieken, U., Kolios, G., Eigenberger, G., 1995. Limiting cases and approximate solutions for fixed-bed reactors with periodic flow reversal. *AIChE J.* 41 (8), 1915–1925. 10.1002/aic.690410809.
- Nova, I., Ciardelli, C., Tronconi, E., Chatterjee, D., Weibel, M., 2009. Unifying redox kinetics for standard and fast NH<sub>3</sub>-SCR over a V<sub>2</sub>O<sub>5</sub>-WO<sub>3</sub>/TiO<sub>2</sub> catalyst. *AIChE J.* 55 (6), 1514–1529. 10.1002/aic.11750.
- Ostwald, W., 1924. Über Katalyse. *Z. Angew. Chem.* 37 (21), 309. 10.1002/ange.19240372115.

- 
- Palai, T., Bhattacharya, P.K., 2013. Kinetics of lactose conversion to galacto-oligosaccharides by  $\beta$ -galactosidase immobilized on PVDF membrane. *Journal of bioscience and bioengineering* 115 (6), 668–673. 10.1016/j.jbiosc.2012.12.014.
- Palai, T., Kumar, A., Bhattacharya, P.K., 2015. Kinetic studies and model development for the formation of galacto-oligosaccharides from lactose using synthesized thermo-responsive bioconjugate. *Enzyme and microbial technology* 70, 42–49. 10.1016/j.enzmictec.2014.12.010.
- Panizza, M., Resini, C., Raccoli, F., Busca, G., Catani, R., Rossini, S., 2003. Oxidation of ethane over vanadia-alumina-based catalysts: co-feed and redox experiments. *Chemical Engineering Journal* 93 (3), 181–189. 10.1016/S1385-8947(02)00319-4.
- Papageorgiou, M., 2006. *Optimierung: Statische, dynamische, stochastische Verfahren*, 3rd ed. Springer, Berlin.
- Pöpken, T., Götze, L., Gmehling, J., 2000. Reaction Kinetics and Chemical Equilibrium of Homogeneously and Heterogeneously Catalyzed Acetic Acid Esterification with Methanol and Methyl Acetate Hydrolysis. *Ind. Eng. Chem. Res.* 39 (7), 2601–2611. 10.1021/ie000063q.
- Purwanto, Deshpande, R.M., Chaudhari, R.V., Delmas, H., 1996. Solubility of Hydrogen, Carbon Monoxide, and 1-Octene in Various Solvents and Solvent Mixtures. *J. Chem. Eng. Data* 41 (6), 1414–1417. 10.1021/je960024e.
- Purwanto, P., Delmas, H., 1995. Gas-liquid-liquid reaction engineering: hydroformylation of 1-octene using a water soluble rhodium complex catalyst. *Catalysis Today* 24 (1-2), 135–140. 10.1016/0920-5861(95)00013-6.
- Radhakrishnan, K., Ramachandran, P.A., Brahme, P.H., Chaudhari, R.V., 1983. Solubility of hydrogen in methanol, nitrobenzene, and their mixtures experimental data and correlation. *J. Chem. Eng. Data* 28 (1), 1–4. 10.1021/je00031a001.
- Radke, C.J., Prausnitz, J.M., 1972. Thermodynamics of multi-solute adsorption from dilute liquid solutions. *AIChE J.* 18 (4), 761–768. 10.1002/aic.690180417.
- Rajendran, A., Paredes, G., Mazzotti, M., 2009. Simulated moving bed chromatography for the separation of enantiomers. *Journal of Chromatography A* 1216 (4), 709–738. 10.1016/j.chroma.2008.10.075.
- Redlingshöfer, H., Fischer, A., Weckbecker, C., Huthmacher, K., Emig, G., 2003. Kinetic Modeling of the Heterogeneously Catalyzed Oxidation of Propene to Acrolein in a Catalytic Wall Reactor. *Ind. Eng. Chem. Res.* 42 (22), 5482–5488. 10.1021/ie030191p.
- Reid, J., 1977. Structural identifiability in linear time-invariant systems. *IEEE Trans. Automat. Contr.* 22 (2), 242–246. 10.1109/TAC.1977.1101474.
- Ruthven, D.M., Ching, C.B., 1989. Counter-current and simulated counter-current adsorption separation processes. *Chemical Engineering Science* 44 (5), 1011–1038. 10.1016/0009-2509(89)87002-2.
- Saad, Y., 2003. *Iterative methods for sparse linear systems*, 2nd ed. SIAM, Philadelphia.
- Santori, G., Luberti, M., Ahn, H., 2014. Ideal adsorbed solution theory solved with direct search minimisation. *Computers & Chemical Engineering* 71, 235–240. 10.1016/j.compchemeng.2014.07.027.
- Sattler, J.J.H.B., Ruiz-Martinez, J., Santillan-Jimenez, E., Weckhuysen, B.M., 2014. Catalytic dehydrogenation of light alkanes on metals and metal oxides. *Chemical reviews* 114 (20), 10613–10653. 10.1021/cr5002436.
- Schäfer, E., Brunsch, Y., Sadowski, G., Behr, A., 2012. Hydroformylation of 1-Dodecene in the Thermomorphic Solvent System Dimethylformamide/Decane. *Phase Behavior–*

- Reaction Performance–Catalyst Recycling. *Ind. Eng. Chem. Res.* 51 (31), 10296–10306. 10.1021/ie300484q.
- Schmidt-Traub, H., Schulte, M., Seidel-Morgenstern, A., 2012. *Preparative chromatography*, 2nd ed. Wiley-VCH, Weinheim, Germany.
- Schmitt, M., Hasse, H., 2006. Chemical Equilibrium and Reaction Kinetics of Heterogeneously Catalyzed *n*-Hexyl Acetate Esterification. *Ind. Eng. Chem. Res.* 45 (12), 4123–4132. 10.1021/ie0504351.
- Schmuck, C., 2013. *Basisbuch Organische Chemie*. Pearson, München.
- Schwaab, M., Pinto, J.C., 2007. Optimum reference temperature for reparameterization of the Arrhenius equation. Part 1: Problems involving one kinetic constant. *Chemical Engineering Science* 62 (10), 2750–2764. 10.1016/j.ces.2007.02.020.
- Seidel-Morgenstern, A., 2004. Experimental determination of single solute and competitive adsorption isotherms. *Journal of Chromatography A* 1037 (1-2), 255–272. 10.1016/j.chroma.2003.11.108.
- Seidel-Morgenstern, A., Guiochon, G., 1993. Modelling of the competitive isotherms and the chromatographic separation of two enantiomers. *Chemical Engineering Science* 48 (15), 2787–2797. 10.1016/0009-2509(93)80189-W.
- Seidel-Morgenstern, A., Keßler, L.C., Kaspereit, M., 2008. New Developments in Simulated Moving Bed Chromatography. *Chem. Eng. Technol.* 31 (6), 826–837. 10.1002/ceat.200800081.
- Selent, D., Franke, R., Kubis, C., Spannenberg, A., Baumann, W., Kreidler, B., Börner, A., 2011. A New Diphosphite Promoting Highly Regioselective Rhodium-Catalyzed Hydroformylation. *Organometallics* 30 (17), 4509–4514. 10.1021/om2000508.
- Shaharun, M.S., Dutta, B.K., Mukhtar, H., Maitra, S., 2010. Hydroformylation of 1-octene using rhodium–phosphite catalyst in a thermomorphic solvent system. *Chemical Engineering Science* 65 (1), 273–281. 10.1016/j.ces.2009.06.071.
- Sheinman, R., Sheintuch, M., 2009. Loop Reactor Design and Control for Reversible Exothermic Reactions. *Ind. Eng. Chem. Res.* 48 (11), 5185–5192. 10.1021/ie801333w.
- Sheintuch, M., Nekhamkina, O., 2004. Comparison of flow-reversal, internal-recirculation and loop reactors. *Chemical Engineering Science* 59 (19), 4065–4072. 10.1016/j.ces.2004.04.037.
- Sheintuch, M., Nekhamkina, O., 2005. The asymptotes of loop reactors. *AIChE J.* 51 (1), 224–234. 10.1002/aic.10287.
- Silveston, P.L., Hudgins, R.R. (Eds.), 2012. *Periodic operation of reactors*. Butterworth-Heinemann, Oxford.
- Smagina, Y., Sheintuch, M., 2009. Control of rotating pulses in a loop reactor. *Journal of Process Control* 19 (6), 954–963. 10.1016/j.jprocont.2008.12.006.
- Smith, M., 2013. *March's advanced organic chemistry: Reactions, mechanisms, and structure*, 7th ed. Wiley, Hoboken.
- Spivey, J.J., 1987. Complete catalytic oxidation of volatile organics. *Ind. Eng. Chem. Res.* 26 (11), 2165–2180. 10.1021/ie00071a001.
- Spivey, J.J., Butt, J.B., 1992. Literature review: deactivation of catalysts in the oxidation of volatile organic compounds. *Catalysis Today* 11 (4), 465–500. 10.1016/0920-5861(92)80039-P.
- Steimel, J., Engell, S., 2016. Optimization-based support for process design under uncertainty: A case study. *AIChE J.* 62 (9), 3404–3419. 10.1002/aic.15400.

- 
- Subramaniam, B., 2010. Exploiting Neoteric Solvents for Sustainable Catalysis and Reaction Engineering: Opportunities and Challenges. *Ind. Eng. Chem. Res.* 49 (21), 10218–10229. 10.1021/ie101543a.
- Subramaniam, B., Akiem, G.R., 2012. Sustainable catalytic reaction engineering with gas-expanded liquids. *Current Opinion in Chemical Engineering* 1 (3), 336–341. 10.1016/j.coche.2012.02.005.
- Sundmacher, K., Kienle, A., Seidel-Morgenstern, A., 2005. *Integrated chemical processes: Synthesis, operation, analysis, and control.* Wiley-VCH, Weinheim.
- Sup Song, K., Klvana, D., Kirchnerova, J., 2001. Kinetics of propane combustion over  $\text{La}_{0.66}\text{Sr}_{0.34}\text{Ni}_{0.3}\text{Co}_{0.7}\text{O}_3$  perovskite. *Applied Catalysis A: General* 213 (1), 113–121. 10.1016/S0926-860X(00)00884-X.
- Suwanayuen, S., Danner, R.P., 1980. Vacancy solution theory of adsorption from gas mixtures. *AIChE J.* 26 (1), 76–83. 10.1002/aic.690260113.
- Tanaka, R., Takayama, H., Morotomi, M., Kuroshima, T., Ueyama, S., Matsumoto, K., Kuroda, A., Mutai, M., 1983. Effects of Administration of TOS and Bifidobacterium breve 4006 on the Human Fecal Flora. *Bifidobacteria Microflora* 2 (1), 17–24. 10.12938/bifidus1982.2.1\_17.
- Thamm, H., Stach, H., Fiebig, W., 1983. Calorimetric study of the absorption of n-butane and but-1-ene on a highly dealuminated Y-type zeolite and on silicalite. *Zeolites* 3 (2), 95–97. 10.1016/0144-2449(83)90192-6.
- Toch, K., Thybaut, J.W., Marin, G.B., 2015. A systematic methodology for kinetic modeling of chemical reactions applied to *n*-hexane hydroisomerization. *AIChE J.* 61 (3), 880–892. 10.1002/aic.14680.
- Van Damme, P.S., Narayanan, S., Froment, G.F., 1975. Thermal cracking of propane and propane-propylene mixtures: Pilot plant versus industrial data. *AIChE J.* 21 (6), 1065–1073. 10.1002/aic.690210604.
- van Leeuwen, P.W.N.M., Claver, C., 2001. *Rhodium catalyzed hydroformylation.* Kluwer Academic Publishers, Dordrecht [etc.].
- Vanden Bussche, K.M., Froment, G.F., 1996. The STAR Configuration for Methanol Synthesis in Reversed Flow Reactors. *Canadian Journal of Chemical Engineering* 74 (5), 729–734.
- Velardi, S.A., Barresi, A.A., 2002. Methanol synthesis in a forced unsteady-state reactor network. *Chemical Engineering Science* 57 (15), 2995–3004. 10.1016/S0009-2509(02)00181-1.
- Veldsink, J.W., Versteeg, G.F., van Swaaij, W., 1995. Intrinsic kinetics of the oxidation of methane over an industrial copper(II) oxide catalyst on a  $\gamma$ -alumina support. *The Chemical Engineering Journal and the Biochemical Engineering Journal* 57 (3), 273–283. 10.1016/0923-0467(94)02872-8.
- Verein Deutscher Ingenieure, 2006. *VDI-Wärmeatlas: [Berechnungsunterlagen für Druckverlust, Wärme- und Stoffübertragung]*, 10th ed. Springer, Berlin, Heidelberg [u.a.].
- Vogl, C., Paetzold, E., Fischer, C., Kragl, U., 2005. Highly selective hydroformylation of internal and terminal olefins to terminal aldehydes using a rhodium-BIPHEPHOS-catalyst system. *Journal of Molecular Catalysis A: Chemical* 232 (1-2), 41–44. 10.1016/j.molcata.2005.01.019.
- Voltz, S.E., Morgan, C.R., Liederman, D., Jacob, S.M., 1973. Kinetic Study of Carbon Monoxide and Propylene Oxidation on Platinum Catalysts. *Ind. Eng. Chem. Prod. Res. Dev.* 12 (4), 294–301. 10.1021/i360048a006.

- Wachsen, O., Himmler, K., Cornils, B., 1998. Aqueous biphasic catalysis: Where the reaction takes place. *Catalysis Today* 42 (4), 373–379. 10.1016/S0920-5861(98)00119-9.
- Wang, S., Murata, K., Hayakawa, T., Hamakawa, S., Suzuki, K., 2000. Dehydrogenation of ethane with carbon dioxide over supported chromium oxide catalysts. *Applied Catalysis A: General* 196 (1), 1–8. 10.1016/S0926-860X(99)00450-0.
- Webb, P.B., Sellin, M.F., Kunene, T.E., Williamson, S., Slawin, Alexandra M Z, Cole-Hamilton, D.J., 2003. Continuous flow hydroformylation of alkenes in supercritical fluid-ionic liquid biphasic systems. *Journal of the American Chemical Society* 125 (50), 15577–15588. 10.1021/ja035967s.
- Westerterp, K.R., Beenackers, A.A., van Swaaij, W.P., 1993. *Chemical reactor design and operation*, 2nd ed. Wiley, Chichester [u.a.].
- Wicke, E., Vortmeyer, D., 1959. Zündzonen heterogener Reaktionen in gasdurchströmten Körnerschichten. *Bericht Bunsengesellschaft* 63, 145–152. 10.1002/bbpc.19590630128.
- Winterberg, M., Tsotsas, E., 2000. Impact of tube-to-particle-diameter ratio on pressure drop in packed beds. *AIChE J.* 46 (5), 1084–1088. 10.1002/aic.690460519.
- Worch, E., 2012. *Adsorption technology in water treatment: Fundamentals, processes, and modeling*. De Gruyter, Berlin, Boston.
- Yang, C., Bi, X., Mao, Z.-S., 2002. Effect of reaction engineering factors on biphasic hydroformylation of 1-dodecene catalyzed by water-soluble rhodium complex. *Journal of Molecular Catalysis A: Chemical* 187 (1), 35–46. 10.1016/S1381-1169(02)00216-9.
- Yao, Y.-F.Y., 1973. The oxidation of hydrocarbons and CO over metal oxides: II.  $\alpha$ -Cr<sub>2</sub>O<sub>3</sub>. *Journal of Catalysis* 28 (1), 139–149. 10.1016/0021-9517(73)90187-5.
- Yaws, C.L., 1999. *Chemical properties handbook: Physical, thermodynamic, environmental, transport, safety, and health related properties for organic and inorganic chemicals*. McGraw-Hill, New York.
- Ye, K., Freund, H., Xie, Z., Subramaniam, B., Sundmacher, K., 2012. Prediction of multi-component phase behavior of CO<sub>2</sub>-expanded liquids using CEoS/GE models and comparison with experimental data. *The Journal of Supercritical Fluids* 67, 41–52. 10.1016/j.supflu.2012.03.007.
- Yu, W., Hidajat, K., Ray, A.K., 2004. Determination of adsorption and kinetic parameters for methyl acetate esterification and hydrolysis reaction catalyzed by Amberlyst 15. *Applied Catalysis A: General* 260 (2), 191–205. 10.1016/j.apcata.2003.10.017.
- Zahn, V.M., 2012. *Adiabatic simulated moving bed reactor: Principle, nonlinear analysis and experimental demonstration*. Shaker, Aachen.
- Zahn, V.M., Yi, C.-U., Seidel-Morgenstern, A., 2011. Analysis and demonstration of a control concept for a heat integrated simulated moving bed reactor. *Chemical Engineering Science* 66 (20), 4901–4912. 10.1016/j.ces.2011.06.055.
- Zhang, R., Miller, J.T., Baertsch, C.D., 2012. Identifying the active redox oxygen sites in a mixed Cu and Ce oxide catalyst by in situ X-ray absorption spectroscopy and anaerobic reactions with CO in concentrated H<sub>2</sub>. *Journal of Catalysis* 294, 69–78. 10.1016/j.jcat.2012.07.005.
- Zhang, Y., Mao, Z.-S., Chen, J., 2002. Macro-kinetics of biphasic hydroformylation of 1-dodecene catalyzed by water-soluble rhodium complex. *Catalysis Today* 74 (1-2), 23–35. 10.1016/S0920-5861(01)00527-2.

---

Zheng, J., Leveueur, S., Taouk, B., Burel, F., Salmi, T., 2016. Kinetic modelling strategy for an exothermic multiphase reactor system, 27 October 2016, Fürstfeldbruck.



# Nomenclature

## Latin Symbols

$A$	$m^2$	surface
$B_{jE}$	-	total amount of $j_E$ elements
$c$	$mol \cdot m^{-3}$	concentration
$c_p$	$J \cdot (mol \cdot K)^{-1}$	heat capacity
$D$	$m^2 \cdot s^{-1}$	dispersion coefficient
$d$	$m$	diameter
$d_f$	-	degree of freedom
$E_A$	$kJ \cdot mol^{-1}$	activation energy
$F$	-	phase ratio
$FIM$	-	<i>Fisher</i> -Information matrix
$\Delta G_f$	$kJ \cdot mol^{-1}$	<i>Gibbs</i> enthalpy of formation
$\Delta G_R$	$kJ \cdot mol^{-1}$	<i>Gibbs</i> enthalpy of reaction
$H$	$mol \cdot (kg_{cat} \cdot Pa)^{-1}$	<i>Henry</i> adsorption constant
$\Delta h_{ads}$	$kJ \cdot mol^{-1}$	sorption enthalpy
$\Delta h_f$	$kJ \cdot mol^{-1}$	enthalpy of formation
$\Delta h_R$	$kJ \cdot mol^{-1}$	enthalpy of reaction
$J$	$kmol \cdot (m^2 \cdot min)^{-1}$	molar flux density
$j_c$	-	index of component
$j_E$	-	index of elements
$j_{it}$	-	index of iteration
$j_{obs}$	-	index of observation
$j_{step}$	-	Index of step
$j_{tact}$	-	index of experimental Loop Reactor tact
$j_{\Theta}$	-	index of optimization parameter
$j_{\omega}$	-	index of catalytic cycle step
$K$	$Pa^{-1}$	adsorption constant
$K$	varies	lumped inhibition coefficient in rate approaches
$K_{eq}$	-	reaction equilibrium constant
$k$	varies	reaction rate constant
$k_{eff}$	$min^{-1}$	effective mass transport coefficient
$k_W$	$W \cdot (m^2 \cdot K)^{-1}$	wall heat transfer coefficient
$L$	$m$	length
$m$	$kg$	mass
$n$	$mol$	amount of substance
$\dot{n}$	$mol \cdot s^{-1}$	molar flux
$q$	$mol \cdot kg_{cat}^{-1}$	load capacity
$P$	-	permutation matrix
$Pe$	-	<i>Peclet</i> number
$p$	$Pa$	pressure
$p^*$	$Pa$	fictitious pressure
$\bar{R}$	$J \cdot (mol \cdot K)^{-1}$	universal gas constant
$r$	$mol \cdot (kg_{cat} \cdot s)^{-1}$	reaction rate
$\bar{M}$	$kg \cdot kmol^{-1}$	molar mass
$S$	$J \cdot K^{-1}$	entropy
$S$	-	sensitivity
$SSR$	-	objective function
$T$	$K$ or $^{\circ}C$	temperature

## Nomenclature

---

$t$	s or min	time
$t$	-	student-t distribution
$tol$	-	tolerance
$U_{seg}$	m	perimeter of reactor segment
$u$	$m \cdot s^{-1}$	velocity
$V$	$m^3$	volume
$\dot{V}$	$m^3/s$	volumetric flux
$W/F$	$(kg_{cat} \cdot s) \cdot m^{-3}$	catalyst weight to flow-rate ratio
$X$	%	conversion
$x$	%	volume fraction
$Y$	%	yield
$y_{obs}$	-	observed system response
$z$	m	spatial coordinate

## Greek Symbols

$\alpha$	-	level of significance
$\beta$	-	element-species-matrix
$\gamma$	-	normalized switching time
$E$	-	diagonal matrix
$\varepsilon$	-	void fraction
$\eta$	$Pa \cdot s$	dynamic viscosity
$\Theta_{opt}$	-	optimization parameter vector
$\kappa$	-	condition number
$\lambda$	-	eigenvalue
$\lambda$	-	<i>Lagrange</i> multipliers
$\lambda_{eff}$	$J \cdot (m \cdot s \cdot K)^{-1}$	effective heat conductivity
$\nu$	-	stoichiometric coefficient
$\pi$	Pa	spreading pressure
$\rho$	$kg \cdot m^{-3}$	density
$\sigma^2$	-	variance
$\tau$	s	residence time
$\Omega$	-	<i>Christiansen</i> matrix
$\omega$	-	reaction step frequency

## Subscripts

ad	adiabatic
B	bottom
cas	cascade
cat	catalyst
fl	fluid
gas	gas phase
ign	ignition
L	ligand
li	liquid phase
mix	mixture
opt	optimization
ox	oxidation
P	particle
per	perturbation
R	reaction
red	reduction
ref	reference
s	solid phase
seg	reactor segment

---

sol	solubility
sw	switch
T	temperature
tot	total
W	wall

### Superscripts

dos	dosing
exp	experiment
F	finish
I	initial
in	inlet
max	maximal
mod	model
$N_C$	- number of components
$N_E$	- number of elements
$N_{exp}$	- number of experiments
$N_{obs}$	- number of observations
$N_R$	- number of reactions
$N_{seg}$	- number of reactor segments
$N_{sp}$	- number of samples
$N_{step}$	- number of cycle steps
$N_{\Theta}$	- number of optimization parameter
out	outlet
sat	saturation

### Abbreviations

AL	alkane
CI	confidence interval
CSTR	continuous stirred tank reactor
ER	<i>Eley/Rideal</i>
FA	frontal analysis
GA	general approach
GC	gas chromatograph
GCCK	general catalytic cycle kinetics
GIT	group increment theory
HC	hydrocarbon
hf	hydroformylation
hg	hydrogenation
iAD	iso-aldehyde
IAS	ideal adsorbed solution
ICP-OES	Inductively Coupled Plasma Optical Emission Spectroscopy
iOL	iso-dodecene
iso	isomerization
LH	<i>Langmuir/Hinshelwood</i>
LR	Loop Reactor
MPI	Max Planck Institute
MvK	<i>Mars/van Krevelen</i>
nAD	n-aldehyde
nOL	n-dodecene
OLS	ordinary least square
PFTR	plug flow tubular reactor
QRD	QR decomposition

rds	rate determining step
RFR	Reverse Flow Reactor
svd	singular value decomposition
Sym	symbols
TMBR	true moving bed reactor
TMS	thermomorphic multicomponent solvent
TPR	temperature programed reduction
VOC	volatile organic compound
WLS	weighted least square

## A. Derivation of Mechanistic Rate Models

Using the GCCK approach (or *Christiansen* methodology), which is amplified in section 2.1, mechanistic rate models in homogeneous, heterogeneous and biological catalysis can be derived. In the following, the derivation of applied rate models is shown.

### A.1 Homogeneous catalysis

#### A.1.1 Hydrogenation of 1-dodecene

In section 2.1.1 were derived rate expressions for the olefin isomerization reaction based on the network and the catalytic cycle shown in figs. 3.1 and 3.2. In analogy to eqs. 2.3-2.6 corresponding expressions can be derived capable to describe the hydrogenation of the terminal olefin. Below are given the most essential steps.

Considering besides the resting state of the catalyst (see figs. 3.2 and 3.3) also the states (2), (3) and (8) involved in the hydrogenation cycle the following eq. A1 can be derived.

$$r_{\text{hg,b}} = \frac{K_{\text{hf},1}^+ K_{\text{hf},2}^+ K_{\text{hg},1}^+ K_{\text{hg},2}^+ C_{\text{nOL}} C_{\text{H}_2} - K_{\text{hf},1}^- K_{\text{hf},2}^- K_{\text{hg},1}^- K_{\text{hg},2}^- C_{\text{AL}}}{\begin{pmatrix} K_{\text{hf},2}^+ K_{\text{hg},1}^+ K_{\text{hg},2}^+ C_{\text{H}_2} & + K_{\text{hf},1}^- K_{\text{hg},1}^+ K_{\text{hg},2}^+ C_{\text{H}_2} & + K_{\text{hf},1}^- K_{\text{hf},2}^+ K_{\text{hg},2}^+ & + K_{\text{hf},1}^- K_{\text{hf},2}^- K_{\text{hg},1}^- \\ + K_{\text{hf},1}^+ K_{\text{hg},1}^+ K_{\text{hg},2}^+ C_{\text{nOL}} C_{\text{H}_2} & + K_{\text{hf},1}^- K_{\text{hf},2}^+ K_{\text{hg},2}^+ C_{\text{nOL}} & + K_{\text{hf},1}^+ K_{\text{hf},2}^- K_{\text{hg},1}^- C_{\text{nOL}} & + K_{\text{hf},2}^- K_{\text{hg},1}^- K_{\text{hg},2}^- C_{\text{AL}} \\ + K_{\text{hf},1}^+ K_{\text{hf},2}^+ K_{\text{hg},2}^+ C_{\text{nOL}} & + K_{\text{hf},1}^+ K_{\text{hf},2}^- K_{\text{hg},1}^- C_{\text{nOL}} & + K_{\text{hf},2}^+ K_{\text{hg},1}^- K_{\text{hg},2}^- C_{\text{AL}} & + K_{\text{hf},1}^- K_{\text{hg},1}^+ K_{\text{hg},2}^- C_{\text{AL}} \\ + K_{\text{hf},1}^+ K_{\text{hf},2}^+ K_{\text{hg},1}^- C_{\text{nOL}} C_{\text{H}_2} & + K_{\text{hf},2}^+ K_{\text{hg},1}^+ K_{\text{hg},2}^- C_{\text{AL}} C_{\text{H}_2} & + K_{\text{hf},1}^+ K_{\text{hf},2}^- K_{\text{hg},2}^- C_{\text{AL}} C_{\text{H}_2} & + K_{\text{hf},1}^- K_{\text{hf},2}^- K_{\text{hg},2}^- C_{\text{AL}} \end{pmatrix}} \quad (\text{A.1})$$

If the step reactions constants from step (hf.2), (hg.1) and (hg.2) (see fig. 3.2) are excluded and rearranged, the eq. A.2 results.

$$r_{\text{hg,b}} = \frac{K_{\text{hf},1}^+ \left( C_{\text{nOL}} C_{\text{H}_2} - \frac{K_{\text{hf},1}^- K_{\text{hf},2}^- K_{\text{hg},1}^- K_{\text{hg},2}^-}{K_{\text{hf},1}^+ K_{\text{hf},2}^+ K_{\text{hg},1}^+ K_{\text{hg},2}^+} C_{\text{AL}} \right)}{\begin{pmatrix} C_{\text{H}_2} & + \frac{K_{\text{hf},1}^-}{K_{\text{hf},2}^+} C_{\text{H}_2} & + \frac{K_{\text{hf},1}^- K_{\text{hf},2}^-}{K_{\text{hf},2}^+ K_{\text{hg},1}^+} & + \frac{K_{\text{hf},1}^- K_{\text{hf},2}^- K_{\text{hg},1}^-}{K_{\text{hf},2}^+ K_{\text{hg},1}^+ K_{\text{hg},2}^+} \\ + \frac{K_{\text{hf},1}^+}{K_{\text{hf},2}^+} C_{\text{nOL}} C_{\text{H}_2} & + \frac{K_{\text{hf},1}^- K_{\text{hf},2}^-}{K_{\text{hf},2}^+ K_{\text{hg},1}^+} C_{\text{nOL}} & + \frac{K_{\text{hf},1}^- K_{\text{hf},2}^- K_{\text{hg},1}^-}{K_{\text{hf},2}^+ K_{\text{hg},1}^+ K_{\text{hg},2}^+} C_{\text{nOL}} & + \frac{K_{\text{hf},2}^- K_{\text{hg},1}^- K_{\text{hg},2}^-}{K_{\text{hf},2}^+ K_{\text{hg},1}^+ K_{\text{hg},2}^+} C_{\text{AL}} \\ + \frac{K_{\text{hf},1}^+}{K_{\text{hg},1}^+} C_{\text{nOL}} & + \frac{K_{\text{hf},1}^- K_{\text{hg},1}^-}{K_{\text{hg},1}^+ K_{\text{hg},2}^+} C_{\text{nOL}} & + \frac{K_{\text{hg},1}^- K_{\text{hg},2}^-}{K_{\text{hg},1}^+ K_{\text{hg},2}^+} C_{\text{AL}} & + \frac{K_{\text{hf},1}^- K_{\text{hg},1}^- K_{\text{hg},2}^-}{K_{\text{hf},2}^+ K_{\text{hg},1}^+ K_{\text{hg},2}^+} C_{\text{AL}} \\ + \frac{K_{\text{hf},1}^+}{K_{\text{hg},2}^+} C_{\text{nOL}} C_{\text{H}_2} & + \frac{K_{\text{hg},2}^-}{K_{\text{hg},2}^+} C_{\text{AL}} C_{\text{H}_2} & + \frac{K_{\text{hf},1}^- K_{\text{hg},2}^-}{K_{\text{hg},2}^+ K_{\text{hg},2}^+} C_{\text{AL}} C_{\text{H}_2} & + \frac{K_{\text{hf},1}^- K_{\text{hg},2}^- K_{\text{hg},2}^-}{K_{\text{hf},2}^+ K_{\text{hg},1}^+ K_{\text{hg},2}^+} C_{\text{AL}} \end{pmatrix}} \quad (\text{A.2})$$

Excluding  $(K_{\text{hf},1}^- K_{\text{hf},2}^- (K_{\text{hg},2}^- + K_{\text{hg},1}^-) \cdot (K_{\text{hf},2}^- K_{\text{hg},1}^- + K_{\text{hg},2}^-))^{-1}$  in the denominator eq. A.3 holds.

$$r_{\text{hg,b}} = \frac{\left( \frac{K_{\text{hf},1}^+ K_{\text{hf},2}^+ K_{\text{hg},1}^+ K_{\text{hg},2}^+}{K_{\text{hf},1}^- K_{\text{hf},2}^- (K_{\text{hg},2}^- + K_{\text{hg},1}^-)} \right) (C_{\text{nOL}} C_{\text{H}_2, \text{li}} - C_{\text{AL}} K_{\text{eq,hg,b}}^{-1})}{\begin{pmatrix} 1 + \left( \frac{K_{\text{hf},1}^+ (K_{\text{hf},2}^- + K_{\text{hf},1}^-)}{K_{\text{hf},1}^- K_{\text{hf},2}^- (K_{\text{hg},2}^- + K_{\text{hg},1}^-)} \right) \left( \frac{K_{\text{hf},1}^+ (K_{\text{hg},2}^- + K_{\text{hf},2}^-)}{(K_{\text{hf},2}^- + K_{\text{hf},1}^-)} C_{\text{nOL}} C_{\text{H}_2, \text{li}} + K_{\text{hg},2}^- C_{\text{AL}} C_{\text{H}_2, \text{li}} + K_{\text{hg},2}^- C_{\text{H}_2, \text{li}} \right) \\ + \frac{K_{\text{hf},1}^+ (K_{\text{hg},2}^- + K_{\text{hg},1}^-) (1 + K_{\text{hf},2}^-)}{K_{\text{hf},1}^- (K_{\text{hg},2}^- + K_{\text{hg},1}^-)} C_{\text{nOL}} + \frac{K_{\text{hg},2}^- (K_{\text{hg},1}^- (K_{\text{hf},1}^- + K_{\text{hf},2}^- + K_{\text{hf},1}^-) + K_{\text{hf},1}^- K_{\text{hf},2}^-)}{K_{\text{hf},1}^- K_{\text{hf},2}^- (K_{\text{hg},2}^- + K_{\text{hg},1}^-)} C_{\text{AL}} \end{pmatrix}} \quad (\text{A.3})$$



Similar to the hydrogenation the exclusion of the term  $(k_{\text{hf},1}^+k_{\text{hf},2}^-k_{\text{hf},3}^-(k_{\text{hf},5}^++k_{\text{hf},4}^-) \cdot (k_{\text{hf},2}^+k_{\text{hf},3}^+k_{\text{hf},4}^+k_{\text{hf},5}^+)^{-1})$  inside the denominator holds eq. A.7.

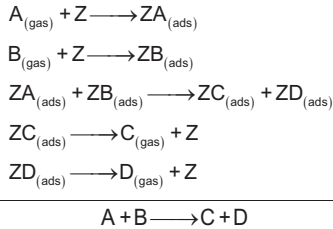
$$r_{\text{hf},b} = \frac{\left( \frac{k_{\text{hf},1}^+k_{\text{hf},2}^+k_{\text{hf},3}^+k_{\text{hf},4}^+k_{\text{hf},5}^+}{k_{\text{hf},1}^-k_{\text{hf},2}^-k_{\text{hf},3}^- (k_{\text{hf},5}^+ + k_{\text{hf},4}^-)} \right) (C_{\text{nOL}}C_{\text{H}_2,\text{II}}C_{\text{CO,II}} - C_{\text{nAD}}K_{\text{eq,hf,b}}^{-1})}{1 + \left( \frac{k_{\text{hf},1}^+k_{\text{hf},4}^+k_{\text{hf},5}^+}{k_{\text{hf},3}^- (k_{\text{hf},5}^+ + k_{\text{hf},4}^-)} \right) C_{\text{H}_2,\text{II}} + \left( \frac{k_{\text{hf},1}^+k_{\text{hf},3}^+k_{\text{hf},4}^+k_{\text{hf},5}^+ (k_{\text{hf},1}^- + k_{\text{hf},2}^-)}{k_{\text{hf},1}^-k_{\text{hf},2}^-k_{\text{hf},3}^- (k_{\text{hf},5}^+ + k_{\text{hf},4}^-)} \right) C_{\text{H}_2,\text{II}}C_{\text{CO,II}}C_{\text{nAD}} + \left( \frac{k_{\text{hf},1}^+k_{\text{hf},5}^+ (k_{\text{hf},3}^-k_{\text{hf},4}^- (k_{\text{hf},1}^- + k_{\text{hf},2}^-) + k_{\text{hf},1}^-k_{\text{hf},2}^- (k_{\text{hf},3}^- + k_{\text{hf},4}^-))}{k_{\text{hf},1}^-k_{\text{hf},2}^-k_{\text{hf},3}^- (k_{\text{hf},5}^+ + k_{\text{hf},4}^-)} \right) C_{\text{nAD}} + \left( \frac{k_{\text{hf},1}^+k_{\text{hf},3}^+k_{\text{hf},4}^+k_{\text{hf},5}^+ (k_{\text{hf},2}^- + k_{\text{hf},1}^-)}{k_{\text{hf},1}^-k_{\text{hf},2}^-k_{\text{hf},3}^- (k_{\text{hf},5}^+ + k_{\text{hf},4}^-)} \right) C_{\text{H}_2,\text{II}}C_{\text{CO,II}} + k_{\text{hf},1}^+k_{\text{hf},1}^-k_{\text{hf},2}^-k_{\text{hf},3}^-C_{\text{nOL}}C_{\text{CO,II}} + \left( \frac{k_{\text{hf},1}^+k_{\text{hf},1}^- (k_{\text{hf},2}^- + k_{\text{hf},2}^-)}{k_{\text{hf},2}^-} \right) C_{\text{nOL}} + \left( \frac{k_{\text{hf},1}^+k_{\text{hf},3}^+k_{\text{hf},4}^-k_{\text{hf},1}^- (k_{\text{hf},5}^+ + k_{\text{hf},2}^-)}{k_{\text{hf},2}^-k_{\text{hf},3}^- (k_{\text{hf},5}^+ + k_{\text{hf},4}^-)} \right) C_{\text{nOL}}C_{\text{H}_2,\text{II}}C_{\text{CO,II}} + \left( \frac{k_{\text{hf},1}^+k_{\text{hf},1}^-k_{\text{hf},4}^+k_{\text{hf},5}^+ (k_{\text{hf},2}^- + k_{\text{hf},2}^-)}{k_{\text{hf},1}^-k_{\text{hf},2}^-k_{\text{hf},3}^- (k_{\text{hf},5}^+ + k_{\text{hf},4}^-)} \right) C_{\text{nOL}}C_{\text{H}_2,\text{II}} + \left( \frac{k_{\text{hf},1}^+k_{\text{hf},4}^+k_{\text{hf},5}^+}{k_{\text{hf},3}^- (k_{\text{hf},5}^+ + k_{\text{hf},4}^-)} \right) C_{\text{H}_2,\text{II}}C_{\text{nAD}} + \left( \frac{k_{\text{hf},1}^+k_{\text{hf},3}^+k_{\text{hf},4}^-k_{\text{hf},5}^+ (k_{\text{hf},1}^- + k_{\text{hf},2}^-)}{k_{\text{hf},1}^-k_{\text{hf},2}^-k_{\text{hf},3}^- (k_{\text{hf},5}^+ + k_{\text{hf},4}^-)} \right) C_{\text{CO,II}}C_{\text{nAD}} \right) \quad (\text{A.7})$$

Using lumped parameters, the final expression of the hydroformylation of 1-dodecene is given by eq. A.8.

$$r_{\text{hf},b} = \frac{k_{\text{hf},b} (T) (C_{\text{nOL}}C_{\text{H}_2,\text{II}}C_{\text{CO,II}} - C_{\text{nAD}} \cdot K_{\text{eq,hf,b}}^{-1})}{\left( K_{\alpha,\text{hf},b}C_{\text{nOL}} + K_{\beta,\text{hf},b}C_{\text{nOL}}C_{\text{CO,II}} + K_{\gamma,\text{hf},b}C_{\text{nOL}}C_{\text{H}_2,\text{II}}C_{\text{CO,II}} + K_{\delta,\text{hf},b}C_{\text{nAD}} + K_{\epsilon,\text{hf},b}C_{\text{H}_2,\text{II}}C_{\text{CO,II}}C_{\text{nAD}} + K_{\zeta,\text{hf},b}C_{\text{nOL}}C_{\text{H}_2,\text{II}} + K_{\eta,\text{hf},b}C_{\text{H}_2,\text{II}}C_{\text{nAD}} + K_{\theta,\text{hf},b}C_{\text{H}_2,\text{II}} + K_{\iota,\text{hf},b}C_{\text{H}_2,\text{II}}C_{\text{CO,II}} + K_{\kappa,\text{hf},b}C_{\text{CO,II}}C_{\text{nAD}} + 1 \right)} \quad (\text{A.8})$$

## A.2 Heterogeneous catalysis: Langmuir/Hinshelwood approach

The *Langmuir/Hinshelwood* mechanism is one of the most used kinetic rate approaches in heterogeneous catalysis (Kumar et al., 2008). For a simplified reaction with two educts and two products ( $A + B \rightarrow C + D$ ) follows (Murzin and Salmi, 2005; Murzin, 2010):



In this case, the surface reaction between the adsorbed components is the rate determining step. So the reaction kinetic can be written as a function of the kinetic constant ( $k_{\text{rds}}$ ) and the surface concentration of the component A and B ( $\Theta_A$  and  $\Theta_B$ ):

$$r_{\text{rds}} = k_{\text{rds}}(T) \cdot \Theta_A \cdot \Theta_B \quad (\text{A.9})$$

To describe the relationship between coverage of a particular gas and its partial pressure above the surface the *Langmuir* adsorption model is often used. The concept assumes identical binding energies of all adsorbed components at all surface sites. Added no interactions between the adsorbed components are accepted (Duong, 1998; Chorkendorff and Niemantsverdriet, 2003; Murzin and Salmi, 2005). Thus, the adsorption (ads) and desorption (des) process holds:

$$r_{\text{ads}} = \frac{d\Theta_{j_c}}{dt} = k_{\text{ads},j_c} \cdot p_{j_c} \cdot \Theta_{\text{free}} \quad \text{and} \quad r_{\text{des}} = -\frac{d\Theta_{j_c}}{dt} = k_{\text{des},j_c} \cdot \Theta_{j_c} \quad (\text{A.10})$$

At equilibrium conditions the adsorption and desorption rates are equal ( $r_{\text{ads}} = r_{\text{des}}$ ). For these conditions the surface concentration of a component  $j_c$  is a function of all empty sites at the catalyst surface.

$$\Theta_{j_c} = K_{j_c} \cdot p_{j_c} \cdot \Theta_{\text{free}} \quad \text{with} \quad K_{j_c} = \frac{k_{\text{ads},j_c}}{k_{\text{des},j_c}} \quad (\text{A.11})$$

Added to the surface conditions of each component the correlation of all empty sites can deviate from the balance equation of all available sites.

$$1 = \Theta_{\text{free}} + \sum_{j_c=1}^{N_c} \Theta_{j_c} = \Theta_{\text{free}} \cdot \left( 1 + \sum_{j_c=1}^{N_c} K_{j_c} \cdot p_{j_c} \right) \quad \Rightarrow \quad \Theta_{\text{free}} = \frac{1}{1 + \sum_{j_c=1}^{N_c} K_{j_c} \cdot p_{j_c}} \quad (\text{A.12})$$

The insertion of eq. A.12 in formula A.11 results in an expression of an adsorption isotherm of each component as a function of temperature and the partial pressures and all present gases.

$$\Theta_{j_c} = \frac{q_{j_c}(T)}{q_{j_c}^{\text{sat}}(T)} = \frac{K_{j_c}(T) \cdot p_{j_c}}{1 + \sum_{j=1}^{N_c} K_j(T) \cdot p_j} \quad (\text{A.13})$$

With this expression and the assumption that all educts and products can be adsorbed at the catalyst surface, the reaction rate of the rate determining step for the fictive chemical reaction results in the following expression:

$$r_{\text{rds}} = \frac{k_{\text{rds}}(T) \cdot K_A(T) \cdot p_A \cdot K_B(T) \cdot p_B}{(1 + K_A(T) \cdot p_A + K_B(T) \cdot p_B + K_C(T) \cdot p_C + K_D(T) \cdot p_D)^2} \quad (\text{A.14})$$

Analyzing the derived *Langmuir/Hinshelwood* approach, including product adsorption, the rate approach can be general formulated by eq. A.15 according to *Hougen/Watson*.

$$r = \frac{\text{Kinetic} \cdot \text{Driving Force}}{(\text{Adsorption Term})^n} \quad (\text{A.15})$$

The temperature dependents of the reaction rate constant and all adsorption constants can be assumed by an *Arrhenius* approach. The kinetic rate approaches of the total oxidation of the hydrocarbons ethylene and propylene as well as of carbon monoxide are shown in eq. 5.1.

### A.3 Biological catalysis

Generally the GCCK approach (or *Christiansen* methodology) is applicable in biological catalysis, too (Helfferich, 2004; Murzin and Salmi, 2005). However, the real determination of the enzyme catalyst concentration is obviously complicated. Based on the chemical structure of an enzyme the catalytic behavior can be vary substantially for different reaction properties. Accordingly, the real reaction mechanism remains unknown. Additional catalyst poison or other effects reduce also the concentration of the catalyst enzyme in resting state. Normally the serious quantification of such transformation effects is not possible. Based on these difficulties the effort of deriving mechanistic kinetic rate approaches in biological catalysis will be avoid. However, to round off the demonstration of the methodology in biological catalysis the derivation of the mechanistic kinetic rate approach of the synthesis of the prebiotic galacto-oligosaccharides (GOS) is shown below.

Positive physiological properties on humans are provided e.g. by GOS. GOS are part of the human breast milk and are considered to be responsible for the bifidogenic effect (Tanaka et al., 1983). The production of GOS is characterized by a consecutive equilibrium limited transgalactosylation reaction of lactose and mono saccharides (Palai and Bhattacharya, 2013; Palai et al., 2015). In that way, lactose (lac) is converted initially to glucose (glu) and galactose (gal) forming in a series polymerization GOS. The hydrolysis of the enzyme-galactose-complex (E[galactose]) occurs in parallel. Preliminary experiments with feed mixtures (lactose + products) and instructive dynamic perturbations with glucose and / or galactose revealed an inhibiting effect on the active catalyst / enzyme (E) and reduce the reaction rate drastically. Based on these experiments the reaction network and the corresponding catalytic cycle are shown in fig. A.1.

First the lactose decomposition to galactose and glucose include the single reaction steps 1, 2, 3 and 6. Additionally the inhibition of the catalyst concentration in resting state by galactose and glucose is considered. Thus, the reaction rate follows eq. A.16.

$$r = \frac{(\omega_1^+ \omega_2^+ \omega_3^+ \omega_6^+ - \omega_1^- \omega_2^- \omega_3^- \omega_6^-) C_E}{\begin{pmatrix} \omega_2^+ \omega_3^+ \omega_6^+ + \omega_1^- \omega_3^+ \omega_6^+ + \omega_1^- \omega_2^- \omega_6^+ + \omega_1^- \omega_2^- \omega_3^- \\ + \omega_1^+ \omega_3^+ \omega_6^+ + \omega_1^+ \omega_2^- \omega_6^+ + \omega_1^+ \omega_2^- \omega_3^- + \omega_2^- \omega_3^- \omega_6^- \\ + \omega_1^+ \omega_2^+ \omega_6^+ + \omega_1^+ \omega_2^+ \omega_3^- + \omega_2^+ \omega_3^- \omega_6^- + \omega_1^- \omega_3^- \omega_6^- \\ + \omega_1^+ \omega_2^+ \omega_3^+ + \omega_2^+ \omega_3^+ \omega_6^- + \omega_1^- \omega_3^+ \omega_6^- + \omega_1^- \omega_2^- \omega_3^- \end{pmatrix} + \begin{pmatrix} \omega_2^+ \omega_3^+ \omega_6^+ \\ + \omega_1^- \omega_3^+ \omega_6^+ \\ + \omega_1^- \omega_2^- \omega_6^+ \\ + \omega_1^- \omega_2^- \omega_3^- \end{pmatrix} \begin{pmatrix} K_7 c_{\text{glu}} \\ + K_8 c_{\text{gal}} \end{pmatrix}} \quad (\text{A.16})$$

Assuming that the glucose elimination (step 3) is irreversible ( $\omega_3^- = 0$ ) eq. A.16 can be simplified to:

$$r = \frac{\omega_1^+ \omega_2^+ \omega_3^+ \omega_6^+ C_E}{\begin{pmatrix} \omega_2^+ \omega_3^+ \omega_6^+ + \omega_1^- \omega_3^+ \omega_6^+ + \omega_1^- \omega_2^- \omega_6^+ + 0 \\ + \omega_1^+ \omega_3^+ \omega_6^+ + \omega_1^+ \omega_2^- \omega_6^+ + 0 & + 0 \\ + \omega_1^+ \omega_2^+ \omega_6^+ + 0 & + 0 & + 0 \\ + \omega_1^+ \omega_2^+ \omega_3^+ + \omega_2^+ \omega_3^+ \omega_6^- + \omega_1^- \omega_3^+ \omega_6^- + \omega_1^- \omega_2^- \omega_3^- \end{pmatrix} + \begin{pmatrix} \omega_2^+ \omega_3^+ \omega_6^+ \\ + \omega_1^- \omega_3^+ \omega_6^+ \\ + \omega_1^- \omega_2^- \omega_6^+ \\ + 0 \end{pmatrix} \begin{pmatrix} K_7 c_{\text{glu}} \\ + K_8 c_{\text{gal}} \end{pmatrix}} \quad (\text{A.17})$$

By substitution of the single step frequencies by the step kinetic constants and some rearrangements eq. A.17 can be written as:

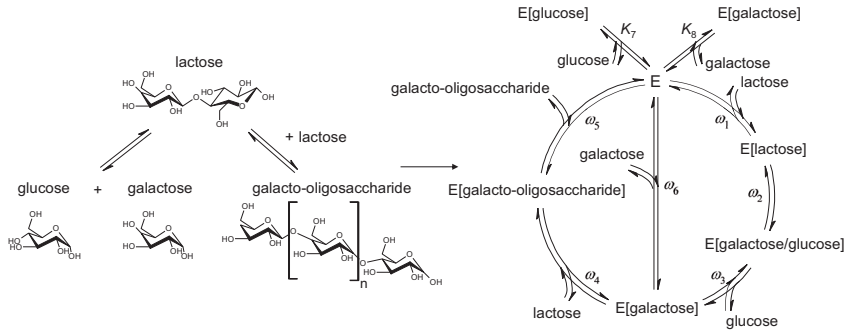


**Figure A.1:** Postulated reaction network of the lactose splitting, the galacto-oligosaccharide formation and the corresponding catalytic cycle at an enzyme catalyst including glucose and galactose inhibition at the enzyme catalyst (Müller et al., 2017)

$$r = \frac{k_1^+ c_{\text{lac}} c_E}{(K_{11} c_{\text{lac}} + (1 + K_{12}) (1 + c_{\text{gal}}/K_6 + K_7 c_{\text{glu}} + K_8 c_{\text{gal}}))} \quad (\text{A.18})$$

The lumped inhibition constants  $K_{11}$  and  $K_{12}$  correspond to the eqs. A.19 and A.20, respectively.

$$K_{11} = \frac{k_1^+}{k_2^+} + \frac{k_1^+}{k_3^+ K_2} + \frac{k_1^+}{k_3^+} + \frac{k_1^+}{k_6^+} \quad (\text{A.19}) \quad \text{and} \quad K_{12} = \frac{k_1^-}{k_2^+} + \frac{k_1^-}{k_3^+ K_2} \quad (\text{A.20})$$

Based on these assumptions the number of unknown parameters can be reduced from 14 to 6. Nevertheless, the parameter estimation is still difficult because of the product of the inhibition constant  $K_{12}$  and the equilibrium constants  $K_{6-8}$ . Subset-Selection methods would reveal such linear combinations. Thus, a further model simplification is possible. More information about model reduction techniques can be found in section 2.3.

At the second reaction, the GOS polymerization from galactose and lactose, the single reaction steps from 4 to 6, are considered (see fig. A.1). In addition, the inhibition behavior of galactose and glucose will be included as well (see eq. A.21).

$$r = \frac{(\omega_5^- \omega_4^+ \omega_5^+ - \omega_6^+ \omega_4^- \omega_5^-) c_E}{\left( \begin{array}{l} \omega_4^+ \omega_5^+ + \omega_6^+ \omega_5^+ + \omega_6^+ \omega_4^- \\ + \omega_6^- \omega_5^+ + \omega_5^- \omega_4^- + \omega_4^- \omega_5^- \\ + \omega_6^- \omega_4^+ + \omega_4^+ \omega_5^- + \omega_6^+ \omega_5^- \end{array} \right) + \left( \begin{array}{l} \omega_4^+ \omega_5^+ \\ + \omega_6^+ \omega_5^+ \\ + \omega_6^+ \omega_4^- \end{array} \right) \left( \begin{array}{l} K_7 c_{\text{glu}} \\ + K_8 c_{\text{gal}} \end{array} \right)} \quad (\text{A.21})$$

Assuming the rate determining polymerization step ( $\omega_4 \ll \omega_5$  and  $\omega_4 \ll \omega_6$ ) eq. A.21 reduces to eq. A.22.

$$r = \frac{(\omega_6^- \omega_4^+ \omega_5^+ - \omega_6^+ \omega_4^- \omega_5^-) c_E}{\left( \omega_6^- \omega_5^+ + \omega_6^+ \omega_5^- + \omega_6^+ \omega_5^+ (1 + K_7 c_{\text{glu}} + K_8 c_{\text{gal}}) \right)} \quad (\text{A.22})$$

By inserting of the single step constants and definition of the equilibrium reaction constant  $K_{\text{eq}}$  (Helfferich, 2004) the mechanistic reaction rate approach of the GOS polymerization follows eq. A.23.

$$r = \frac{k_4^+ (c_{\text{gal}} c_{\text{lac}} - c_{\text{GOS}} \cdot K_{\text{eq}}^{-1}) c_{\text{E}}}{(c_{\text{gal}} + K_6 (1 + c_{\text{GOS}} K_5^{-1} + K_7 c_{\text{glu}} + K_8 c_{\text{gal}}))} \quad (\text{A.23})$$

On closer inspection of the derived reaction rate approaches (eqs. A.18 and A.23) the single step equilibrium constants  $K_{6-8}$  are part of both. Correspondingly the parameter estimation of the rate laws has to be simultaneously at the available experimental data. Additionally based on slightly simplification the most significant used reaction rate approach in biological catalysis, the *Michaelis/Menten* kinetic, can be derived (Helfferich, 2004).

#### A.4 Equilibrium constant

The chemical equilibrium of a reaction is reached, if the free enthalpy  $G$  (also Gibbs free energy) offers a minimum. On the one hand this enthalpy can be calculated using the total differential equation as function of pressure  $p$ , temperature  $T$  and the amount of substance of the involved components  $n_{j_c}$ .

$$dG = \left( \frac{\partial G}{\partial T} \right)_{p,n} \cdot dT + \left( \frac{\partial G}{\partial p} \right)_{T,n} \cdot dp + \sum_{j_c=1}^{N_c} \left( \frac{\partial G}{\partial n_{j_c}} \right)_{T,p,n} \cdot dn_{j_c} \quad (\text{A.24})$$

On the other hand the *Gibbs-Helmholtz* equation can be used, which connect the free enthalpy with the entropy  $S$  and enthalpy  $H$ .

$$dG = -S \cdot dT + V \cdot dp + \sum_{j_c=1}^{N_c} \mu_{j_c} \cdot dn_{j_c} = dH - T \cdot dS \quad (\text{A.25})$$

If temperature and pressure is assumed to be constant and the chemical potential of each component  $\mu_{j_c}$  is applied, the total differential equation holds:

$$\Delta G_{\text{R}} = 0 = \sum_{j_c=1}^{N_c} \left( \mu_{j_c}^{\text{st}}(T) + \tilde{R}T \cdot \ln \left( \frac{p_{j_c}}{p^0} \right) \right) \cdot dn_{j_c} \quad (\text{A.26})$$

Further changes of the amount of substance can be described by the extent of reaction  $\xi$ .

$$\Delta G_{\text{R}} = 0 = \left( \sum_{j_c=1}^{N_c} \mu_{j_c}^{\text{st}}(T) \cdot \nu_{j_c} + \tilde{R}T \cdot \sum_{j_c=1}^{N_c} \ln \left( \frac{p_{j_c}}{p^0} \right) \right) d\xi \quad (\text{A.27})$$

The first part of eq. A.27 corresponds to the *Gibbs* free energy at standard conditions, which is tabulated for the major part of chemical substances. The second part can be replaced by the definition of the equilibrium constant  $K_{\text{eq}}$ . Thus, eq. A.28 holds.

$$\Delta G_{\text{R}}^{\text{st}} = -\tilde{R}T \cdot \ln(K_{\text{eq}}) \quad (\text{A.28})$$

The transformation of eq. A.28 to the equilibrium constant leads to final expression.

$$K_{\text{eq}} = \exp \left( \frac{-\Delta G_{\text{R}}^{\text{st}}}{\tilde{R}T} \right) \quad (\text{A.29})$$



## B. Reactor Models

### B.1 Mass balance

The derivation of the partial mass balance from the general mass balance occurred on a fixed and time constant control volume of random size and form. The basis is the verbal formulation of the differential balance equation in section 2. The accumulation term of a component  $j_c$  is defined as follows.

$$\frac{dm_{j_c}}{dt} = \frac{d}{dt} \int_V \rho_{j_c}(t, \mathbf{z}_k) dV = \int_V \frac{\partial \rho_{j_c}(t, \mathbf{z}_k)}{\partial t} dV \quad (\text{B.1})$$

The inlet and outlet flows of the convection part are described by an integral of the mass flow density across the control volume surface.

$$-\int_A \rho_{j_c} u_{\text{gas},k,j_c} n_k dA \quad (\text{B.2})$$

The negative sign of  $n_k$  has to be considered because of the flow direction definition. Accordingly, inlet flows are defined as positive and outlet flows as negative. Using the definition of the mass diffusion current density (eq. B.3):

$$j_{k,j_c} = \rho_{j_c} (u_{\text{gas},k,j_c} - u_{\text{gas},k}) \quad (\text{B.3})$$

and the Gauss theorem (is used to transfer the surface integral in a volume integral), eq. B.2 can be described by eq. B.4. The mass dispersion is later described by 1.Fick's law.

$$-\int_V \frac{\partial}{\partial \mathbf{z}_k} (\rho_{j_c} u_{\text{gas},k} + j_{k,j_c}) dV \quad (\text{B.4})$$

To consider chemical reaction inside the control volume, which changes the mass of the observed component  $j_c$ , the mass specific source density is introduced (see eq. B.5).

$$\int_V \sigma_{j_c} dV = \int_V \tilde{M}_{j_c} \cdot \sum_{j_R=1}^{M_R} \nu_{j_c,j_R} r_{j_R} dV \quad (\text{B.5})$$

Thus, summarizing the accumulation, convection and diffusion as well as the source term for one component  $j_c$ , the partial mass balance in integral form can be written as follows.

$$\int_V \frac{\partial \rho_{j_c}(t, \mathbf{z}_k)}{\partial t} dV = -\int_V \frac{\partial}{\partial \mathbf{z}_k} (\rho_{j_c} u_{\text{gas},k} + j_{k,j_c}) dV + \int_V \sigma_{j_c} dV \quad (\text{B.6})$$

Considering the random size and shape of the fixed control volume, the integrand for all terms disappear, so that the partial differential mass balance equation in local form results in eq. B.7.

$$\frac{\partial \rho_{j_c}}{\partial t} = -\frac{\partial}{\partial \mathbf{z}_k} (\rho_{j_c} u_{\text{gas},k} + j_{k,j_c}) + \sigma_{j_c} \quad \text{with} \quad j_c = 1, \dots, N_c \quad (\text{B.7})$$

Using the definition of the component concentration (eq. B.8), the final partial concentration balance equation is defined by eq. B.9.

$$\rho_{j_c} = c_{j_c} \cdot \tilde{M}_{j_c} \quad (\text{B.8})$$

$$\frac{\partial c_{j_c}}{\partial t} = -\frac{\partial}{\partial \mathbf{z}_k} (c_{j_c} u_{\text{gas},k,j_c} + j_{k,j_c}) + \sum_{j_R=1}^{M_R} \nu_{j_c,j_R} r_{j_R} \quad (\text{B.9})$$

## B.2 Energy balance

Initial point of the energy balance equation in temperature form is the specific enthalpy in substantial formulation.

$$c_{\text{tot}} \frac{\partial h}{\partial t} - \frac{\partial p}{\partial t} = - \frac{\partial q'_k}{\partial z_k} + \sum_{j_c=1}^{N_c} \dot{f}_{k,j_c} j_{k,j_c} - \pi_{jk} \frac{\partial u_j}{\partial z_k} \quad (\text{B.10})$$

To transfer this balance, the total differential of the enthalpy is introduced in eq. B.10.

$$\frac{dh}{dt} = \left( \frac{\partial h}{\partial T} \right)_{p,x_{j_c}} \frac{dT}{dt} + \left( \frac{\partial h}{\partial p} \right)_{T,x_{j_c}} \frac{dp}{dt} + \sum_{j_c=1}^{N_c} \left[ \left( \frac{\partial h}{\partial x_{j_c}} \right)_{T,p,x} \frac{dx_{j_c}}{dt} + \left( \frac{\partial \Delta h_{\text{mix}}}{\partial x_{j_c}} \right)_{T,p,x} \frac{dx_{j_c}}{dt} \right] \quad (\text{B.11})$$

Using the specific heat capacity  $c_p$ , the specific partial enthalpy  $h_{j_c}$  of component  $j_c$  and the specific partial mixture enthalpy  $\Delta h_{\text{mix},j_c}$ , the total differential equation of the enthalpy can be written as:

$$\frac{dh}{dt} = c_p \frac{dT}{dt} + \left( \frac{\partial h}{\partial p} \right)_{T,x_{j_c}} \frac{dp}{dt} + \sum_{j_c=1}^{N_c} \left[ h_{j_c} \frac{dx_{j_c}}{dt} + \Delta h_{\text{mix},j_c} \frac{dx_{j_c}}{dt} \right] \quad (\text{B.12})$$

This equation inserted in eq. B.10 holds eq. B.13

$$\left( c_{\text{tot}} c_p \frac{\partial T}{\partial t} + \left( c_{\text{tot}} \left( \frac{\partial h}{\partial p} \right) - 1 \right) \frac{dp}{dt} \right) + c_{\text{tot}} \cdot \sum_{j_c=1}^{N_c} \left[ \left( h_{j_c} + \Delta h_{\text{mix},j_c} \right) \frac{dx_{j_c}}{dt} \right] = - \frac{\partial q'_k}{\partial z_k} + \sum_{j_c=1}^{N_c} \dot{f}_{k,j_c} j_{k,j_c} - \pi_{jk} \frac{\partial u_j}{\partial z_k} \quad (\text{B.13})$$

The accumulation term of the molar ratio can be substituted by the molar ratio balance (see eq. B.14).

$$c_{\text{tot}} \frac{dx_{j_c}}{dt} = - \frac{\partial \mathcal{J}_{k,j_c}}{\partial z_k} + \sum_{j_R=1}^{N_R} \nu_{j_c,j_R} r_{j_R} + \frac{\partial \mathcal{J}_{\text{mix},j_c}}{\partial z_k} \quad (\text{B.14})$$

Further the energy flow vector  $q'_k$  is split in the heat flow because of heat conduction and/or radiation and the enthalpy diffusion flow.

$$q'_k = q_k + \sum_{j_c=1}^{N_c} \frac{j_{k,j_c}}{\dot{M}_{j_c}} \cdot (h_{j_c} + \Delta h_{\text{mix},j_c}) \quad (\text{B.15})$$

To model the differential balance equation, the temperature field is transferred from the substantial to the local formulation by the operator equation (see eq. B.16).

$$\frac{dT}{dt} = \frac{\partial T}{\partial t} + u_{\text{gas},k} \frac{\partial T}{\partial z_k} \quad (\text{B.16})$$

Finally, using the eqs. B.14-16, the energy balance in temperature form can be written as follows.

$$c_{\text{tot}} c_p \frac{\partial T}{\partial t} + \left( c_{\text{tot}} \left( \frac{\partial h}{\partial p} \right) - 1 \right) \frac{dp}{dt} = \left( -c_{\text{tot}} c_p u_{\text{gas},k} \frac{\partial T}{\partial z_k} + \sum_{j_R=1}^{N_R} (-\Delta h_{R,j_R}) r_{j_R} - \frac{\partial q_k}{\partial z_k} \right. \\ \left. + \sum_{j_R=1}^{N_R} r_{j_R} \sum_{j_c=1}^{N_c} \Delta h_{\text{mix},j_c} \nu_{j_c,j_R} + \sum_{j_c=1}^{N_c} \dot{f}_{k,j_c} j_{k,j_c} - \pi_{jk} \frac{\partial u_j}{\partial z_k} \right. \\ \left. + \sum_{j_c=1}^{N_c} \frac{j_{k,j_c}}{\dot{M}_{j_c}} \left( \frac{\partial h_{j_c}}{\partial z_k} \right) + \sum_{j_c=1}^{N_c} \frac{j_{k,j_c}}{\dot{M}_{j_c}} \left( \frac{\partial \Delta h_{\text{mix},j_c}}{\partial z_k} \right) \right) \quad (\text{B.17})$$

Using the first derivative with respect to the local position of the heat flow, the heat conduction over the reactor shell can be explained by eq. B.18.

$$\frac{dq_k}{dz_k} = k_w \cdot \frac{U}{A_b} (T_u - T) \quad (\text{B.18})$$

However, at kinetic parameter estimation problems the additional solving of a thermal energy balance is quite difficult because of parameter correlation. Therefore, the use of an empirical polynomial approach is suitable as well (see eq. B.19).

$$T(z) = P_{T,1}z^2 + P_{T,2}z + P_{T,3} \quad (\text{B.19})$$

By means of eq. 2.25 predictions of temperature profiles are not possible. Accordingly, experimental temperature data are needed to estimate  $P_{T,1-3}$  separately.

### B.3 Two phase mass transfer model

The two phase model (see fig. B.1) assumes that the molar flux of a component  $j_c$  is in equilibrium conditions.

$$J_{j_c, \text{gas}} = J_{j_c, \text{li}} \quad (\text{B.20})$$

Using the definition of the molar flux from the bulk phase to the boundary layer

$$J_{j_c, \text{gas}} = n_{j_c, \text{gas}} - n_{j_c, \text{gas}}^* \quad \text{or} \quad J_{j_c, \text{li}} = n_{j_c, \text{li}}^* - n_{j_c, \text{li}} \quad (\text{B.21})$$

in combination with the perfect gas law, eq. B.20 can be written as follows.

$$\frac{p_{j_c, \text{gas}} V_{\text{seg, gas}}}{\bar{R} \cdot T} - \frac{p_{j_c, \text{gas}}^* V_{\text{seg, gas}}}{\bar{R} \cdot T} = c_{j_c, \text{li}}^* V_{\text{seg, li}} - c_{j_c, \text{li}} V_{\text{seg, li}} \quad (\text{B.22})$$

This equation can be reformed to  $c_{j_c, \text{li}}^*$ , considering the *Henry* absorption isotherm ( $p_{j_c}^* = H_{j_c} \cdot c_{j_c}^*$ ) to the final eq. B.23.

$$c_{j_c, \text{li}}^* = \frac{\frac{p_{j_c, \text{gas}} V_{\text{seg, gas}}}{\bar{R} \cdot T} + c_{j_c, \text{li}} V_{\text{seg, li}}}{\frac{H_{j_c} V_{\text{seg, gas}}}{\bar{R} \cdot T} + V_{\text{seg, li}}} \quad (\text{B.23})$$

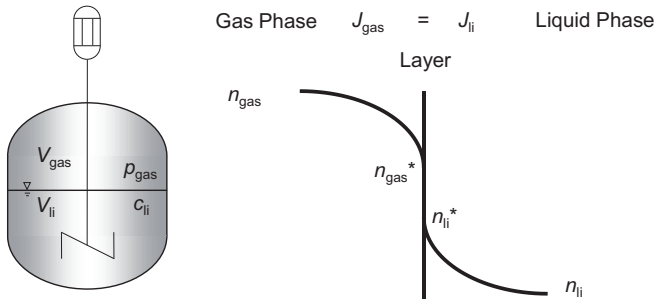


Figure B.1: Molar amount profile of a component over a gas liquid boundary layer

## B.4 Loop reactor model for experimental data prediction

A well-established classification of continuum models for fixed bed reactor simulations was drafted by Froment et al. (Froment and Bischoff, 1990). The models differ between which phases are considered in the modeling. Frequently often single pseudo-homogeneous or heterogeneous phase models with respect to the spatial resolution are used. Considering phase transitions between gas, liquid and solid phases additional information are required.

The derived partial mass balances as well as the thermal energy balance based on the control volume illustrated in fig. B.2. The one dimensional effective reactor model is presented by a pseudo-homogeneous model neglecting interphase transport limitations. Based on the weighed catalyst mass for each reactor, a constant void fraction  $\varepsilon$  is assumed. For all gas phase components, the ideal gas law is applied. Due to large temperature gradients inside the catalyst fixed bed, gas phase properties and gas velocity are calculated as function of temperature. Radial heat transfer through the reactor jacket is measured separately and considered in reactor modeling.

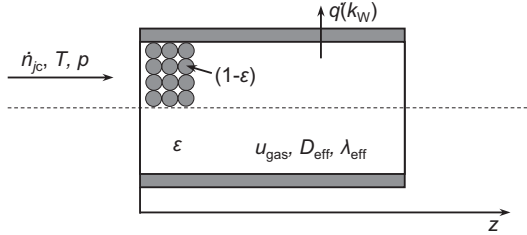


Figure B.2: Control volume for the reactor model

### B.4.1 Mass balance

The partial molar flux balance for component  $j_c$  is defined by eq. B.24:

$$\varepsilon \frac{\partial \dot{n}_{j_c}}{\partial t} = -u_{\text{gas}} \frac{\partial \dot{n}_{j_c}}{\partial z} + D_{\text{eff},j_c} \frac{\partial^2 \dot{n}_{j_c}}{\partial z^2} + \frac{m_{\text{cat}} \dot{V}_{\text{tot}}}{V_{\text{seg}}} \sum_{j_R=1}^{N_R} v_{j_R/j_c} \cdot r_{j_R} \quad (\text{B.24})$$

The used initial and boundary conditions according to (Danckwerts, 1953) are defined by:

$$\dot{n}_{j_c}(t=0, z) = \dot{n}_{j_c}^0 \quad u_{\text{gas}} \dot{n}_{j_c}^{\text{in}} = u_{\text{gas}} \dot{n}_{j_c} \Big|_{z=0} - D_{\text{eff},j_c} \frac{d\dot{n}_{j_c}}{dz} \Big|_{z=0} \quad \frac{d\dot{n}_{j_c}}{dz} \Big|_{z=L_{\text{seg}}} = 0 \quad (\text{B.25})$$

### B.4.2 Thermal energy balance

The thermal energy balance including radial heat transfer through the reactor jacket is specified as follows:

$$\left( \varepsilon (\rho c_p)_{\text{gas}} + (1-\varepsilon) (\rho c_p)_s \right) \frac{\partial T}{\partial t} = -(\rho c_p)_{\text{gas}} u_{\text{gas}} \frac{\partial T}{\partial z} + \lambda_{\text{eff}} \frac{\partial^2 T}{\partial z^2} + \frac{m_{\text{cat}}}{V_{\text{seg}}} \sum_{j_R=1}^{N_R} (-\Delta h_R)_{j_R} r_{j_R} + k_W \frac{U}{A_B} (T_U - T) \quad (\text{B.26})$$

With the initial and boundary conditions according to (Danckwerts, 1953):

$$T(t=0, z) = T^0 \quad (\rho c_p)_{\text{gas}} u_{\text{gas}} T^{\text{in}} = (\rho c_p)_{\text{gas}} u_{\text{gas}} T \Big|_{z=0} - \lambda_{\text{eff}} \frac{dT}{dz} \Big|_{z=0} \quad \frac{dT}{dz} \Big|_{z=L_{\text{seg}}} = 0 \quad (\text{B.27})$$

### B.4.3 Parameterization

Physical properties of the gas phase components  $j_c$  and the solid catalyst phase are temperature dependent, because of the large temperature fluctuations inside the reactor fixed bed. The respective values are shown in the following.

**Catalyst heat capacity** The heat capacity of the catalyst particles in  $\text{J} \cdot (\text{kg}_{\text{cat}} \cdot \text{K})^{-1}$  is measured as function of temperature using DSC 111 calorimeter (*Setaram*). The approximation is given by eq. B.28.

$$c_{p,\text{cat}}(T) = -2365 - 0.481 \cdot T + 585 \cdot \ln(T) \quad (\text{B.28})$$

**Gas phase heat capacity** the heat capacity of several gas phase components in  $\text{J} \cdot (\text{mol} \cdot \text{K})^{-1}$  is calculated by a polynomial equation. The corresponding parameters are taken from (Yaws, 1999).

$$c_{p,\text{gas},j_c}(T) = P_{c_p,\text{gas},j_c,1} + P_{c_p,\text{gas},j_c,2} T + P_{c_p,\text{gas},j_c,3} T^2 + P_{c_p,\text{gas},j_c,4} T^3 + P_{c_p,\text{gas},j_c,5} T^4 \quad (\text{B.29})$$

**Table B.1:** Used parameters for single component heat capacity calculation (eq. B.29) (Yaws, 1999)

	$P_{c_p,\text{gas},1}$	$P_{c_p,\text{gas},2}$	$P_{c_p,\text{gas},3}$	$P_{c_p,\text{gas},4}$	$P_{c_p,\text{gas},5}$
$\text{C}_2\text{H}_4$	32.083	$-1.4831 \cdot 10^{-2}$	$2.4774 \cdot 10^{-4}$	$-2.3766 \cdot 10^{-7}$	$6.8274 \cdot 10^{-11}$
$\text{C}_3\text{H}_6$	31.298	$7.2449 \cdot 10^{-2}$	$1.9481 \cdot 10^{-4}$	$-2.1582 \cdot 10^{-7}$	$6.2974 \cdot 10^{-11}$
$\text{O}_2$	29.526	$-8.8999 \cdot 10^{-3}$	$3.8083 \cdot 10^{-5}$	$-3.2629 \cdot 10^{-9}$	$8.8607 \cdot 10^{-12}$
$\text{CO}$	29.556	$-6.5807 \cdot 10^{-3}$	$2.0130 \cdot 10^{-5}$	$-1.2227 \cdot 10^{-8}$	$2.2617 \cdot 10^{-12}$
$\text{CO}_2$	27.437	$4.2315 \cdot 10^{-2}$	$-1.9555 \cdot 10^{-5}$	$3.9968 \cdot 10^{-9}$	$-2.9877 \cdot 10^{-13}$
$\text{H}_2\text{O}$	33.933	$-8.4186 \cdot 10^{-3}$	$2.9906 \cdot 10^{-5}$	$-1.7825 \cdot 10^{-8}$	$3.6934 \cdot 10^{-12}$
$\text{N}_2$	29.342	$-3.5395 \cdot 10^{-3}$	$1.0076 \cdot 10^{-5}$	$-4.3116 \cdot 10^{-9}$	$2.5935 \cdot 10^{-13}$

Depending on the current gas phase composition, the total gas phase heat capacity is calculated by the sum of all components.

$$c_{p,\text{gas,tot}}(T) = \sum_{j_c=1}^{N_c} x_{j_c} \cdot c_{p,\text{gas},j_c}(T) \quad (\text{B.30})$$

**Enthalpy of formation** Similar to the gas phase heat capacity, the enthalpy of formation in  $\text{kJ} \cdot \text{mol}^{-1}$  is calculated for each reactant and product component as function of temperature by a polynomial of second degree. The corresponding parameters for each component are listed in table B.2 (Yaws, 1999).

$$H_{f,\text{gas},j_c}(T) = P_{H_f,\text{gas},j_c,1} + P_{H_f,\text{gas},j_c,2} T + P_{H_f,\text{gas},j_c,3} T^2 \quad (\text{B.31})$$

**Table B.2:** Used parameters for enthalpy of formation calculation (eq. B.31) (Yaws, 1999)

	$P_{Hf, gas, jc, 1}$	$P_{Hf, gas, jc, 2}$	$P_{Hf, gas, jc, 3}$
C <sub>2</sub> H <sub>4</sub>	63.053	-4.1076 · 10 <sup>-2</sup>	1.6598 · 10 <sup>-5</sup>
C <sub>3</sub> H <sub>6</sub>	37.334	-6.5191 · 10 <sup>-2</sup>	2.8085 · 10 <sup>-5</sup>
O <sub>2</sub>	0	0	0
CO	-112.190	8.1182 · 10 <sup>-3</sup>	-8.0425 · 10 <sup>-6</sup>
CO <sub>2</sub>	-393.422	1.5913 · 10 <sup>-4</sup>	-1.3945 · 10 <sup>-6</sup>
H <sub>2</sub> O	-241.800	0	0

**Enthalpy of reaction** The enthalpy of reaction of all considered reaction is calculated by the law of *Hess* (eq. B.32). The corresponding single component formation enthalpies were calculated by eq. B.31 and the stoichiometric coefficient can be read from the reaction network (see fig. 5.2).

$$\Delta H_{R,jR}(T) = \sum_{jc=1}^{N_c} \nu_{jc} \cdot H_{t,jc}(T) \quad (B.32)$$

#### B.4.4 Effective axial energy dispersion

The effective axial heat conductivity for the standard model can be calculated by *Zehner, Bauer and Schlünder* as shown in (*Verein Deutscher Ingenieure*, 2006).

$$\frac{\lambda_{ax}}{\lambda_{gas}} = K_{bed} + \frac{Pe_0}{K_{ax}} \quad \text{with} \quad Pe_0 = \frac{u_{gas}(\rho c_p)_{gas} d_p}{\lambda_{gas}}, \quad K_{ax} = 2 \quad (B.33)$$

The axial heat conductivity of the gas phase components in W·(m·K)<sup>-1</sup> is calculated by a polynomial of second degree (eq. B.34). The corresponding parameters are listed in tab. B.3 (Yaws, 1999).

$$\lambda_{jc}(T) = P_{\lambda_{jc},1} + P_{\lambda_{jc},2} \cdot T + P_{\lambda_{jc},3} \cdot T^2 \quad (B.34)$$

**Table B.3:** Used parameters for single component heat conductivity calculation (eq. B.34) (Yaws, 1999)

	$P_{\lambda_{jc},1}$	$P_{\lambda_{jc},2}$	$P_{\lambda_{jc},3}$
C <sub>2</sub> H <sub>4</sub>	-0.00123	3.6219 · 10 <sup>-5</sup>	1.2459 · 10 <sup>-7</sup>
C <sub>3</sub> H <sub>6</sub>	-0.01116	7.5155 · 10 <sup>-5</sup>	6.5558 · 10 <sup>-8</sup>
O <sub>2</sub>	0.00121	8.6157 · 10 <sup>-5</sup>	-1.3346 · 10 <sup>-8</sup>
CO	0.00150	8.2713 · 10 <sup>-5</sup>	-1.9171 · 10 <sup>-8</sup>
CO <sub>2</sub>	-0.01183	1.0174 · 10 <sup>-4</sup>	-2.2242 · 10 <sup>-8</sup>
H <sub>2</sub> O	0.00053	4.7093 · 10 <sup>-5</sup>	4.9551 · 10 <sup>-8</sup>
N <sub>2</sub>	0.00309	7.5930 · 10 <sup>-5</sup>	-1.1014 · 10 <sup>-8</sup>

Depending on the current gas phase composition, the total gas phase heat conductivity is calculated by the sum of all components.

$$\lambda_{gas,tot}(T) = \sum_{jc=1}^{N_c} x_{jc} \cdot \lambda_{jc}(T) \quad (B.35)$$

### B.4.5 Effective axial mass dispersion

The effective axial mass dispersion is described by eq. B.36. For this expression averaged and space independent for the molecular dispersion  $D_m$  for each species in the gas phase are assumed. The first term on the right hand side is obtained from the fixed bed porosity (Verein Deutscher Ingenieure, 2006). The mass *Peclet* number is defined in eq. B.37.

$$\frac{D_{ax}}{D_m} = \frac{D_{bed}}{D_m} + \frac{Pe_0}{K_{ax}} \quad \text{with} \quad \frac{D_{bed}}{D_m} = 1 - \sqrt{1 - \varepsilon} \quad (\text{B.36})$$

$$Pe_0 = \frac{u_{gas} d_p}{D_m} \quad (\text{B.37})$$

The molecular axial dispersion for each gas phase species is calculated by the basis of (Hirschfelder et al., 1964).

### B.4.6 Heat transfer through reactor jacket

The effective heat transmission coefficient through the reactor shell is measured experimentally. Therefore, the catalyst fixed bed is heated up to a maximum of 700 °C. If the temperature is reached the gas flow is set zero. Thus, the cooling curve of the catalyst fixed bed is recorded (see fig. B.3). Subsequent the effective heat transmission coefficient is estimated as function of the temperature. The corresponding expression and estimated parameters are shown in eq. B.38.

$$k_w(T) = 7.539 \cdot 10^4 \cdot \exp\left(\frac{-8200}{T}\right) + 0.71 \quad \text{in} \left(\text{W} \cdot (\text{m}^2 \cdot \text{K})^{-1}\right) \quad (\text{B.38})$$

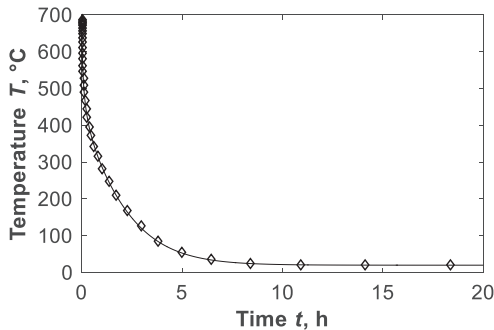


Figure B.3: Cooling curve of the catalyst fixed bed over time ( $u_{gas} = 0$ )

### B.5 Simulation study for improved Loop Reactor operation

The LR concept is prepared to total oxidize autothermal lean waste gas streams (Sheintuch and Nekhamkina, 2005). Variations in feed concentrations and total flow-rate within the reactor bounds can be successfully controlled within ignited conditions by the used controller concept developed by (Zahn et al., 2011) (section 6.2.2). An increase of the VOC inlet concentration or the total flow-rate above the designed reactor limits leads to a local overheating of the reactor cascade. However, in industrial application the exhaust gas flow properties offer temporal fluctuations. Accordingly, the maximum and minimum values can be beyond the specified limits of the LR plant. For such situations usually a surge drum is required to average the inlet values and stabilize the LR process.

In this work the idea of an improved dosing concept is studied to prevent a reactor overheating avoiding hot spots and catalyst deactivating (fig. B.4). The experimental realization is already introduced in fig. 6.17. The additional dosing of feed gas between the reactor segments (see Feed 2 in fig. 6.17 and fig. B.4) can be used to split the overloaded exhaust gas stream in two parts. Accordingly, the VOC amount is decreased within the reaction zone of one segment. If required, a dilution of both feed fluxes (Feed I and Feed II) with nitrogen or air provides an additional adiabatic temperature rise decrease. Basic requirement of this proceeding is a preheated second reactor segment in the cascade. For this purpose, in the parametric study the reactor cascade is enlarged by a third segment. Thus, two segments are available for the total oxidation and one segment is heated up again.

First simulation results are shown in fig. B.5. The results are created using the full total oxidation kinetic model determined by the GCCK approach in section 5. The reactor and catalyst fixed bed geometry is adopted from the experimental part in section 6.4.1. As overall inlet conditions a total volumetric flux of  $1000 \text{ l}\cdot\text{h}^{-1}$  and a propylene molar ratio of 1 % is used. To illustrate the effect of the second dosing position the split ratio of the total inlet molar flux is varied (100:0 / 95:5 / 90:10). The remaining parameters are set constant and adopted from the experimental study (section 6.4). Based on the autothermal operation mode, both feed fluxes are on ambient temperature.

The simulated temperature, conversion and yield profiles of the standard operation mode (fig. B.5) correspond to the single reactant results from section 6.3. The maximum temperature of the exothermal reaction front is above  $850 \text{ }^\circ\text{C}$ . In this reaction front, total conversion of the propylene reactant is achieved. Based on the observed reaction network CO and  $\text{CO}_2$  is produced, in which CO is immediately total oxidized to  $\text{CO}_2$ . This intermediate production of CO and the corresponding total oxidation to  $\text{CO}_2$  illustrates the importance of the reaction kinetic investigation in section 5. If the maximum temperature goes below  $600 \text{ }^\circ\text{C}$  a total hydrocarbon conversion to  $\text{CO}_2$  is not ensured.

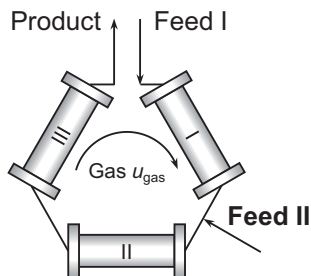


**Figure B.4:** Loop Reactor scheme for an advanced dosing concept using three reactor segments

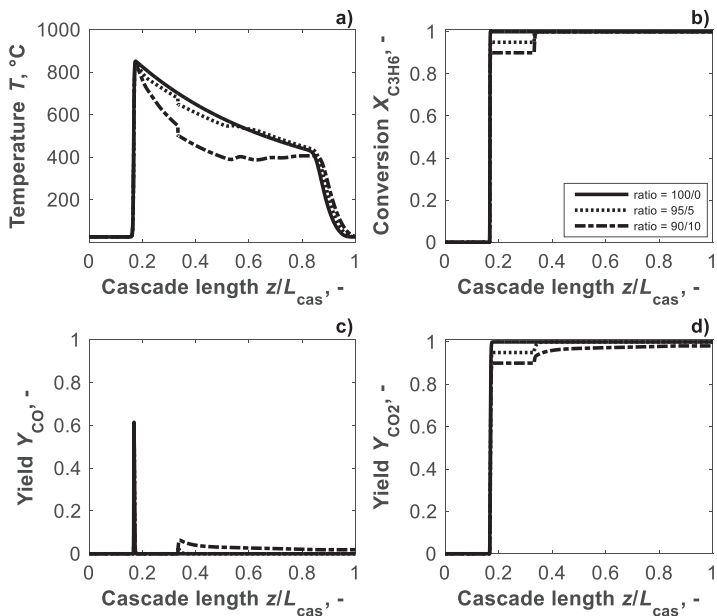


**Figure B.5:** Cyclic steady state profiles of (a) reaction temperature, (b) conversion of propylene and (c and d) yield of CO and CO<sub>2</sub>, respectively, in closed loop operation mode (section 6.2.2;  $T_{sw} = 400$  °C) for different split ratios of the total molar inlet flux. Dosing positions are in front of the first and second reactor segment ( $z/L_{cas} = 0$  and 0.33) ( $\dot{V}_{tot} = 1000$  l·h<sup>-1</sup>;  $x_{C_3H_6}^{in} = 1$  %)

If the split ratio is increased, the residence time of the first reactor segment is increased as well. As aforementioned in the theoretical analysis (section 6.3.2) and experimental part (section 6.4.3) the maximum temperature of the reaction front can be decreased by increasing the residence time. The modeled values for the different split ratios are shown in fig. B.6. The calculated propylene conversion and product yields are related to the total reactant inlet ( $x_{C_3H_6}^{in,feed I} + x_{C_3H_6}^{in,feed II}$ ). Accordingly, the conversion and CO<sub>2</sub> yield profiles offer a step between the first and second formed reaction front. A further increase of the

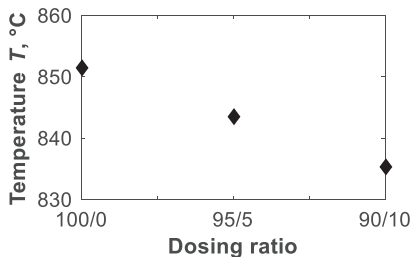


**Figure B.6:** Simulated maximum temperature of the exothermal reaction front for several studied dosing ratios

split ratio leads to partial extinction of the reactor cascade. Based on the second cold inlet feed, the entrance temperature of the second segment is decreased. Related to this, the reaction temperature inside the second segment is insufficient to total oxidize the produced carbon monoxide.

In summary it can be mentioned that the improved dosing concept offer the potential to decrease the maximum temperature in a defined range. However, split ratios beyond the limit lead to partial extinction of the reactor cascade.

### B.6 Estimation of reactant ignition temperature

The estimation of the ignition temperature of a reactant species can be approximated by a zeroth order reaction approach (with  $k_0(T)$ , reaction rate constant of the zeroth order reaction). The corresponding reactor pipe mass balance is shown in eq. B.39.

$$u_{\text{gas}} \frac{dc}{dz} = -k_0(T) \quad (\text{B.39})$$

The integration over the reactor length and the concentration bounds holds:

$$\frac{L_{\text{seg}}}{u_{\text{gas}}} = -\frac{1}{k_0(T)} (c^{\text{out}} - c^{\text{in}}) \quad (\text{B.40})$$

If total conversion is assumed ( $c^{\text{out}} = 0$ ) and the reaction rate constant is replaced by an initial reaction rate of a first order reaction (see eq. B.41):

$$k_0(T) = k(T) c^{\text{in}} = k_{\infty} \exp\left(\frac{-E_A}{RT_{\text{ign}}}\right) c^{\text{in}} \quad (\text{B.41})$$

the ignition temperature  $T_{\text{ign}}$  can be provided by the explicit expression in eq. B.42.

$$T_{\text{ign}} = \frac{E_A}{\bar{R} \ln\left(\frac{L_{\text{seg}} k_{\infty}}{u_{\text{gas}}}\right)} \quad (\text{B.42})$$

### B.7 Definition of traveling front velocities

Spatio-temporal patterns of reactor dynamics as well as forced unsteady state operations have been extensively studied in literature (Wicke and Vortmeyer, 1959; Lauschke and Gilles, 1994; Luss and Sheintuch, 2005). Based on this knowledge the thermal and exothermal reaction front velocities can be determined.

#### Thermal front

The propagation of temperature disturbances in packed beds can be approximated by a simplified pseudo-homogeneous energy balance neglecting heat transfer, reaction and heat dispersal. Thus, eq. 2.50 results in eq. B.43.

$$\left(\varepsilon(\rho c_p)_{\text{gas}} + (1-\varepsilon)(\rho c_p)_{\text{cat}}\right) \frac{\partial T}{\partial t} = -(\rho c_p)_{\text{gas}} u_{\text{gas}} \frac{\partial T}{\partial z} \quad (\text{B.43})$$

Using the following manipulation of the energy balance the thermal front velocity  $u_T$  can be given by eq. B.44.

$$u_T = -\frac{\partial T/\partial t}{\partial T/\partial z} = -\frac{dz}{dt}\bigg|_T = \frac{\varepsilon(\rho C_p)_{\text{gas}}}{\left(\varepsilon(\rho C_p)_{\text{gas}} + (1-\varepsilon)(\rho C_p)_{\text{cat}}\right)} u_{\text{gas}} \quad (\text{B.44})$$

In general, the volumetric heat capacity of the gas phase is by orders of magnitude smaller than of the catalyst. Accordingly, the following expression is suggested.

$$(\rho C_p)_{\text{gas}} \ll (\rho C_p)_{\text{cat}} \quad (\text{B.45})$$

Thus, eq. B.4 can be simplified to eq. B.46.

$$u_T \approx \frac{\varepsilon(\rho C_p)_{\text{gas}}}{(1-\varepsilon)(\rho C_p)_{\text{cat}}} u_{\text{gas}} \quad (\text{B.46})$$

### Exothermic reaction front

The deviation of the exothermic reaction front velocity is considerably more difficult than the thermal front because of the strongly coupled energy and mass balance via the reaction term. First detailed modeled analysis of the exothermic reaction front and the identification of the principal properties were done by (Frank-Kamenetskii, 1959; Wicke and Vortmeyer, 1959; Kiselev and Matros, 1980; Burghardt et al., 1999).

The origin of the deviation is the already presented pseudo-homogeneous energy (eq. 2.50) and molar flux (eq. 2.47) balance of the LR system. Neglecting heat and mass dispersal as well as mass accumulation the balances can be reduced to eqs. B.47 and B.48, respectively.

$$\left(\varepsilon(\rho C_p)_{\text{gas}} + (1-\varepsilon)(\rho C_p)_{\text{cat}}\right) \frac{\partial T}{\partial t} + (\rho C_p)_{\text{gas}} u_{\text{gas}} \frac{\partial T}{\partial z} = \frac{m_{\text{cat}}}{V_{\text{seg}}} (-\Delta H_R) R \quad (\text{B.47})$$

$$u_{\text{gas}} \frac{d\dot{n}_{j_c}}{dz} = \frac{m_{\text{cat}} \dot{V}_{\text{tot}}}{V_{\text{seg}}} v_{j_c} \cdot R \quad (\text{B.48})$$

The steady state molar flux balance can be rearranged considering the reaction rate  $R$  and insert in the energy balance. Thus, the energy balance results in eq. B.49.

$$\left(\varepsilon(\rho C_p)_{\text{gas}} + (1-\varepsilon)(\rho C_p)_{\text{cat}}\right) \frac{\partial T}{\partial t} + (\rho C_p)_{\text{gas}} u_{\text{gas}} \frac{\partial T}{\partial z} = (-\Delta H_R) \frac{u_{\text{gas}}}{V_{\text{tot}} v_{j_c}} \frac{\partial \dot{n}_{j_c}}{\partial z} \quad (\text{B.49})$$

Using the manipulation of eq. B.50 for the exothermic reaction front velocity and insert them in eq. B.49, eq. B.51 holds.

$$u_R = -\frac{\partial T/\partial t}{\partial T/\partial z} = -\frac{dz}{dt} \quad (\text{B.50})$$

$$\left(\varepsilon(\rho C_p)_{\text{gas}} + (1-\varepsilon)(\rho C_p)_{\text{cat}}\right) u_R + (\rho C_p)_{\text{gas}} u_{\text{gas}} = \frac{(-\Delta H_R)}{V_{\text{tot}} v_{j_c}} u_{\text{gas}} \frac{\partial \dot{n}_{j_c}}{\partial T} \quad (\text{B.51})$$

The integration occurred in the temperature range from the inlet  $T^{\text{in}}$  to the maximum  $T^{\text{max}}$  and for concentration from the initial  $c_{j_c}^0$  to zero, which corresponds to total conversion. Additionally, using the thermal front velocity  $u_T$  (eq. B.44) and the adiabatic temperature rise (eq. B.52) the exothermic reaction front velocity follows to eq. B.53.

$$\Delta T_{\text{ad}} = \frac{(-\Delta H_R) c_{j_c}^0}{(\rho C_p)_{\text{gas}} (-v_{j_c})} \quad (\text{B.52})$$

$$u_R = \left(1 - \frac{\Delta T_{ad}}{\Delta T}\right) u_T \quad \text{with} \quad \Delta T = T^{\max} - T^{\text{in}} \quad (\text{B.53})$$

### C. Single Component Adsorption Isotherms

Corresponding to fig. 5.6c single component adsorption isotherms of all measured reactants and products are shown in fig. C.1. Single component experimental adsorption isotherms are described by *Henry-Langmuir* adsorption models (eq. 5.8). The adsorption parameters are presented in tab. 5.1. In fig. C.2 single component experimental adsorption isotherms are described via simplified *Langmuir* isotherm models (eq. 5.6). Corresponding adsorption parameters are presented in tab. 5.2.

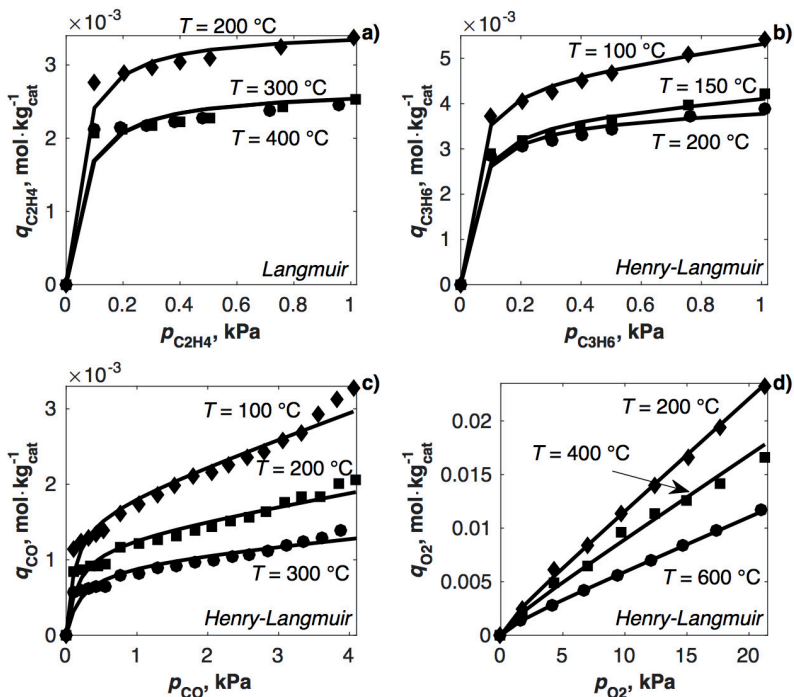


**Figure C.1:** Single component adsorption isotherms for different temperatures for (a) ethylene, (b) propylene, (c) carbon monoxide and (d) oxygen described by *Henry-Langmuir* adsorption models (eq. 5.8), estimated adsorption parameters from tab. 5.1

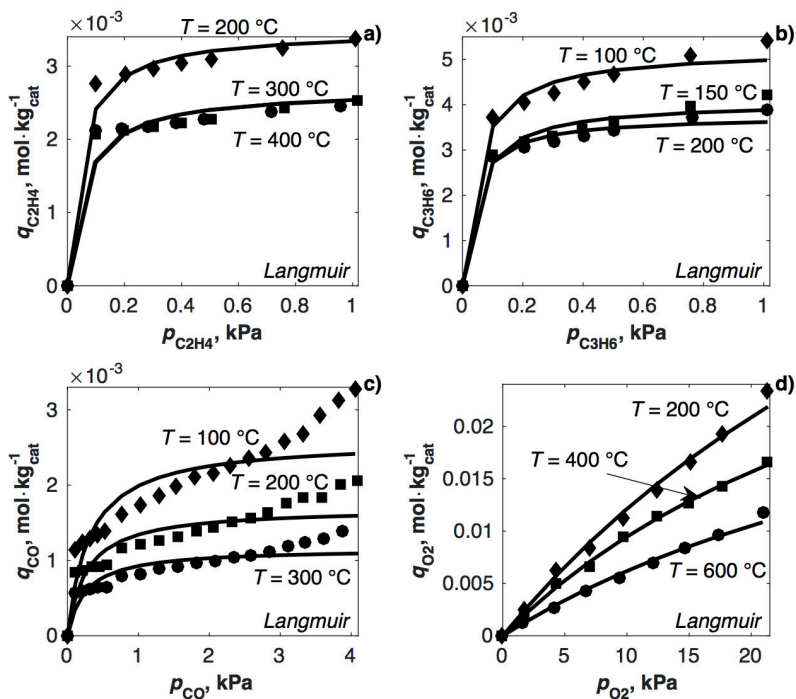
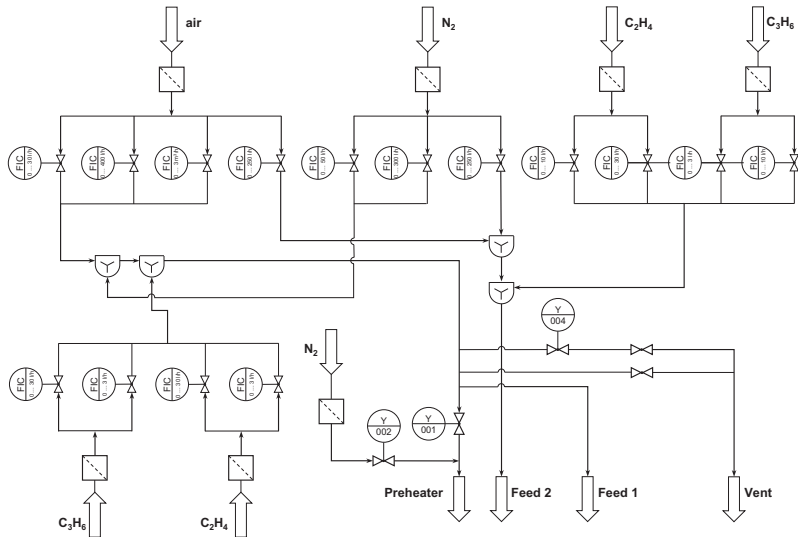


Figure C.2: Single component adsorption isotherms for different temperatures for (a) ethylene, (b) propylene, (c) carbon monoxide and (d) oxygen described by *Langmuir* adsorption models (eq. 5.6), estimated adsorption parameters from tab. 5.2

## D. Schematic Illustrations of the Loop Reactor Plant

In this section the schematic illustration of the gas supply unit (fig. D.1) and the analytic unit (fig. D.2) of the Loop Reactor plant (fig. 6.17) are shown corresponding to the explanation of section 6.4.



**Figure D.1:** Schematic illustration of the gas supply unit including gas mass flow controller (*Bronkhorst*) and magnetic valves (*Bürkert*) of the Loop Reactor plant, explained in more detail in section 6.4

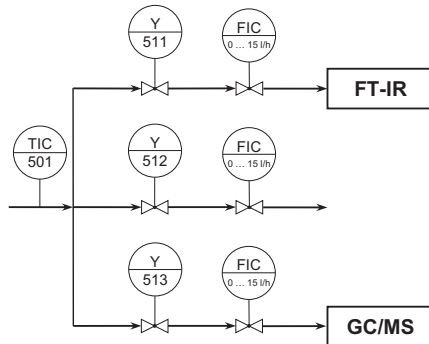


**Figure D.2:** Schematic illustration of the analytic unit including gas mass flow controller (*Bronkhorst*) and magnetic valves (*Bürkert*) of the Loop Reactor plant, explained in more detail in section 6.4